CHARGE TRANSPORT THROUGH SINGLE-MOLECULE JUNCTIONS

EXPERIMENTS AND THEORY

CHARGE TRANSPORT THROUGH SINGLE-MOLECULE JUNCTIONS

EXPERIMENTS AND THEORY

Proefschrift

ter verkrijging van de graad van doctor
aan de Technische Universiteit Delft,
op gezag van de Rector Magnificus prof. ir. K. C. A. M. Luyben,
voorzitter van het College voor Promoties,
in het openbaar te verdedigen op vrijdag 19 juni 2015 om 15:00 uur

door

Mickael Lucien PERRIN

natuurkundig ingenieur
geboren te Thonon-les-Bains, Frankrijk.

Dit proefschrift is goedgekeurd door de promotor:

Prof. dr. Herre S.J. van der Zant

Samenstelling promotiecommissie:

Rector Magnificus,	voorzitter
Prof. dr. Herre S.J. van der Zant,	Technische Universiteit Delft, promotor
Dr. Joseph M. Thijssen	Technische Universiteit Delft
Prof. dr. Jan H. van Esch	Technische Universiteit Delft
Prof. dr. Jan M. van Ruitenbeek	Universiteit Leiden
Dr. Michel Calame	University of Basel, Switerland
Prof. dr. Maarten Wegewijs	RWTH Aachen University, Germany
Prof. dr. Diana Dulić	University of Chile, Chile
Prof. dr. Peter Steneken	Technische Universiteit Delft, reservelid

Keywords: single-molecule electronics, charge transport, mechanically controllable break junction, two- and three-terminal measurements, quantum chemistry, density functional theory, non-equilibrium Green's functions

Printed by: Proefschriftmaken.nl || Uitgeverij BOXPress

Published by: Uitgeverij BOXPress, 's-Hertogenbosch

Front & Back: Mickael L. Perrin

Casimir PhD Series, Delft-Leiden 2015-06

ISBN 978-90-8593-221-5

An electronic version of this dissertation is available at
`http://repository.tudelft.nl/`.

CONTENTS

1

INTRODUCTION

In this chapter, an introduction to the field of molecular electronics is provided. We start with a brief history of the research field, after which the state of the art is introduced. Finally, we speculate on some of the ultimate goals, and discuss the main challenges hindering the realization of reliable functional single-molecule devices.

1

1.1. MOLECULAR ELECTRONICS

Since the beginning of molecular electronics, the field has been driven by the dream of incorporating molecular components as functional elements in electronic devices (see Fig.1.1). When in the 70's the first single-molecule diode was proposed[1], the main advantage of using molecular devices laid in their small size. The transistors, at that time, where mostly made from galium arsenide (GaAs) or silicon carbide (SiC) and had channel lengths of several microns[2]. The use of nanometer-sized molecules therefore sounded very appealing for electronic purposes. Consequently, besides the rectifier, applications such as a molecular processor[3], interconnects[4], logic gates[5], memory devices[6] and shift registers[7] were proposed.

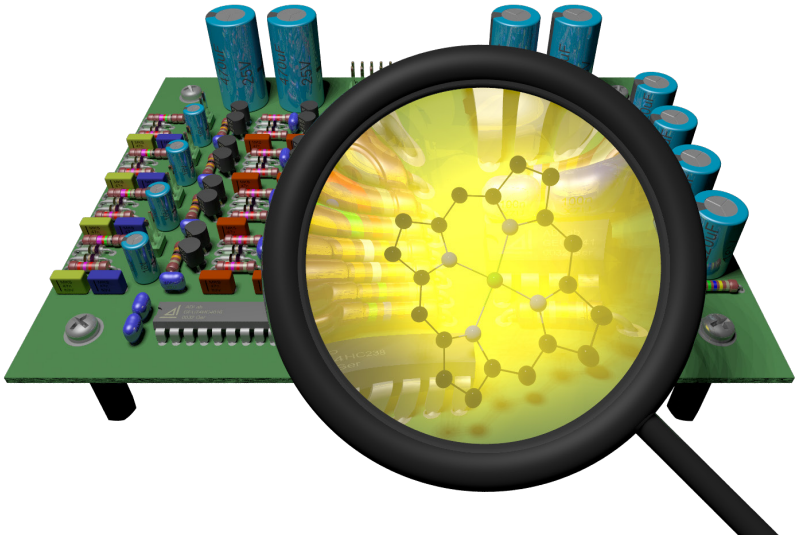

Figure 1.1: **Incorporating molecules in electronic devices: the dream of molecular electronics.**

However, due to the lack of suitable technologies for electrically contacting individual molecules, experimental investigations mainly focused on electron transfer processes in molecules in gas-phase and liquid-phase systems[8]. Driven by advances in technology, many different types of devices have been realized on large ensembles of molecules using self-assembled monolayers (SAMs), such as molecular logic gates[9], switches[10], photon-based logic gates[11], rectifiers[12], memory cells[13], organic light emitting diodes[14], solar cells[15, 16], etc...

Meanwhile, steps towards single-molecule devices were made, and in 1995 a current was sent through a single molecule[17]. Using a scanning tunneling microscope, researchers measured the resistance of a single C_{60} molecule. In this experiment, however, no current-voltage characteristics were recorded and information about the density of states of the molecule was lacking. In 1997, the first true metal-molecule-metal junction was realized containing a single molecule[18]. This was achieved using a mechanically controllable break-junction, which had been used previously to successfully study single-atom quantum point contacts[19, 20]. In this groundbreaking experiment, the researchers measured the current though a single benzene-

1,4-dithiol molecule at room temperature. Thiol end groups were used to form a stable metal-molecule-metal junction. In addition, steps in the current-voltage characteristics were observed as a result of the discreteness of the molecular levels, thereby revealing the quantum nature of the junction.

In 2000, researchers used the electromigration technique to sandwiched a C_{60} molecule between two gold electrodes[21]. By applying a voltage on a third gate, the current between the source and the drain could be regulated, thereby creating the very first single-molecule transistor. Although the device showed transistor behaviour, its performances greatly lack behind that of semiconducting transistors[1].Besides being small, semiconducting transistors are also highly reliable and fast to switch. Therefore, in the domain of computation and especially for high-performance computing, single molecules are no match for semiconducting transistors, and will probably never be.

Molecules, on the other hand, can provide additional functionalities compared to semiconductors. Using synthetic chemistry, an almost endless choice of molecular structures and compositions is available. With the proper knowledge, one can design single molecules that can perform a variety of tasks which would be unthinkable in solid-state devices, or would require a very high degree of complexity. As molecules can react to external stimuli, such as light[22], force[23], pH[24], sound[25] and magnetic field[26], it is not surprising that many more applications for single-molecule devices have been found. Researchers have build electromechanical amplifiers[27], optical switches[28, 29], diodes[30], chemical switches[31], mechanical switches[23], potentiometers[32], solar cells[22], light emitter[33], pH sensors[24], acoustical sensors[25], magnetic field sensors[26], negative tunneling devices[34], qubits [35, 36], etc... For all of these devices, the desired functionality was obtained by tuning the properties of just a single molecule. This does not only render these devices very small, but also potentially with a very high sensitivity (gas sensors could for instance react on single O_2 molecules). Moreover, the knowledge gained at the single-molecule scale can change the way practical problems are approached in, for instance, sensing, solar-energy harvesting, thermo-electrics and catalysis.

Ultimately, full-scale electronic circuit may be build from single molecules, possibly by means of self-assembly. One could imagine solutions containing different kinds of molecular components such as wires, diodes, transistors, or memory elements, being mixed and self-assembling on a surface into a fully operational electronic circuit. The creation of such circuits could occur at dramatically lower costs compared to the ones of current semiconductors, without requiring complex machines and procedures. One could even think of going beyond the limitations of semiconductors, by incorporating also switches, different kind of sensors, motors, or light emitters, etc. The combination of functionalities would be close to endless, such as for example light-driven molecular motors, or sensors which emit light upon

[1] During the last decades, and supported by billions of dollars invested each year, the semiconductor industry has exponentially decreased the size of the transistor, while increasing the number of transistors per chip from a few thousand up to a few billion[2]. Being in the micron range in the 1970's and 1980's, by 2000 their size dropped below 100 nm, and will go down to 10 nm in 2015. The down-scaling is expected to go as low as 5 nm in 2020.

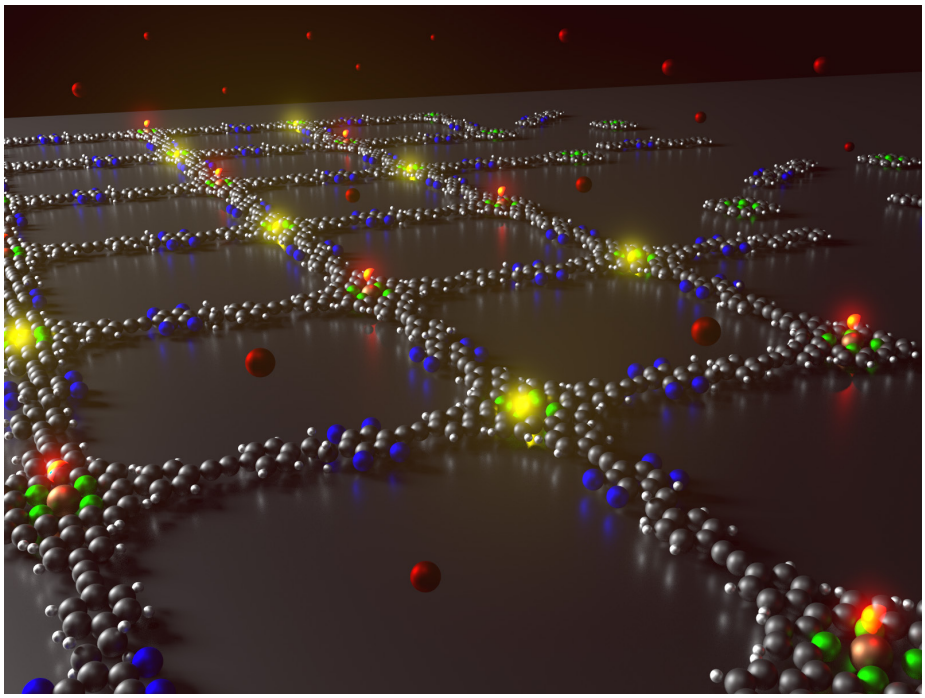

Figure 1.2: **Artist impression of a self-assembling gas sensor.** The red balls floating around represent gas molecules, for instance oxygen. When bound to the Fe-porphyrins (red glow), the Au-porphyrin start to emit yellow light. The porphyrins are connected to each other via a molecular wire.

detection of gas or humidity, of which an artist impression is presented in Fig. 1.2.

1.2. CHALLENGES IN THE FIELD

Despite tremendous progress, the field of molecular electronics is still in its infancy, and many challenges remain to be solved. In the following section, we briefly highlight some of them.

1.2.1. CONTACTING A MOLECULE

One of the major problems is the lack of reproducibility and the intrinsic and extrinsic junction-to-junction variations in quantities such as the conductance. It is well-known that molecular charge transport measurements are strongly influenced by the electrode geometry and the surface chemistry. It is for this reason that numerous ways of forming molecular junctions have been –and are still being– developed such as the scanning tunneling microscope (STM)[37], the mechanically controllable break junction (MCBJ)[18], electron-beam lithography[38], electrochemical plating[39], electromigration[40], focused ion-beam lithography[41], electrodeposition[42], shadow mask evaporation[43], atomic force microscopy (AFM)[44], on-wire lithography[45], crossed wires[46], gold nanoparticles[47], hanging mercury drop junctions[48], eutectic GaIn droplets[49], nanopores[50] and con-

ducting polymers such as PEDOT:PSS[51]. Each of these methods has advantages and drawbacks, and no 'ultimate' method has been developed so far. However, in general, techniques allowing to probe single-molecule junction geometries in a statistically manner are very popular. A few well-known examples are the MCBJ[34, 52–57], the AFM[58–60], and the STM[61–70]. These methods allow to repeatedly fuse and break the contacts and form a 'new' junction in every cycle. As such, one can measure charge transport through hundreds or even thousands of junctions and statistically address the variability in junction formation[52]. It has been found that the variability can significantly be reduced by choosing the proper anchoring group[71, 72]. Moreover, large bulky molecules that can bind in various ways tend to increase the spread in conductance[73, 74]. Also, inter-molecular interactions such as π–π-stacking[54, 64] may play an important role.

1.2.2. UNDERSTANDING THE PHYSICS

Countless studies have been performed at the single-molecule level, thereby greatly increasing the understanding of the different aspects of charge transport such as the role of the anchoring groups[71, 72], the molecular conjugation[55], the molecular conformation[61, 63], or the inelastic contributions to transport[75–77]. Such studies are of crucial importance in understanding the basic ingredients of charge transport. However, to understand many of the physical processes occurring in a molecular junction such as the bond mechanics, charge transfer at the interface, the push-back effect, image-charge formation, level alignment, charging effects due to transport, or magnetic anisotropy, one needs to go beyond conductance measurements[78]. For that purpose, additional probes (see Fig. 1.3 for some examples) such as force[79], thermopower[66], heat dissipation[80], gate[21, 43, 81], distance dependence[34, 56, 82, 83], raman scattering[84], light[85], magnetic fields[86, 87], fluorescence[25, 33] and superconductivity[88–90] have been used. In addition, effects such as quantum interference[91–93] could be exploited for device applications[31, 68, 94].

Another popular approach to gain more insight is by using the low-temperature STM/AFM technique and study molecules on surfaces. Although these molecules are not in a junction geometry, *i.e.*, sandwiched between electrodes, such studies can provide valuable information as they allow to directly image a single molecule. The STM has been used extensively in characterizing electronic structures, for instance during single-bond formation[95]. In addition, it has been used to study potential profiles across molecules[96], visualize molecular orbitals[97], even when hybridized with metallic atoms[98]. The AFM, on the other hand, measures forces on the nano-scale, and can be used to chemically identify individual atoms[99], obtain the chemical structure of molecules[100], and even deduce bond orders[101].

Each method provides a small piece of the puzzle, and one can hope that in time our knowledge increases to a point where the physical processes occurring in a single-molecule junction are understood and can be exploited for novel device applications.

1.2.3. EXPERIMENTS VS. THEORY

Another major challenge is to reduce the mismatch between theory and experiments. Quantum chemistry calculations such as tight-binding, density functional theory (DFT) or Hatree Fock (HF), often used in combination with the non-equilibrium

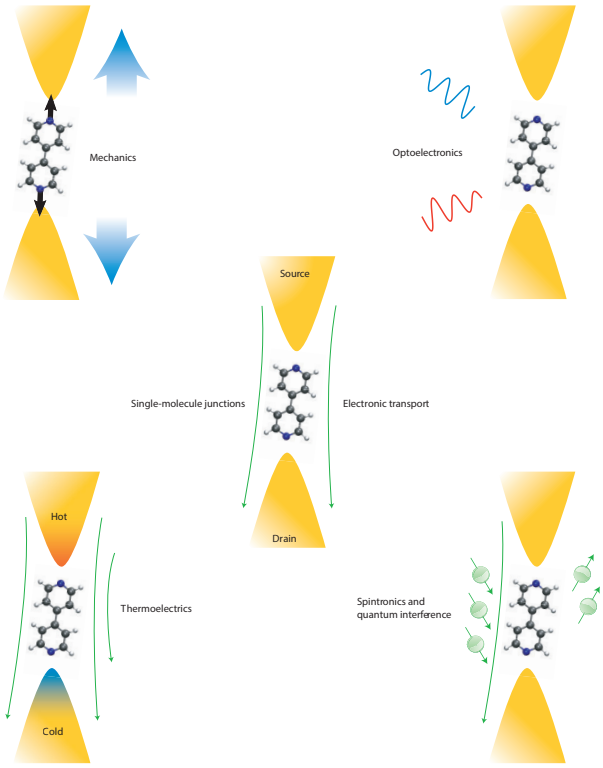

Figure 1.3: **Studying single molecules beyond charge transport.** Image reproduced from Aradhya *et al.*[78].

Green's function (NEGF) formalism for transport, only poorly reproduce experiments. In particular, predicting transport gaps and the position of the Fermi energy has proven to be challenging.

In the HF method, the electron exchange is calculated exactly but within the mean field approximation, thereby neglecting electron correlations. As a result, HF, generally speaking, predicts energies that are too high[102]. DFT, following the Hohenburg–Kohn theorem, can, in principle, determine the ground state and excited state of a system, provided that the functional describing the electron exchange and electron correlation is known exactly[103]. In practice, however, the functionals are semi-empirical approximations, leading to an underestimation of the band gaps[102]. This is due to the mean-field approach, in which the electrons are effectively non-interacting[104]. In addition, DFT (neither does HF) does not take dynamical effects such as screening of added electrons or holes into account, which play an important role during charge transport[56, 105]. As a result, junction conductances are usually overestimated[106] or even show incorrect trends[107].

In pursuit for quantitative agreement, new methods are being investigated, such as post-HF methods, functionals correcting for long-range self-interactions[108], dispersion corrected functionals[109], or hybrid functionals such as B3LYP in which

part of the electron exchange is done exactly within the HF approximation[110]. The most accurate method to date is the GW method[102], in which screening effects are also taken into account. Moreover, GW accounts for the addition and removal of charge, which occurs during charge transport. However, despite the good agreement between experiments and theory, this method is computationally very expensive, rendering it intractable for most of the molecules studied experimentally. In addition, the results can strongly depend on the underlying starting point[111], and the calculations can be challenging to converge[112].

One way to account for charge addition and removal is to extended DFT and include self-energies correction schemes, as is for instance done in DFT+Σ[113]. In this approach, the calculations consist of two parts. First, DFT calculations are performed in the gas-phase for the neutral molecule, and the molecule with ±1 electron. This is to account for the difference between the DFT molecular orbitals and the gas-phase chemical potentials. Second, from the charge distribution of the molecule in the three charge states, one can calculate the polarization energy associated with the image-charges formed in the metallic electrodes upon addition and removal of a charge. Both contributions yield a correction which is applied to the DFT orbitals as calculated in a junction configuration, *i.e.*, with the molecule sandwiched between the two metallic electrodes. DFT+Σ calculations quantitatively reproduce reasonably well conductance values[57, 114] and thermopower[107], as well as current-voltage characteristics[113], while being computationally much less expensive than GW calculations. DFT+Σ, however, takes into account the charge distribution in the gas phase, thereby neglecting charge transfer at the interface due to the hybridization of the molecular orbitals with the states of the electrodes. This transfer is important for two reasons. First, the molecule in a junction geometry could carry a net charge, leading to a significant asymmetry in the renormalization of the occupied and unoccupied levels. Second, the orbitals of a gas-phase molecule and a molecule in a junction could have a different character due to the formation of interface states. To account for these effects, one can for instance consider the molecule in a junction configuration and obtain the charge distribution of the different charge states by using a gate to add and remove charge from the molecule. This approach has been used for successfully explaining polarization-induced level renormalization in single-molecule experiments[56].

Altogether, despite some agreement between experiments and theory, a general theory which accurately predicts molecular properties at a computationally tractable price in still lacking.

1.3. DISSERTATION OUTLINE

In this dissertation, charge transport through single organic molecules is investigated. For this purpose, the two- and three-terminal mechanically controllable break junction (MCBJ) technique is used. In addition, quantum chemistry calculations are performed for a more in-depth understanding of the charge transport properties. The outline of this dissertation is as follows:

Chapter 2 briefly discusses the theoretical background of charge transport through single-molecule junctions.

Chapter 3 describes the MCBJ technique as implemented in Delft, together with some of the measurement schemes.
Chapter 4 presents conductance measurements performed on a series of porphyrine derivatives at room temperature. The influence of the chemical structure on the junction formation is investigated.
Chapter 5 focuses on a single porphyrin derivative, ZnTPPdT-Pyr, which is studied both at room and cryogenic temperatures using conductance histograms and current-voltage characteristics.
Chapter 6 presents low-temperature spectroscopy measurements on ZnTPPdT, in which large shifts of the molecular levels upon changes in electrode separation are observed. Using three-terminal MCBJ devices and quantum chemistry calculations, the observed level shifts are attributed to the presence of image-charges in the electrodes.
Chapter 7 investigates charge transport through dihydro-anthracene. For this particular molecule, pronounced negative differential conductance is observed. Our findings can be understood using an intuitive two-site model, which is supported by quantum chemistry calculations.
Chapter 8 presents theoretical guidelines for an efficient single-molecule diode. Based on a two-site model, the role of the chemical structure is investigated, and in particular, the influence of the substituted side-groups.
Chapter 9 describes the realization of gate-tunable single-molecule diode. Using the molecular design guidelines discussed in the previous chapter, a diode with very high rectification ratios is designed and measured. In addition, the presence of a gate electrode is used to shift the molecular levels, allowing for tuning of the diode's rectification ratio.

2

THEORY

In this chapter, the basic theoretical concepts required to understand charge transport through single molecules are reviewed. We start with the concept of molecular orbitals, after which resonant electron tunneling is discussed. We then expand our description towards three-terminal devices in which a gate electrode is present. Finally, we touch upon higer-order processes such as the Kondo effect and elastic/inelastic cotunneling.

Parts of this chapter have been published in Chem. Soc. Rev. **44**, 902-919 (2015) [115].

As a result of the small size of typical molecules, charge transport though single molecules is dictated by the laws of quantum mechanics. In general, the properties of the molecular junction depend on the ratios between the different energy scales involved in transport. It is therefore instructive to have a more detailed look at these energies. The first important energy scale is the *confinement energy* (Δ). The small size of the molecule causes spatial confinement of the charge carriers (either electrons or holes) on the molecule, leading to the formation of a discrete energy spectrum with various level spacings. A rough estimate of Δ can be obtained from the particle-in-a-box model, yielding $\Delta = \frac{\hbar^2}{2m_e}\left(\frac{\pi}{L_i}\right)^2 \approx 0.4$ eV for a cube with a side of 1 nm. The spatial confinement has a second effect. Since the charge carriers are close to each other, one needs to account for the Coulomb interactions between them, which is called the *charging energy* $E_C = e^2/2C$, where e is the electron charge, and C the capacitance of the molecule to its environment. A typical value for E_C is hundreds of meV. The third important energy is the *thermal energy* k_bT, where k_b is the Boltzmann constant. This energy scale determines the broadening of the observed features as a result of thermal fluctuations. At room temperature the thermal energy is about 25 meV, while at 4 K this energy is only 0.36 meV.

2.1. MOLECULAR ORBITALS

As mentioned above, the charge carriers on the molecule are only allowed to populate discrete energy states, of which the shape is determined by the potential landscape formed by the nuclei. These states are called molecular orbitals. Electrons fill these orbitals starting from the ones with the lowest available energy before filling higher ones. This is known as the *Aufbau principle*. Each orbital can be occupied by at most two electrons, as dictated by the *Pauli exclusion principle*. By definition, the orbital with the highest energy which is fully occupied is called the *highest occupied molecular orbital* (HOMO). The HOMO is to organic semiconductors and quantum dots what the valence band is for inorganic semiconductors. The same analogy exists between the *lowest unoccupied molecular orbital* (LUMO) and the conduction band.

A common method to obtain the electronic structure of a molecule is density functional theory (DFT). After diagonalizing the computed Hamiltonian, the eigenvectors describe the molecular wave functions, while the eigenvalues represent the molecular orbital energies. As an example, the right panel of Fig. 2.1 presents the energy spectrum of a benzene dithiol molecule in gas phase, *i.e.*, in the absence of interaction with the environment. The left panel of Fig. 2.1 shows the isosurface of the wave function of the HOMO and the LUMO. The energy difference between the HOMO and LUMO is called the *HOMO-LUMO gap*, and can be experimentally determined from UV/vis spectroscopy.

2.2. CHARGE TRANSPORT

When describing charge transport through a molecule one also has to take into account the fact that the number of electrons on the molecule changes. Therefore, the energy required to add or remove electrons from the system needs to be considered. The energy required to remove an electron from the molecule and bring it to the vacuum level is called the *ionization potential* (IP). The energy released when an elec-

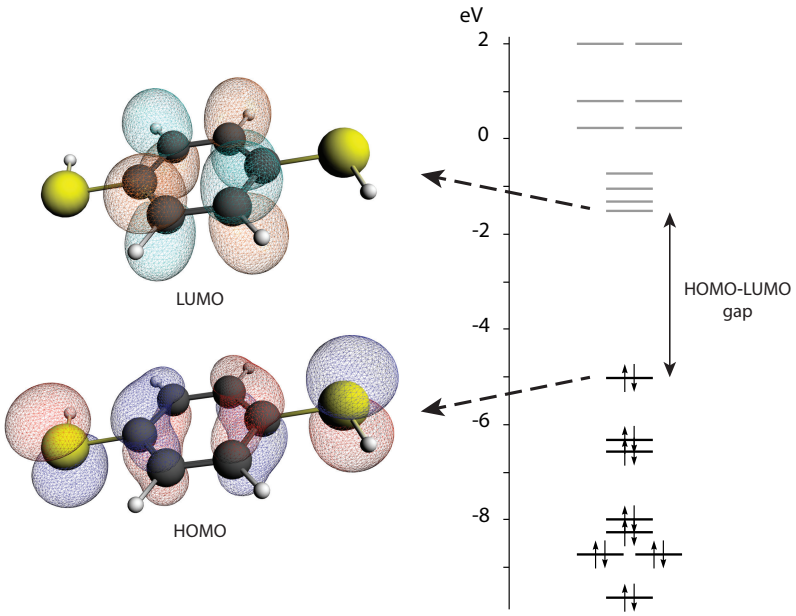

Figure 2.1: **Molecular orbitals of benzene dithiol.** The right panel shows the energy spectrum of the molecular orbitals in the neutral state obtained from DFT. The black lines represent the orbitals occupied with two electrons (arrows); the gray lines indicate the unoccupied orbitals. The left panel presents isosurfaces of the HOMO and LUMO.

tron is added is the *electron affinity* (EA). As a molecule can be (dis)charged multiple times, the total density of states of a molecule can be modelled as a set of chemical potentials, as depicted in Fig. 2.2a. The energy difference between $\mu_{N\to N+1}$ and $\mu_{N-1\to N}$ is referred to as the transport gap, or *addition energy* (E_{add}). $\mu_{N\to N+1}$ is the energy required to add an electron to the molecule, and is therefore equivalent to the EA. The same holds for $\mu_{N-1\to N}$ and the IP. The transport gap is different from the HOMO-LUMO gap, as it consists of the level splitting plus the electrostatic contributions to the energy (*i.e.*, charging energy, image charge corrections, push-back effect) while the HOMO-LUMO gap includes the level splitting only.

When a molecule is brought in the vicinity of the electrodes, the presence of the metallic surface has several important consequences. First, the electrodes act as reservoirs for charge carriers. Those reservoir also have a chemical potential, which at 0 K is equal to the *Fermi energy* (ϵ_F). For T>0 K, the energy distribution of the electrons in the electrodes is smeared out by thermal broadening and given by the Fermi-Dirac distribution function

$$f_\alpha(E) = \frac{1}{1+\exp(\frac{\epsilon-\mu_\alpha}{k_B T})}, \tag{2.1}$$

where ϵ is the electron energy, k_B the Boltzmann constant, μ_α the chemical potential of reservoir α (α is either the source (S) or the drain (D)) and T the temperature. In equilibrium, the chemical potential of both electrodes is equal (see Fig. 2.2b) and no current flows. From statistical mechanics we know that for particles to flow, a

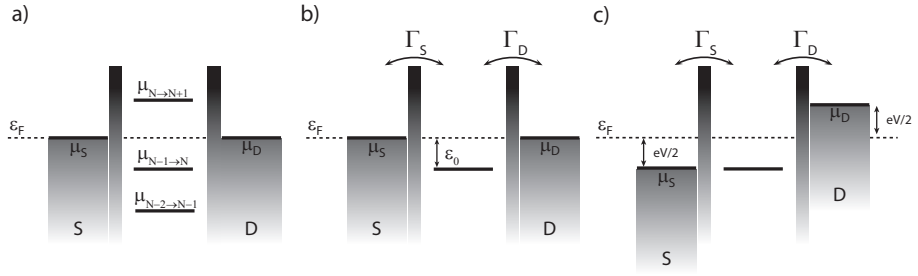

Figure 2.2: **Chemical potential diagram.** (**a**) Schematic representation of a molecular junction consisting of a set of chemical potentials. Here, N represents the number of electrons of the neutral molecule. (**b,c**) Single-level model, in which transport is described by the level alignment ϵ and the electronic coupling Γ. In equilibrium (**b**), no current can flow. Upon application of a bias (**c**), the chemical potential of the leads are different and current flows once the level is inside the bias window.

difference in chemical potential is required. By symmetrically applying a bias voltage V, the chemical potential of the electrodes is shifted according to

$$\mu_s = \epsilon_f + eV_b/2, \tag{2.2}$$

$$\mu_d = \epsilon_f - eV_b/2. \tag{2.3}$$

This results in occupied states in the source, and empty states in the drain. For convenience, the energy range between the chemical potential of the source and the drain electrode is called the *bias window*. When no molecular level is present in the bias window, transport is blocked, as the electrons do not have the necessary energy to occupy/empty an orbital (see Fig. 2.2b). Increasing the bias voltage across the junction increases the bias window, and as soon as the chemical potential of one of the electrodes is aligned with the molecular level (see Fig. 2.2c), the blockade is lifted and current flows.

The presence of the electrodes also causes the molecular states to hybridize with the states of the gold. Electrons can therefore tunnel from and towards the molecule with a finite probability. According to Heisenberg's uncertainty principle, their finite residence time on the molecule allows for a finite window of electron energies to tunnel, effectively resulting in a broadening of the molecular levels. The electron transfer rate from the source to the molecule (Γ_S) and from the molecule to the drain (Γ_D) depends on the overlap of the wave function of the molecule and those of the electrodes, and defines the level broadening. The total coupling ($\Gamma = \Gamma_S + \Gamma_D$) is a measure for the overall hybridization, and determines the amount of current through the molecule. One can distinguish three different transport regimes, depending on the ratio of Γ, Δ, E_C, and $k_B T$. For a detailed description of the three regimes, see reference [116–118]. Here, we will only briefly introduce them.

In the *weak coupling* limit where $\Gamma \ll \Delta, E_C, k_B T$, the level broadening can be neglected. The density of states on the molecule is given by a series of discrete levels represented by Dirac delta functions and only integer charges are allowed to tunnel. Charge transport occurs sequentially through the succession of two first-order processes. In addition, it is incoherent as the long residence time on the molecule

causes the electrons to lose information about their phase. Transport in this regime mostly occurs for physisorbed molecules which are weakly bound to the electrodes. The current can be calculated from the master equation, describing the occupation probabilities of the electron on the different levels.

For most of the molecules covalently bonded to the electrodes, however, transport occurs in the *intermediate coupling* regime where $\Gamma, k_B T \lesssim E_C, \Delta$ the level broadening has to be taken into account. In this regime, transport occurs through resonant tunneling, which is a first-order process. In addition, transport is coherent, and effects involving the phase of the electrons (e.g. quantum interference) can be observed. The transmission through the molecule can be obtained from the Non-Equilibrium Green's Function (NEGF) formalism[119], which states that

$$T(\epsilon) = \mathrm{Tr}\{\frac{\Gamma_S(\epsilon)\Gamma_D(\epsilon)}{\Gamma_S(\epsilon)+\Gamma_D(\epsilon)}[\mathbf{G}-\mathbf{G}^\dagger]\}, \tag{2.4}$$

where $\mathbf{G}(\epsilon)$ is the retarded Green's function

$$\mathbf{G}(\epsilon) = \frac{1}{(\epsilon\mathbf{S}-\mathbf{H}-\Sigma_S-\Sigma_D)}. \tag{2.5}$$

Here, $\mathbf{H}$ is the Hamiltonian of the molecule, Σ the complex energy-dependent self-energy matrix ($\Sigma_{S,D} = \Lambda_{S,D}(\epsilon) + i\Gamma_{S,D}(\epsilon)$) describing the interaction between the molecule and each electrode, and $\mathbf{S}$ the symmetric overlap matrix. More specifically, $\Lambda_{S,D}(\epsilon)$ accounts for level shifts as a results of the hybridization of the molecular orbitals with the states of the leads. $\Gamma_{S,D}(\epsilon)$, on the other hand, describes the tunnelling of charge carriers from and to the molecules, as defined before.

In the case of small molecules, the chemical potentials are typically much larger than the bias voltage which can be applied in experiments. Transport is then dominated by the level closest to the Fermi energy (see Fig. 2.2b) and one refers to this approximation as the *single-level model*. As a result of the nearly uniform density of states of gold near the Fermi energy, another commonly made assumption is the *wide-band limit*, in which $\Gamma(\epsilon)$ is taken to be energy independent and $\Lambda(\epsilon)$ is neglected. The density of states of states is then given by

$$D(\epsilon) = \frac{4\Gamma_S\Gamma_D}{[\epsilon-\epsilon_0]^2 + [\Gamma_S+\Gamma_D]^2}, \tag{2.6}$$

where ϵ_0 is the energy difference between the single level and the Fermi energy. Rather than being a discrete Dirac delta function, the density of states is now Lorentzian broadened due to the hybridization of the molecular orbitals with the electrodes. The current though such a junction can be obtained using the Landauer-Buttiker formalism[119] and is given by

$$I = \frac{e}{\hbar}\int \frac{\mathrm{d}E}{2\pi} T(\epsilon)[f_S(\epsilon) - f_D(\epsilon)], \tag{2.7}$$

where $f_S(\epsilon)$ and $f_D(\epsilon)$ are the Fermi-Dirac distribution of the leads. In the low-temperature limit where $k_B T \ll \Gamma$ the expression for the current can be solved analytically and becomes

$$I(V) = \frac{4G_0}{e}\frac{\Gamma_S\Gamma_D}{\Gamma_S+\Gamma_D}\left[\arctan\left(\frac{\epsilon_0+\frac{eV}{2}}{\Gamma_S+\Gamma_D}\right)-\arctan\left(\frac{\epsilon_0-\frac{eV}{2}}{\Gamma_S+\Gamma_D}\right)\right], \tag{2.8}$$

where $G_0 = \frac{2e^2}{h}$. Note, that when on resonance ($\epsilon_0 = 0$), and with $\Gamma_S = \Gamma_D$, the expression for the current becomes $I \propto \frac{\Gamma_S\Gamma_D}{\Gamma_S+\Gamma_D} = \Gamma_D/2$, indicating a linear dependence of the current on Γ. This is characteristic for a first-order process.

From expression 2.8, it becomes clear that, in the intermediate regime, transport is mainly determined by the alignment with respect to the Fermi energy and the electronic coupling. To illustrate the role of ϵ_0, Fig. 2.3a presents IVs for various ϵ_0 for fixed $\Gamma_{S,D}$. The plot shows a step in the current which corresponds to the lifting of blockade by resonant tunneling. The position of the step shifts with ϵ_0 according to $V_{step} = 2\epsilon_0/\epsilon$, as a result of the symmetric voltage drop across the two barriers. The sharpness of the step and the current after the steps depend on $\Gamma_{S,D}$ and are therefore the same for all the curves. The low-bias current increases for decreasing ϵ. The transmission curves, shown in the inset on a logarithmic scale, consist of Lorentzians centered around ϵ and broadened by $\Gamma_S + \Gamma_D$.

Figure 2.3b presents IVs for various $\Gamma_{S,D}$ and for fixed ϵ_0. The situation is now different. The location of the step remains the same for all curves, but its sharpness and the maximum current increase for increasing Γ. The low-bias current also increases. The transmission curves, shown in the inset on a logarithmic scale, consist of Lorentzians centered around ϵ and broadened by $\Gamma_S + \Gamma_D$. Independent on the electronic coupling, the transmission through the level has a maximum of unity.

In the strong coupling regime were $\Gamma, k_BT > E_C, \Delta$, the electronic states of the molecular quantum dot and electrode are significantly hybridized and blockade effects are washed out by quantum fluctuations of the molecular charge. In this regime, transport is resonant, but the charge on the dot is no longer restricted to integer multiples of the electron charge and partial charging of the dot is allowed. This

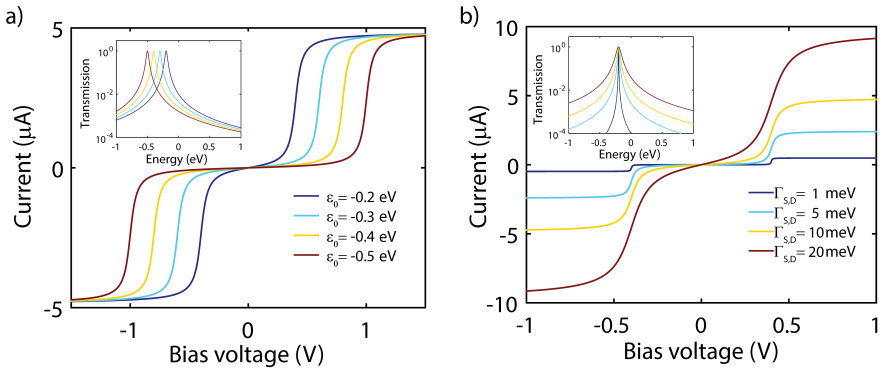

Figure 2.3: **The role of level alignment and electronic coupling.** (**a**) Current-voltage characteristics for various values of ϵ_0 and a fixed $\Gamma_{S,D}$ of 10 meV. (**b**) Current-voltage characteristics for various values of $\Gamma_{S,D}$ and a fixed ϵ_0 of -0.2 eV.

partial charging shifts the energy levels with increasing bias voltage, introducing an additional level broadening. As for a strong coupling a significant overlap of the wave function of the molecule and those of the electrodes is required, this regime is mainly relevant in the case of small molecules. For a more detailed description of this regime, see reference [116].

2.3. ELECTROSTATIC GATING

To gain more insight in the density of states of a molecule, for instance its addition energy, the number of accessible charge states or the presence of excited states, a third electrode can be used. This *gate electrode* couples only electrostatically to the molecular quantum dot, and allows to shift its electrostatic potential. Applying a positive voltage on the gate attracts the electrons and hence shifts down the chemical potentials of the molecule. Applying a negative voltage, on the other hand, repels the electrons and shifts up the chemical potentials on the molecule. Hence, by applying a positive gate voltage one can shift the EA down through the E_F, thereby reducing the molecule. Similarly, the molecule can be oxidized upon application of a negative gate voltage.

In a typical three-terminal measurement, both the bias and gate voltage are swept, allowing to create a colour-coded current map. Such a plot is referred to as a *stability diagram*, of which an idealized example is depicted in Fig. 2.4a. Here, the transition from the (white, high current) single-electron tunneling (SET) regions to the (black, low current) blockade regions occurs when a chemical potential of the molecule alignes with the Fermi energy of one of the electrodes. Inside the black diamond-shaped regions, also called *Coulomb diamonds*, transport is blocked and the number of electrons on the molecule is fixed to an integer value. The size of the diamond of the charge state with N-electrons can be used to determine the addition energy of the junction. Between consecutive black regions the charge on the molecule increases/decreases by one for increasingly positive/negative gate voltages. The diamond edges show up as bright resonances in the differential derivative ($^{dI}/_{dV}$, see

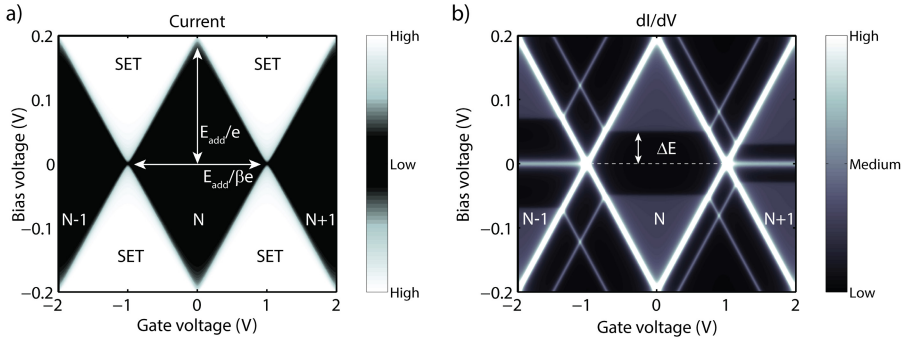

Figure 2.4: **Stabilty diagram** (**a**) Current map versus bias and gate voltage. The black areas correspond to regions where transport is blocked. In the white areas, the blockade is lifted by resonance tunneling and single-electron tunneling (SET) occurs. β is the gate coupling parameter. (**b**) Differential conductance map of (a). Molecular levels show up as bright resonances forming the diamond edges. In addition, lines as a result of resonant tunneling though excited states in the SET regime and inelastic cotunneling in the blockade region are visible.

Fig. 2.4b). These resonances cross each other in *charge degeneracy points*, where the molecule is either in one charge state, or the other. Inside the SET regime, additional eletronic and/or vibrational excited states can appear, resulting in lines running parallel to the diamond edge.

2.4. HIGHER-ORDER PROCESSES

In the previous section, only resonant tunneling was considered in which one electron tunnels resonantly from the source to the drain. In second-order processes, two particles are involved and hence their contribution to the current scales with Γ^2, rather than Γ. As a result, these processes only play a role in the intermediate and strong coupling regime. Here, we will briefly discuss elastic and inelastic cotunneling, and the Kondo effect.

ELASTIC COTUNNELING

When no level is in the bias window, the number of electron on the molecule cannot change as not enough energy is provided to allow them do so. Nevertheless, an electron can tunnel off the molecule, leaving it temporarily in a forbidden "virtual" state, as depicted in Fig. 2.5. This is allowed, as long as another electron tunnels into the molecule in the same quantum process in a time set by Heisenberg's uncertainty principle. The final state then has the same energy as the initial one, but one electron has been transported through the molecule. This process is called *elastic cotunneling*, as the energy of the molecule remains unchanged. It can occur at arbitrarily low bias, and leads to a nonzero background conductance in the blockade region. Thus elastic cotunneling is always present but its magnitude depends on Γ_S, Γ_D and ϵ_0.

2.4.1. INELASTIC COTUNNELING

A cotunneling event can also leave the molecule in an excited state. Similar to elastic cotunnelling, the electron on the molecule tunnels to the drain. At the same time, an electron from the source tunnels onto the molecule, but in this case it occupies a vibrational and/or excited electronic state which is ΔE higher in energy. As the energy of the molecule changes during the process, this is called *inelastic cotunneling*. For energy conservation reasons, this process can only occur if the applied bias voltage

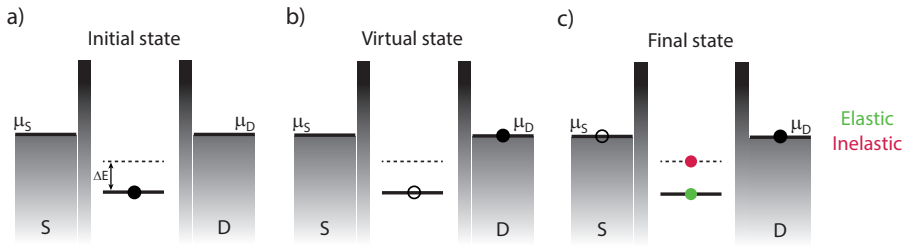

Figure 2.5: **Elastic and inelastic cotunneling** (**a**) In the initial state, the level is occupied, with an excited state ΔE higher in energy. (**b**) The electron can tunnel from the level to the drain, leaving the in a "virtual" state. (**c**) An electron tunnels from the source to the molecule. This can either be to the level or to the excited state, in the case of elastic and inelastic cotunneling, respectively.

is at least equal to ΔE/e. Therefore, for $V > \Delta E/e$, an additional transport channel becomes available, leading to a sudden increase in current. In the stability diagram, inelastic cotunneling excitations appear inside the Coulomb diamonds as horizontal lines, as the process is gate independent (see Fig. 2.4b). Furthermore, these lines are expected to intersect at the diamond boundary with the corresponding excitation line inside the SET region caused by resonant transport through the same vibrational and/or excited electronic state.

2.4.2. KONDO EFFECT

The last transport mechanism we will briefly touch upon is the Kondo effect. For a detailed review, we refer to reference[120]. Here, only the basic principle will be discussed.

Let's consider an unpaired electron localized on a molecule, for instance due to a magnetic atom, connected to two electrodes. This electron has a magnetic spin moment of $S = 1/2$. In the off-resonant transport regime, resonant transport is blocked and the number of electrons on the molecule is fixed. However, as mentioned previously, elastic cotunnelling can still occur, and these cotunnelling electrons interact with the unpaired electron. More specifically, they screen the magnetic moment of the unpaired electron. This screening results in a build up of states in the leads at the Fermi level. As a result, in the stability diagram, the Kondo effect shows up as a zero-bias resonance (white horizontal lines at zero bias in charge state $N \pm 1$, see Fig. 2.4b) for an odd number of electrons on the molecule, which connects the two degeneracy points of the Coulomb diamond. The width of the resonance is related to the Kondo temperature T_K, which is typically 10-50K for molecules. The Kondo effect can also occur for molecules with larger spins, such as $S = 1$, in which case T_K is much smaller[83].

3

EXPERIMENTAL

In this chapter, the mechanically controllable break-junction technique is introduced. We first review the basic principles, and then discuss its experimental realisation, ranging from the measurement set-up, the electronic read-out, the sample fabrication, and the different measurement schemes.

3.1. MECHANICALLY CONTROLLABLE BREAK-JUNCTION TECHNIQUE

In 1985, Moreland and Ekin[121] introduced 'break' junctions to study tunneling between superconductors. At that time, they used a thin wire of a superconducting material that was soldered on top of a glass bending beam. By bending the substrate in a 3-point-bending mechanism they literally 'broke' the junction. They controlled the force that was applied on the beam using an electromagnetic actuator. Several modifications to this concept have been realized later on, initially by Zhou *et al.*[122], who introduced the name Mechanically Controllable Break Junction (MCBJ). A few years after, in 1997, the first single-molecule junction was measured using this technique[18]. Besides measurements on molecular junctions, MCBJs have also extensively been used to study quantum point contacts and monatomic metallic chains[19, 20, 123–126].

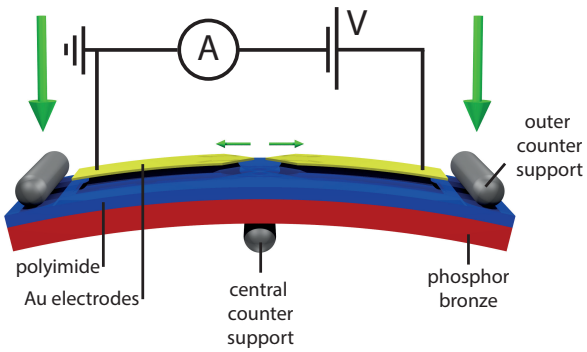

Figure 3.1: **Schematic illustration of the MCBJ technique.** The sample is bend in a three-point bending mechanism. The large green arrows indicate the force applied to bend the sample. The small green arrows represent the attenuated displacement of the electrodes.

The working principle behind the MCBJ technique is as follows. A thin metallic wire is positioned on top of a flexible substrate. In most cases gold is used because of its noble character. The wire can either be a macroscopic gold-wire, in the case of a notched-wire junction, or a lithographically fabricated one. By bending the substrate in a three-point mechanism, the gold wire streches and eventually breaks, thereby forming two gold surfaces. These surfaces can be used as electrodes to contact molecules. The spacing between the electrodes can be tuned by adjusting the bending of the sample. After the rupture of the gold wire, the electrodes can be fused again to reform the contact. A schematic illustration of the technique is shown in Fig. 3.1.

The MCBJ technique has several advantages such as a sub-picometer tuning of the electrode separation. This is a result of a geometrical attenuation factor, which describes the ratio between the displacement of the actuator and the one of the electrodes (more on the attenuation ratio in section 3.7). MCBJs also offer a high junction stability. In particular, one can apply voltages across a molecular junction ranging from 0.5 V at room temperature, up to 2-3 V at 4.2 K. In addition, at

low termerature, once a gap is formed, its size does not significantly change over time, even after hours[127]. Moreover, the technique is ideal for statistical studies, as the electrodes can be fused and broken repeatedly, allowing to collect data on hundreds, or even thousands of junction, each with a different atomic arrangement. Finally, the technique can easily be adapted for use at high vacuum and cryogenic temperatures[19, 20], or in a liquid environment using a liquid cell[128].

3.2. THREE-TERMINAL MCBJ

To gain additional spectroscopic information, a third electrode can be added in the MCBJ devices, as for example implemented by Martin *et al.*[129]. This *gate electrode* is located close to the molecule and needs to be electrically insulated from the source and the drain electrodes. As such, by applying a voltage on the gate, one changes the electrostatic potential of the molecule[130]. Energy shifts of the molecular transport level are then induced, from which additional information about the molecule can be obtained such as the presence of vibrational modes and excited states[21, 131] and the presence of vibrationally induced effects such as Franck-Condon blockade[132]. The gate has also played a crucial role in studying Kondo Physics [81, 133], and superconductivity[88]. Moreover, as a gate electrode allows to repel and attract electrons, it can be used to oxidize and reduce molecules[43], and investigate molecular transport properties for different charge states. Three-terminal devices have also been employed to reveal the fine structure of individual single-molecule magnets[86] and the presence of magnetic anisoptry[87, 134]. They also enabled the read-out[35] and driving[36] of a single nuclear spin, which can be used as molecular quantum bit.

The fabrication process of a three-terminal devices needs to ensure that the gate couples only electrostatically to the molecule. This can be achieved by electrically insulating the gate from the source/drain electrodes and from the molecule. However, contributions to the current caused by various mechanism (quantum tunneling, electron hopping, etc.) can lead to a parasitic current between the gate and the drain. This *gate leakage* can overshadow the molecular signature, and should therefore be kept as low as possible. The main challenge in fabrication is thus to design a junction geometry, in combination with the right material choice, which reduces as much as possible the gate leakage, but maximizes the electric field reaching the molecule. A few concepts should be kept in mind. First, for thin barriers (<2-3 nm) the gate leakage originates mostly from quantum tunneling, which decreases exponentially with increasing insulator thickness. Moreover, increasing the insulator thickness increases the voltage at which it breaks down. However, a thicker insulator also means that the ratio between the applied voltage and the obtained level shift, also called the *gate coupling*, becomes smaller. The total level shift that can be reached in an experiment is the product of the gate coupling and the breakdown voltage, and depends non-trivially on the insulator thickness, the junction geometry and the insulator material. To maximize the gate coupling, a thin insulator is needed with a high dielectric constant. To maximize the breakdown voltage, one can use an insulator with a high breakdown voltage and/or increase its thickness. Typically gate dielectric

materials are for example silicon oxide (SiO_2), aluminum oxide (Al_2O_3) and hafnium oxide (HfO_2).

Besides maximizing the total level shift caused by the gate field, one should also compare the level shift with the energy separation between the closest chemical potential of the molecular junction and the Fermi energy of the electrodes. To oxidize an/or reduce a molecule, the associated chemical potential needs to cross the Fermi energy. Therefore, as the total level shift induced by the gate is limited, the molecules used as single-molecule transistors are typically >1 nm. Smaller molecules have a too high level splitting, so that their charge state cannot be changed with the gate. In section 3.4.2, the fabrication of an improved version of the gated MCBJ will be discussed.

An interesting room-temperature alternative is electrochemical gating[135]. Here, the measurements are performed in an electrolyte. By applying a positive voltage on the electrolyte, the negative ions are attracted towards the electrode, resulting in a higher concentration of positive ions close to the molecule, effectively gating the molecular junction. Here, large level shifts up to 0.8 eV have been reported[136]. However, as much of the fine structure is smeared out by temperature broadening, only resonant tunneling can be investigated. Here, we will not discuss this method further; for more information we refer to the literature on this subject[137].

3.3. SET-UP

3.3.1. MECHANICS

What follows below is the Delft realization of the MCBJ technique. For a detailed description of the set-up and its characteristics, see the detailed review article by Martin *et al.*[127] Here, we will only review the main features. The set-up is based on a dipstick design (see Fig. 3.2a and c), with the three point-bending mechanism located at the bottom (see Fig. 3.2e). The bending of the sample is controlled by a bending actuator, based on a brushless servo motor (Faulhaber), a precision gearhead with an attenuation of 246:1, and a differential screw drive with a pitch of 250 μm/turn.

In the second generation set-up this pitch has been reduced to 150 μm/turn. The motor is located at the top of the dipstick (see Fig. 3.2b). Its rotation is transferred to the screw via a backlash-free insulating elastomer coupling and a ferrofluidically sealed rotary feedthrough. The up and down movement of the screw is transfered to the two outer counter supports of the three-point bending mechanism. The step size of the screw drive is about 0.1 μm, corresponding to about 5 picometer in electrode distance, for a attenuation factor of about $5{\cdot}10^{-5}$ (for the calibration, see section 3.7.1). The bending can also be modified in a continuous fashion. A typical bending speed is 0.5–5 μm/s, corresponding to 25–250 pm/s on the electrode scale. Every time the motor direction is reversed, a backlash of several microns is present due to the screw drive.

In the second generation design, the actuator can also be pushed with a piezoelectric element. The piezo-element pushes against a cantilever mechanism which moves up and down the center counter support of the three-point bending mechanism. The cantilever is present to amplify the piezo displacement of 60 μm/1000 V by a factor of 4.6 to 280 μm/1000 V. This piezo element allows for much higher ac-

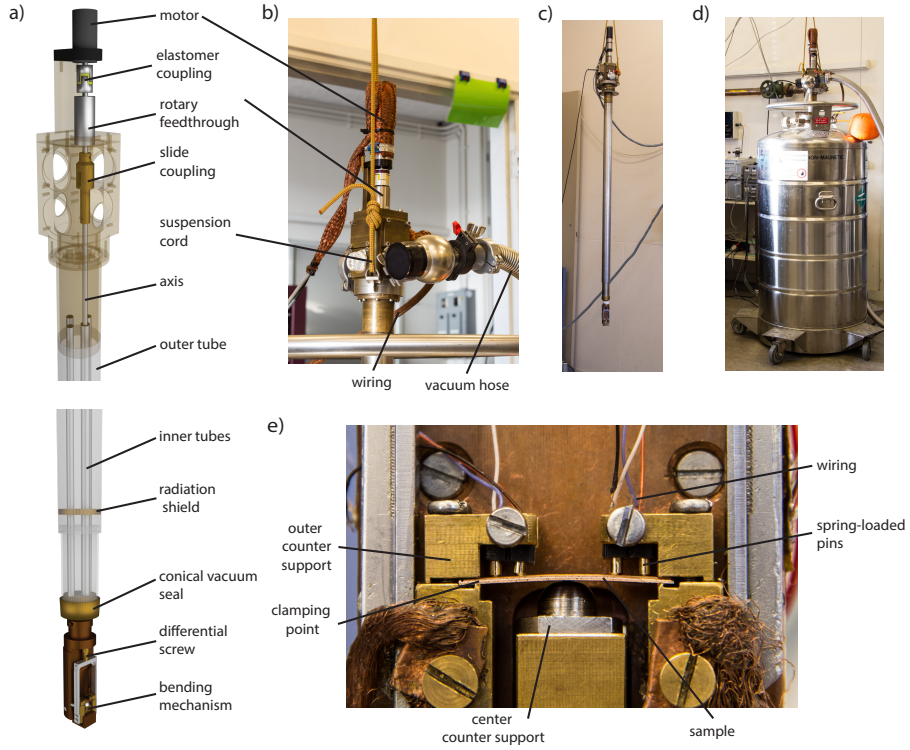

Figure 3.2: **Illustration of the MCBJ set-up**. (**a**) Schematic drawing of the top part of the set-up (top panel) and the bending mechanism (bottom panel). The stainless steel outer tube and brass top part have been rendered semi-transparent to illustrate the mechanics. (**b**) Top part of the set-up. (**c**) Overview photograph showning the whole dipstick. (**d**) Photograph showing the dipstick inside a liquid helium vessel for measurements at 4.2 K. (**e**) Bending-mechanism of the MCBJ set-up.

tuator speeds of 800 μm/s (3000 V/s) which results in a electrode speed of 40 nm/s. Moreover, the piezo element does not suffer from backlash. However, the drawback is that it has a limited range of operation (280 μm versus >3 mm for the servo motor). In addition, it performs poorly at cryogenic temperatures and in practice is only used at room temperature.

The wiring to the sample and the axis runs from top to bottom through protective eriflon tubes. Those tubes are held in place by cicular brass rings, which also act as radiation shields. The outer tube is made of stainless steel due to its low thermal conductance. The set-up can be closed with the conical vacuum seal at the bottom. During measurements, the set-up is typically pumped to a high vacuum of $<5{\cdot}10^{-6}$ mbar. For operation at cryogenic temperatures, the dipstick is either submerged in a dewar of liquid nitrogen (77 K) or inserted directly into a liquid helium vessel (4.2 K), as shown in Fig. 3.2d.

3.3.2. ELECTRONICS

All measurement electronics is hosted by a shielded rack. The individual modules are accessed via optically coupled isolation amplifiers of which the power is supplied by two separate batteries. This full galvanic isolation of the different circuits is ideal for low-interference measurements. The measurement rack can accommodate several home-built units (developped by Raymond Schouten, TU Delft), like voltage sources, current sources, current-voltage converters and voltage amplifiers. For the MCBJ measurements, a home-build logarithmic current-voltage is used, which allows for current measurements across almost nine orders of magnitude. In addition, it is equipped with temperature-drift compensation.

The measurement electronics is accessed and read out using an ADwin Gold (Jaeger Messtechnik GmbH), which hosts an analog-digital (AD), a digital-analog (DA) converter and an on-board digital signal processor operating at 40 MHz. This enables real-time analysis and fast feedback control. The maximum data acquisition rate is about 200kHz at a resolution of 16 bit.

3.3.3. OPERATION

The measurements are controlled using home-made Python routines. All routines in which timing is crucial, such as such as recording an IV, or recording the conductance as a function of time are programmed in the low-level ADbasic programming language. Those routines are then compiled, loaded as a process in the ADwin and executed by the on-board digital signal processor. Python is used to coordinate the execution of the various processes, operate the motor controller, get the data from the ADwin, and plot the measurements in real-time.

3.4. SAMPLE FABRICATION

3.4.1. TWO-TERMINAL SAMPLES

The fabrication of two-terminal lithographic MCBJ samples is based on the design of Martin *et al.*[129] and occurs in the Kavli NanoLab at Delft. The fabrication steps, illustrated in Fig. 3.3 are the following:

Step 1

- As a starting point, polished phosphorous bronze wafers (50x50x0.5 mm) are used. On such wafers, 10 samples can be fabricated. Each sample contains 4 junctions.
- Clean the wafer by ultrasonication for 5 min in acetone and isopropanol.

Step 2

- Apply the adhesion promoter VM651 (HD Microsystems) (soak for 30 s) and spin for 55 s at 3000 rpm.
- Bake for 1 min at 110°C.
- Spin-coat the wafer with polyimide PI2610 (HD Microsystems) for 55 s at 800 rpm.

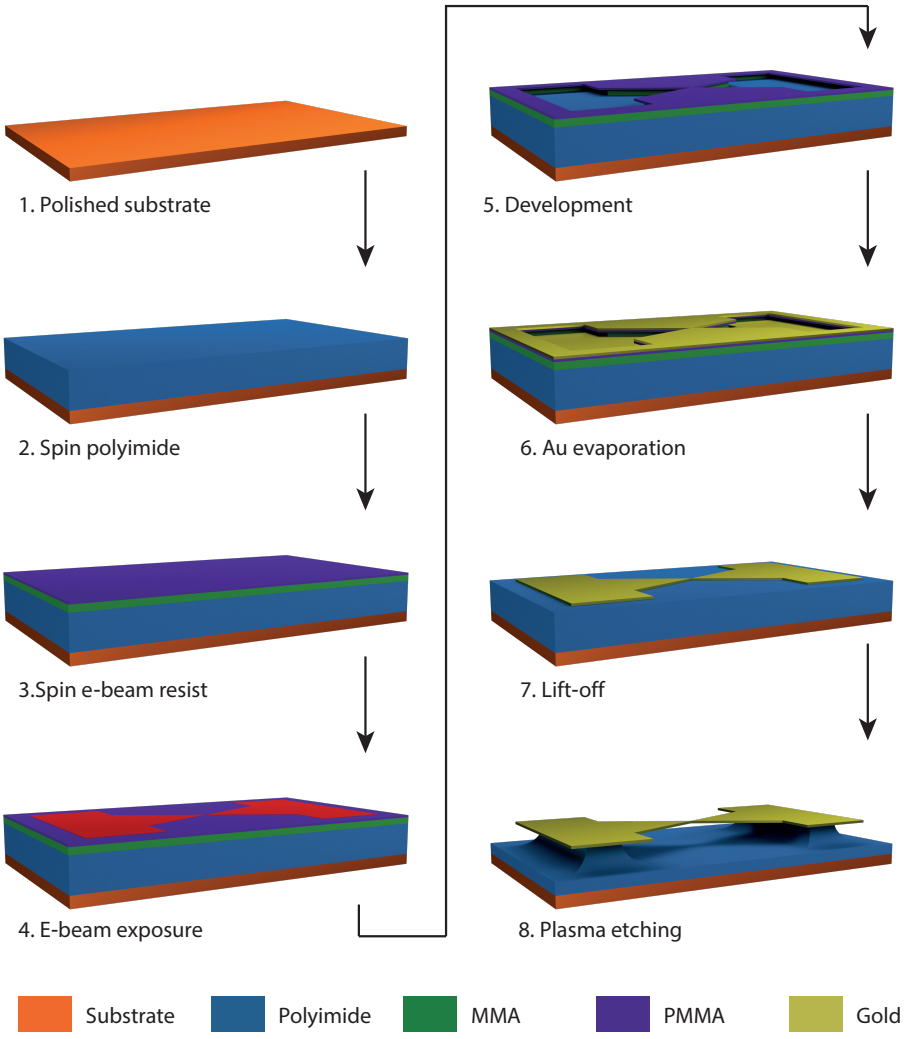

Figure 3.3: **Fabrication scheme for two-terminal samples.** See text for an explanation of the eight different steps.

- Cure the wafer for 30 min in a vacuum oven at a temperature of 300°C. The thickness of the resulting polyimide layer is around 6 μm. Without the vacuum, the polyimide is not properly cured.

Step 3

- Cover the wafer with a methylmethacrylate-methacrylic acid solution (MMA(17.5)MAA 8% in ethyl-L-lactate, Microchem)) and spin-coat for 55 s at 3000 rpm.
- Bake for 7 min at 175 °C. The resulting layer thickness should be around

320 nm. This layer has a high sensitivity and is present to facilitate lift-off.

- Cover the wafer with a PMMA 950k resist solution (4% in anisole, Microchem) and spin-coat for 55 s at 6000 rpm.
- Bake for 7 min at 175 °C. The resulting layer thickness should be around 110 nm.

Step 4

- Write the MCBJ structures (Leica electron-beam pattern generator EBPG5000+). The bridge and fine leads are written with a beam size of 3 nm, a beam step-size of 2 nm and a dose of 950 μC/cm^2. The coarse leads and the pads are written with a beam size of 82 nm, a beam step-size of 58 nm and a dose of 750 μC/cm^2.

Step 5

- Develop the pattern for 90 s in a mixture of methyl-isobutylketone (MIBK) and isopropanol (volume ratio 1:3), followed by 20 s in IPA.

Step 6

- Electron-beam evaporation (Temescal FC-2000) of 2 nm of titanium (0.5 Å/s) and 80 nm of gold (1.0 Å/s). The base pressure of the evaporation chamber should be $<2\cdot10^{-6}$mbar.

Step 7

- Lift-off in hot acetone for 1-2h and a rinse with acetone.
- Cover the wafer with a PMMA 350k resist solution (3% in anisole, Microchem) and spin-coat for 55 s at 2000 rpm. This layer acts as protection layer during the laser cutting of the samples.
- Bake for 2 min at 175 °C.
- The wafers are then cut into individual devices using laser-cutting (ILT Fineworks B.V., Enschede, the Netherlands).

Step 8

- Remove the protection layer of the individual samples by immersion in hot acetone for 10 min.
- Etch the polyimide using a reactive ion etcher (Leybold Heraeus) with a gas flow of 50 sccm of O_2 gas and 8.5 sccm of CF_4, a pressure of 0.2 mbar and a RF power of 30 W. The resulting oxygen plasma yields a nearly isotropic etch profile with a suspended electrode length of about 2 μm. The etched polyimide is measured *in-situ* using an laser interferometer.

Scanning electron microscope (SEM) images of a two-terminal sample can be found in Fig. 3.5a and Fig. 3.5b. For clarity, the images have been colorized, each material in a different color.

3.4.2. THREE-TERMINAL SAMPLES

As discussed in Chapter 1, the concept behind three-terminal samples is to fabricate a third electrode that can tune the electrostatic potential of the molecule. The gate electrode is electrically isolated from the source and drain electrodes, and hence couples only electrostatically with the molecule independently from that of the the source/drain electrodes. The design of such samples is more complicated than for two terminals as it requires different materials and material thicknesses. As a result, fabrication steps 3-7 of Fig. 3.3 need to be repeated for each material and when different material thicknesses are required. We have used such gated samples in Chapter 6, which have been fabricated according to the recipe published by Martin *et al.*[129]. Scanning electron microscope (SEM) images of those devices can be found in Fig. 3.5c and d. However, the voltage which can be applied between the gate of those devices and the source/drain electrodes is limited to 3 V. This is due to the thickness of the plasma-enhanced native aluminum oxide (Al_2O_3, 2-3 nm). With bias voltages applied between the source/drain up to 2 V, as for instance used in Chapter 9, the gate voltage is at most 1 V. A way to remedy to this is to increase the breakdown voltage of the gate dielectric, which can be achieved by increasing the oxide thickness. To illustrate this, we assume an increase of the oxide thickness from 3 nm to 8 nm. Assuming a breakdown voltage of 1 V/V, this results in a breakdown voltage of 8 V. With 2 V applied on the source/drain, the voltage which can be applied on the gate is now 6 V. This is six times higher than in the original design. Even though the gate coupling decreases linearly with oxide thickness, this is outweighted by the much larger gate range.

FABRICATION

What follows below is an improved version of the sandwiched-type three-terminal samples, in which the break-down voltage of the gate oxide has been increased to 8 V. This has been achieved by increasing the thickness of the gate oxide using atomic layer deposition (ALD). In addition, the number of e-beam lithography steps has been reduced from 5 to 4. The six fabrication steps are depicted in Fig. 3.4 and described in detail below.

Step 1

- As a starting point, polished phosphorous bronze wafers (50x50x0.5 mm) are used. On such a wafer, 10 samples are fabricated. Note that the wafers are thicker than for the two-terminal samples.
- Clean the wafers by ultrasonication for 5 min in acetone and isopropanol.
- Apply the adhesion promoter VM651 (HD Microsystems) (soak for 30 s) and spin for 55 s at 3000 rpm.
- Bake for 1 min at 110°C.
- Spin-coat the wafers with polyimide PI2610 (HD Microsystems) for 55 s at 800 rpm.
- Cure the samples for 30 min in a vacuum oven at a temperature of 300°C. The thickness of the resulting polyimide layer is around 6 μm.

Step 2

- Cover the wafer with a methylmethacrylate-methacrylic acid solution (MMA(17.5)MAA 8% in ethyl-L-lactate, Microchem)) and spin-coat for 55 s at 3000 rpm.
- Bake for 7 min at 175 °C. The resulting layer thickness should be around 320 nm.
- Cover the wafer with a PMMA 950k resist solution (4% in anisole, Microchem) and spin-coat for 55 s at 6000 rpm.
- Bake for 7 min at 175 °C. The resulting layer thickness should be around 110 nm.
- Write gate pads and markers with a beam size of 57 nm, a beam step-size of 40 nm and a dose of 750 μC/cm^2.
- Develop the pattern for 90 s in a mixture of methyl-isobutylketone (MIBK) and isopropanol (volume ratio 1:3), followed by 20 s in IPA.
- Electron-beam evaporation of 5 nm of titanium (0.5 Å/s) and 55 nm of gold (1.0 Å/s). To detect the markers, the contrast should be set to the maximum (99%) as both the substrate and the markers are metallic. For Au thicknesses <50 nm, the markers cannot be found during e-beam exposure due to poor contrast.
- Lift-off in hot acetone for 1-2 h and rinse with acetone.

Step 3

- Cover the wafer with a methylmethacrylate-methacrylic acid solution (MMA(17.5)MAA 8% in ethyl-L-lactate, Microchem)) and spin-coat for 55 s at 3000 rpm.
- Bake for 7 min at 175 °C.
- Cover the wafer with a PMMA 950k resist solution (4% in anisole, Microchem) and spin-coat for 55 s at 6000 rpm.
- Bake for 7 min at 175 °C.
- Write the gate with a beam size of 3 nm, a beam step-size of 2 nm and a dose of 1100 μC/cm^2.
- Develop pattern for 90 s in a mixture of methyl-isobutylketone (MIBK) and isopropanol (volume ratio 1:3), followed by 20 s in IPA.
- Electron-beam evaporation of 2 nm of titanium (0.5 Å/s) and 80 nm of Al (1.0 Å/s). The chamber pressure should be $<5{\cdot}10^{-7}$ mbar to reduce oxidation of titanium and ensure a good electrical contact between the gate and the gate pads.
- O_2 plasma for 10 s (300 W, 100 mbar, 60 sccm O_2).

- 40 cycles plasma-enhanced atomic layer deposition (Oxford Instruments, 0.10–0.12 Å/s) with a stage temperature of 100°C. The number of cycles can be increased to 50. However, the increased oxide thickness renders the lift-off more delicate. For oxide thicknesses above 60 cycles the lift-off becomes problematic, and above 70 also the gate itself starts to lift-off. The stage temperature is important as well. For higher temperatures, notably >150°C, the PMMA starts to reflow and degass, affecting thereby the written pattern.
- Lift-off in hot acetone for 1-2 h and rinse with acetone.

Step 4

- Cover the wafer with a methylmethacrylate-methacrylic acid solution (MMA(17.5)MAA 8% in ethyl-L-lactate, Microchem)) and spin-coat for 55 s at 3000 rpm.
- Bake for 7 min at 175 °C.

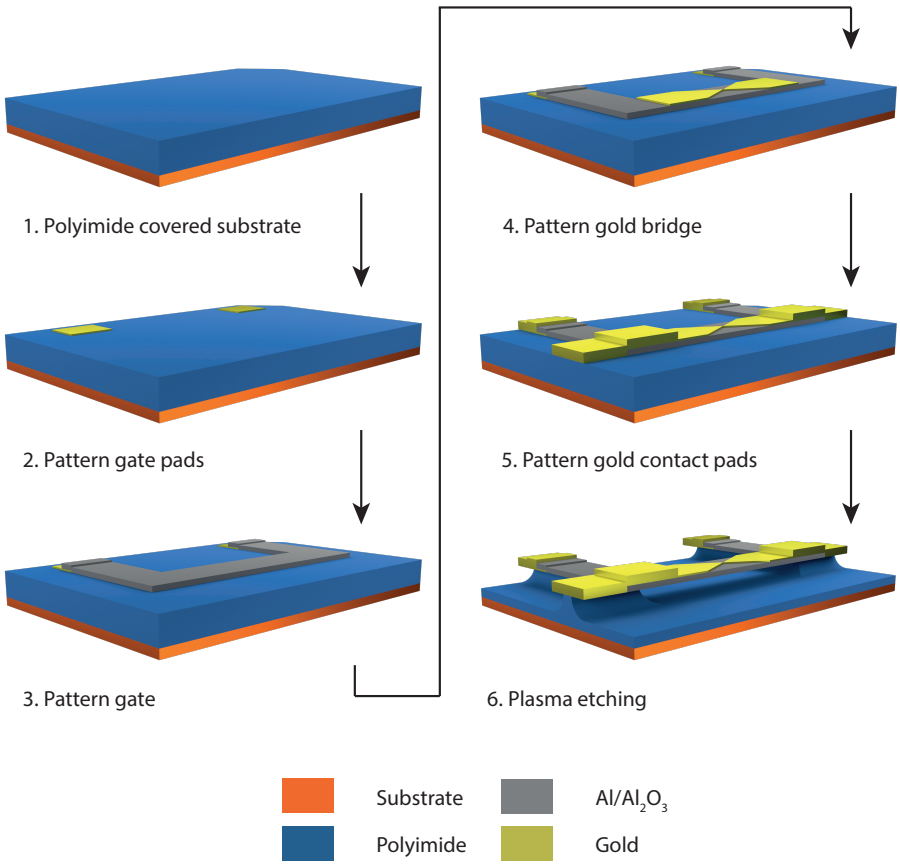

Figure 3.4: **Fabrication scheme for three-terminal samples.**

- Cover the wafer with a PMMA 950k resist solution (4% in anisole, Microchem) and spin-coat for 55 s at 6000 rpm.
- Bake for 7 min at 175 °C.
- Write the bridge with a beam size of 3 nm, a beam step-size of 2 nm and a dose of 1100 μC/cm^2.
- Develop the pattern for 90 s in a mixture of methyl-isobutylketone (MIBK) and isopropanol (volume ratio 1:3), followed by 20 s in IPA.
- Electron-beam evaporation of 15 nm of Au (1.0 Å/s). Base pressure <5·10^{-7}mbar.
- Lift-off in hot acetone for 1-2 h and rinse with acetone.

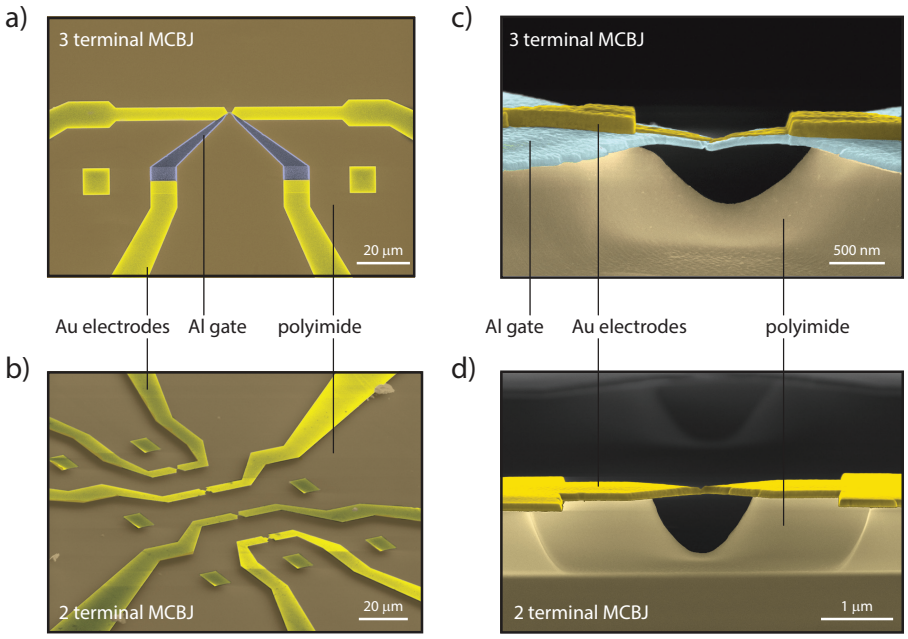

Figure 3.5: **False-color SEM pictures of a two-terminal device and a three-terminal device fabricated according to the original recipe by Martin *et al.*[129].** (**a**) Top view of a three-terminal sample. (**b**) 3D view of two-terminal devices. (**c**–**d**) Side view of three- and two-terminal devices, respectively.

Step 5

- Cover the wafer with a methylmethacrylate-methacrylic acid solution (MMA(17.5)MAA 8% in ethyl-L-lactate, Microchem)) and spin-coat for 55 s at 3000 rpm.
- Bake for 7 min at 175 °C.

- Cover the wafer with a PMMA 950k resist solution (4% in anisole, Microchem) and spin-coat for 55 s at 6000 rpm.
- Bake for 7 min at 175 °C.
- The fine leads are written with a beam size of 3 nm, a beam step-size of 2 nm and a dose of 950 μC/cm^2. The coarse leads and the pads are written with a beam size of 82 nm, a beam step-size of 58 nm and a dose of 750 μC/cm^2.
- Develop the pattern for 90 s in a mixture of methyl-isobutylketone (MIBK) and isopropanol (volume ratio 1:3), followed by 20 s in IPA.
- Electron-beam evaporation of 2 nm of titanium (0.5 Å/s) and 120 nm of Al (1.0 Å/s). The chamber pressure should be $<5{\cdot}10^{-7}$ mbar to reduce the oxidation of the titanium layer. The thickness of the gold can be increased to 125-130 nm if necessary, for instance due to a thicker bridge. However, for Au thickness above 130 nm, the lift-off becomes problematic. As a rule of thumb, the MMA lift-off layer should be not more than about three times thicker than the material to be deposited. Our MMA layer is about 320 nm, so already an Au layer of 120 nm is on the edge. This problem could be circumvent by using a thicker MMA layer. However, a thicker layer also reduces the contrast of the e-beam, rendering it difficult to find the markers.
- Lift-off in hot acetone for 1-2 h and rinse with acetone.
- Cover the wafer with a PMMA 350k resist solution (3% in anisole, Microchem) and spin-coat for 55 s at 2000 rpm. This layer acts as protection layer during the laser cutting.
- Bake for 2 min at 175 °C.
- The wafers are then cut into individual devices using laser-cutting (ILT Fineworks B.V., Enschede, the Netherlands).

Step 6

- Remove the protection layer by immersion in hot acetone for 10 min.
- Etch the polyimide using a reactive ion etcher (Leybold Heraeus) with a gas flow of 50 sccm of O_2 gas and 8.5 sccm of CF_4, a pressure of 0.2 mbar and a RF power of 30 W. The etched polyimide is measured *in situ* using an laser interferometer.

SEM images of the improved (ALD enhanced) three-terminal samples, taken at different magnifications, can be found in Fig. 3.6. For clarity, the images have been colorized. The thin and narrow gold wire is laying on top of the gate, both of which are suspended. We note that during the lift-off of the aluminum/aluminum oxide, not all material is properly lifted-off, resulting in some irregularities at the edges. This is due to the very high toughness of the aluminum oxide. Those fringes are only of aesthetic concern, and do not affect the proper functioning of the devices.

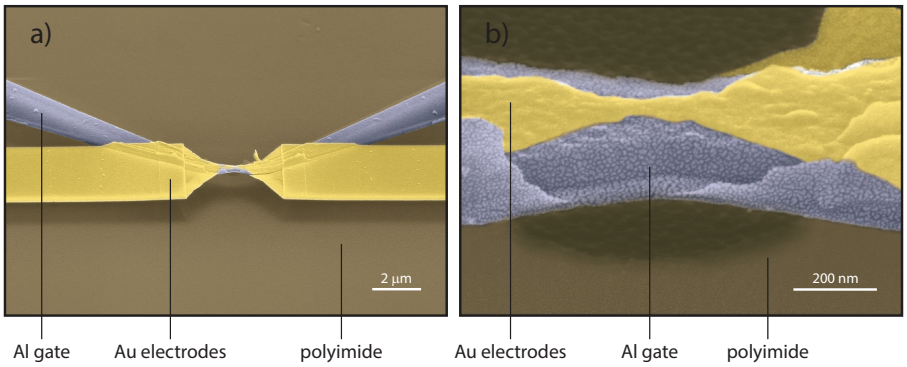

Figure 3.6: **False-color SEM pictures of the ALD enhanced three-terminal samples.**

CHARACTERIZATION OF THE GATE LEAKAGE

To characterize the gate leakage current, an IV was recorded at 6 K between the gate and the source/drain on a sample fabricated as described above. The measurement was performed on an unbroken bridge; the gate was not broken as well. The resolution in bias is 0.3 mV. The scan rate was set to 100 kHz with an averaging of 2000 samples, resulting in an effective sampling rate of 50 Hz. To reduce charging effects due to the very high resistance, a settling time of 80 ms was used for each bias point. Figure 3.7 shows the current recorded for voltages between -8 V and 8 V. The leakage current remains below 10 pA, except around -8 V, where it reaches 25 pA. As the onset of the current for negative voltage starts around 7.5 V, the total voltage difference between the source/drain and the gate should not exceed this value.

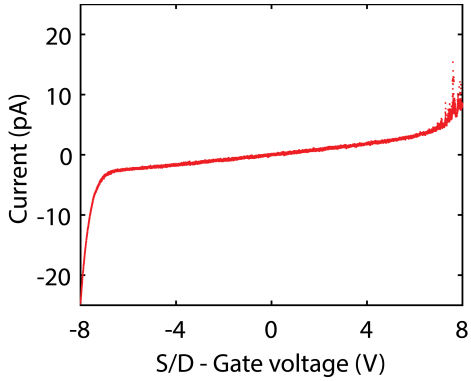

Figure 3.7: **Gate leakage.** IV recorded between the source/drain and the gate.

3.5. MOLECULE DEPOSITION

The deposition of the molecule occurs either via self-assembly from solution or via drop-casting on the sample, depending on the type of molecule to be deposited. For H_2-TPP, H_2-TPPdT, and Ru-TPPdT (see Chapter 4), the samples were submerged for 1

hour in the molecular solution (0.1 mM in acetone). For ZnTPPdT-Pyr and ZnTPPdT-Pyr (see Chapter 6 and Chapter 5), the samples were submerged in a 0.1 mM solution of the molecule dissolved in dichloromethane (DCM). In the case of dihydroanthracene (AC) and anthracene (AC), acetyl-protected thiols were used. To ensure the acetyl-group was cleaved off during self-assembly, the samples were submerged in the molecular solution (0.1 mM in DCM) for 24 hours. For the diode molecule DPEdT-2F and its symmetry counterpart DPEdT, first a 0.1 mM solution was made using DCM. The molecules were then deprotected using tetrabutylammonium hydroxide[138, 139] (Bu_4NOH) and drop casted on the sample, after which the system was immediately pumped.

3.6. MEASUREMENT SCHEMES

Throughout this dissertation, several measurement schemes will be employed. Here, we will discuss some of the most used ones.

3.6.1. BREAKING TRACE

One of the typical measurements is the recording of *breaking traces* at room temperature. During such a measurement, the conductance is monitored during the stretching of the wire. The bending of the sample can be realised using the motor or the piezo-element. For an example of such a measurement we refer to Fig. 3.8f-g, in which the conductance versus displacement curve is plotted on a linear and logarithmic scale, respectively. Here, a few characteristic features of a clean gold junction are observed, which can be illustrated with molecular dynamics simulations (MD). Figure 3.8a-e presents junction geometries selected from a MD simulated breaking sequence. In the metallic regime (a), the conductance goes down gradually, until the diameter of the wire becomes comparable to the *de Broglie* wavelength of the electrons, and the conductance becomes quantized (b). In the case of gold, where mainly the 6s valence electrons conduct[140], each atom has only one fully transmitting transport channel, yielding conductance steps from 4-5 G_0 down to 1 G_0, which corresponds with the formation of a single-atom chain[141] (c). Upon increased stretching, the 1 G_0 contact ruptures and the electrode surface relaxes (d), forming a gap of around 0.5 nm[142] at room temperature. This relaxation is accompanied by a drop in conductance of a 3 to 4 orders of magnitude at room temperature, and sometimes more than 6 to 7 orders of magnitude at cryogenic temperature, where the formation of monoatomic gold chains consisting of multiple atoms is more likely[125]. After the drop in conductance, the remaining contribution to the current is vacuum tunneling, of which transport can be described using the single-barrier Simmons model[143]. Vacuum tunneling decreases exponentially with distance, resulting in a linear decay of the current on a logarithmic scale. Once the conductance drops below $1{\cdot}10^{-6}$ G_0, the junction is fused to typically 20-30 G_0. This ensures a full atomic rearrangement. However, if the junction is fused too far, the probability of forming molecular junctions can be reduced[144]. A new breaking trace measurement can then be started.

During breaking, the conductance is typically recorded at a rate of 1 kHz for an electrode speed of 6 nm/s, with no settling time. For slower speeds, the sampling rate is decreased such that the number of points remains approximatively the same in each braking trace. Typical bias voltages are 50 to 150 mV.

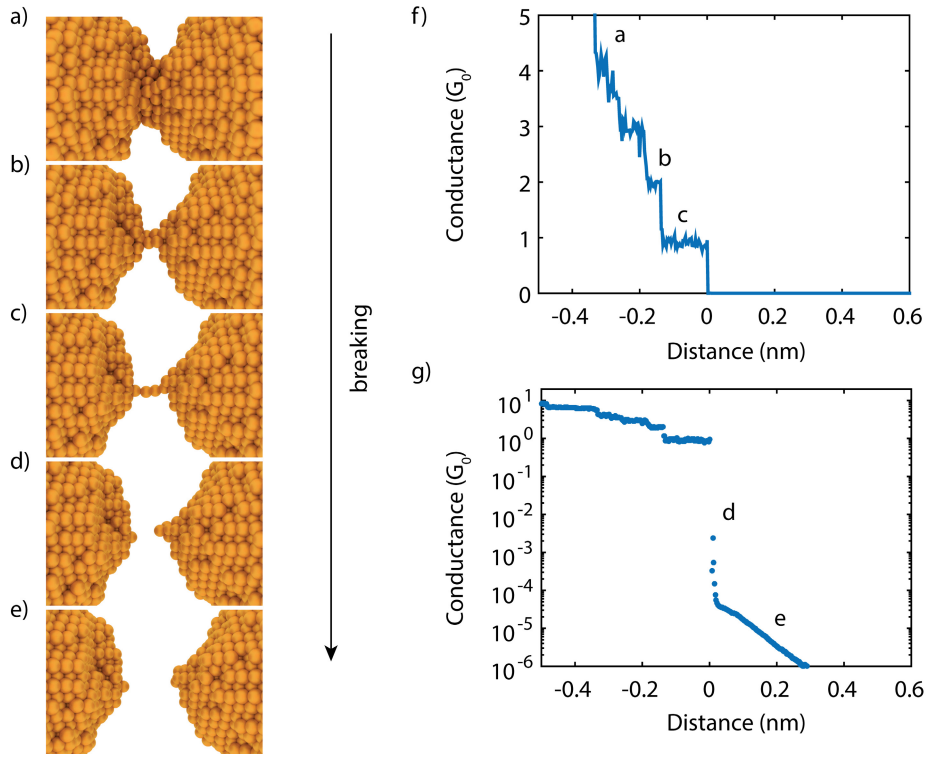

Figure 3.8: **Breaking trace measurements.** (**a–f**) Illustrations of a gold nano-contact upon breaking. The position of the gold atoms are obtained from molecular dynamics simulations performed with the MBN Explorer package[145], using the Sutton-Chen many-body potential. In the simulations, the initial temperature was set to 100 K, and the time steps to 1 ps. The position of the atoms of the most outer gold layer was fixed, and displaced outward at a speed of 0.5 Å/ns. The total simulation time was 60 ns. (**b,c**) Experimental conductance versus displacement plot on a linear and logarithmic scale, respectively. The displacement is set to zero at the rupture of the single-atom contact. The characters a–e correspond to the junction geometries shown in (a–e).

3.6.2. CURRENT-VOLTAGE CHARACTERISTICS

The most often used measurement scheme throughout this dissertation is the current-voltage characteristic (IV), in which the current is recorded as a function of applied bias voltage. All measurements start at zero bias voltage. The voltage is then ramped to positive values until a set maximum bias voltage. The bias is then ramped back down to zero and subsequently to a set minimum bias voltage is reached. When this bias has been reached, the bias is ramped back to zero. The maximum and minimum bias are typically equal. This bias sweep method is used to avoid applying high voltages at once on the junction. Typically, 1300 points in bias are used, which for a bias range of -1 to 1 V corresponds to a resolution of 3 mV. The current is measured at a rate of 100 kHz, and averaged over 2000 samples, resulting in an effective sampling rate of 50 Hz. For each point in bias, a settling time of 20 ms is used.

Although a single IV provides valuable spectroscopic information, the strength of the MCBJ lays in the fact that IVs can be recorded at various electrode spacings, al-

lowing to investigate the influence *e.g.* of the interface on the molecular levels and the stretching of the molecule on its electronic structure. For this purpose the used two different methods have been developed, illustrated in Fig. 3.9 and Fig. 3.10.

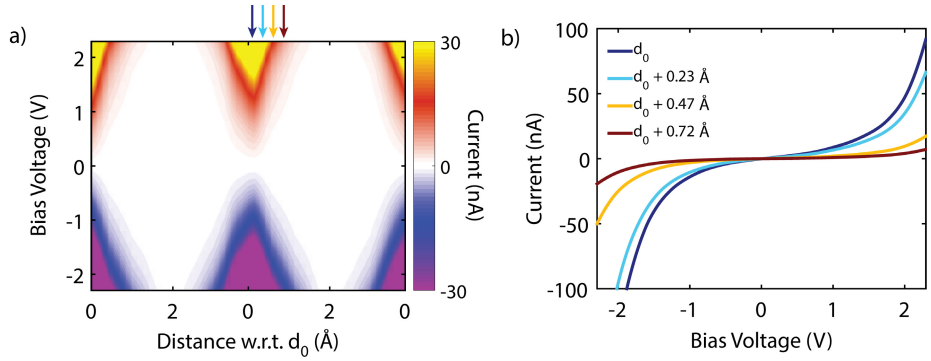

Figure 3.9: **Systematic IV series.** (**a**) Current map as a function of bias voltage and electrode displacement. The arrows mark the position at which the IVs shown in (b) have been recorded. (**b**) Example IVs recorded during the systematic IV series shown in (a).

In the *systematic IV series*, the junction is broken at room temperature, and as soon as a molecular feature is observed in the IVs (for instance step-like features), the set-up is submerged in liquid helium, thereby cooling the sample to about 6 K. When this base temperature is reached, IVs are recorded as a function of electrode separation. The motor is stopped during the recording of the IV and stepped for 0.1 μm ($\approx$ about 5.5 pm) in between the IVs. This process is repeated hundreds of times, and the electrode motion is reversed for a set upper and lower low-bias conductance, which is obtained from a linear fit of the IV at low bias (<50 mV). It is important to note that for this method the electrodes are never fused, making it ideal to investigate the stability of a molecular junction. In addition, the conductance range is usually 1–2 orders of magnitude and the linear amplifier is used.

As the electrode spacing itself is not precisely known, the distance at the start of a series is called d_0. The electrode displacement used in the systematic IV series is relative to that particular spacing. In Fig. 3.9a and b an example of such a measurement is shown. The measurement is recorded on a sample with gold only and starts in the tunneling regime. Figure 3.9a shows a colormap of the current as a function of bias voltage and electrode separation. The electrode separation is initially increased with 2 Å, after which the motor motion is reversed. The electrode displacement is brought back to d_0, completing thereby 1 cycle. In Fig. 3.9a, two full cycles are shown. For particular separations marked by the coloyellow lines, IVs are plotted in Fig. 3.9b, showing the expected shape for tunneling through a single barrier, and the exponential reduction in current with increasing distance. This method will been extensively used in Chapter 6 and Chapter 7.

The second method, or the *IV breaking series* is very similar, except from the fact that the upper conductance limit for motion reversal is in the metallic regime, typi-

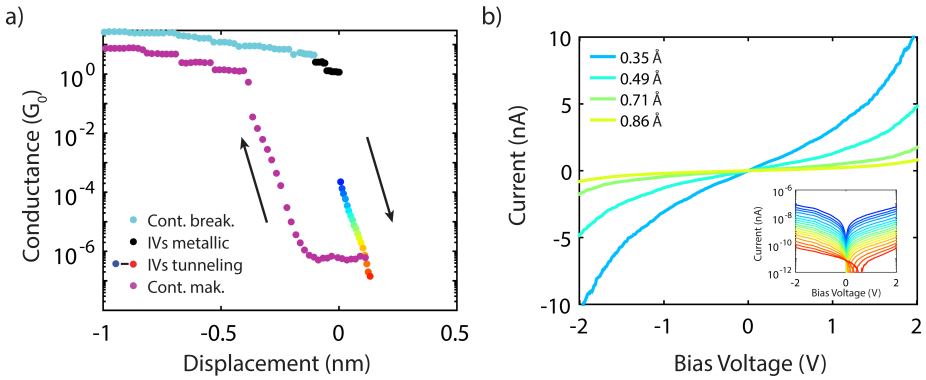

Figure 3.10: **IV breaking series.** (**a**) Conductance evolution during an IV breaking series. For a description, see the text. (**b**) Example IVs recorded during the IV breaking series shown in (a). The positions at which the IVs have been recorded correspond to the colored dots in the tunneling regime. The inset shows all the IVs recorded in the tunneling regime on logarithmic scale. The exponential decrease in current with distance, corresponding to tunneling through a single barrier, is clearly visible.

cally above 15 G_0. This fusion ensures a reconfiguration of the junction for every cycles, providing valuable information about the variability in junction formation. This method will be extensively used in Chapter 7. In this scheme, the junctions are typically first cooled down to 4 K and then broken. An example of such a measurement is shown in Fig. 3.10a and b. A typical measurement occurs as follows: the junction starts in the metallic regime (cyan dots in Fig. 3.10a), with a conductance above 15 G_0. With a continuous motion of the motor (speed 2-4 μm/s), the junction is broken until the conductance, measured at 100 mV, drops below 3 G_0. Below this threshold, the motor motion is stopped, and IVs are recorded with a bias voltage of typically 100 mV. In between the different IVs, the motor is stepped with 0.1–0.5 μm, corresponding to about 5–25 pm on the electrode scale. For each IV, the low-bias conductance is calculated (see black dots), and once its value drops below 0.01-0.001 G_0, the bias range is increased to 1-2.5 V. The dots ranging from blue to red in Fig. 3.10a indicate the position at which the IVs have been recorded with a full bias range in the tunneling regime. A few IVs recorded in the tunneling regime are shown in Fig. 3.10b. Those IVs again exhibit the expected single-barrier behaviour. For currents <200 pA, one should switch between the logarithmic amplifier and the linear amplifier. [1] The stepping of the motor continues until a set conductance or minimum current is reached, after which the logarithmic amplifier is used to initialize the junction to >15 G_0 with a continuous motion of the motor (speed 2-4 μm/s). A new cycle is then started.

We would like to point out a few points concerning these measurements. First, IVs are only recorded during the breaking of the junction, not during the making. Sec-

[1] For currents below about 200 pA, the RC-time of the logarithmic amplifier starts to dominate, and charging effects, such as an opening of the IVs, become visible. For this reason, in collaboration with Raymond Schouten (TU Delft), a module was designed which could switch from the logarithmic amplifier to a linear one during the measurements. The switching is controlled using Python and occurs once the current measured by the logarithmic amplifier drops below the saturation current of the linear amplifier. The linear amplifier supports gains varying between 1M and 100G. Typically, it is used with a gain of 100M.

ond, the electrode displacement has been set to zero at the rupture point of the 1 G_0 plateau. Third, the dots in the breaking and making do not overlap; this is a result of the backlash in the mechanics. The backlash is larger than reported previously[127] and in section 3.7.1, most likely because of wearing of the screw drive due to years of measurements. Finally, the difference between the logarithmic and linear amplifier can clearly been seen in Fig. 3.10a when comparing the conductance of the orange-red dots in the tunneling regime, and the purple dots in the making. The conductance in the making is limited by the leakage current of the logarthmic amplifier, yielding a noisefloor just below $1{\cdot}10^{-6}$ G_0. The conductance of the orange-red dots is recorded with the linear amplifier, which goes at least one order of magnitude lower in conductance.

3.6.3. CURRENT-VOLTAGE CHARACTERISTICS WITH GATE

In Chapter 6, systematic IV series are recorded on three-terminal samples based on the original design by Martin *et al.*[129]. In such devices, the leakage currents through the gate dielectric were tested at room temperature on unbroken junctions before performing the experiment. IV characteristics were recorded between the source-drain bridge and the gate. The maximum bias voltage was increased until a leakage current of about 20 pA was observed. The voltage at which that particular leakage current was achieved (typically around 2 V) was taken as the maximum voltage difference applied between the source/drain and the gate during the experiments. To ensure the continuity of the gate, its conductance was monitored during the breaking of the source-drain and checked regularly during the measurements. Similar to the two-terminal measurements, several schemes can be used here.

In the first one, a systematic IV series was started at room temperature. Once the IVs showed clear step-like features, the setup was rapidly cooled down to 6 K. At this temperature, during the systematic IV series, a gate diagram was recorded for fixed electrode spacing after each 50-th IV by sweeping both the bias voltage and gate voltage. For a more detailed description of the resulting stability diagrams, see Chapter 2. Upon application of a gate voltage, a settling time of 100 ms was used for each gate voltage. The step size of the electrode separation between the IVs was typically set to 0.1–0.2 μm.

In the second measurement scheme, used in Chapter 9, the junctions were repeatedly broken and fused, similar to the IV breaking series in two-terminal devices. The measurements are started with the junction in the metallic regime, with a conductance >10 G_0. The junction is then broken in a continuous fashion until a set conductance in the tunneling regime. This value is molecule dependent, but is typically between $1{\cdot}10^{-4}$ and $1{\cdot}10^{-5}$ G_0. An IV is then recorded. If the IV shows the molecular feature one is looking for, such as steps, rectification, negative differential conductance, etc., a stability diagram is recorded. In the case the IV is not as required, the junction is fused continuously and a new measurement is started. By performing measurements is this way, one can very specifically look for particular features in the IVs, and record stability diagram only on 'interesting' junction. This is in contrast to the systematic IV series, and can considerably speed up the measurements. It should be evident that, prior to this approach, a very extended characterisation of

the molecule is required.

3.7. ATTENUATION RATIO CALIBRATION

In MCBJ samples, the attenuation ratio is the ratio between the displacement of the pushing rod bending the sample, and the displacement at the level of the electrodes[146]. For lithographic break-junctions this value is typically between $1{\cdot}10^{-4}$ and $1{\cdot}10^{-6}$[20], depending on the junction geometry. It is this high value which leads to the high resolution in electrode displacement and junction stability. As a comparison, notched wire junctions[20] have an attenuation ratio between $1{\cdot}10^{-2}$ and $1{\cdot}10^{-3}$.

The calibration of the attenuation ratio can be performed in several ways. One way is to analyse the length of the 1 G_0 plateaus obtained during conductance histograms (in practice all points between 1.4 G_0 and 0.7 G_0 are considered part of the plateau). When making a histogram of the length of the 1 G_0 plateau, a peak is usually visible, which corresponds to the size of a gold atom[147]. For stable contacts (mostly at cryogenic temperatures), monatomic chains of several atoms can be formed, yielding multiple peaks in such a length histogram. From the position of the peaks in the length histogram, one can calculate the attenuation ratio, knowing that the size of a gold atom is about 0.25 nm[147]. This method can be used both at room temperature as well as at cryogenic temperatures. However, one has to keep in mind that the number of traces required to construct a decent length histogram is at least 1000-2000. Using the piezo-element at room temperatures, this required number of traces can be reached in about an hour, while using the motor several days to several weeks can be necessary.

Another way to calibrate the attenuation ratio involves low-temperature IVs recorded on a clean sample, *e.g.* on which no molecules have been deposited. For the calibration, IVs are recorded in the tunneling regime for various electrode spacings. The IVs are then fitted to the Simmons model[143] for vacuum tunneling, from which the electrode separation is obtained. From the change in inter-electrode spacing, the attenuation ratio can be determined.

The third way is to make use of the Gundlach oscillations[147]. Gundlach oscillations are periodic oscillations which occur in tunnel junctions at very high biases. When the bias voltage applied exceeds the work junction of the electrodes, part of the single tunneling barrier becomes classically accessible. The wave-function in that region then consists of the superposition of the incoming and reflected electron waves thereby forming resonant states. Upon increase of the bias voltage, every time a new resonant state enters the bias window an additional transport channel is opened and a maximum in the transmission arises. Calibration occurs as follows: while increasing the bias voltage, one monitors the current. In order to determine the electric field strength, a feedback loop on the piezo voltage is used to keep the current constant. From the periodicity in the conductance, the field strength can be calculated. Using this parameter, one can calculate, for a fixed voltage, the electrode spacing. In the high-bias regime, the piezo response scales linearly with bias voltage, allowing to

relate the change in piezo voltage to a change in electrode spacing.

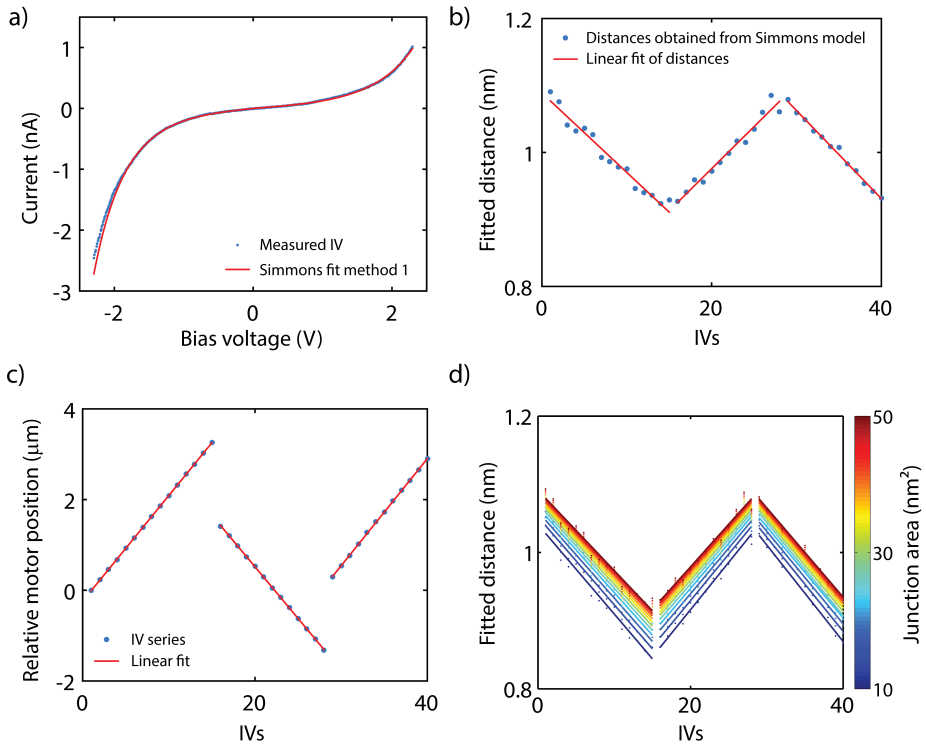

Figure 3.11: **Calibration of the attenuation ratio of a two-terminal MCBJ sample.** (**a**) The blue dots represent an IV recorded for fixed electrode spacing on a two terminal MCBJ sample. The black line is a fit according to the Simmons model. Positive and negative bias were fitted separately. For the fit, the junction area was set to 28 nm^2. The obtained (average) electrode spacing is 1.04 nm and the fitted barrier height 2.37 eV. (**b**) Fitted distances obtained for an IV series, as described in (a). The yellow line represents a linear fit through the fitted distances for breaking and fusing of the junction. (**c**) Motor position for the IV series shown in (b) with a linear fit. The jumps in motor position are due to backlash in the setup. (**d**) Dependence on the junction area of the fitted distances obtained for the IV series.

3.7.1. TWO-TERMINAL SAMPLES

To calibrate the attenuation ratio of the two-terminal samples we use the method involving low-temperature IVs. A typical IV in the vacuum regime can be found in Fig. 3.11a. Transport through a single-barrier, in this case through vacuum, can be described using the Simmons model. The tunneling current as a function of voltage is described by the following expression

$$I(V_b) = \frac{eA}{4\pi^2\hbar d^2}\left[\begin{array}{c}(\phi - \frac{eV_b}{2})\exp(-\frac{2d}{\hbar}\sqrt{2m_e(\phi - \frac{eV_b}{2})}) \\ -(\phi + \frac{eV_b}{2})\exp(-\frac{2d}{\hbar}\sqrt{2m_e(\phi + \frac{eV_b}{2})})\end{array}\right] \tag{3.1}$$

where, A is the junction area, ϕ the barrier heigth (in this case the work function of the electrodes), d the barrier width, and e the electron charge. We note that this for-

mula holds for a rectangular tunneling barrier and for $|eV_b| < \phi$, and assume that the work function of the electrodes is equal. In practice, however, the work function of the electrodes can be different, introducing an asymmetry in the IV. To account for the asymmetry, positive and negative bias were fitted separately. By fitting the experimental data, one can obtain the junction area, the barrier heigth and the barrier width. To reduce the number of fit parameters, the junction area was initially fixed to 30 nm^2. For the distance, the average of negative and positive bias was used. Figure 3.11b presents the fitted distance for a series of consecutive IV measurements. Figure 3.11c shows the motor displacement during the same IV series. Using a linear fit through both the fitted distances and the motor position, we obtain an average attenuation ratio of $5.52 \cdot 10^{-5}$. To investigate the influence of the fixed junction area on the fit, we varied its value between 10 nm^2 and 50 nm^2. The resulting fitted distances are shown in Fig. 3.11d, including the linear fits through the data points. The graph shows that the junction area has little influence on the obtained attenuation ratios. The average of the resulting ratios is $5.49 \cdot 10^{-5} \pm 0.160 \cdot 10^{-5}$. This value matches well the one obtained previously[144], and is consistent with other methods, *e.g.* room-temperature breaking traces. Therefore, throughout this dissertation, an attenuation ratio of $5.5 \cdot 10^{-5}$ will be used for the two-terminal MCBJ samples.

3.7.2. THREE-TERMINAL SAMPLES

For the three-terminal MCBJs fabricated following the Martin *et al.*[129] design, the attenuation ratio from literature was used. Using a very similar method as described above for the two-terminal samples using IV-characteristics, Martin *et al.* found the attenuation ratio to be about $1.5 \cdot 10^{-5}$. The difference in attenuation ratio is attributed to the different junction geometry.

For the new design of the gated MCBJ samples discussed in section 3.4.2, the attenuation factor was calibrated using low-temperature breaking traces. For this purpose, more than 4500 traces were recorded at a motor speed of 4.0 μm/s and a bias voltage of 0.1 V. The junctions were fused to 20 G_0 to ensure atomic rearrangement, and broken until the resolution limit of the logarithmic amplifier had been reached, which is $< 1 \cdot 10^{-6}$ G_0. Figure 3.12a shows a few typical breaking traces, which have been offset horizontally for clarity. Of each trace, the length of the $1G_0$ plateau was determined by subtracting the motor position corresponding to the last data point above 0.7 G_0 from the one with the first point below 1.4 G_0. In Fig. 3.12a, the detected 1 G_0-plateaus are indicated with purple lines. The traces are colored according to their 1 G_0 plateau length.

Figure 3.12b presents a histogram (blue) of the 1 G_0 plateau length obtained from all 4565 breaking traces. The bar-plot shows a broad peak around 5.5 μm which is steeper on the left side than on the right side, suggesting that monatomic chains with more than 1 gold atom are also formed. From a Gaussian fit (Gaus. fit 1, yellow line) to the right side of the peak, the asymmetry becomes more evident. Gaus. fit 1 accounts for the formation of single-atom chains, and to reveal the contribution of chains consisting of more than one atom, Gaus. fit 1 is subtracted from the data. This yields the histogram shown in Fig. 3.12c., where a peak around 11 μm is visible. This peak corresponds to the formation of gold dimers. To estimate their contribution, the data

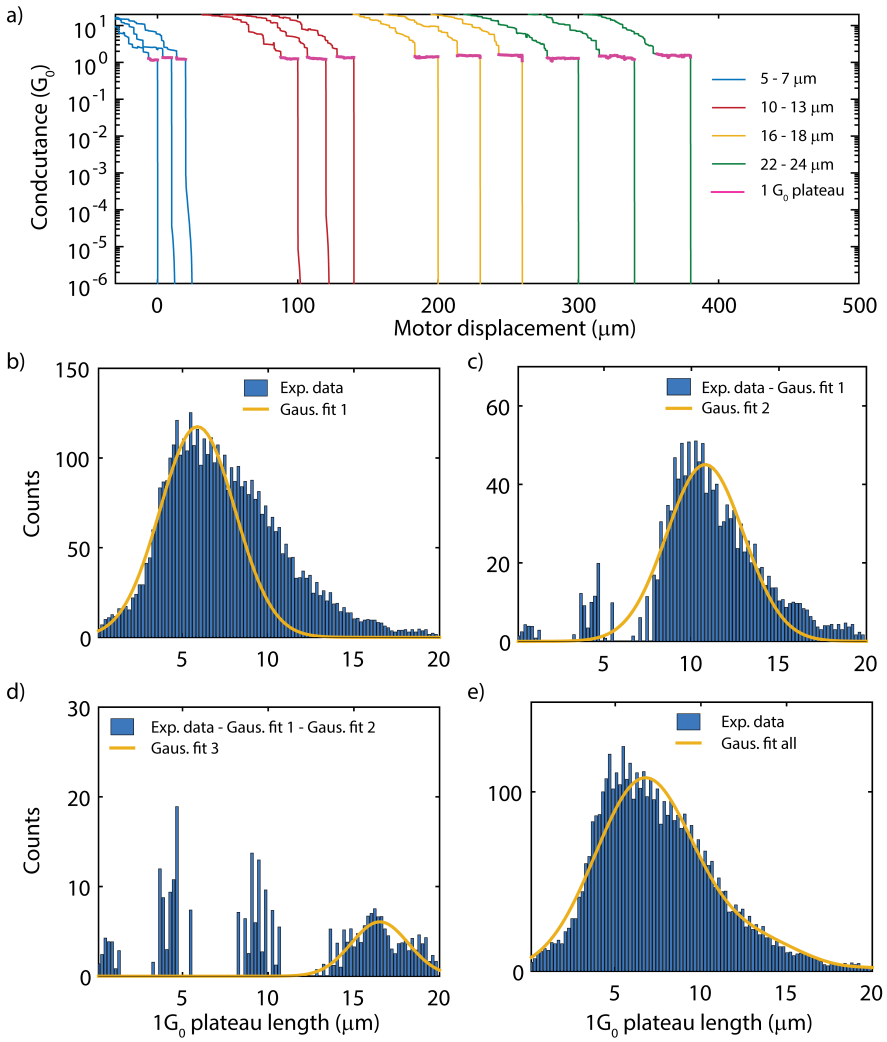

Figure 3.12: **Calibration of the attenuation ratio of a three-terminal MCBJ sample.** (**a**) Examples of breaking traces, with in red the length of the 1 G_0 plateau. The traces have been colored according to the 1 G_0 plateau length. (**b**) Histogram of the 1 G_0 plateau length, together with a Gaussian fit to estimate the occurrence of single-atom chains. (**c**) Histogram of the 1 G_0 plateau length from which the Gaussian fit of (b) has been subtracted, together with a Gaussian fit to estimate the occurrence of two-atom chains. (**d**) Histogram of the 1 G_0 plateau length from which the Gaussian fit of (b) and (c) have been subtracted, together with a Gaussian fit to estimate the occurrence of three-atom chains. (**e**) Histogram of the 1 G_0 plateau length with the sum of the Gaussian fits of (b), (c) and (d).

is again fitted to a Gaussian function (Gaus. fit 2). This fitting and subtraction process is iterative and can be repeated several times, revealing the contribution of even longer chains at each cycle. By subtracting Gaus. fit 2 from the data, the contribution of three- or more atoms chains is revealed (see Fig. 3.12d). Here, a peak around 16 μm is observed, which is again fitted (Gaus. fit 3). At this point, the iterative pro-

cess is stopped. One has to keep in mind that every time a fit is subtracted from the data, the total number of counts in the histogram drastically decreases, and as a result its occurrence. From the area of the Gaussian, we can estimate the occurrence probability of the one-, two- and three-atom chains. We find that the one-atom has a probability of 70.2%, the two-atom chain of 27.1%, and the three-atoms chain of 2.7%. As chains of four or more atoms have a occurrence of << 1%, they will not be considered.

Figure 3.12e shows the experimental data with the sum of the three Gaussian fits. The overall fit reproduces the experimental data well. From the average motor position we obtained an average of 5.6 μm per gold atom, from which we calculate an attenuation ratio of $4.4{\cdot}10^{-5}$. This value is larger than the one obtained by Martin *et al.*[129] A reason could be the different geometry of the junction. In the new design, the substrate thickness has been increased from 300 μm to 500 μm. In addition, the polyimide thickness has been increased from 3 μm to 6 μm, and the thickness of the gate has been changed from 60 nm to 80 nm.

We finally note that in the 1 G_0 length histogram of Fig. 3.12, the peaks for two- or more atom chains only become clear after subtraction of the Gaussian fit. In the article by Untiedt *et al.*[147], the peaks are more pronounced. The difference might be due to the very different electrode speed used. In our case we use an electrode speed of 0.18 nm/s, as this is the upper limite of the speed we can reach at low temperature. For STM set-ups the speed is typically >10 nm/s, which favors the formation of longer chains[148].

4

INFLUENCE OF CHEMICAL STRUCTURE ON THE STABILITY AND THE CONDUCTANCE OF PORPHYRIN SINGLE-MOLECULE JUNCTIONS

In this chapter, we investigate charge transport through single porphyrin derivatives. We find that stable molecular junction can form stable junctions without thiol anchoring groups. Adding thiol end groups and pyridine axial groups to the porphyrin backbone, increases the stability of the junctions and leads to an large spread in conductance, respectively. Our results suggest that various junction configurations can be formed, and that for a reliable junction formation of non-rod-like molecules, careful design the molecule is crucial.

Parts of this chapter have been published in Angewandte Chemie International Edition **50**, 11223 –11226, (2011) [73].

The idea of using porphyrin molecules as building blocks of functional molecular devices has been widely investigated with a view to applications in nanoscience, molecular electronics, and photonics [149, 150]. The structural flexibility and well-developed synthetic chemistry of porphyrins allows their physical and chemical properties to be tailored by choosing from a wide library of macrocycle substituents and central metal atoms. Nature itself offers magnificent examples of processes that utilize porphyrin derivatives, such as the activation and transport of molecular oxygen in mammals and the harvesting of sunlight in plant photosynthetic systems. In order to exploit the highly desirable functionality of porphyrins in artificial molecular devices, it is imperative to understand and control the interactions that occur at the molecule-substrate interface, in particular the way in which a single molecule binds to a pair of metallic electrodes. Such interactions largely depend on the electronic and conformational structures of the adsorbed molecules, which can be studied using techniques such as scanning tunneling microscopy (STM)[98, 151–153], UV Photoemisson Spectroscopy (UPS)[154], X-Ray Photoemission Spectroscopy (XPS)[150] and on a theoretical level with density functional theory (DFT)[155]. Recent studies on conjugated rod-like molecules have shown that the molecular conductance can be significantly affected by the binding geometry[156] and the coupling of the π-orbitals to the leads[23].

4.1. EXPERIMENTS

In this Chapter, we study the interaction of the π-electrons of more complex, non-rod-like porphyrin molecules with the electrodes and investigate strategies to reduce it by modifying the chemical structure of the porphyrin molecule. For this, we have developed a new experimental approach, which provides new insight into the detailed nature of the conductance of single molecules. We have used the series of molecules represented in Fig. 4.1a-c to examine the influence of the molecular structure on the formation of porphyrin single-molecule junctions. Since the thiol group is most commonly used to contact rod-like molecules to form straight molecular bridges[62], we first compared the porphyrin molecule (5,10,15,20-tetra(p-phenyl)porphyrin, abbreviated as H_2-TPP) without thiol termination (Fig. 4.1a) to a nearly identical molecule with two thiol groups on opposite sides of the molecule (5,15-di(p-thiophenyl)-10,20-di(p-tolyl)porphyrin, abbreviated as H_2-TPPdT, Fig. 4.1b). To investigate the influence of the molecular backbone geometry on the junction formation we further studied a thiol terminated porphyrin molecule with two bulky pyridine axial groups attached via an octahedral Ru^{II}-ion ([Ru^{II}(5,10,15,20-tetra(p-phenyl)porphyrin)(pyr)2] abbreviated as Ru-TPPdT, Fig. 4.1c). Due to steric hindrance these groups can be expected to reduce the direct interaction of the metal electrodes with the π-face of the porphyrin[152].

Prior to electrical characterization, the molecules of interest were deposited using self-assembly from solution. To study the conductance of these molecules we used lithographic mechanically controllable break junctions (MCBJ) in vacuum at room temperature. The lay-out is shown in Fig. 4.1d. This device architecture allows sub-angstrom control over the electrode displacement through a deflection of

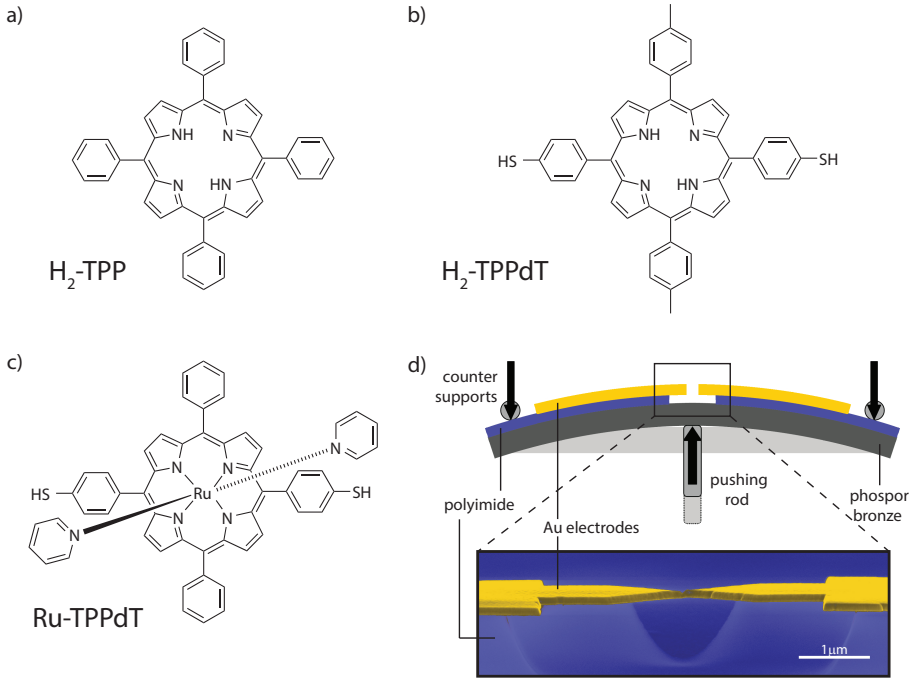

Figure 4.1: **Experimental method.** Chemical structure of (**a**) H_2-TPP (**b**) H_2-TPPdT and (**c**) Ru-TPPdT. (**d**) Top: lay-out of the mechanically controllable break junction (MCBJ). Bottom: scanning electron micrograph of a MCBJ device (colorized for clarity). The scale bar shows that the suspended part of the electrode bridge is about 1.5 μm long.

the substrate center in a three-point bending mechanism. During repeated breaking and fusing of the electrodes, the current was measured at a fixed bias voltage and the junction conductance was determined as a function of electrode stretching. Details concerning the synthesis of the molecule and the experimental procedures can be found in Chapter 3.

4.2. RESULTS

4.2.1. CONDUCTANCE HISTOGRAM

Sets of 1000 consecutive breaking traces from individual junctions were then analyzed numerically to construct 'trace histograms' of the conductance ($\log_{10}$(G) versus the electrode displacement d)[54, 157]. This statistical method maps the breaking dynamics of the junctions beyond the point of rupture of the last monatomic gold contact (defined as d=0), which has a conductance of one quantum unit $G_0 = 2e^2/h$. Areas of high counts represent the most typical breaking behavior of the molecular junctions. Figure 4.2 presents 'trace histograms' as well as examples of individual breaking traces for an acetone reference sample (a) and junctions exposed to H_2-TPP (b), H_2-TPPdT (c) and Ru-TPPdT (d). For all three porphyrin molecules as well

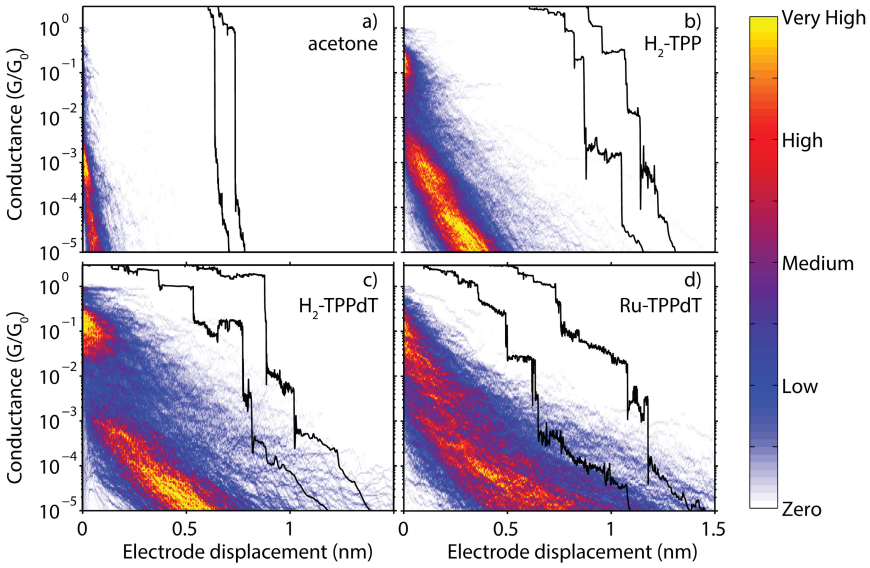

Figure 4.2: **Trace histograms of the different molecules.** Trace histograms constructed from 1000 breaking traces for (**a**) acetone, (**b**) H_2-TPP, (**c**) H_2-TPPdT and (**d**) Ru-TPPdT. Regions of high counts represent the most probable breaking behavior of the contact. The black curves are examples of individual breaking traces (offset for clarity). For the construction of the histograms d=0 for each curve was set to the point where the conductance drops sharply below 1 G_0. All histograms were taken at a bending speed of 30 μm/s (on the scale of the electrodes, this bending is translated to a stretching on the order of 1.8 nm/s) and a bias voltage of 150 mV. No data selection schemes have been utilized.

as for the reference samples which was exposed to acetone several junctions have been measured. Here, we only show a typical set of junctions. In the junction which was exposed to the pure solvent, *i.e.*, without porphyrin molecules (Fig. 4.2a), the Au-bridge initially gets stretched until a single-atom contact is formed and a plateau around the conductance quantum ($G \sim G_0$) is observed (only visible in the individual traces shown in black). Upon further stretching, the monatomic contact is broken and the conductance decreases sharply and abruptly to 10^{-3} G_0. Beyond this point, electron tunneling between the electrodes leads to a fast conductance decay with stretching (visible as the orange tail), as expected for a single tunneling barrier.

In contrast, introducing the porphyrin molecules by self-assembly on the junctions leads to pronounced plateaus at different conductance values in the sub-G_0 regime. These plateaus can be flat or sloped[23, 63]. The representative breaking traces that are included in Fig. 4.2b-d display a set of such plateaus. Averaging over 1000 traces does not lead to a narrow region of high counts in the histograms, in contrast to measurements on rod-like molecules[54, 63, 144, 158]. In the trace histogram of H_2-TPP (Fig. 4.2b), however, there are two distinct regions with high counts; a high-conductance region (HCR) around 10^{-1} G_0, and a sloped low-conductance region (LCR) below 10^{-3} G_0. For H_2-TPPdT (Fig. 4.2c) both the HCR and LCR are longer than for H_2-TPP; thus, adding the thiol end groups to H_2-TPP increases the plateau length. Adding the thiol to H_2-TPP also reduces the slope of the LCR. In Ru-TPPdT

(Fig. 4.2d) the HCR and LCR cannot be distinguished anymore: only one long region sloping from 10^{-1} G_0 to 10^{-5} G_0 is present, which has a shallower slope compared to H_2-TPP and H_2-TPPdT, and an increased length.

From the trace measurements we come to the following conclusions. First, a stable molecular junction can be formed even when no chemically distinct anchoring groups are present. Second, there is no qualitative difference between the trace histograms of H_2-TPP and H_2-TPPdT molecules. There is only an increased length of the area of high counts, which can be interpreted as an increase in junction stability. Third, by adding two pyridine axial groups to the molecules (that is, for Ru-TPPdT), the region of high counts in the trace histogram becomes even longer, and the variability in conductance increases.

4.2.2. TIME TRACES

Additional information about molecular junction configurations can be gained by measuring the evolution of the junction conductance over large time intervals at fixed electrode distances[159]. To obtain such 'time traces', we opened the junction in small steps using a servo motor at 77 K. This low temperature enhances their stability due to a reduced surface diffusion without causing extensive changes in molecular conductance[144]. We then measured the conductance in the range from 1 G_0 to 10^{-4} G_0 at various fixed electrode spacings and for time periods exceeding several hours. Due to the exceptional control over the electrode separation in the MCBJ[144, 159], conductance jumps in these measurements can be attributed to reconfigurations of the molecule in the junction rather than mechanical interference of the setup.

Typical time traces of junctions exposed to pure acetone, H_2-TPT, H_2-TPPdT and Ru-TPPdT are presented in Fig. 4.3a-d. As can be seen in Fig. 4.3a, a stable contact is formed at 1 G_0 in the clean junction. A slight increase in the electrode spacing leads to abrupt breaking of the contact to a conductance value around 10^{-4} G_0. In contrast to this sharp drop, the presence of porphyrin molecules leads to the formation of junctions with conductances in the region between 1 G_0 and 10^{-3} G_0 (H_2-TPP Fig. 4.3b, H_2-TPPdT Fig. 4.3c and RuTPPdT Fig. 4.3d). Below 10-3 G_0, the H_2-TPP molecule (Fig. 4.3b) exhibits a sudden conductance drop to below 10^{-5} G_0. In contrast, thiol terminated H_2-TPPdT and Ru-TPPdT (Fig. 4.3c-d) form molecular junctions over the whole range between 1 G_0 and 10^{-4} G_0. The observations support the conclusions drawn from the trace histograms: adding thiol and pyridine groups increases the junction stability and leads to a variety of molecular geometries with different conductance values.

A closer inspection of the time traces reveals interesting information on the behavior of the molecule in the junction. Since the electronic noise is much smaller than the width of the observed bands of the measured conductance values, we conclude that what appears to be noise in the time traces is in fact a sign of small variations in the molecular configuration[159]. Large jumps in the conductance (Fig. 4.3c-d) indicate that a molecular junction can spontaneously change configuration. In

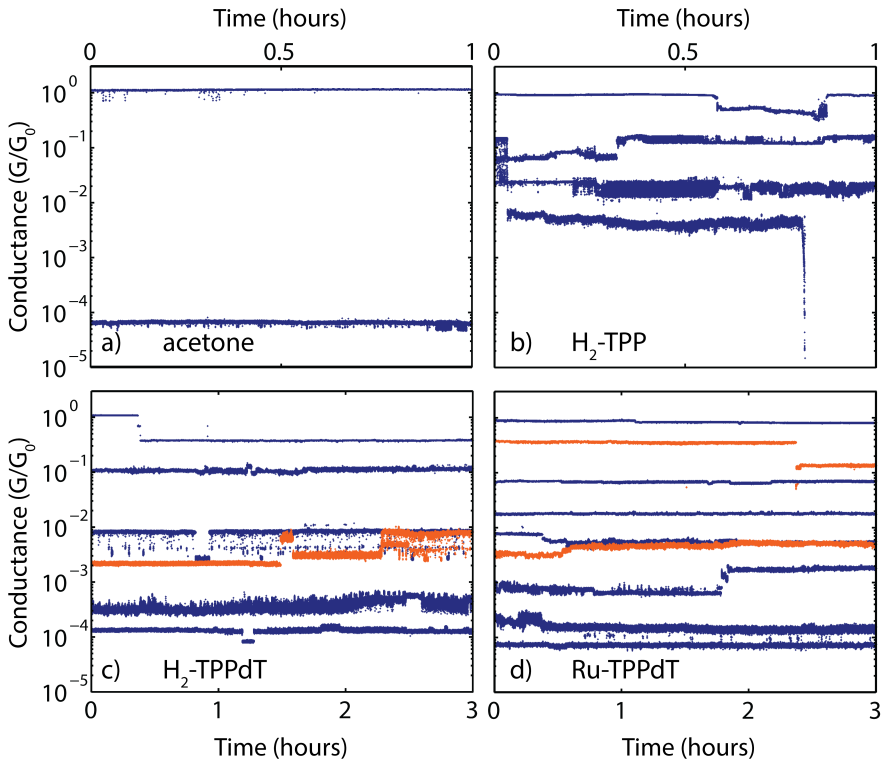

Figure 4.3: **Time traces of the different molecules.** Conductance versus time plots for (**a**) acetone, (**b**) H_2-TPP, (**c**) H_2-TPPdT and (**d**) Ru-TPPdT taken at bias voltage of 150 mV. The traces originate from the same opening event and are taken at an interval of 50 pm. Several lines are displayed in orange for clarity. The observed conductance variations (noise on the trace) are due to small changes in the molecular configuration. Larger jumps are attributed to spontaneous reconfiguration of the molecular junction.

Fig. 4.3c random telegraph noise between two conductance values is observed indicating the possibility of forming several meta-stable configurations. Furthermore, Fig. 4.3d shows that a particular junction conductance can be reached from different starting values (blue and orange traces in the middle of the figure).

4.3. DISCUSSION

The presence of such a large range of molecular adsorption geometries contrasts with most studies on long rod-like molecules, which generally assume a straight bridging configuration of the molecule with both thiol groups connected to the electrodes (see Fig. 4.4a). For H_2-TPPdT, such a configuration could be expected. However, the high affinity of the porphyrin π-cloud for metal surfaces likely stabilizes other configurations, such as sketched in Fig. 4.4b and Fig. 4.4c (the configuration shown in Fig. 4.4b is likely destabilized by adding the pyridine axial groups, as the one shown is Fig. 4.4c may be stabilized, as displayed in Fig. 4.4d). A stable junction configuration can be formed without thiol groups[160] and recent break junction experiments have

demonstrated that benzene moieties can bind directly to gold electrodes[161, 162]. Furthermore, it has been reported that the lateral coupling of p orbitals to electrodes influences the single-molecule conductance of rod-like molecular wires[62, 163]. Such coupling becomes more likely when laterally extended molecules are probed. In addition, tetraphenylporphyrin molecules have internal degrees of freedom, which can influence the charge transport on a single-molecule level[164]. STM studies indicate that tetraphenylporphyrins can bind to Au(111) through an interaction with their phenyl side groups[153]. On gold surfaces, their conformation can change through rotations of side groups and buckling of the center[98]. Such variations in the adsorption geometry, which can be expected to lead to different conductance values, are likely the origin of the variety of junction configurations that we observe.

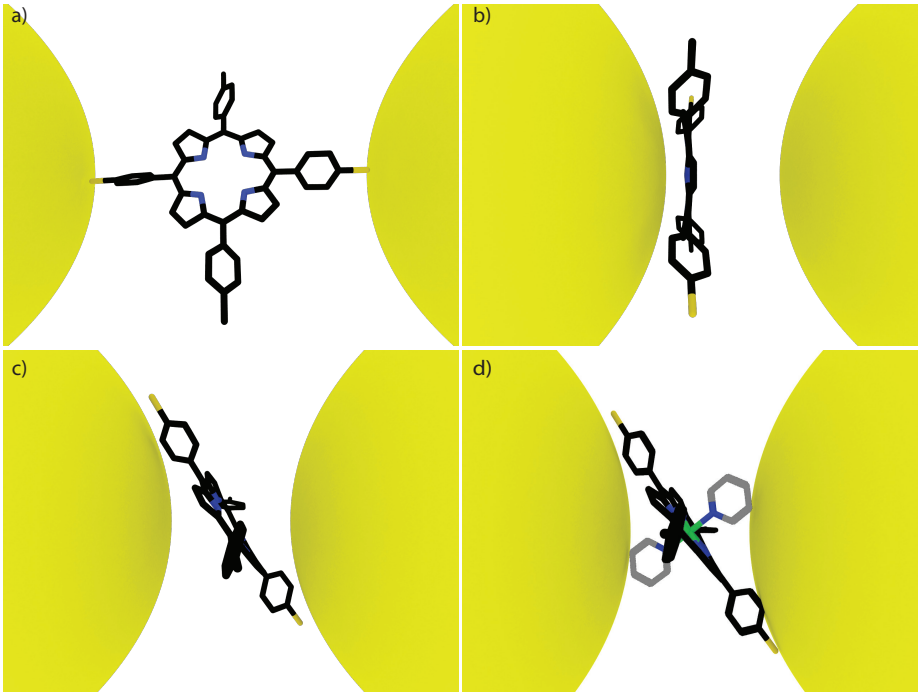

Figure 4.4: **Illustration of four possible configurations of a porphyrin molecule in the junction.** (**a**) Bridging configuration of H_2-TPPdT. (**b**), STM-like configuration of H_2-TPPdT. (**c**) Intermediate configuration of H_2-TPPdT. (**d**) Intermediate configuration of Ru-TPPdT stabilized by two bulky pyridine groups (shown in grey).

4.4. CONCLUSION

In summary, we have electrically probed different junction configurations of porphyrin molecules. We have demonstrated that porphyrin molecules can form stable bridging molecular junctions even without thiol anchoring groups. Adding the thiol end groups and pyridine axial groups to the porphyrin backbone, respectively, increases the stability of the junctions and leads to an increased spread in conduc-

tance. This is a result of the formation of different junction configurations. To enable the reliable formation of stable porphyrin junctions, molecules with well-defined adsorption geometries will be required. Quantum chemistry calculations could yield more insight into their design as well as the configurations and the conductance of porphyrin single-molecule junctions. Finally, we expect that multiple junction configurations with considerable variation in the measured conductance values can also be observed for other non-rod-like molecules.

5

CHARGE TRANSPORT IN A ZINC–PORPHYRIN SINGLE-MOLECULE JUNCTION

We have investigated charge transport in ZnTPPdT-Pyr molecular junctions using the lithographic MCBJ technique at room temperature and cryogenic temperature (6 K). We combine low-bias statistical measurements with spectroscopy of the molecular levels using I(V) characteristics. This combination allows us to characterize the transport in a molecular junction in detail. This complex molecule can form different junction configurations, which is observed in trace histograms and in current-voltage (I(V)) measurements. Both methods show that multiple stable single–molecule junction configurations can be obtained by modulating the inter-electrode distance. In addition, we demonstrate that different ZnTPPdT-Pyr junction configurations can lead to distinct spectroscopic features with the same conductance values. We show that statistical low-bias conductance measurements should be interpreted with care, and that the combination with I(V) spectroscopy represents an essential tool for a more detailed characterization of the charge transport in a single molecule.

Parts of this chapter have been published in Beilstein Journal of Nanotechnology **2**, 714–719, (2011) [74].

The break junction method represents a popular choice to investigate the electronic transport through metal-molecule-metal junctions[18, 61, 63, 165–169]. While repeatingly breaking and fusing two metallic electrodes, the low-bias conductance is monitored as a function of electrode displacement. Such low-bias transport measurements have been extensively used to study the molecular conductance dependence of rod-like molecules on their length[166, 170], their conformation[61, 63] and their anchoring groups[168, 169]. However, as the bias range is very limited, the main contribution to the current is off-resonant transport. As such, spectroscopic information about molecular energy levels involved in the charge transport is lacking.

5.1. EXPERIMENTS

Here, we investigate charge transport through a Zinc porphyrin with an axial pyridine ligand in both the low-bias and the high-bias regime. Porphyrins are interesting for this purpose as they are complex, non-rod-like molecules that can form different stable configurations[153, 154], especially when functionalized with metal-bound axial pyridine ligands[73]. Using the mechanically controllable break junction technique (MCBJ), we study the low-bias conductance as a function of electrode displacement. In addition, we use current-voltage measurements for different electrode spacings to gain spectroscopic information in the high-bias regime.

The MCBJ technique is an elegant way to control the spacing between two metallic electrodes with a sub-atomic ($<10^{-10}$ m) resolution[20, 124, 171]. This control is achieved by bending a substrate with a pair of partially suspended electrodes in a three-point bending mechanism. Upon bending of the substrate, a nanosized gap is formed between the electrodes, which can be mechanically adjusted and which is impressively stable on the order of hours, even at room temperature[144, 159]. The layout of the technique is schematically presented in Fig. 5.1b.

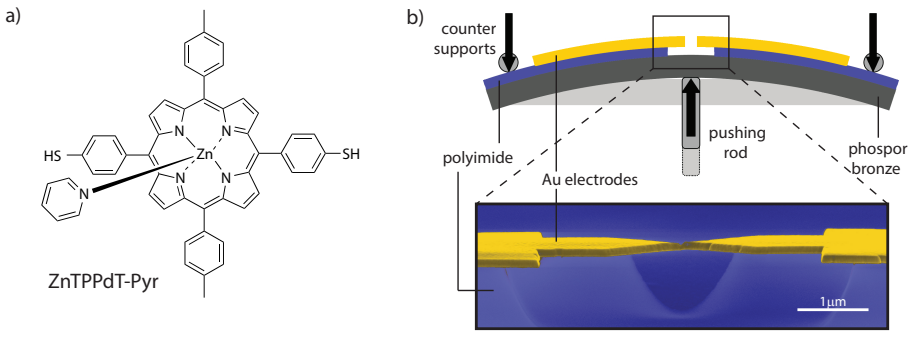

Figure 5.1: **Experimental method.** (**a**) Structural formula of ZnTPPdT-Pyr. (**b**) Top: lay-out of the mechanically controllable break junction (MCBJ). Bottom: scanning electron micrograph of a MCBJ device (colorized for clarity). The scale bar shows that the suspended bridge is about 1.5 μm.

All experiments are performed in high vacuum ($<10^{-6}$ mbar). Prior to the exper-

iments, [Zn^{II}(TPPdT)(Pyr)] (TPPdT stands for (5,15-di(p-thiolphenyl)-10,20-di(p-tolyl)porphyrin, Pyr for pyridine, see Fig. 5.1a for the structural formula, abbreviated as ZnTPPdT-Pyr in the following) is dissolved in dichloromethane (DCM) and deposited on the unbroken electrodes using self-assembly from solution. Two thiol groups on opposite sides of the molecule are used as anchoring groups. After deposition, the junctions are broken in vacuum at room temperature. The aforementioned stability of the electrodes allows us to characterize charge transport through ZnTPPdT-Pyr by performing two types of experiments. First, we measure at room temperature the low-bias conductance of the molecule as a function of electrodes stretching. Second, we perform spectroscopy of the molecular levels by measuring current-voltage characteristics, I(V)s, at fixed electrode spacings; This has been done both at room temperature and cryogenic temperature (6K). For more details concerning the experiments, sample fabrication, etc., see Chapter 3.

5.2. RESULTS

5.2.1. CONDUCTANCE HISTOGRAMS

To obtain the conductance value of the most probable contact geometry we repeatedly break and fuse the electrodes[52, 165, 172]) between conductances of $1{\cdot}10^{-5}$ G_0 and 10 G_0, while measuring the current at a fixed bias voltage (100 mV). Each breaking event produces a 'breaking trace' of the conductance (plotted as $\log_{10}(G)$) versus the electrode displacement (d). Sets of 500 consecutive breaking traces from individual junctions are then binned in time and in electrode displacement. As we are interested in the breaking dynamics of the junctions beyond the point of rupture of the last monatomic gold contact (defined as d=0), only conductance values below one quantum unit $G_0 = 2e^2/h$ (the resistance of a single gold atom) are considered. The results are plotted as two-dimensional 'trace histograms', in which areas of high counts represent the most typical breaking behavior of the molecular junction[53, 158].

In Fig. 5.2 we show trace histograms as well as examples of individual breaking traces for a junction exposed to (a) the solvent DCM and (b) ZnTPPdT-Pyr. All measured curves are included, i.e., no data selection has been employed. We measured several samples with ZnTPPdT-Pyr molecules as well as DCM references. The features shown in Fig. 5.2a and Fig. 5.2b. are representative for all these measurements. In the junction that was exposed to the pure solvent without porphyrin molecules (Fig. 5.2a), the Au-bridge is stretched until a single-atom contact is formed, visible (only in the individual traces in the inset) as a plateau around the conductance quantum ($G{\sim}G_0$). Upon further stretching, the monatomic contact is broken and the conductance decreases sharply and abruptly to $\sim 10^{-3}$ G_0 due to relaxation of the electrode tips. Beyond this point, electron tunneling between the electrodes leads to a fast conductance decay with stretching (visible as the orange tail), as expected for tunneling through a single barrier.

In contrast to this fast tunneling decay, introducing the porphyrin molecules by self-assembly on the junction leads to pronounced plateaus at different conductance values in the sub-G_0 regime. The observation of such plateaus in the

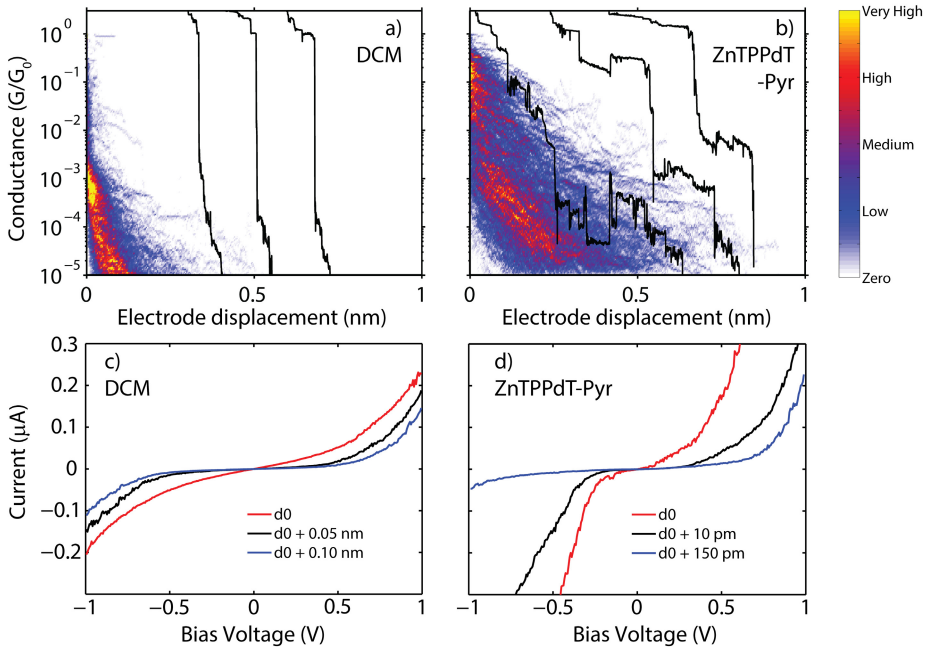

Figure 5.2: **Room temperature characterisation.** Trace histograms constructed from 500 consecutive breaking traces taken at room temperature and 100mV bias for junctions exposed to (**a**) the solvent DCM only and (**b**) ZnTPPdT-Pyr. Regions of high counts represent the most probable breaking behavior of the contact. The black curves are examples of individual breaking traces (offset along the horizontal axis, d, for clarity). For the construction of the trace histograms the zero of the relative electrode displacement for each curve was set to the point where the conductance drops sharply below 1 G_0. (**c**,**d**) Current-voltage characteristics taken at various electrode spacings starting from the initial value d_0 of junctions exposed to (**c**) the solvent DCM, and (**d**) ZnTPPdT-Pyr.

breaking traces is commonly taken as a signature of the formation of a molecular junction[52, 165, 172]. Figure 5.1b shows that the plateaus can be horizontal or sloped. Some traces consist of a few plateaus at different conductance values. The representative breaking traces that are included in Fig. 5.2b display a set of such plateaus. In strong contrast to measurements on rod-like molecules, averaging over 500 traces does not lead to a narrow region of high counts in the trace histograms. Instead, two distinct regions with high counts are visible; a high-conductance region around 10^{-1} G_0, and a sloped low-conductance region ranging from 10^{-5} G_0 to 10^{-5} G_0. Although clear plateaus are observed in the single breaking traces, averaging over hundreds of traces washes out the molecular signature. Hence, a complementary method is required to study charge transport in more detail.

5.2.2. CURRENT-VOLTAGE CHARACTERISTICS AT 300K

We have therefore measured current-voltage (I(V)) characteristics at fixed electrode spacing, in the 10^{-2}- 10^{-5} G_0 conductance region. In between the I(V)'s, the inter-electrode distance was gradually increased or decreased in steps of about 10 pm, without fusing the electrodes to form a metallic contact. In this way, changes in

molecular junction configurations occurring as a function of electrode spacing can be accurately probed. I(V)'s recorded at room temperature for a few settings of the electrodes spacing of junctions exposed to DCM and ZnTPPdT-Pyr are presented in Fig. 5.2c and Fig. 5.2d, respectively. All presented I(V)'s originate from the same breaking sequence.

I(V)'s of a junction exposed to DCM (Fig. 5.2c) exhibit the characteristic single-barrier tunneling shape and show the expected current decrease upon increasing the electrode spacing. In contrast, I(V) characteristics on the ZnTPPdT-Pyr junction show a sharper current onset, marked by arrows in Fig. 5.2d. This observation may be viewed as a molecular fingerprint as they correspond to the onset of resonant transport through an energy level of the molecule (either vibrational or electronic). Interestingly, the current onset strongly depends on the inter-electrode distance. At d_0 it is located around -250 mV. After a step of about 10 pm in the electrode distance, the onset shifted to around -350 mV. Increasing the inter-electrode distance with an additional 140 pm, shifts the onset at negative bias to a location outside the bias window. Note furthermore the asymmetry in the curves in Fig. 5.2d, which increases as they electrode moves further apart (e.g. the blue curve in this figure). For the three I(V)'s we have also determined the conductance at the same bias voltage as used to construct the trace histograms, i.e., at 100 mV. For the red, black and blue I(V) curve we obtain conductance values of $2.0{\cdot}10^{-3}$ G_0, $1.6{\cdot}10^{-4}$ G_0 and $1.6{\cdot}10^{-4}$ G_0 respectively. Interestingly, small changes in electrode distance (~10 pm) can induce big changes in the shape of the I(V) characteristics and the low-bias conductance (compare e.g. the red and black curves). Opening the junction further (black and blue curves) results in an equal conductance value at 100 mV, but different I(V) shapes.

5.2.3. CURRENT-VOLTAGE CHARACTERISTICS AT 4K

Spectroscopic features become more pronounced at low temperature as the junction stability increases and thermal broadening decrease. We therefore cooled down the junctions to cryogenic temperature (6 K) while keeping the zero-bias conductance at a fixed value (around $1{\cdot}10^{-4}$ G_0) with a feedback loop. Fig. 5.3 we present low temperature I(V) characteristics of junctions exposed to (a) DCM and (b) ZnTPPdT-Pyr solution, for different electrode spacings. IV's of the junction exposed to DCM show the characteristic tunneling shape, without any molecular signature, as was also found at room temperature. A notable difference, however, is the significant reduction of the noise.

The IV's of the ZnTPPdT-Pyr containing junction now show sharp step-like features, which are more pronounced than that in Fig. 5.2d. We numerically determined the differential conductance (dI/dV) as displayed in Fig. 5.3c. In the dI/dV's, the step-like features are visible as resonances, which have been marked in the figure with arrows of the corresponding color. For clarity, the dI/dV's have been offset vertically, and the dI/dV representated by the black curve magnified 100 times. The origin of those resonances can be electronic or vibrational[43, 131, 173]. Independently on their origin, their position reveals the alignment of the corresponding energy level with respect to the Fermi Energy of the electrodes[43]. For a distance of

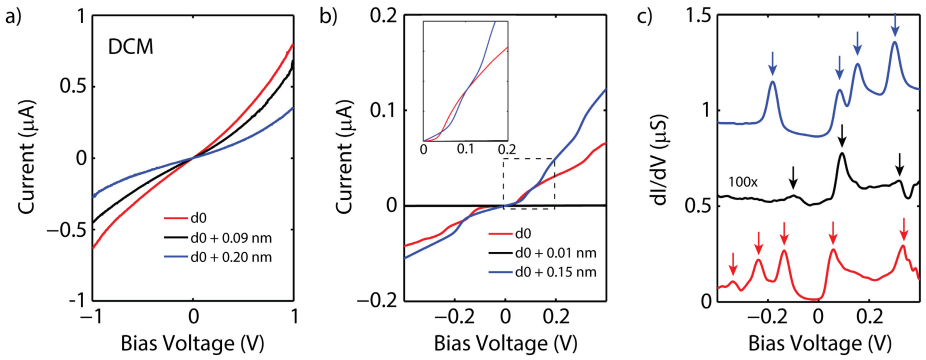

Figure 5.3: **Cryogenic (4 K) temperature characterisation.** (**a**,**b**) I(V) characteristics of junctions exposed to (**a**) DCM and (**b**) ZnTPPdT-Pyr. The DCM sample clearly shows vacuum tunneling behavior. The molecular sample exhibits Coulomb blockade and steps. (**c**) dI/dV of a junction exposed to a ZnTPPdT-Pyr solution, offset vertically for clarity. Resonances correspond to electronic or vibrational energy levels of the molecular junction. Note, for the black line the dI/dV has been multiplied by 100.

d_0 (red curve), five pronounced resonances are present, located at -339 mV, -283 mV, -153 mV, 58 mV and 334 mV. For the conductance at 100 mV we obtain a value of $2.1{\cdot}10^{-3}$ G_0. Increasing the distance by 10 pm (black curve) drastically changes the molecular energy spectrum, with one distinct resonance at 94 mV, and two fainter peaks around -99 mV and 319 mV. Here, the conductance at 100 mV is $1.2{\cdot}10^{-5}$ G_0. Increasing the distance with an additional 500 pm (blue curve) again leads to changes in the molecular energy spectrum; four pronounced resonances are now located at -238 mV, -136 mV, 58 mV and 334 mV. For the conductance we again obtain a value of $2.1{\cdot}10^{-3}$ G_0.

5.3. DISCUSSION

Comparing first the red and black curve in Fig. 5.3c, we see that within an electrode displacement of 10 pm, the number of energy levels involved in the electronic transport as well as their energy has drastically changed. A major jump of two orders of magnitude in the low-bias conductance is observed as well. This suggests an abrupt change in the molecule-electrode interaction, presumably caused by a change in molecular configuration. A similar change in molecular configuration was also observed in the room temperature IV's for the red and black curve; the onset for current shifted by -100 mV and the conductance dropped one order of magnitude within 10 pm. These observations support the conclusion drawn from the trace histogram measurements: The molecule can adopt different stable configurations, leading to plateaus at different conductance values in the breaking traces. Comparing the red and blue curve in Fig. 5.3c, which are taken are at a separation of 510 pm, we see that their molecular energy spectrum strongly differ, but that their low-bias conductance is similar (Fig. 5.3b, inset). Similar behavior is also observed at room temperature (Fig. 5.2d). This suggests that different stable junction configurations with very different spectroscopic signatures can exhibit the same low-bias conductance.

For most of the low-bias break junction measurements on rod-like molecules it is assumed that repetitive fusing and breaking of the molecular junction provides the most probable conductance value[52, 165, 172]. Multiple conductance peaks are often attributed to the formation of multiple molecular bridges connected in parallel[165, 174]. The strength of the metal-molecule chemical bond is considered to play a central role in determining the single molecule conductance values. Our results on the Zn porphyrin molecule with a pyridine axial group show that different conductance values can also result from stretching or fusing a molecular junction. As considerable changes in the conductance values and spectra already occur for a displacement as small as 10 pm, we conclude that neither the chemical molecule-electrode bond nor the electrode configuration itself can be held responsible. More likely, varying the electrode distance changes the molecular configuration, which in turn leads to abrupt changes in the molecule-electrode interaction. Our findings also show that I(V) characteristics taken at different electrode spacings can exhibit very distinct spectroscopic features but a similar low bias conductance. This indicates that different junction geometries can lead to similar conductance values in the trace histograms. Therefore, as changes in the molecular junction conformation are not always reflected in the low-bias trace histograms, supporting high bias IV-characteristics are essential for the interpretation of such histograms.

5.4. CONCLUSION

In summary, we investigated charge transport in ZnTPPdT-Pyr molecular junctions using the lithographic MCBJ technique. We combined low-bias statistical measurements with spectroscopy measurements of the molecular levels using I(V) characteristics. This unique combination allows us to probe different junction configurations and monitor changes in the molecular level alignment upon fusing or breaking of a molecular junction. Both methods show that multiple stable single–molecule junction configurations can be obtained by stretching or fusing the junction. In addition we demonstrate that different ZnTPPdT-Pyr junction configurations can lead to different spectroscopic features for similar low-bias conductance values. Thus, I(V) spectroscopy measurements can provide additional information compared to statistical low-bias conductance histograms, enabling a more in-depth characterization of the charge transport through a single molecule.

6

LARGE TUNABLE IMAGE-CHARGE EFFECTS IN SINGLE-MOLECULE JUNCTIONS

The characteristics of molecular electronic devices are critically determined by metal-organic interfaces, which influence the arrangement of the orbital levels that participate in charge transport. Studies on self-assembled monolayers (SAMs) show (molecule-dependent) level shifts as well as transport-gap renormalization, suggesting that polarization effects in the metal substrate play a key role in the level alignment with respect to the metal's Fermi energy. Here, we provide direct evidence for an electrode-induced gap renormalization in single-molecule junctions. We study charge transport in single porphyrin-type molecules using electrically gateable break junctions. In this set-up, the position of the occupied and unoccupied levels can be followed in situ and with simultaneous mechanical control. When increasing the electrode separation, we observe a substantial increase in the transport gap with level shifts as high as several hundreds of meV for displacements of a few Ångstroms. Analysis of this large and tunable gap renormalization with image-charge calculations based on atomic charges obtained from density functional theory confirms and clarifies the dominant role of image-charge effects in single-molecule junctions.

Parts of this chapter have been published in Nature Nanotechnology **8**, 282-287 (2013) [56].

6.1. INTRODUCTION

In self-assembled monolayers (SAMs), the influence of the molecule-metal interface on the alignment of the molecular orbital level with respect to the Fermi energy of the substrate has been extensively studied with UV and X-ray photo-emission spectroscopy (UPS and XPS)[175–178], Kelvin probe measurements[179, 180], and scanning tunneling spectroscopy[181]. Such measurements have indicated the formation of an interfacial dipole that is associated with substantial work-function shifts[175–179, 181], which affect all molecular orbitals in a similar way. Several mechanisms causing this interfacial dipole have been identified. In physisorbed systems the compression of the tail of the electron density outside the metal ("pillow" or "push-back" effect) plays an important role, while for chemisorbed systems charge transfer causes, in addition, a surface dipole to be formed near the metal-molecule interface[175, 177, 182, 183]. Additionally, straining the molecular junction may shift the orbital levels[65]; upon stretching or compression of the molecular junction, the shifts of the occupied and unoccupied level were found to be nearly uniform for the frontier orbitals[184]. Finally, the interaction of the (almost) neutral molecule with its own image-charge distribution at zero bias may also lead to a uniform level shift. This effect is present in both physisorbed and chemisorbed systems.

In contrast to the previously mentioned effects, UPS experiments probing the ionization and electron addition energies for decreasing layer thicknesses[185] have shown that the occupied levels move up and the unoccupied ones down in energy, – this is called 'gap renormalization'. Transport gap renormalization has also been observed in single-molecule devices[43, 131] and is commonly explained by the formation of image charges in the metal upon addition or removal of electrons from the molecule[102, 105, 186]. This effect occurs repeatedly when a current is passing through it and is particularly apparent in molecules that are weakly coupled to the electrodes.

When varying the electrode separation, the molecular orbital levels are therefore subject to a uniform shift, combined with gap renormalization. Hence, distinguishing the dominant trend in single-molecule junctions requires the combination of an adjustable electrode separation with an electrostatic gate. Although mechanical control over molecular conductance has been reported in various studies[32, 65, 76, 82, 83, 129, 181, 187], in only very few reports it has been combined with an electrostatic gate[82, 129]. In particular, systematic studies based on explicit monitoring of the dependence of occupied and unoccupied orbital levels on molecule-electrode distance are lacking.

6.2. CURENT-VOLTAGE CHARACTERISTICS

We have investigated the influence of the metal electrodes on the energy levels in single-molecule junctions using two- and three-terminal mechanically controllable break junctions (MCBJs) in vacuum at 6 K. This architecture (shown in Fig. 6.1b) allows the distance between the electrodes to be tuned with picometer precision by bending the flexible substrate supporting partially suspended electrodes[20, 28, 53, 54, 164, 173, 188]. In three-terminal MCBJ devices an additional gate electrode allows electrostatic tuning of the energy levels of the molecular junction[129]. The

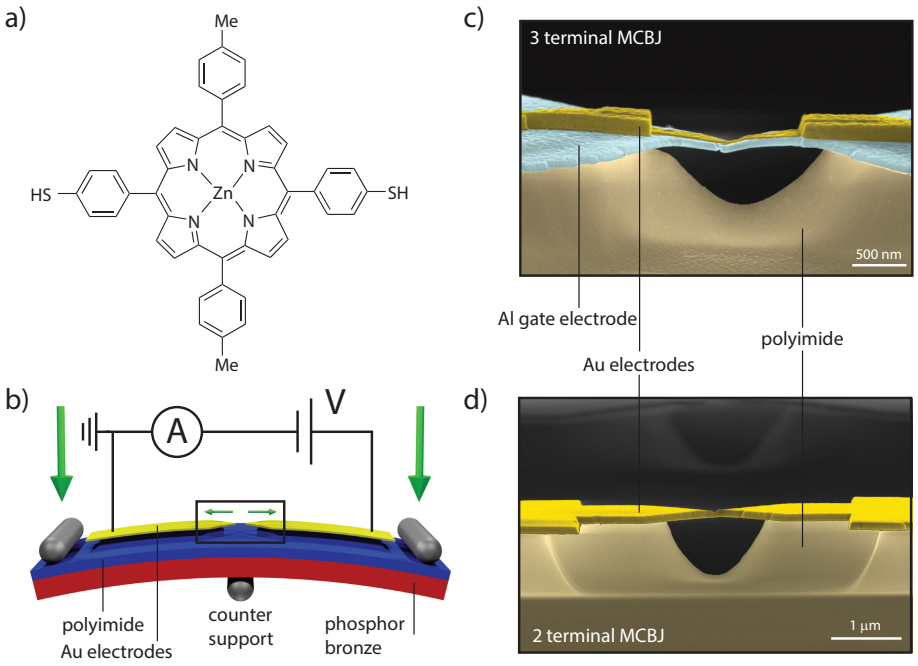

Figure 6.1: **Illustration of the experiments.** (**a**) Structural formula of ZnTPPdT. (**b**) Lay-out of the mechanically controllable break (MCBJ) junction set-up. (**c**) Colorized SEM image of a three-terminal MCBJ device. The gate is made of aluminum and covered with an plasma-enhanced native aluminum oxide layer. The gold electrodes are deposited on top of the gate dielectric. (**d**) Colorized SEM image of a two-terminal MCBJ.

molecules in this study were thiolated porphyrins, which offer great architectural flexibility and rich optical properties. The thiol-terminated Zn-porphyrin molecules [Zn(5,15-di(p-thiolphenyl)-10,20-di(p-tolyl)porphyrin)], abbreviated as ZnTPPdT and shown in Fig. 6.1a, were dissolved in dichloromethane (DCM, 0.1 mM) and deposited on the unbroken electrodes using self-assembly from solution. The electrodes were then broken in vacuum at room temperature, cooled down and current-voltage *I-V* characteristics were recorded as a function of electrode spacing. All measurements were performed at 6 K. Details concerning these "systematic I-V series" and other experimental procedures (synthesis of the molecules, measurement setup, calibration of the attenation factor, etc.) are provided in Chapter 3. Scanning electron micrograph of the MCBJ devices are presented in Fig. 6.1c and d.

In Fig. 6.2a we present typical *I-V* characteristics of a two-terminal MCBJ (sample A) that has been exposed to a solution of ZnTPPdT. We start monitoring the junction-breaking or fusing process at some electrode separation which we call d_0. All characteristics show very low current around zero bias, indicating that transport occurs in the weak-coupling (Coulomb-blockade) regime. Steps at higher bias mark the transition to sequential tunneling transport[117]. In the differential conductance, dI/dV, these steps are visible as peaks (see Fig. 6.2b). The peak location identifies the position of the molecular orbital level with respect to the Fermi energy of the electrodes.

We will refer to these peaks as resonances from now on. Figure 6.2a and b show that with decreasing inter-electrode distance, the spacing between the resonances is strongly reduced.

We have studied eight different junctions, which all displayed similar mechanically tunable resonances in *dI/dV*. The same trends are also present in asymmetric junctions, as shown in section A.2 of the appendix. Devices exposed to pure solvent,

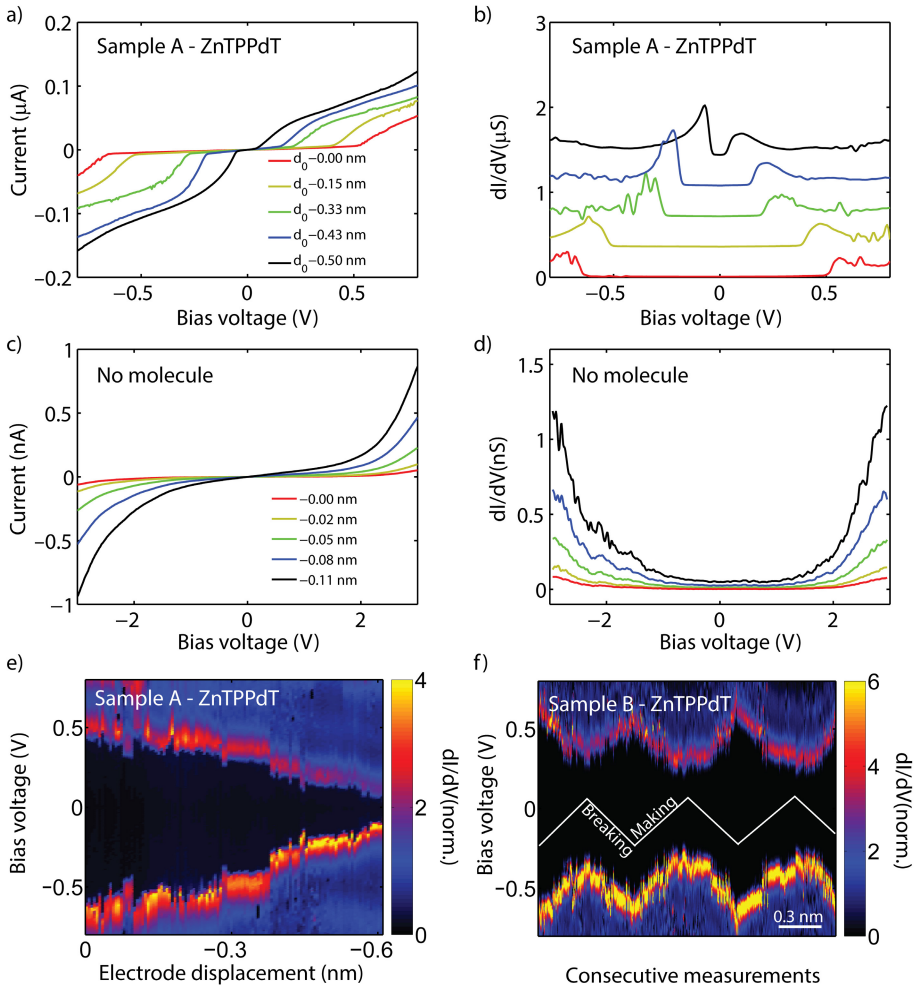

Figure 6.2: **Mechanical gating of charge transport in ZnTPPdT junctions.** (**a**) Current-voltage characteristics and (**b**) differential conductance for MCBJ devices which have been exposed to a solution of ZnTPPdT. In (**c**) and (**d**) the same quantities are plotted for junctions exposed to the pure solvent (DCM). (**e,f**) Two-dimensional visualization of *dI/dV* for ZnTPPdT as a function of bias voltage and electrode displacement (**e**) while fusing sample A and (**f**) for three making/breaking cycles of a different device (sample B). A clear dependence of the Coulomb gap on the electrode spacing is visible. The differential conductance has been normalized and the estimated electrode displacement is relative to d_0, the initial electrode separation.

in contrast, showed featureless characteristics, typical of vacuum tunneling through a single barrier (see Fig. 6.2c and Fig. 6.2d). As the inter-electrode distance is reduced, the maximum current in these clean junctions increases smoothly, as a result of the decreasing tunneling barrier width.

To visualize the systematic evolution of the resonance position for hundreds of *dI/dV* curves, we have plotted a two-dimensional map of consecutive I-V measurements in Fig. 6.2e, where the gradual shift of the resonances becomes even more apparent. Due to the stability of the electrodes and the fine control over their spacing[73, 159], the energy levels can be shifted over several hundreds of meV by purely mechanical means.

In the following, we will refer to these shifts as *mechanical gating* and quantify them in terms of an efficiency factor, the *mechanical gate coupling* (MGC). The MGC is expressed in V/nm and defined as the ratio between the shift of each resonance and the electrode displacement required to achieve this shift. From Fig. 6.2e, for example, we find a MGC of about 1 V/nm, with a slight asymmetry for positive and negative bias which may be caused by differences in capacitive coupling to the two electrodes. The reverse process (opening the junction) leads to a widening of the Coulomb gap, as illustrated in Fig. 6.2f, where several consecutive opening and closing cycles are shown for a different sample. The figure clearly shows that the resonances shift consistently and with similar magnitudes, demonstrating the robustness of the effect and the stability of the setup.

While recording systematic I-V series, we occasionally observe a very weak dependence of the resonance positions on the electrode separation, and conversely, occasionally observe MGC's as large as 1.5 V/nm (see section A.1 of the appendix for the statistics of the MGC's). This is probably due to a rearrangement of the molecule inside the junction[73, 74]. Alongside gradual changes in the position of the resonances, the plots in Fig. 6.2e and Fig. 6.2f display sudden irreversible jumps in the *dI/dV*'s. These differences and variations could be caused by atomic-scale changes in the geometry of the molecular junction. Evidence of similar rearrangements has also been obtained during room-temperature conductance measurements on porphyrin molecules[73]. Throughout all the samples, however, the trends remain the same; reducing the electrode distance brings the resonances closer together, whereas increasing the distance moves them further apart.

6.3. GATE DIAGRAMS

To obtain additional information about the origin of the shifts of the molecular orbital levels involved in charge transport, we employed electrically gated mechanical break junctions[129]. The electrostatic gate in these devices controls the potential on the molecule and lowers/raises all molecular orbital levels for positive/negative gate voltage[117], as shown in Fig. 6.3c. Keeping the electrode spacing fixed, we measure the current as a function of both the bias- and gate voltage and plot *dI/dV* as a two-dimensional map; in this paper we will refer to such a plot as a gate diagram.

In such a gate diagram the resonances associated with an occupied level move away from the Fermi level with increasing gate voltage. An unoccupied level, on the other hand, moves closer to the Fermi level and thus displays the opposite trend. This

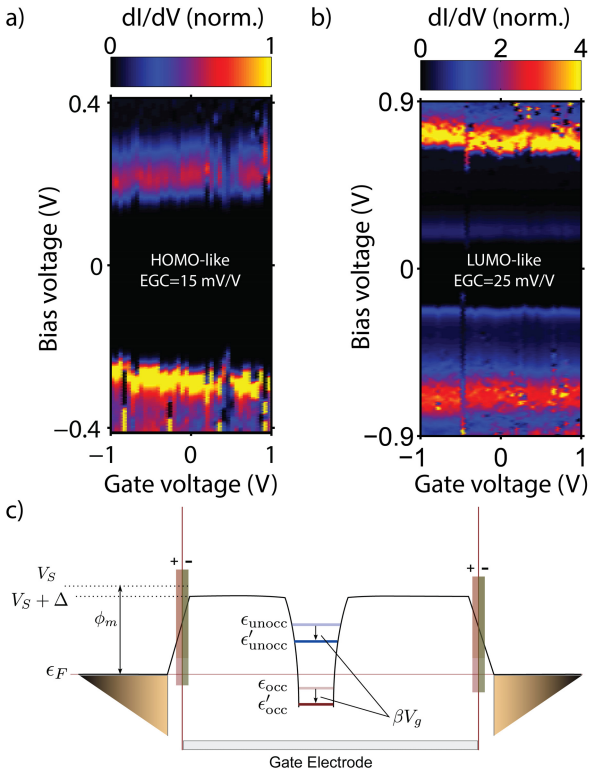

Figure 6.3: **Level shifts by electrostatic gating.** (**a,b**) Gate diagrams recorded on sample C for different junction configurations and during different breaking events. Color-coded dI/dV plotted versus gate- and bias voltage. The slope of the lines allows us to attribute resonances in (**a**) to an occupied level (HOMO-like, located approx at 0.3eV for zero gate voltage) and those in (**b**) to an unoccupied level (LUMO-like, located approx at 0.75eV for zero gate voltage). (**c**) The effect of a rigid shift of the levels under electrostatic gating by a potential V_g applied to a gate electrode below the junction for an occupied and unoccupied level. Here, β is the electrostatic gate coupling, ϕ_m the metal work function, Δ the shift of the potential V_S outside the surface due to the presence of the molecule, and ϵ_F the Fermi energy of the metal. ϵ_{occ}, ϵ_{unocc} and ϵ'_{occ}, ϵ'_{unocc} are the occupied and unoccupied levels for $V_g = 0$ and $V_g \neq 0$, respectively.

allows us to identify the resonance in Fig. 6.3a as the HOMO, whereas Fig. 6.3b shows an unoccupied level (this is not the LUMO of the gas phase molecule, see below). The HOMO level position depends on the gate voltage with an *electrostatic gate coupling* (EGC) of about 15 mV V^{-1}; for the unoccupied level, we find an EGC of about 25 mVV^{-1}. Figure 6.4a and Fig. 6.4b show the mechanical gate plots recorded immediately after the measurements shown in Fig. 6.3a and Fig. 6.3b, respectively. Both the occupied and unoccupied levels move away from the Fermi level while we increase the distance between the electrodes (MGC = 0.40 V/nm for the occupied and 0.18 V/nm for the unoccupied level). This implies a widening of the gap and means that the mechanism behind the shifts cannot be a rigid change in the work function only, but must also include a transport-gap renormalization. It is the combination of electrostatic and mechanical gating which leads us to this conclusion, and in the following we will demonstrate using density functional theory (DFT) based calcula-

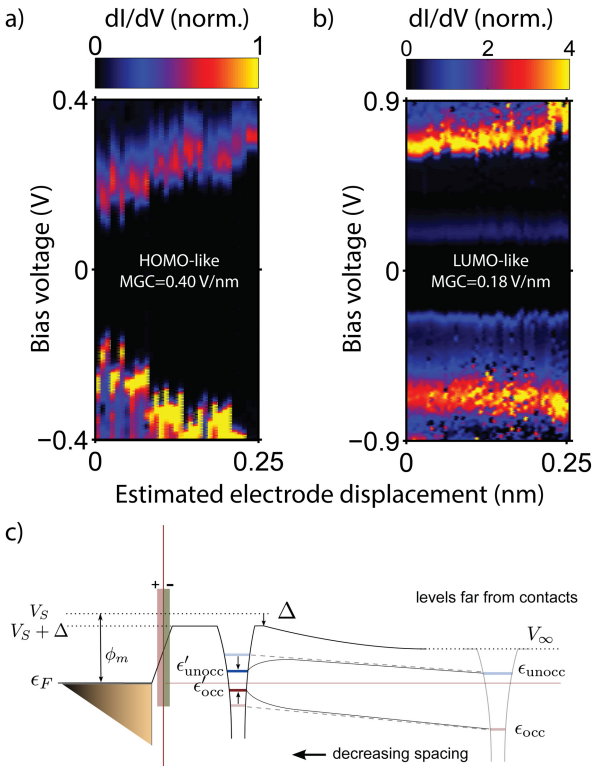

Figure 6.4: **Level shifts by mechanical gating.** (**a,b**) Systematic I-V series of sample C, recorded right after Fig. 6.3 a and b, respectively. (**a**) HOMO-like (located approx at 0.3eV for zero displacement) and (**b**) LUMO-like level (located approx at 0.75eV for zero displacement) both move away from the Fermi energy for increasing electrode spacing. (**c**) The shift of the occupied and unoccupied molecular orbital levels with the distance to the metal. The effects contained in Δ shift all levels in the same direction, while image-charge effects are responsible for occupied and unoccupied levels moving closer to the Fermi energy of the metal (gap renormalization). Again, ϕ_m represents the metal work function, Δ the interfacial dipole, V_∞ the potential at infinity, V_S the potential at the surface and ϵ_F the Fermi energy. ϵ_{occ}, ϵ_{unocc} and ϵ'_{occ}, ϵ'_{unocc} are now the occupied and unoccupied levels of the molecule in gas phase and at the interface, respectively.

tions that this gap renormalization is caused by the formation of image charges upon charge addition to/removal from the molecule.

6.4. DFT CALCULATIONS

We now turn to the theoretical analysis of the experimentally observed phenomena. Using a quantum chemistry approach[189] we study the electronic structure of the molecules in gas phase and sandwiched between gold atoms in the junctions, as well as their transport properties (see section A.3 of the appendix for more details). In agreement with the literature, our calculations predict a chemisorbed system[190–192] with ZnTPPdT acting as acceptor, and the hollow site as the most stable configuration. Figure 6.5 shows the computed zero-bias transmission of the single-molecule junction. We find that the low-bias transport is dominated by the HOMO

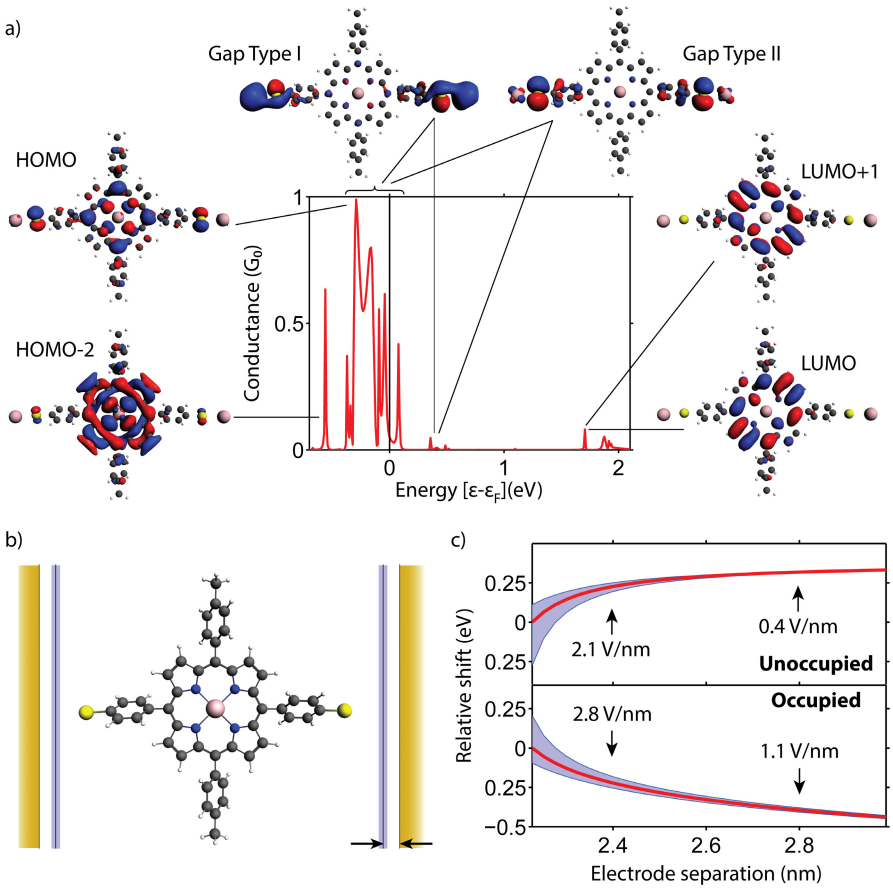

Figure 6.5: **Transport calculation and image-charge model.** (**a**) Zero-bias transmission and molecular orbital levels of ZnTPPdT coupled to Au, from DFT and DFT+NEGF calculations, respectively. The Fermi energies are with respect to the Fermi energy of the metal electrodes, marked by the vertical black line. ZnTPPdT is located at 2.59 Å from each lead, with hollow-site binding. (**b**) Image-charge model geometry, with the image plane located 1 Å outside the first atomic layer (uncertainty bands derived from a 0.25 Å deviation). (**c**) Shifts predicted by the image-charge model (with uncertainties) showing the occupied- and unoccupied-levels both shifting towards ϵ_f for decreasing electrode separation with MGC's in the range of 0.4–2.8 V/nm, assuming a symmetrically applied bias. These values may be significantly reduced for realistic electrode geometries.

and HOMO-2 states of the molecule coupled to gold atoms (illustrated in Fig. 6.5a), visible as peaks in the transmission near the Fermi level.

We also observe that the resonances which correspond to the gas-phase LUMO and LUMO+1 levels are located far above the Fermi level of the leads (although the precise location of these resonances cannot accurately be predicted within DFT). Being more strongly localized at the center of the molecule than the better-hybridizing HOMO-like orbitals, they are expected to have poor conductance properties, and as a consequence are characterized by very narrow peaks in the calculations. A few additional peaks occur slightly above the Fermi energy, and inspection of these states

reveals that they have no direct gas-phase counterpart. They are new states, which essentially consist of those parts of the gas-phase HOMO and LUMO that are located on the arms of the molecule and stabilized by the presence of the interface. Forcing an extra electron onto the molecule by applying a positive gate voltage indeed shows that charge is added to these levels, rather than to a LUMO state.

As discussed above, there is a correction Δ to the background potential which represents a work function shift, as illustrated in Fig. 6.4c. This shift is usually treated empirically, and is typically negative on Au surfaces. Experiments have reported shifts in the range -0.5 to -1 eV for H_2TPP and ZnTPP films[175, 182], without the presence of the thiols in ZnTPPdT. This corrections is, in principle, distance dependent, and leads to a uniform shift of the occupied and unoccupied levels. This is in contrast with the experimentally observed gap renormalization, indicating that, although this effect may, to some extent, be present, it is not the dominant mechanism responsible for the large level shifts.

Image-charge effects, including their contribution to gap renormalization, can, in principle, be assessed by performing GW calculations[102, 193, 194], which allow for the determination of the ionization potentials and electron addition energies. However, such calculations are infeasible for the large molecules of this study. Instead, we calculate image-charge effects using classical electrostatics based on the atomic charges on the molecule obtained from DFT. In the region where the transport is blocked (corresponding to zero bias and gate) the molecule is approximately, but not exactly, neutral. We call this the 'reference state'. The combination of the negatively charged thiols with the positive core of the molecule in the reference state can lead to a contribution of the image charges effect to the uniform shift. This contribution either moves the levels up or down, depending on the exact charge distribution in the junction. To include gap renormalization, one also has to consider the different charged states of the molecule. To access the different charge states in the junction, we added or removed one electron from the molecule by applying a local gate field, in the spirit of a $\Delta-$ SCF method (see section A.4 of the appendix for more details). The image-charge effect corrections are calculated for the different charge states by summing the electrostatic interactions of the atomic charges between two parallel plates with all image charges. The position of the image plane is taken to be 1.0 ± 0.25 Å outside the metal surface, as is usually done in the literature[106, 195, 196]. For comparison with experiment, the distance between the electrodes has been varied.

The calculated shifts, illustrated in Fig. 6.4c, predict an image-charge contribution to the MGC's in the range of 1.1–2.8 V/nm for an occupied level, and 0.4–2.1 V/nm for an unoccupied level depending on electrode separation. The different molecular orbital levels (shown in Fig. 6.5a) thus experience different image charge effects, as observed in the experiments, although the calculated MGC's are larger than the experimental ones. This can be due to the sharp contacts in the MCBJ experiment, which imply a smaller image-charge effect than the large parallel-plate contacts used in the calculation. We modeled the reduction of the image-charge effect with finite contacts, finding it to be roughly a factor of $1.5-2$ (see section A.6 of the appendix for more details), bringing the calculations into better agreement with the experimental shifts. To investigate the sensitivity to the orientation of ZnTPPdT in the junction, we have also rotated the molecule in the calculations and found that the shifts remain essentially the same for angles within 45°, see section A.5. In the

same section, we also show that similar trends are found when the molecule is connected to top and/or bridge sites.

To assess the contribution to the molecular orbital level shifts originating from structural deformation of the molecule, we performed DFT calculations for increasing gold-gold distance while letting the molecule relax between the contacts. We found that the energy shifts of the occupied and unoccupied level are at most of the order of 50-60 meV, and more importantly, do not lead to transport-gap renormalization, but rather cause an uniform, upward shift (see section A.7 of the appendix for more details). In addition, the HOMO is predicted to move up for increasing electrode-spacing, while the experiments show the opposite trend.

We conclude that image-charge effects can largely explain the experimentally observed distance dependence of the position of the molecular orbital levels with respect to the Fermi level of the contacts. Our calculations further reveal that the contributions to the image charge effect of the charge distribution in the reference state contributes substantially (roughly half as much as the gap renormalization) to the MGC of the molecular orbital levels.

The time needed for forming image charges is associated with the plasma frequency of the metallic contacts, corresponding to an energy of a few *e*V. This is short enough to be relevant even in co-tunneling processes. In recent years, several attempts have been made to capture the image charge-induced gap renormalization using either single point charges[106, 197] or atomic charge distributions[105, 196, 198], based on DFT results for gas-phase molecules. In the present system, however, it seems that the states used for electron transport are defined by the presence of the contacts. Therefore, taking the atomic charge distributions for the different charge states inside the junctions is the appropriate starting point for calculating image-charge effects.

6.5. CONCLUSION

In summary, we have studied the influence of the electrode separation on the molecular orbital levels in porphyrin single-molecule junctions using electrostatically-gated MCBJ devices. Using this method we demonstrate experimentally a combined effect of mechanical and electrostatic gating of the molecular levels. We find that both occupied and unoccupied levels move significantly towards the Fermi level upon reduction of the electrode spacing. We attribute this dominantly to gap renormalization as a result of electron interaction with image charges in the metal leads. Our findings are corroborated by DFT-based calculations. The experiments show surprisingly large level shifts, suggesting that image-charge effects may be responsible for the large spread in conductance values that is often observed in single-molecule junctions. These effects should therefore be considered in quantitative comparisons between computations and experiment. At present, calculations for molecular devices result at best in the prediction of trends, or they shed light on the possible transport mechanisms. Improvements in geometric and electrostatic control may bring quantitative agreement between the two closer. We have demonstrated that capturing the image-charge effects is a crucial step in this development. From a different perspective, the observed effects may be exploited to mechanically

gate single molecules and thereby tune the alignment of the orbital levels.

A. APPENDIX

A.1. MGC ANALYSIS

Using the data of sample A and B of the Fig. 6.6, we studied the MGC in more detail. Additional data for samples A and B are shown in Fig. 6.6a and Fig. 6.6c. Of both samples, we first extracted the resonance positions (see Fig. 6.6b and Fig. 6.6d). In regions where the peaks were shifting continuously (ie, not jumping), we used a linear

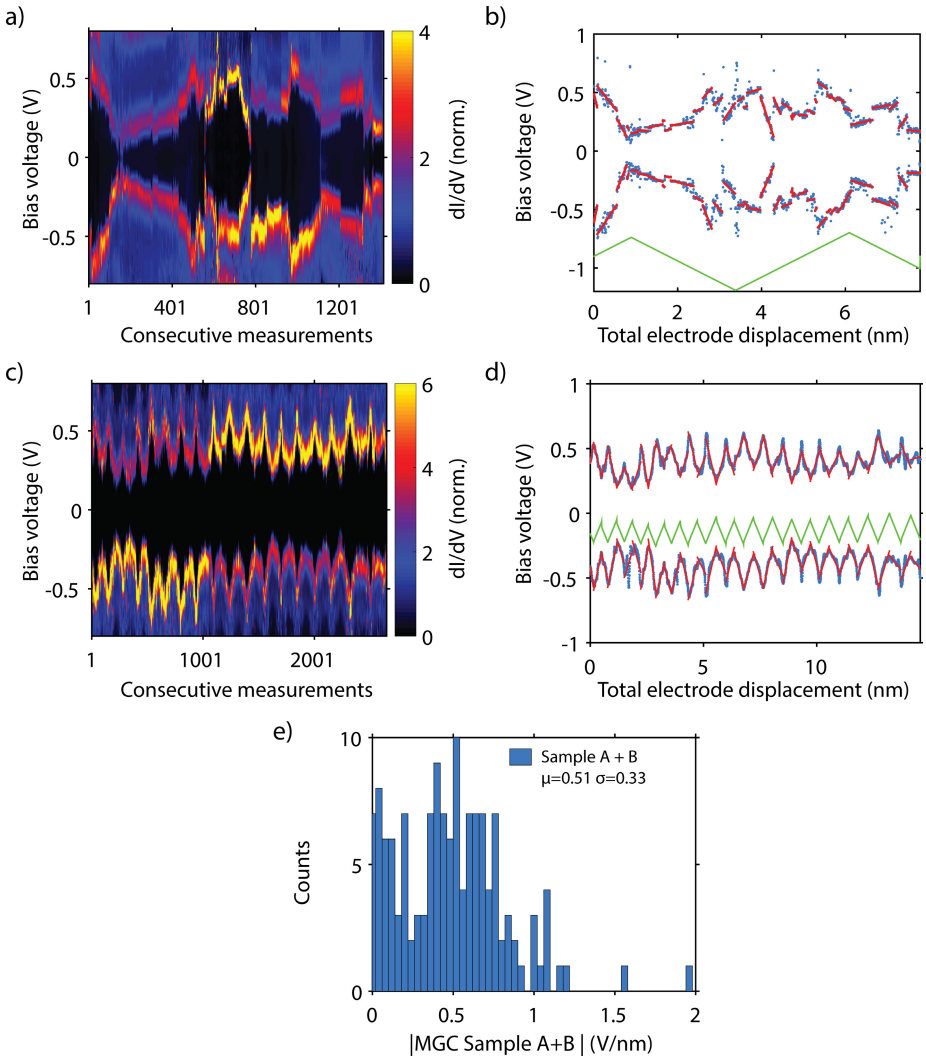

Figure 6.6: **Analysis of the MGC.** (**a,c**) Systematic IV series recorded on (**a**) sample A and (**c**) B respectively. Plotted is dI/dV as a function of IV number and bias. (**b,d**) Resonance position extracted from the data of (a,c) respectively. The red lines are linear fits of the peak shifts. The green line represents the motor displacement. A positive slope means the electrode distance is reduced, while a negative slope represents opening the contact. (**e**) Occurrence of the different MGC for sample A and B combined.

fit to approximate the MGC. A histogram of all those MGC is presented in Fig. 6.6e. Interestingly, Fig. 6.6a shows various jumps in the resonance position, which are presumably caused by changes in configurations. As ZnTPPdT is a non-rod-like molecule, it can form molecular junctions with various geometries, as has been reported previously for similar molecules[73].

A.2. MEASUREMENTS ON NON-THIOLATED ZINC PORPHYRIN

To investigate the role of the junction asymmetry, we have performed experiments on non-thiolated porphyrins (ZnTPP) and found similar level shifts as in their thiolated counterpart ZnTPPdT. In Fig. 6.7, we show dI/dV of systematic IV series on a ZnTPP molecular junction upon (a) breaking and (b) making. The plot shows resonances, which indicate a stable molecular junction can be formed, even without thiol groups. This is in agreement with previous results on such molecules[73]. (c) and (d) show an IV recorded at the position marked by the red line in (a) en (b) respectively. In contrast to the measurement on the ZnTPPdT molecules, a clear asymmetry is now observed, with resonances visible predominantly for positive bias voltages. This suggests the coupling to the electrodes is highly asymmetric. Despite the asymmetric coupling, the resonances move in a similar way as for ZnTPPdT, i.e. they move towards higher bias upon increase of the electrode separation.

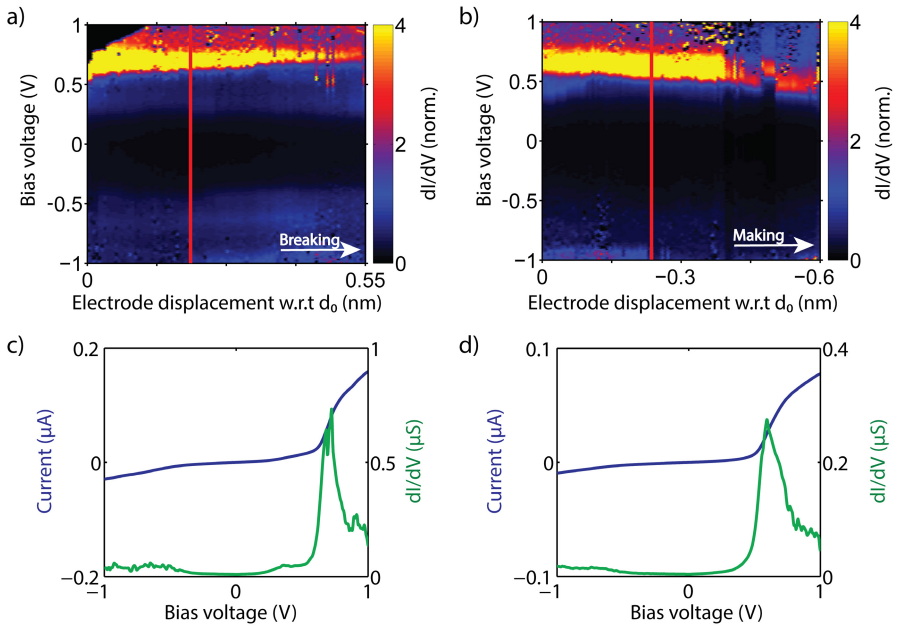

Figure 6.7: **Measurements on ZnTPP.** Systematic IV series on a ZnTPP molecular junction upon (**a**) breaking and **b**) making. (**c**) and (**d**) show an IV recorded at the position marked by the red line in (a) en (b), respectively.

A.3. ELECTRONIC STRUCTURE AND TRANSPORT METHODS

The results presented here are based on the combination of 3 principal tools: molecular Density Functional Theory (DFT) calculations, transport calculations based on the Non-Equilibrium Green's Functions formalism (NEGF) in combination with DFT[199, 200], and a 2-plane image-charge model. All DFT-based calculations were

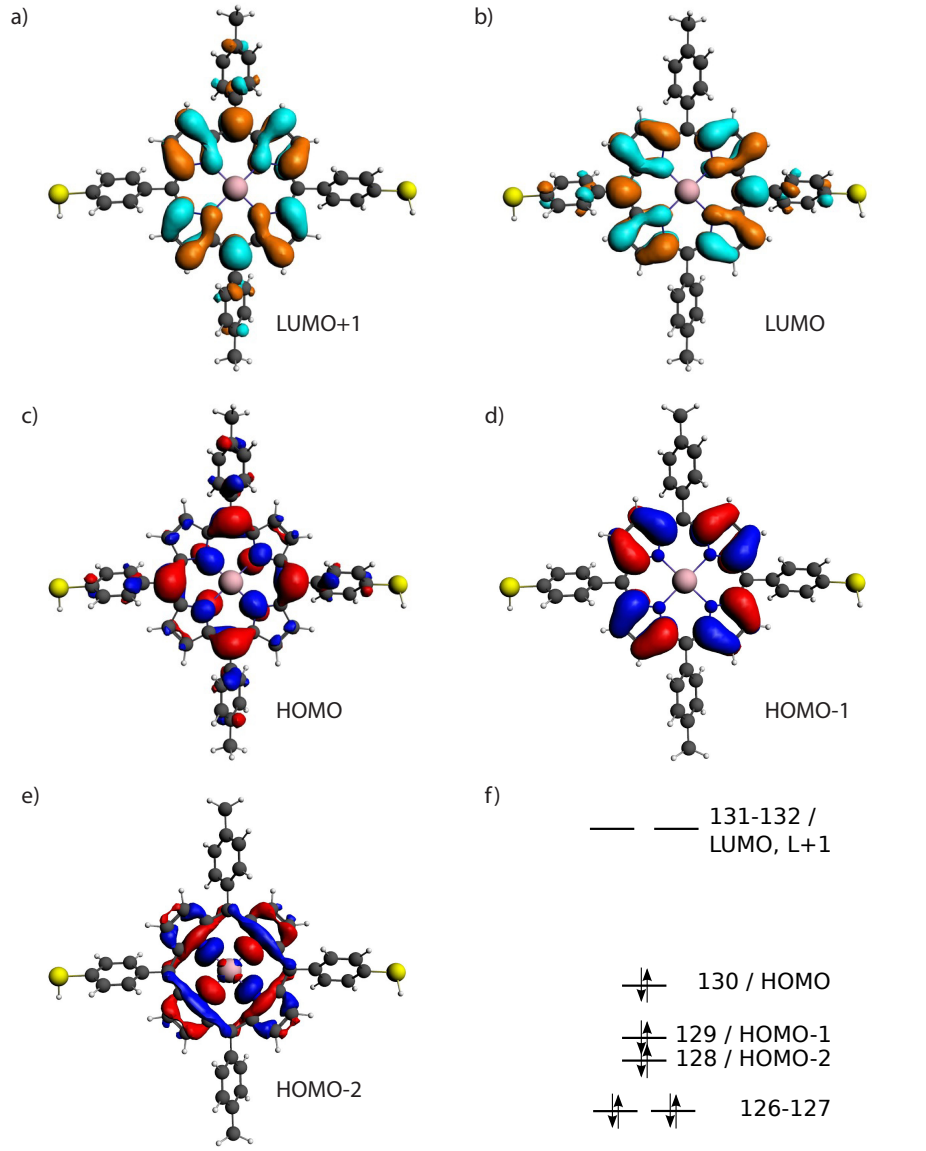

Figure 6.8: **Electronic structure and orbitals of ZnTPPdT.** (**a**–**e**) Orbitals of gas-phase ZnTPPdT, together with (**f**) the charge-neutral states energy-level diagram, corresponding to occupation up to and including the HOMO orbital. Orbitals should be compared with fragment orbitals in Fig. 6.5.

performed using the ADF/Band quantum-chemistry software package, originally developed by the Baerends group[201–203] at the Free University of Amsterdam. The NEGF formalism for modeling transport has been implemented by us as an extension to ADF/Band.

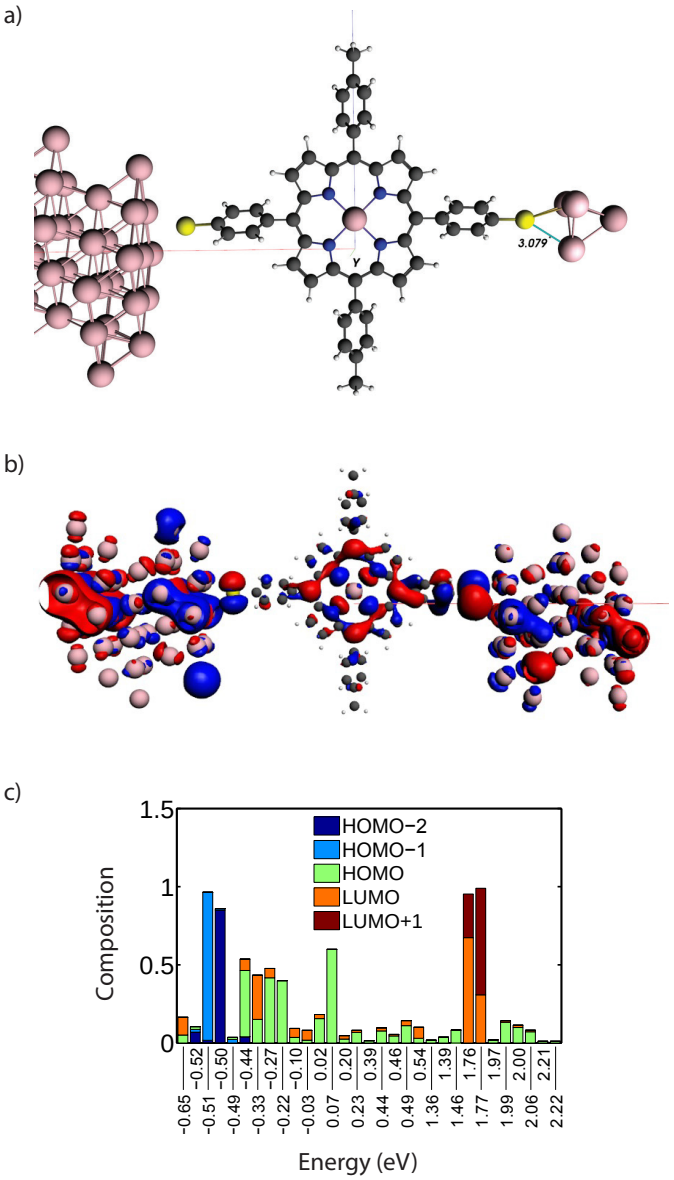

Figure 6.9: **ZnTPPdT binding and conduction.** (**a**) Left side shows orientation relative to (111) surface layer, right side shows positions of only nearest hollow-site neighbors. (**b**) Representative geometry for a 2–terminal transport calculation, with a conjugated HOMO-level wavefunction. (**c**) Decompositions of the peaks in Fig. 6.5 into symmetry classes derived from gas-phase molecular orbitals.

We first optimized the geometry for the gas-phase molecule and for a fragment where the two hydrogen atoms attached to the sulfur atoms are replaced by gold atoms. Both geometries were optimized using a DZ Slater-type orbital local basis-set using the PBE GGA functional. Results were converged to energy changes of less than 10^{-3} hartree, energy gradients of less than 10^{-3} hartree/Å maximum and $6.7 \cdot 10^{-4}$ hartree/Å RMS. The charge-state calculations were performed with this geometry using the VWN LDA functional, and to match the later DFT+NEGF calculations, with a DZ basis-set on the molecule and a SZ basis-set on the gold. The resulting orbital structure is shown in Fig. 6.8 for the neutral gas-phase molecule, together with a few frontier orbitals, which should be compared to the orbitals in Fig. 6.5, where they are shown for the fragments consisting of the molecule with the H atoms of the thiols replaced by two Au atoms.

For the transport calculations we used a binding geometry based on a phenyl ring bonded to a gold surface via a gold-thiol hollow-site binding. We have mostly used a 0° tilt angle, although we have also studied other geometries, as is shown further on. The calculations indicate a charge on the thiols of $0.1 - 0.3e$. This strongly suggests that they chemisorb to Au when relaxed, with the molecule acting as an acceptor, in agreement with previous calculations on systems with this type of bonding[190–192, 204–206]. However, the molecule excluding the thiols is slightly positively charged in the junction, and the balance between these determines the sign level shift due to the interaction of the added/removed charge with the already present molecular charge distribution, which in turn drives the slight asymmetry in shifts of the HOMO and LUMO levels.

Figure 6.5 shows the transmission of a typical transport calculation for a 2-terminal device geometry, which we modeled as illustrated in Fig. 6.9a. The corresponding peak compositions in Fig. 6.9c help us to understand the molecular origins of the transport channels. They are constructed by projecting the orbitals of the transport calculations back onto the fragment orbitals illustrated in Fig. 6.5a.

Most of the fragment orbitals can be related to gas-phase orbitals by considering their symmetry on the molecule. For a number of states, the correspondence is less

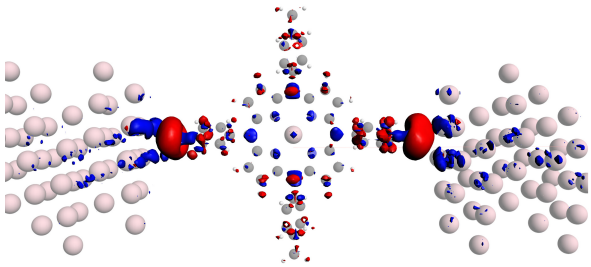

Figure 6.10: **Charging Pattern on Adding an Electron by Electrostatic Gating.**
Difference in charge density obtained by adding one electron via the gate field over the molecule in the junction. Red areas have charge added, blue is where it is removed, as the unoccupied state is filled. Orbital symmetry indicates that a HOMO-like state with most density on the arms, rather than a LUMO level, is being addressed.

trivial. These are formed in the gap between the gas-phase HOMO and LUMO (see Fig. 6.5a), due to hybridization with the gold. Their wavefunction is located mostly on the arms, and appears to be stabilized by the interface. In the following, when referring to the remaining orbitals (HOMO, LUMO, etc.) while considering fragment-orbitals, we actually intend the character of the corresponding gas-phase molecular orbitals.

Combined with the calculations of Fig. 6.9c, and the charging pattern in Fig. 6.10, we thus find transport near ϵ_f dominated by the states derived from the molecular HOMO level and hybridizations with the gold leads. The (gas-phase) HOMO-1 and HOMO-2 orbitals, by contrast, hybridize much less due to most of their wavefunction being localized on the central part of ZnTPPdT. HOMO-2 is still present in our calculations as a very narrow resonance, but we find that the gas-phase HOMO-1 becomes a deeper lying state in the fragment, which does not hybridize at all.

A.4. IMAGE-CHARGE EFFECTS

To analyze image-charge effects we use an extension of the method used by Kaasbjerg and Flensberg[105], and Neaton *et al.*[197, 198]. We first note that the experimentally relevant molecular levels (see Fig. 6.8) are those near the Fermi level of the Au nanocontacts. The LUMO and LUMO+1 in the gas phase are too far above the Fermi energy to be addressed in transport (at a calculated EA of roughly 2 eV). Instead, we expect the gap states to act as electron transport channels. We take the atomic charges for a representative molecule-plus-contacts geometry (in a NEGF+DFT calculation) at zero bias as the reference configuration. The atomic charges in that state are denoted q_j, located at $\mathbf{r}_j$. The image charges are denoted as $q_j^I = -q_j$, located at $\mathbf{r}_j^I$. Changing the *total* charge on the molecule by $\pm 1e$ induces changes in the

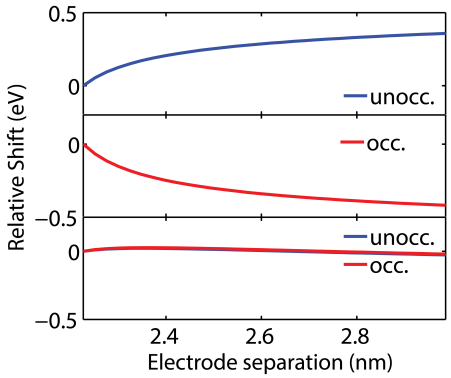

Figure 6.11: **Different contributions to the image-charge effect.**
Lower panel: image charge effect due to the reference charge term (first term) of (6.1) for both the occupied and unoccupied level. The two curves are not identical but very close. Upper and middel panel: image charge effect due to the changes in the atomic charges occurring during transport (second term of (6.1)) for the occupied and unoccupied levels (red and blue line respectively). The total image charge effect shown in Fig. 6.5c is the sum of these two contributions. The shifts in chemical potential are half the values shown on the vertical axis, which represent the bias voltage needed to access the relevant molecular orbital in the transport process.

atomic charges which we denote by δq_i. These charges add up to $\pm 1e$, depending on whether we consider ionisation or electron addition. We actually calculate these δq_i by constraining the charge on the molecule to be one unit higher or lower than that of the reference configuration. This is done by applying an extra gate potential on the molecule only, which acts as a Lagrange parameter for the charge constraint. This method is in the spirit of a Δ-SCF method[207], with the subtlety that we only change the charge on the molecule, for which we need the molecular 'gate' potential as a Lagrange parameter[208].

The molecular levels observed in transport are chemical potentials, i.e., energy differences between different charge states. The (distance dependent) electrostatic contribution to the molecular orbital level is given by:

$$\Delta_{\mathrm{ES}} = \pm \sum_i \delta q_i \left(\sum_j \frac{q_j^I}{|\boldsymbol{r}_i - \boldsymbol{r}_j^I|} + \frac{1}{2} \sum_{i,j} \frac{\delta q_j^I}{|\boldsymbol{r}_i - \boldsymbol{r}_j^I|} \right), \tag{6.1}$$

where the plus-sign is for the unoccupied, and the minus for occupied levels. The first term in this equation is the Coulomb interaction between the atomic charge differences δq_i and the images q_j^I of the atomic charges q_j of the charge distribution in the reference state. The second term contains the interaction between the atomic charge differences δq_i and their own images. Its dominant contribution is negative for unoccupied levels and it becomes more negative with decreasing electrode separation, with a reverse trend for occupied levels. In the case where there would be only a single point where the charge is added, the second term in Eq. (6.1) reduces to the familiar form $1/|4z|$, where z is the distance to the image plane[197, 198]. This second term does not depend on the reference configuration – it only depends on the changes in the molecular charge that occur during to transport. We show the contribution of the two individual terms in Eq. 6.1 in Fig. 6.11. The role of the gap states as transport channels, together with the rather inhomogeneous charge distribution in the reference state necessitates the use of the reference and oxidized/reduced states *in the junction*, in contrast to gas-phase charge distributions[198]. We iterate the

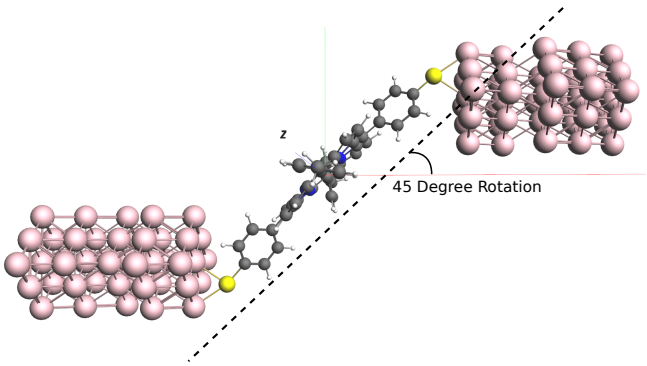

Figure 6.12: **Image effects under rotation of ZnTPPdT.**
Example of a (transport) geometry with ZnTPPdT at 45°. Calculations of the shifts of the effective EA (unoccupied) and IP (occupied) levels for angles between 0° and 45° show that the MGC derived from the derivatives of the curves is robust with respect to the 0° case.

sum over the image charges until convergence (typically 100 reflections with respect to the two image planes).

A.5. INFLUENCE OF JUNCTION GEOMETRIES

We have also addressed the reliability of the predicted MGC by considering the case where ZnTPPdT is *not* perpendicular to the electrodes. We do not expect that the molecule lies flat (angle ~ 90°) on one surface, as no highly asymmetric bias-coupling was observed. For rotations up to 45°, as illustrated in Fig. 6.10, the effect appears to weaken slightly with angle, but the MGC predicted by the derivatives with gap size vary by < 10% for these rotations. This is consistent with the image-charge effects being dominated by the charging of the S atoms near the interface. At higher angles there may be different charging patterns due to different charge-injection pathways and an increase of the effect of image charges generated by atoms near the center of the molecule.

In addition to rotations of the molecule in the junction, we have also considered the effects of different binding geometries on the calculated MGC. Specifically, we have considered top-site and bridge-site bindings on both sides, as well as an asym-

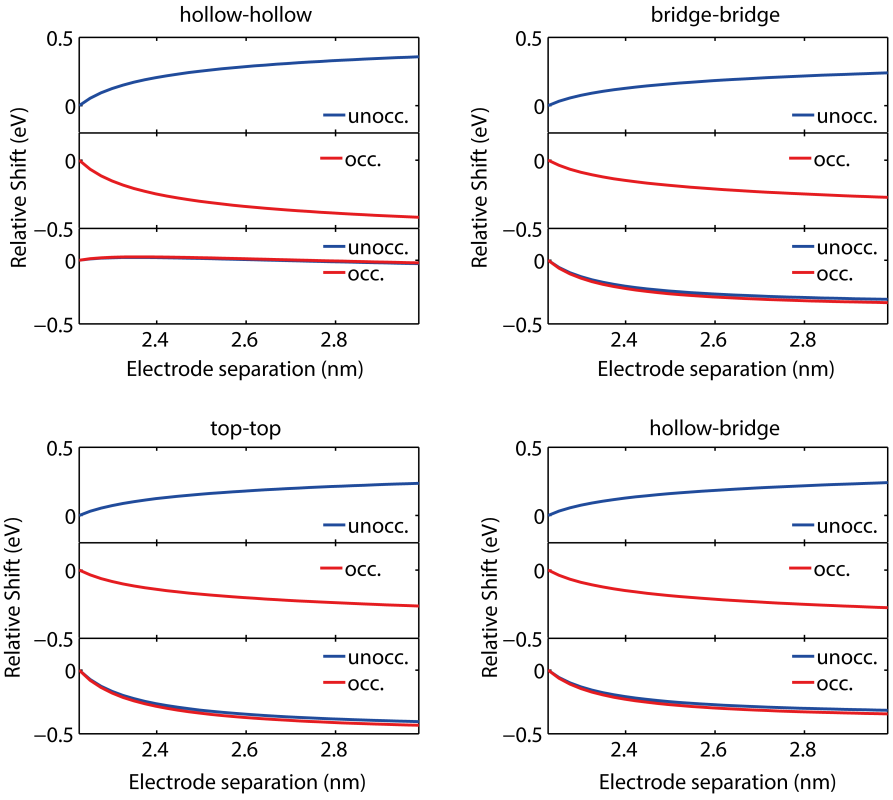

Figure 6.13: **Image-charge effect for various junction geometries**. Similar plot as in Fig. 6.11 for different binding geometries. For all of these, the contribution of the charge differences occurring during transport to the image-charge renormalizes the transport-gap.

metric combination with a hollow-site at one electrode and a bridge site at the other. The contributions to the image charge effect due to the charges of the reference state and the transport charges (first and second term in Eq. (6.1)) for those geometries are plotted in Fig. 6.13.

We find that for all binding geometries the change in charge distribution as charge is added to/removed from the junction remains mostly concentrated on the arms, near the interface. Hence, for the second term in Eq. (6.1), we find similar magnitudes of the level shifts which renormalize the transport gap. Reducing the electrode separation leads to a positive shift of the occupied level, which moves up towards the Fermi energy. The unoccupied level experiences a negative shift and moves down towards the Fermi energy.

The second term, on the other hand, is affected by the sign of the charge transfer. As this sign is geometry-dependent, its contribution to Δ can be either negative or positive, as we noted previously. We would like to stress that transport gap renormalization is observed for all geometries, and hence, the explanatory power of the model does not depend on a particular binding geometry.

Finally, we remark that the polarization which we model here is the result of many-body effects which can be accessed in a GW approach[209, 210]. However, such calculations are computationally infeasible for large molecules like porphyrins, though GW studies for small molecules have shown the response to be well-fit by an image-potential outside the image plane of the metal contact[102, 106, 197], supporting the use of our simpler model.

A.6. CORRECTIONS FOR ELECTRODE GEOMETRY

In the model calculations, the electrodes are taken as two infinite parallel planes. However, this geometry leads to an overestimation of the image-charge effect when compared to more realistic electrode shapes. To investigate this effect, we used COMSOL Multiphysics 4.2 and calculated the image-charge effect using a finite element electrostatic solver for charges between elliptical electrodes.

The electrodes were modelled as ellipsoids with the semi-axis along the transport axis fixed at 1 nm, as illustrated in Fig. 6.14. The semi-axes perpendicular to transport were varied from 0.2 nm to 5 nm. This enables us to calculate the image-charge effect in the large electrode limit (almost parallel planes) and for electrodes of a few Å across, which is the expected size of a few-atom contact in a MCBJ experiment. For these junction geometries, we first calculate the polarization energy for a point charge e in the center of the junction. We found that to account for finite electrodes, the level shifts obtained from the parallel plane model should be divided by 1.5–2.

We have also calculated the reduction factor for the molecular charge distribution modeled as point charges at the positions of the atoms. For the charge distribution we used the distributions from Fig. 6.5, in which an electron is added/removed from the molecule by applying a positive/negative voltage on the gate, see Fig. 6.14. Here we find similar reduction factors. These calculations thus imply that for more realistic electrodes, the range of MGC predicted by the image-charge model would be reduced from 0.4–2.8 V/nm to the range 0.2–1.4 V/nm, in better agreement with the measurements of Fig. 6.2 and Fig. 6.4.

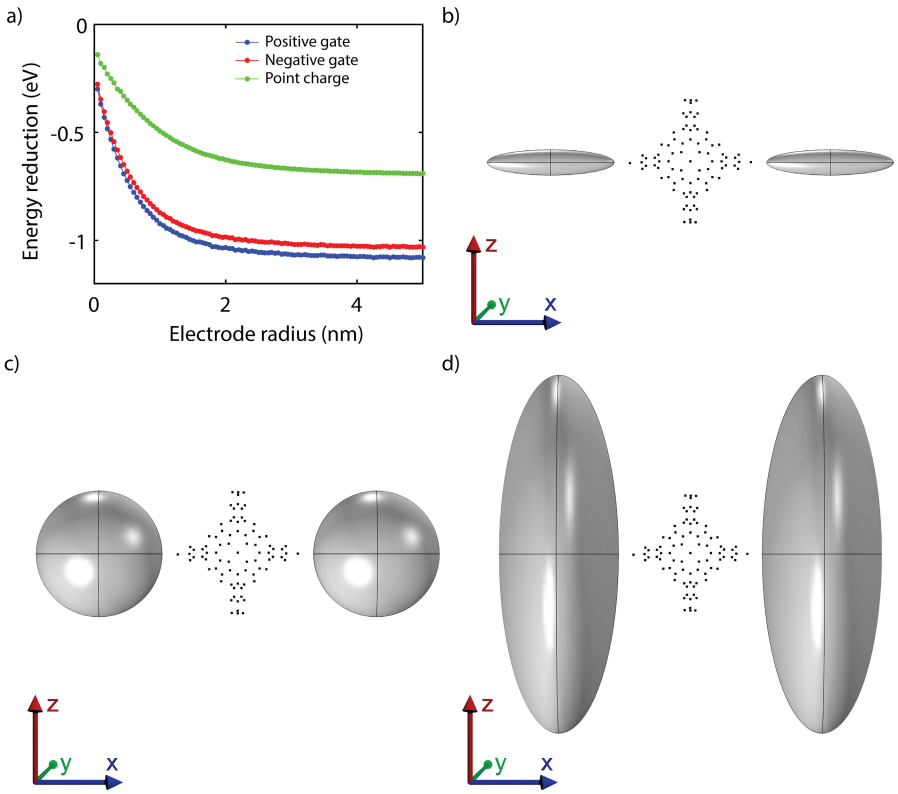

Figure 6.14: **Correction of magnitude of image-charge effect for finite contacts.** (**a**) Image charge correction as a function of electrode radius for the charge distributions obtained when applying a positive and a negative gate (see Fig. 6.4) and a point charge e in the center of the junction. (**b–d**) Geometry used in Comsol Multiphysics 4.2 to calculate the image charge correction for an electrode radius of (**b**) 0.2 nm, (**c**) 1 nm, and (**d**) 3 nm. The semi-axis of the ellipsoids along x-axis was set to 1 nm.

A.7. STRETCHING OF THE MOLECULE

To investigate the effect of streching the molecule on the energy of the orbitals, we started with the geometry shown in Fig. 6.15a and varied the Au–Au distance from 22.8 to 26.8 Å in steps of 0.02 Å. The Au-Au distance is defined as the distance between the two inner Au layers. For every step, we optimized the geometry of the molecule using a triple-ζ plus polarization (TZP), Slater-type orbital local basis-set and the PBE GGA functional, while keeping the gold atoms fixed. Results were converged to energy changes of less than 10^{-3} hartree, energy gradients of less than $1 \cdot 10^{-3}$ hartree/Å maximum and $6.7 \cdot 10^{-4}$ hartree/Å RMS. The equilibrium separation is 23.9 Å, as can be seen when looking at the minimum of the total energy (see Fig. 6.15b). The resulting energies for the HOMO, and the LUMO are shown in Fig. 6.15d. From the derivative of the total energy with respect to distance we obtain the force (see Fig. 6.15c). The figure shows that the breaking force of the Au-S bond around 1.3 nN, in agreement with literature[60] and occurs around 24.9 Å. Figure 6.15d shows the energy of the HOMO and LUMO until the breaking of the Au–S bond. Comparing the energy of the frontier orbital in the equilibrium situation (23.9 Å) with the breaking of the

Au–S bond, we obtain a maximum shift of 67.7 meV for the HOMO and 45.5 meV for the LUMO. Although those maximum shifts are significant, they only occur when the Au–S is broken. In addition, their distance dependence is opposite to the transport-gap renormalization observed in Fig. 6.2 and Fig. 6.4, indicating that although the molecule may be stretched during the experiments, this mechanism is not the one dominating the observed level shifts.

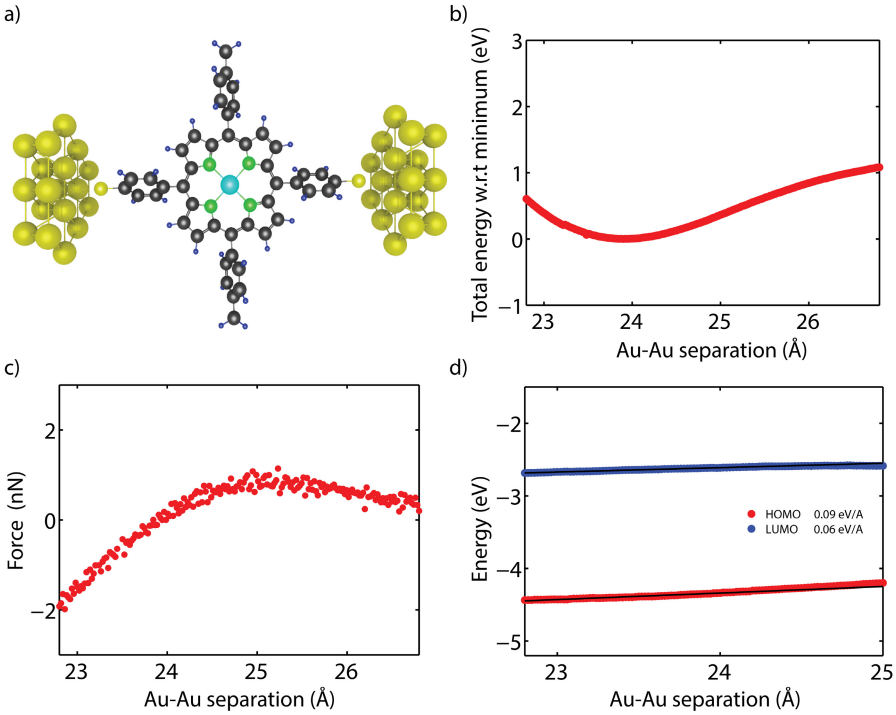

Figure 6.15: **Stretching the molecule.** (**a**) Junction configuration for lowest total energy (23.9 Å Au–Au separation). (**b**) Total energy versus Au–Au separation, shifted with respect to its minimum. (**c**) Force versus Au–Au separation curve. The breaking force of the Au–S bond is around 1.3 nN. (**d**) Energy of the frontier orbitals as a function of Au–Au separation.

7

LARGE NEGATIVE DIFFERENTIAL CONDUCTANCE IN SINGLE-MOLECULE BREAK JUNCTIONS

Molecular electronics aims at exploiting the internal structure of molecules and their electronic orbitals for constructing functional building blocks[1]. To date, however, the overwhelming majority of experimentally realised single-molecule junctions can be described as single quantum dots, where transport is mainly determined by the alignment of the molecular orbital levels with respect to the Fermi energies of the electrodes[130] and the electronic coupling with those electrodes[23, 64]. Particularly appealing exceptions include molecules in which two moieties are twisted with respect to each other[61, 63] and molecules in which quantum interference effects are possible[91, 92]. Here we report on the experimental observation of pronounced negative differential conductance in the current-voltage characteristics of a single-molecule in break-junctions. The molecule of interest consists of two conjugated arms, connected by a non-conjugated segment, resulting in two coupled sites. A voltage applied across the molecule pulls the energy of the sites apart, suppressing resonant transport through the molecule and causing the current to decrease. A generic theoretical model based on a two-site molecular orbital structure captures well the experimental findings, which are confirmed by a density functional theory with non-equilibrium Green's functions calculations that include the effect of the bias. Our results point towards a conductance mechanism mediated by the intrinsic molecular orbitals alignment of the molecule.

Parts of this chapter have been published in Nature Nanotechnology **9**, 830–834 (2014) [34].

1. INTRODUCTION

Negative differential conductance (NDC), characterised by a decrease in current for increasing voltage, is a widely used feature in electronic semiconductor devices. NDC has also been observed in molecular devices based on self-assembled monolayers (SAMs) and on single molecules[86, 211–214]. In some devices the NDC feature could be explained by features of the electrodes or the interface [211, 212], or by bias-dependent barriers[213], while in others it was attributed to intra-molecular features such as spin or phonon blockade[86], or conformational switching[214]. In most cases, the NDC effects were rather small; large NDC effects (with a peak-to-valley ratio exceeding 2), have only been observed in SAMs[215, 216], where they are due to chemical[217] or redox[218] reactions inside the SAM or traps at the electrode interface[219].

2. EXPERIMENTS AND RESULTS

We investigate an intrinsic and pronounced NDC effect in a single thiolated arylethynylene molecule with a 9,10-dihydroanthracene core (AH, see Fig. 7.1a)[220]. The molecule is studied using mechanically controllable break-junctions (MCBJs) which offer high electrode-stability and fine tuning of the electrode spacing[20]. This

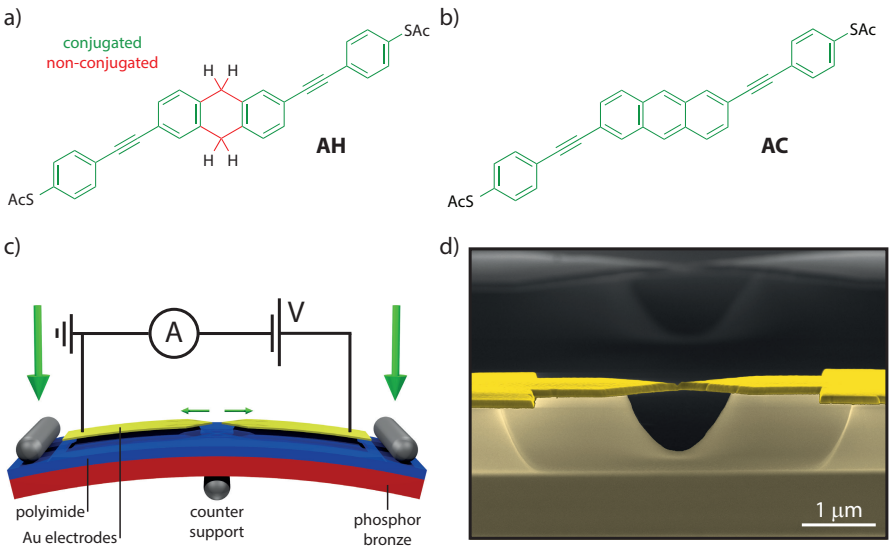

Figure 7.1: **Illustration of the experiment.** (**a**) Structure of a thiolated arylethynylene with a 9,10-dihydroanthracene core. To emphasize the broken conjugation of the molecule, the conjugated parts have been colourised in green; the non-conjugated parts in red. (**b**) Structure of a thiolated arylethynylene with an anthracene core. The green bonds indicate that the molecule is fully conjugated. (**c**) Layout of the MCBJ set-up. The large vertical green arrow represent the force applied to bend the sample. The small green arrow illustrate the attenuated electrode displacement as a result of the bending. The current through the molecular junction is recorded upon application of a bias voltage. (**d**) Colourised scanning electron microscope image of a MCBJ device.

control is realised by bending a flexible substrate in a three-point bending geometry (see Fig. 7.1c). Upon bending of the substrate, the gold wire deposited on top (see Fig. 7.1d for a scanning electron micrograph) is stretched until it breaks. The two sides of the broken wire then act as electrodes, whose separation can be adjusted with picometer resolution[188]. The molecules were deposited on the unbroken gold electrodes using self-assembly from a 0.1 mM solution in dichloromethane for 24 hours. The setup was pumped to a pressure below $5 \cdot 10^{-6}$ mbar and cooled down to a temperature of 6 K, after which current-voltage (IV) characteristics were recorded. For comparison, we also performed detailed studies on a molecule with a anthracene core that, in contrast to AH, is fully conjugated [220] (AC, see Fig. 7.1b). For more details about the experimental procedures, see Chapter 3.

2.1. IV SERIES

Figure 7.2a presents a typical IV curve measured in a device exposed to a solution of AH. At low bias, the current exhibits a pronounced negative differential conductance (NDC) feature: starting from zero bias, the current initially increases, but after 60 mV, it sharply decreases. The IV characteristic is nearly symmetric around zero bias, with a similar peak occurring at -60 mV. At higher bias (see Fig. 7.2b), the current increases again, and the IV curve has the characteristic shape corresponding to tunnelling through a single barrier. The thin black line in Fig. 7.2b is a fit of the experimental IV characteristic to the Simmons model[143].

We have also recorded IV characteristics at various electrodes spacings[56]. Figure 7.2c and Fig. 7.2d show the results for a typical sample. These figures show that the NDC feature is tunable by mechanical control of the electrode distance. This mechanical tuning can be seen most clearly in the IV characteristics of Fig. 7.2c. The NDC feature is very pronounced at short electrode separation (d_0), and remains visible when the electrode separation increases by more than an Ångstrom. The maximum current decreases with increasing electrode separation, for both positive and negative bias voltage. The tunnelling background follows a similar trend. The inset in Fig.7.2b shows the background current as measured at 1 V as a function of electrode separation. The linear dependence in this semi-log plot confirms that the background can be described by a single tunnelling barrier of which the width increases when increasing the electrode spacing. The peak-to-valley ratio increases from 3.0 to 7.1 with increasing electrode spacing, while the peak position shifts slightly outward. Figure 7.2d presents a current map in which the electrode spacing is successively increased and decreased. The total measurement took almost nine hours, and did not show any significant changes, demonstrating the stability of the NDC effect. In section A.1.1, we show data recorded in a similar way on two other samples.

2.2. IV BREAKING SERIES

In the above mentioned experiments, the electrodes were displaced over about a tenth of a nanometer without fusing the electrodes in order to study the stability of the junction. To investigate to what extent the molecular configuration is important for the observation of NDC, we have repeatedly broken and fused the electrodes to create a new molecular junction in each cycle. While breaking, we recorded IV characteristics for increasing electrode spacing[55]. This approach thus combines the

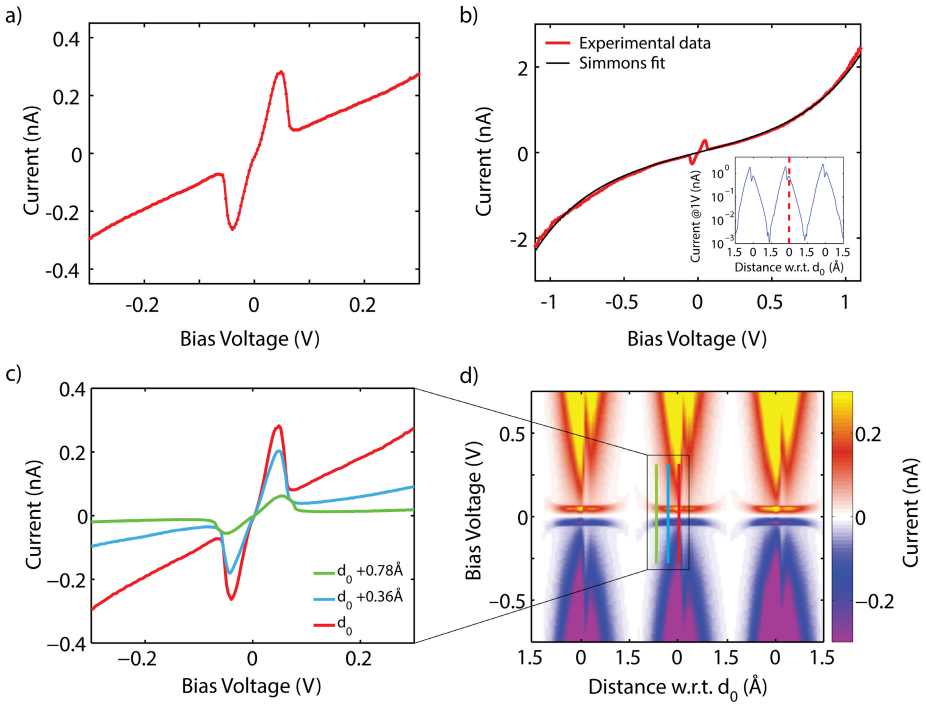

Figure 7.2: **Negative differential conductance effect: mechanical tunability and stability.** (**a**–**b**) Typical IV characteristic for (**a**) low bias and (**b**) the full bias range. The black line is a fit to the Simmons model, with an electrode spacing of 11.0 Å. (**c**) Low-bias IV characteristics for increasing electrode separation. (**d**) Map of the IV characteristics recorded from left to right while repeatedly increasing and reducing the electrode spacing. The spacing is relative to d_0, the electrode separation, at which the NDC feature is most pronounced. The IVs shown in (c) are recorded at the positions marked by the coloured lines.

advantages of spectroscopy of the molecular levels with a statistical assessment of the variation in the molecular junction formation. In the following, we will refer to this method as the *IV breaking series*, i.e., series of measurements for which the electrodes are fused before each breaking event. This is to be contrasted to the IV series described in the previous paragraphs and presented in Fig. 7.2, in which the electrodes are not fused.

Figure 7.3a presents IV characteristics measured during a particular breaking event for increasing inter-electrode spacing. As in Fig. 7.2c, the NDC effect is clearly visible and it persists up to the largest electrode separation, while the low-bias conductance changes over several orders of magnitude. By linearly fitting the current at low bias, a conductance breaking trace can be constructed, as shown in Fig. 7.3b. In this plot, the electrode displacement is set to zero at the rupture point of the last metallic atomic contact, for which the conductance quantization shows up as a plateau at 1 G_0. For increasing electrode separation, the mono-atomic gold chain breaks, leading to a drop in conductance and the formation of a molecular junction. Upon further breaking, the conductance gradually decreases.

To perform a statistical analysis of the occurrence of NDC, we measured IV se-

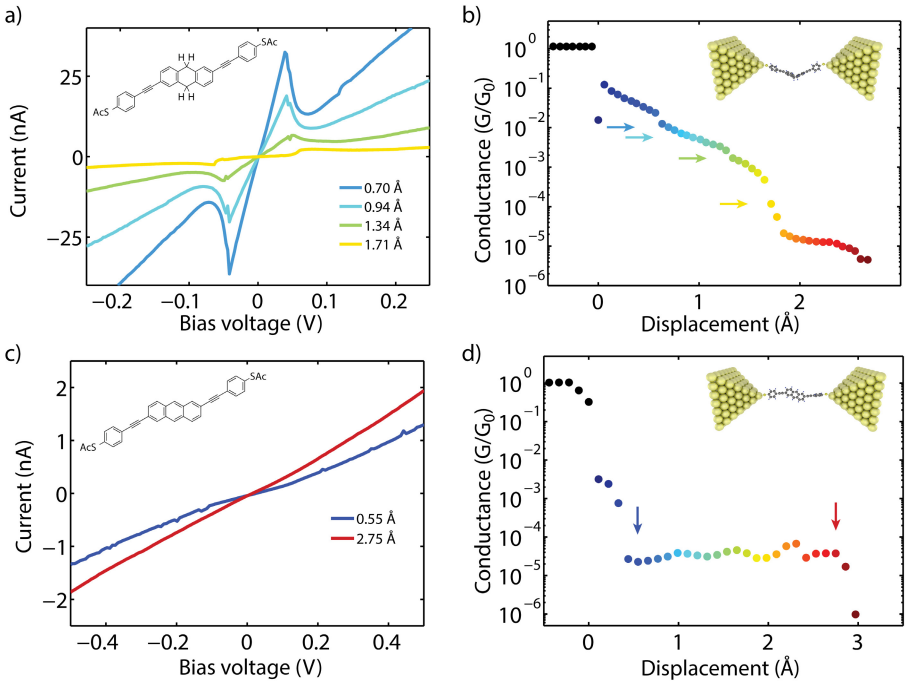

Figure 7.3: **IV breaking series on AH and AC.** (**a**,**c**), IV characteristics recorded during one breaking event on (**a**) AH and (**c**) AC. (**b**,**d**) Breaking traces showing the low-bias conductance vs. electrode displacement obtained by a fit on each IV characteristic in an IV breaking series recorded on a junction exposed to (**b**) AH and (**d**) AC. The coloured arrows indicate the location in the breaking trace at which the IV characteristics shown in (a) and (c) respectively are recorded. The insets present a possible junction configuration as obtained from molecular dynamics simulations.

ries during 693 breaking events in total, recorded in three different samples (see section A.1.2 for more details.). We distinguish three types of series: 1) series without a molecule (tunnelling IV characteristics with no plateau in the conductance trace), 2) series with a molecule but without NDC (IV characteristics that show steps, or IV characteristics with a plateau in the conductance versus displacement trace) and 3) series with a molecule and NDC. In 503 cases (72.6% of the events), no molecule was trapped in between the electrodes; 190 traces (27.4% of all the series), on the other hand, show molecular features. Of those series, 144 (about 75% of the molecular junctions) exhibited NDC, with peak-to-valley ratios ranging from 1.5 to 15.

Using the same IV breaking series approach, we performed measurements on the conjugated AC molecule, shown in Fig. 7.3c and Fig. 7.3d. Figure 7.3c shows typical IV characteristics for increasing inter-electrode spacing. The characteristics are monotonic and do not show NDC. Looking at the breaking trace shown in Fig. 7.3d, a plateau at 1 G_0 is again visible, followed by a drop in conductance. A plateau in the conductance trace is then visible, indicating that a molecular junction has been formed (blue dots). For increasing displacement a conductance plateau is observed after which the conductance drops sharply (red dots). We find that in about 33% of the breaking traces (510 series in total; 3 different samples) molecules are present in

the junction. In those 170 junctions, 166 show no NDC. In the remaining 4, NDC is observed.

In summary, a comparison of the measurements conducted on the two molecules shows two distinct differences. Firstly, the evolution of the conductance for increasing electrode distance is gradual for AH, spanning a wide range of conductances, whereas for AC a clear step is observed. Secondly, the statistics show that the NDC effect is very prominent in AH (75% in case a molecular junction is formed) and almost absent in AC (2%).

3. CALCULATIONS

3.1. DFT + NEGF

To gain more insight in the origin of the NDC effect, we have also investigated AH using density functional theory (DFT) and the non-equilibrium Green's function formalism (NEGF). Calculations were performed for the molecule in gas-phase using the Amsterdam Density Functional (ADF) quantum chemistry package with the GGA exchange-correlation functional and the triple-ζ plus polarization basis set [202, 203]. For details concerning the DFT calculation and the estimation of the parameters, we refer to section . Previous studies show that for this molecule, transport is dominated by the highest occupied molecular orbital (HOMO) as it is closest to the Fermi energy (ϵ_F)[221]; the lowest unoccupied molecular orbital (LUMO), on the other hand, is located about 2.5 eV above ϵ_F. Inspection of the spectrum reveals that the HOMO and HOMO-1 are nearly degenerate (with an energy spacing $\Delta = 18$ meV), and that they have a bonding/anti-bonding character)[222]. This directly reflects the chemical composition of the AH molecule, which consists of two conjugated arms, connected by a non-conjugated segment, as illustrated in Fig 7.1a. To see this, we transform the HOMO and HOMO-1 into an equivalent set of localized molecular orbitals (LMOs) by addition and subtraction[92]. This leads to one LMO located on the left half of the molecule and the other on the right half, as shown in Fig. 7.4a. The two LMOs can be viewed as two units in series, which are weakly coupled. Transport through the molecule can therefore be described using a model consisting of two sites, coupled to each other via a small coupling parameter τ, as illustrated in Fig. 7.4b. This inter-site coupling can be estimated from the energy difference Δ between the HOMO and HOMO-1 obtained from DFT as τ=9.1 meV. The tunnel coupling of each site to its lead is characterized by Γ.

3.2. TWO-SITE MODEL

The NDC effect can readily be explained from such a two-site model[92, 167, 222, 223]. At zero bias, the two sites are in resonance with each other and the conductance is high (see Fig. 7.4c). Upon application of a bias voltage V, however, the energies of the two sites shift in opposite energy direction due to the Stark effect. DFT calculations in the presence of an electric field across the molecule show that a fraction α of the bias drops inside the molecule. When the two LMOs shift apart and $\alpha eV \gg 2\tau$, the current is substantially suppressed and the NDC feature sets in. For this two-site model, the current through the system can be calculated analytically using NEGF (see section A.2.1, where we also show that the analytical IV is reproduced by DFT + NEGF calculations). In Fig. 7.4d we show an experimental IV characteristic from

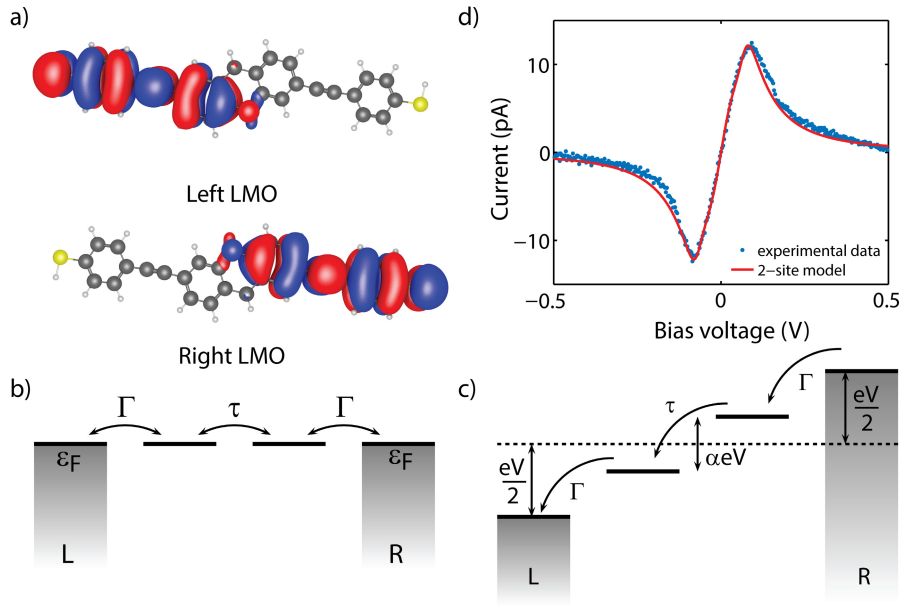

Figure 7.4: **Two-site model.** (**a**) The left and right LMO obtained by taking the sum and the difference of the HOMO and HOMO-1, which are shown in Fig. S4. (**b**) Since the LMOs are each located on one side of the molecule, the junction can be modelled by two sites in series, left and right, coupled by τ. The sites are coupled to the leads by Γ. In the strong-coupling regime, transport through the molecule is coherent. Due to the symmetry of the molecule, the two sites, at ϵ_L and ϵ_R, are in resonance at zero bias, and the conductance is high. (**c**) Upon application of a bias, the sites are pulled off resonance by αeV, where α is the fraction of the voltage drop occurring inside the molecule. Although τ does not change significantly as a function of bias voltage, the off-resonance condition leads to a reduction of the elastic transport through the molecule, lowering the conductance of the junction. (**d**) Background-corrected IV characteristics recorded on sample A with a fit to the two-site model using α =0.74, τ=24.1 meV, Γ=10.2 meV. To match the absolute values of current, a prefactor of $7.2{\cdot}10^{-5}$ was used.

which the background current has been subtracted, and a fit to the analytical expression of the two-site model. The excellent agreement supports the use of this model to describe transport through AH. Note that similar ab-initio calculations on AC do not show an NDC effect, as expected from its conjugation, which extends across the whole molecule.

3.3. LEVEL (MIS)ALIGNMENT

The calculation in Fig. 7.4d takes the two sites to be in resonance with the Fermi energy at zero bias and assumes the voltage drop across the electrode-molecule tunnel barriers to be symmetric over the junction, as this matches the observed IV characteristics of more than half of the IV breaking series. In the remaining measurements (see section A.2.3 for more details and the statistics) the IV characteristics show a gap at low bias. The presence of a gap can be explained by the sites being slightly off-resonant with the Fermi energy at zero bias. Our experiments therefore allow for quantification of the level alignment in a statistical way. If we assume a symmetric division of the applied voltages across the contacts, we find that the misalignment

ranges from 0 to 225 meV. We furthermore note that the NDC feature is also reproduced when considering more detailed quantum chemistry calculations involving the full self-energies of the metal electrodes and with a potential difference applied on the gold electrodes using the BAND package[189] (see section A.2.3).

3.4. STRETCHING OF THE MOLECULE

An intriguing aspect of the experiment is the gradual decrease of the conductance with increasing electrode separation, without the presence of clear conductance plateaus. Conductance histogram on AH at room temperature do indicate conductance plateaus below $1{\cdot}10^{-6}$ G_0,[55, 222] which are not accessible in our experiments. It is important to realize that there is a distinct difference between the AH and AC molecule. AC is a rigid molecule, while AH can bend in the middle due to the broken conjugation. Molecular dynamics (MD, see section A.3) simulations confirm this and show that the junction evolves differently for the two molecules during breaking. AC, being rigid, remains in a planar configuration during the stretching of the electrodes, as illustrated in the inset of Fig. 7.3d. AH, on the other hand, shows a gradual evolution from a bent geometry (see Fig. 7.3b) to a more planar configuration for larger separations. During this process, the parameters τ, Γ and α that determine the conductance gradually change (see section A.2.5). In particular the variation of τ may explain the gradual conductance decrease.

3.5. DIODE

We finally note that AH is a symmetric molecule, hence the two sites are on resonance with each other at zero bias. Introducing an asymmetry in the molecule can shift the sites apart, significantly changing the behaviour of the device. For example, if at zero bias the left site is higher in energy than the right site, a negative bias voltage would only pull them further apart (compare with Fig. 7.4d). They would therefore never move into resonance and the current remains low. At positive bias, on the other hand, they would align at a particular bias, increasing the current dramatically until the bias is so large that they are pulled off resonance again and the current decreases. This difference in behaviour at positive and negative bias means that such a molecule acts as a rectifier. We note here that unlike most report on single-molecule diodes[67, 224], this rectification is also present in the case of symmetric couplings to the leads. DFT + NEGF calculations on a particular asymmetric AH derivative (see section A.2.6) indeed confirm this rectifying concept, with rectification ratios of the order of 400.

4. CONCLUSION

In conclusion, we have observed a reproducible NDC effect in junctions containing a single AH molecule with a strong suppression of the current through the molecule at high bias. The NDC effect can be accurately described by a two-site model. Importantly, the model shows that the origin of the NDC effect is an internal resonance of two weakly coupled sites inside the molecule. It is therefore intrinsic to the molecule and largely insensitive to the metal-molecule interface. The model is confirmed by DFT + NEGF calculations and can be applied to any molecule consisting of two weakly-coupled halves and used to design specific electronic functionalities. In particular, we predict rectifier behaviour with large rectification ratios in case of asym-

metric molecules. From a more general point of view, our results introduce a new, widely applicable route towards more complex molecular components which may contain multiple weakly coupled sites.

A. APPENDIX

A.1. MEASUREMENTS

IV SERIES AH CRYOGENIC TEMPERATURE (6 K)

Without fusing the electrodes, we studied two other samples that show a robust and distance tunable NDC effect. Data recorded on device B and C is presented in Fig. 7.5. Sample A is shown in previously.

IV BREAKING SERIES AH CRYOGENIC TEMPERATURE (6 K)

In Fig. 7.6, we show the statistics for the low-temperature IV breaking series. We distinguish three types of series: 1) series without a molecule (featureless tunnelling IV characteristics with no plateau in the conductance trace), 2) series with a molecule but without NDC (IV characteristics that show steps, or IV characteristics with a plateau in the conductance versus displacement trace) and 3) series with a molecule and NDC.

In Fig. 7.7 we show an additional measurement of an IV series, complementary to one shown in Fig. 7.3a and b. Figure 7.7b shows the low-bias conductance of a breaking trace, constructed by fitting at low bias the IVs at various electrode spacings.

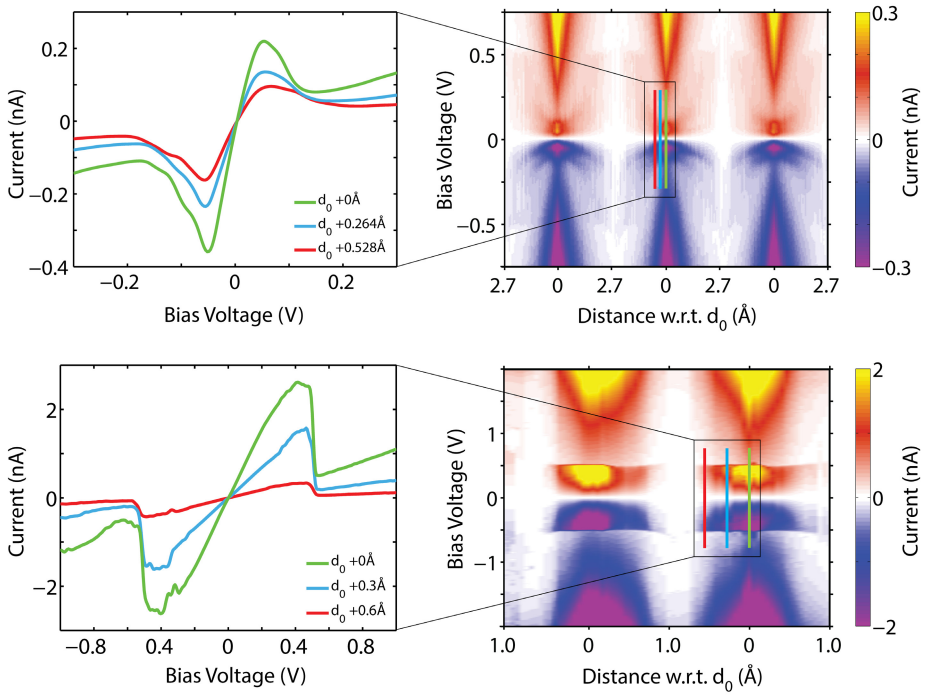

Figure 7.5: **Current as a function of bias voltage and electrode separation.** The right-hand side shows a map of the IV characteristics at various electrode spacings for (**a**) sample B, and (**b**) sample C. The spacing is relative to d_0, the shortest electrode separation, at which the NDC feature is most pronounced. On the left, several low-bias IV characteristic are shown, recorded at the positions marked by the coloured lines in the current map (panels of the right side).

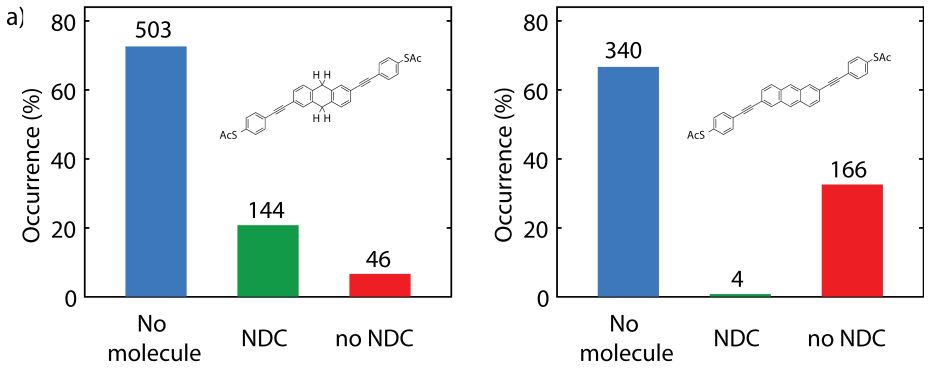

Figure 7.6: **Statistics of the IV breaking series.** Probability of forming a junction without molecule, with molecule and NDC, and with molecule without NDC for (**a**) AH and (**b**) AC

The arrows indicate the position at which the IV characteristics shown in Fig. 7.7a are recorded. As in Fig. 7.3a and b, NDC is very pronounced and visible over a large conductance range.

AH ROOM-TEMPERATURE IVS

Room-temperature measurements are more challenging than the ones at low temperatures as molecular junctions tend to be less stable. Nevertheless, we have observed NDC in more than 50 IV breaking series recorded on two different chips. Figure 7.8 presents one typical IV breaking series, with NDC being clearly visible. Note that in the room-temperature measurements (also the ones in the next section), the sample bending is controlled using a piezoelectric actuator, while for the low-temperature data, a brushless motor is used. Interestingly, all IV characteristics recorded at room temperature show a gap (see also section A.2.4). The reason for this is presently not clear to us and is a subject for further investigations.

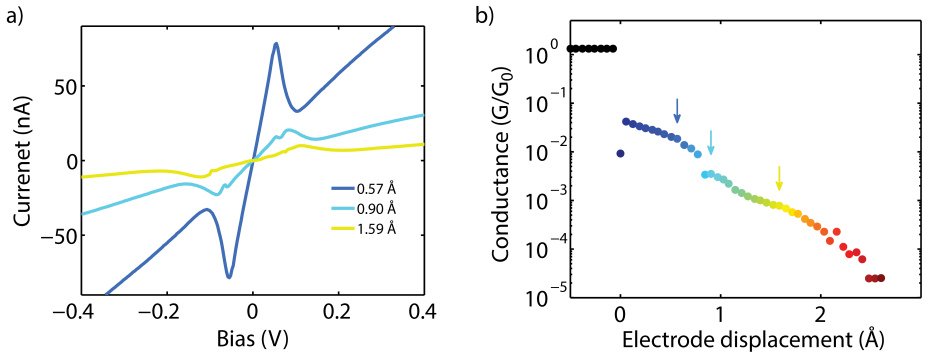

Figure 7.7: **IV breaking series at 6 K on AH.** (**a**) IV characteristics recorded during a IV breaking series on AH at 6 K. (**b**) Low-bias breaking trace. The coloured arrows indicate the location in the breaking trace at which the IV characteristics shown in (a) are recorded.

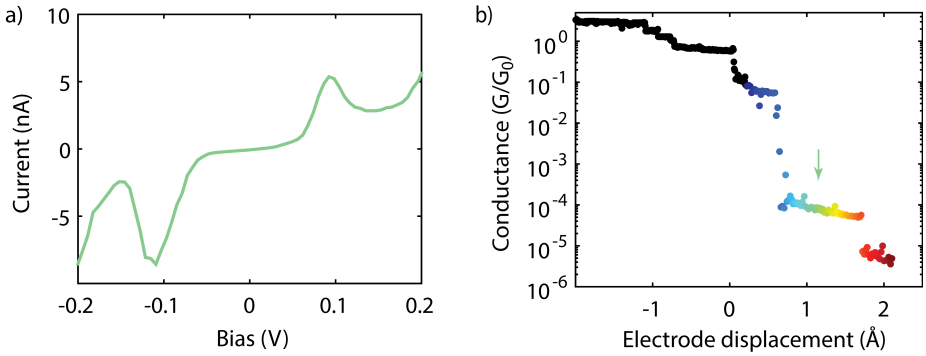

Figure 7.8: **IV breaking series at room temperature on AH.** (**a**) IV characteristics recorded during an IV breaking series on AH at room temperature. (**b**) Low-bias breaking trace. The coloured arrow indicates the location in the breaking trace at which the IV characteristic shown in (a) is recorded.

ROOM-TEMPERATURE CONDUCTANCE HISTOGRAMS

Both AH and AC have been extensively studied before in literature[55, 220–222] using conductance histograms. As a comparision with the published literature, Fig. 7.9 shows conductance histograms recorded on the two molecules at room temperature in ambient conditions. Both molecules were dissolved in dichloromethane at a concentration of 0.1mM. For AC, tetrabutylammonium hydroxide was used to cleave of the acetyl groups after which a drop of the molecular solution was deposited on the sample. For AH, tetrabutylammonium hydroxide cannot be used. Instead, the sample was kept for 24h in solution for self-assembly.

Figure 7.9a shows a conductance histgram for gold exposed to solvent only. Here, only tunnelling traces are visible. Figure 7.9b presents a histogram of AH. No clear molecular plateaus are visible down to the noise level of our set-up. The AH histogram is different from the one exposed to solvent only, as it shows additional counts over a wide range of conductance values. Inspection of the individual traces shows that many that contributed to these counts are slanted. The histogram resembles the one measured in literature[55, 222], although we are not able to reach the same level of noise ($1{\cdot}10^{-8}$ G_0). It is interesting to note that the histogram of AH shows more counts at high conductance levels than AC, in accordance with our low-T data. A similar observation is also reported in a recent review paper[222] in which slanted traces start at conductances as high as $1{\cdot}10^{-2}$ G_0. The existence of conductance values over a wide range and thus the absence of a clear conductance plateau is consistent with the gradual change of the molecular conformation and the accompagnying change in the parameters defining the conductance, as discussed previously.

Figure 7.9c shows a histogram for AC, where clear conductance plateaus are found around $3{\cdot}\ 10^{-5}$ G_0, in agreement with the measurements shown in literature[55, 222]. This value also matches well with the plateau in the breaking trace shown in Fig. 7.3 that was obtained at cryogenic temperature.

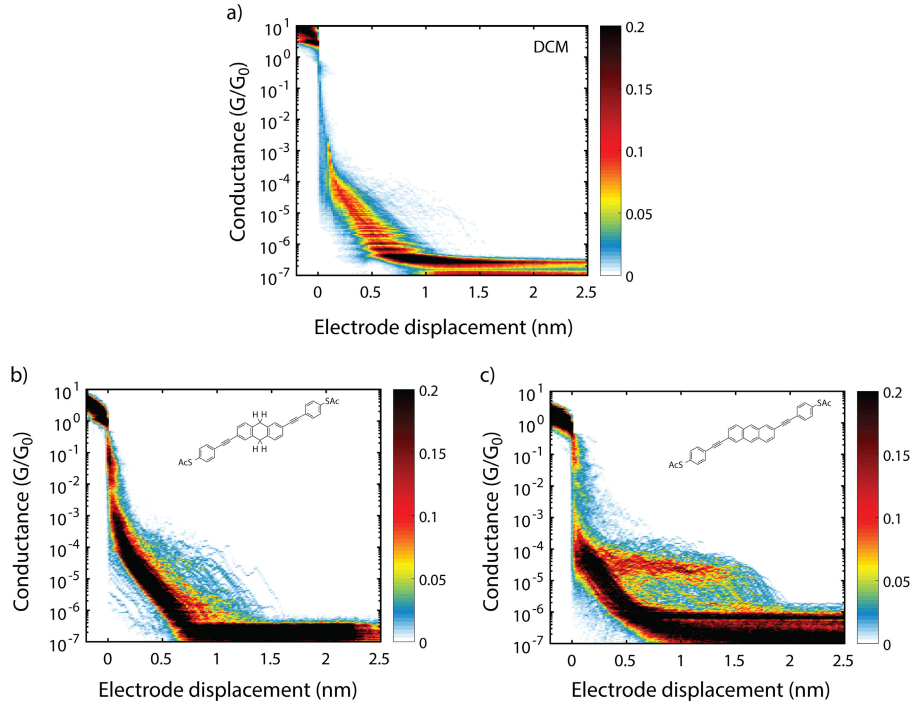

Figure 7.9: **Conductance histograms at room temperature.** Conductance histogram recorded on (**a**) bare gold, (**b**) AH and (**c**) AC. For all three histograms the bias voltage was set to 100mV, the electrode speed to 5nm/s. The noisefloor of our setup is around $3{\cdot}10^{-7}$ G_0. The area of high counts below that value is caused by noise and is not molecular in nature.

7

A.2. TWO-SITE MODEL

ANALYTICAL DERIVATION

The Hamiltonian of the two-site system (see Fig. 7.4a and b) is given by

$$\boldsymbol{H} = \begin{pmatrix} \epsilon_0 + \frac{1}{2}\alpha eV & -\tau \\ -\tau & \epsilon_0 - \frac{1}{2}\alpha eV \end{pmatrix}. \tag{7.1}$$

The eigenstates of this Hamiltonian correspond to the bonding (π) and antibonding (π^*) orbitals, of which the energy are $\epsilon_1 = \epsilon_0 - \frac{1}{2}\Delta$ and $\epsilon_2 = \epsilon_0 + \frac{1}{2}\Delta$, where the energy splitting Δ in the presence of a bias voltage is given by

$$\Delta = \sqrt{(\alpha eV)^2 + (2\tau)^2}. \tag{7.2}$$

We now symmetrically couple the left and right sites to the corresponding leads in the wide-band limit:[225, 226]

$$\boldsymbol{\Gamma}_\mathrm{L} = \begin{pmatrix} \Gamma & 0 \\ 0 & 0 \end{pmatrix}, \qquad \boldsymbol{\Gamma}_\mathrm{R} = \begin{pmatrix} 0 & 0 \\ 0 & \Gamma \end{pmatrix}. \tag{7.3}$$

The transmission is given by[199, 225, 226]

$$\mathscr{T}(\epsilon) = \mathrm{Tr}\left\{\boldsymbol{\Gamma}_\mathrm{L}\boldsymbol{G}^r(\epsilon)\boldsymbol{\Gamma}_\mathrm{R}\boldsymbol{G}^a(\epsilon)\right\}, \tag{7.4}$$

where $\boldsymbol{G}^r(\epsilon)$ and $\boldsymbol{G}^a(\epsilon)$ are the retarded and advanced Green's functions, respectively. The former is given by

$$\boldsymbol{G}^r(\epsilon) = \left(\epsilon\mathbf{1} - \boldsymbol{H} + \frac{\mathrm{i}}{2}(\boldsymbol{\Gamma}_\mathrm{L} + \boldsymbol{\Gamma}_\mathrm{R})\right)^{-1}, \tag{7.5}$$

while $\boldsymbol{G}^a(\epsilon) = \boldsymbol{G}^r(\epsilon)^\dagger$. Evaluating the transmission yields

$$\mathscr{T}(\epsilon) = \frac{(2\tau)^2}{(\Gamma/2)^2}\frac{(\Gamma/2)^2}{(\epsilon-\epsilon_1)^2+(\Gamma/2)^2}\frac{(\Gamma/2)^2}{(\epsilon-\epsilon_2)^2+(\Gamma/2)^2}. \tag{7.6}$$

The current can be calculated via[199, 225, 226]

$$I = \frac{2e}{\hbar}\int\frac{\mathrm{d}\epsilon}{2\pi}\big(f_\mathrm{L}(\epsilon) - f_\mathrm{R}(\epsilon)\big)\mathscr{T}(\epsilon), \tag{7.7}$$

where $f_\mathrm{L}(\epsilon)$ and $f_\mathrm{R}(\epsilon)$ are the Fermi functions of the left and right lead, respectively. In the low-temperature limit, these become step functions. Distributing the bias voltage symmetrically over the leads, *i.e.*, $\mu_\mathrm{L} = \epsilon_F + \frac{1}{2}eV$ and $\mu_\mathrm{R} = \epsilon_F - \frac{1}{2}eV$, we obtain

$$I = e\frac{\Gamma}{h}\frac{(2\tau)^2}{\Delta^2+\Gamma^2}\Bigg[\arctan\left(\frac{\frac{1}{2}eV-\epsilon_1}{\Gamma/2}\right)+\arctan\left(\frac{\frac{1}{2}eV+\epsilon_1}{\Gamma/2}\right)+\frac{\Gamma}{2\Delta}\ln\left(\frac{\left(\frac{1}{2}eV-\epsilon_1\right)^2+(\Gamma/2)^2}{\left(\frac{1}{2}eV+\epsilon_1\right)^2+(\Gamma/2)^2}\right)+$$
$$\arctan\left(\frac{\frac{1}{2}eV-\epsilon_2}{\Gamma/2}\right)+\arctan\left(\frac{\frac{1}{2}eV+\epsilon_2}{(\Gamma/2)}\right)-\frac{\Gamma}{2\Delta}\ln\left(\frac{\left(\frac{1}{2}eV-\epsilon_2\right)^2+(\Gamma/2)^2}{\left(\frac{1}{2}eV+\epsilon_2\right)^2+(\Gamma/2)^2}\right)\Bigg]. \tag{7.8}$$

7

DFT + NEGF CALCULATIONS ON AH

To validate the two-site model, we performed DFT + NEGF calculation on AH. Calculations were performed using the Amsterdam Density Functional (ADF) quantum chemistry package with the GGA PBE exchange-correlation functional and the triple-ζ plus polarization (TZP) basis-set. [202, 203]. Transmissions were calculated by coupling the p_z-orbitals of the sulphur atoms to wide-band electrodes with a coupling strength of 100 meV. A bias voltage was applied to the molecule by introducing a uniform electric field along the axis connecting the sulphur atoms.

Figure 7.10c shows the transmission of AH for a bias voltage of 0 V and 1 V. At 0 V the HOMO and HOMO-1 are nearly degenerate and located close to the Fermi energy (which the calculations predict to be around -4.8 eV). The HOMO and HOMO-1 are displayed in Fig. 7.10a and bm respectively. The HOMO and HOMO-1 peaks move apart for increasing bias voltage, while their amplitude is reduced. This trend is more clearly visible in a map of the transmission as a function of energy and bias voltage (see Fig. 7.10d). The bias dependence of the energy difference Δ between the HOMO and HOMO-1 is shown in Fig. 7.10e. The bias dependence follows the trend predicted by the two-site model. Fitting Eq. 8.2 to the calculated data points yields $\alpha = 0.48$ and τ=9.1 meV.

The current can be calculated by integrating the transmission (see Eq 8.6). The red line in Fig. 7.10f shows the IV characteristic calculated using DFT+NEGF. The Fermi energy is set to be on resonance with the HOMO. This calculation takes into

account all molecular orbitals and reproduces the observed NDC behaviour. The dashed blue line is a fit to the two-site model, using Γ=24.2 meV. Note that Γ in the DFT+NEGF calculation is the coupling to the only thiol atoms, while in the two-site model Γ is the coupling to one of the sites, *i.e.*, one arm of the molecule. The two values of Γ therefore cannot be compared directly. The two-site model shows excellent agreement with the DFT+NEGF calculation, demonstrating that the HOMO and HOMO-1 dominate the current through the molecule.

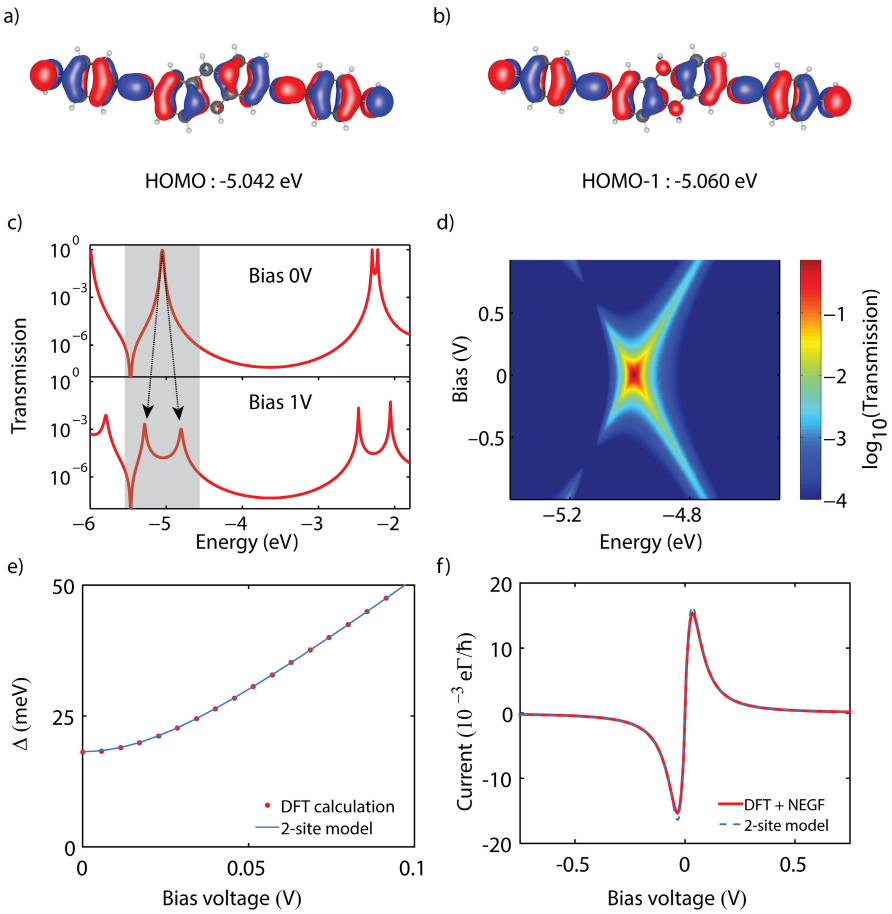

Figure 7.10: **DFT + NEGF calculations on AH.** (**a**) HOMO of AH. (**b**) HOMO-1 of AH. (**c**) Transmission of AH as a function of energy at a bias of 0 V and 1 V. At zero bias, the HOMO and HOMO-1 are nearly degenerate (at -5.05 eV), resulting in a single peak in the transmission. At finite bias voltage the peaks move apart. (**d**) Map of the transmission as a function of energy and bias voltage, showing the voltage dependence of the peak positions. (**e**) Energy difference Δ between the HOMO and HOMO-1 for increasing bias voltage, obtained from DFT (red dots). The blue line represents a fit to the two-site model (Eq. 8.2), with $\alpha = 0.48$ and τ=9.1 meV. **f**, IV characteristic calculated using DFT + NEGF (solid red, Γ=100 meV) and using the two-site model (dashed blue, Γ=24.2 meV.)

ALIGNMENT WITH THE FERMI ENERGY

In the measurements shown in Fig. 7.2 and Fig. 7.3, both sites are on resonance with the Fermi energy at zero bias. To investigate this alignment in more detail, we performed additional DFT calculations.

First, to relax the geometry, we used the ADF package and connected the molecule to two hollow sites of the gold electrodes. We then varied the Au-Au distance from 17.00 to 31.00 Å in steps of 0.04 Å (where the Au-Au distance is defined as the distance between the two inner Au layers). For every step, we optimized the geometry of the molecule using a triple-ζ plus polarization (TZP), Slater-type orbital local basis-set and the PBE GGA functional, while keeping the gold atoms fixed. Results were converged to energy changes of less than 10^{-3} hartree, energy gradients of less than $1 \cdot 10^{-3}$ hartree/Å maximum and $6.7 \cdot 10^{-4}$ hartree/Å RMS. The junction geometry with the lowest total energy is found for a Au-Au distance of 26.56 Å, and is shown in Fig. 7.11a.

To compute the transmission of the equilibrium junction geometry under bias, we used the BAND extension of ADF, in which the electrodes are taken into account fully self-consistently[189]. For the calculation, we used a triple-ζ plus polarization (TZP), Slater-type orbital local basis-set and the LDA functional. Fig. 7.11b presents the transmission (in black, on the left axis), with the energy relative to the Fermi energy. The HOMO/HOMO-1 are nearly degenerate and located 0.4 eV below the Fermi

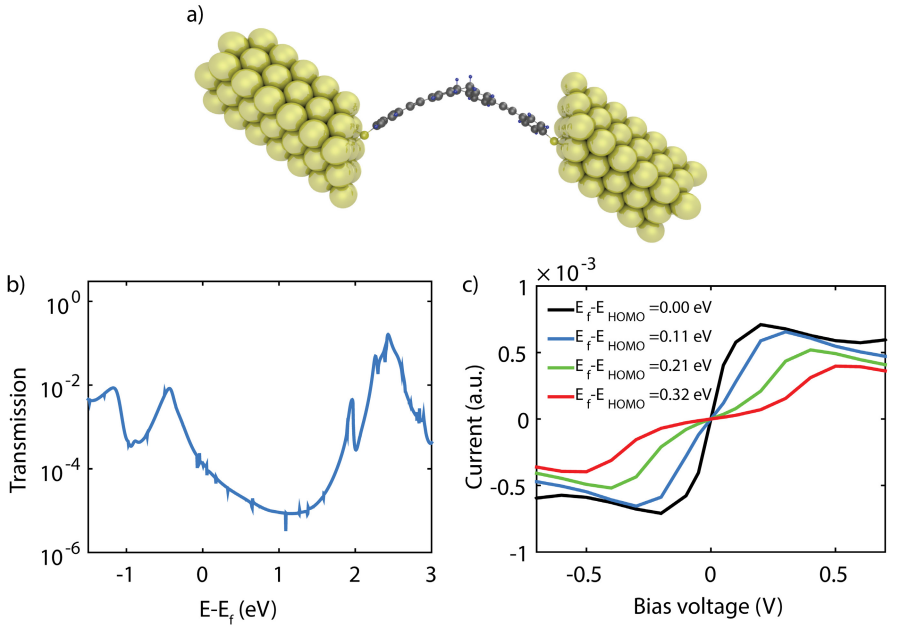

Figure 7.11: **DFT calculations of AH including gold electrodes using the BAND package.** (**a**) Relaxed junction geometry. (**b**) Transmission computed using DFT + NEGF. All energies are relative to the Fermi energy. The location of the HOMO is -0.42 eV. (**c**) IV characteristics computed for various values of the Fermi energy. For the black line, the Fermi energy is choosen to be on resonance with the HOMO. For the blue, green and red line the level (mis)alignement is increased.

energy. The first unoccupied orbital appears to be around 2.4 eV above the Fermi energy.

To calculate the current, we applied a potential difference between the electrodes. By intergrating the transmission for all bias points (see Eq. 8.2), we computed the IV characteristics. Figure 7.11c shows IV characteristics for various locations of the Fermi energy. When on resonance with the HOMO, the IV characteristic shows a clear NDC feature. For an increasing misalingment, a gap appears, as is also sometimes observed in the experiments (see next section).

VARIATION IN THE LEVEL ALIGNMENT

In the experimental IV characteristics recorded during the IV breaking series, some series show IV characteristics with a gap around zero bias, *i.e.*, a reduction of the conductance. Two examples are depicted in Fig. 7.12a. We analysed statistically all the IV breaking series showing NDC and determined the gap size. The results are presented as a histogram in Fig. 7.12b. The gap size was estimated by determining the peak separation in the numerical derivative of the IV characteristic, as shown in the inset of

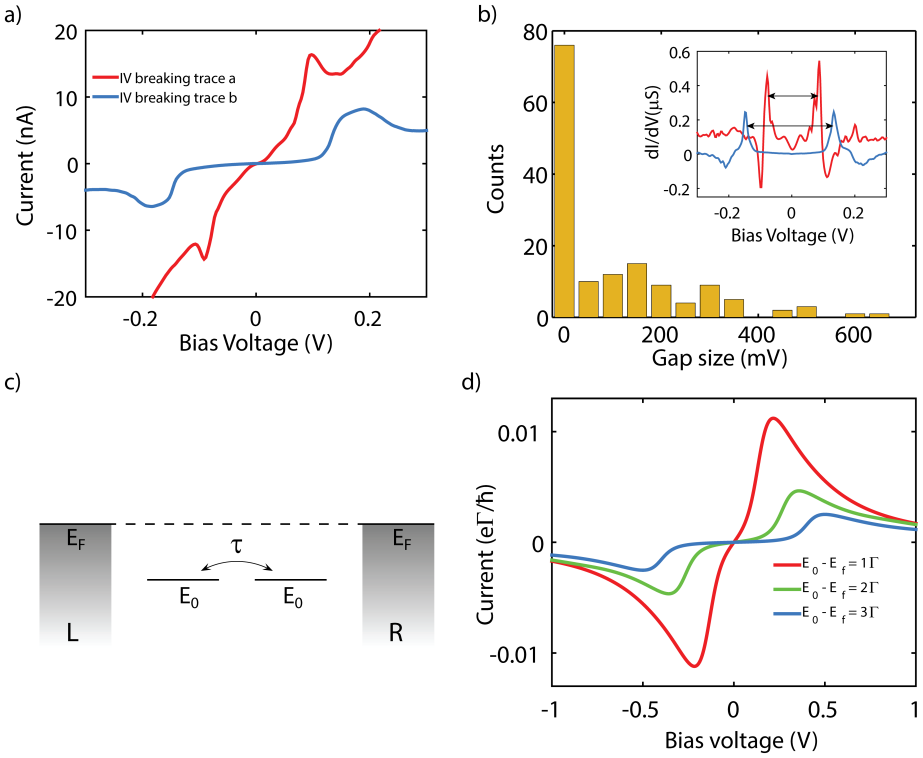

Figure 7.12: **Gap in the IV characteristics.** (**a**) Typical IV characteristics with a gap, recorded during two different IV breaking series probing two different junction configurations. (**b**) Histogram of the gap size. Inset: Numerical derivative of the IV characteristics shown in (a). The gap size has been determined from the voltage difference between the peaks, as indicated by the black arrows. (**c**) Two-site model, with the two sites not aligned with Fermi enegy at zero bias. (**d**) IV characteristics calculated using expression 7.8 for different energies of the sites at zero bias. Increasing the energy difference between the Fermi energy and the sites increases the size of the gap.

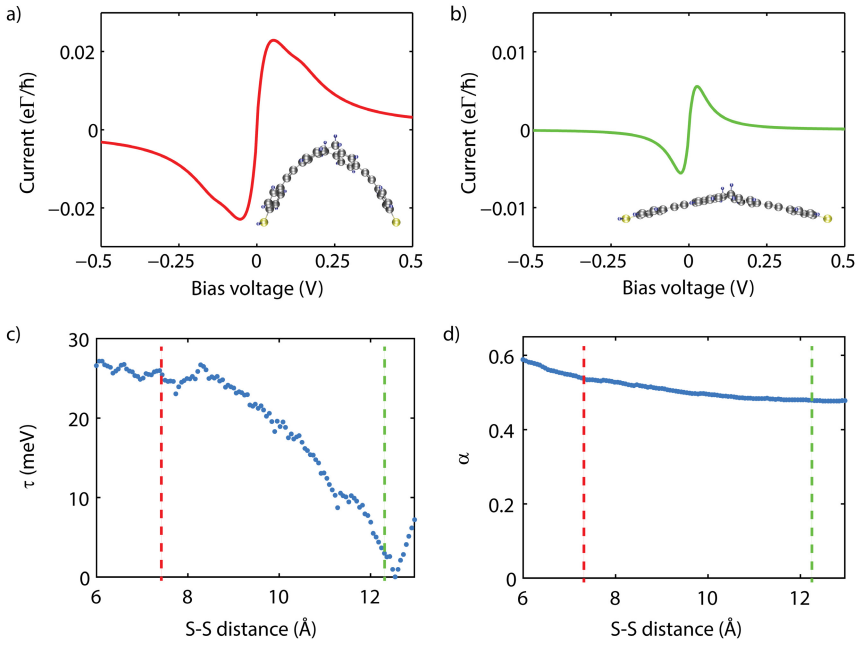

Figure 7.13: **Distance dependence of NDC.** IV calculated using DFT+NEGF for a fully bend (**a**) and partially bend (**b**) molecule. The inset show the geometry of the molecule. (**c**) Distance dependence of τ. (**d**) Distance dependence of α. The two dashed lines indicate at which distances the IVs shown in (a) and (b) have been calculated.

7

Fig. 7.12b. From Fig. 7.12b, we find that the two sites are preferably (in almost half of the series) on resonance with the Fermi energy at zero bias (no gap in the IV characteristics). In the other half, a gap is visible, which can be as large as 600 mV. Such a gap corresponds to a misalignment of the two sites by about 225 meV with respect to the Fermi energy of the electrodes, assuming α is 0.5 and the molecule is symmetrically coupled to the electrodes (see Fig. 7.12c). Figure 7.12d shows IVs calculated using eq. 7.8 for different level alignments, with a gap visible for a misalignment $E_0 - E_f$ comparable to or large than Γ.

DISTANCE DEPENDENCE

In the experimental data (see Fig. 7.5), the current at the NDC peak decreases with increasing distance, whereas the peak position remains nearly the same. In the model, the decrease in current can be accounted for by including a distance dependence of the parameters τ, α and Γ. In the following each of these parameters will be investigated.

We first performed DFT calculations in gas phase for increasing S–S distance, in which we fixed the S-S distance while letting the molecule relax. The S–S distance was increased in steps of 0.04 Å. Figure 7.13a and Fig. 7.13b show an IV calculated for a S–S distance of 16.0 Å and 24.4 Å respectively. The insets illustrate the molecular conformation. In both cases NDC is visible. As in Fig. 7.10e, the energy difference between the HOMO and HOMO-1 was fitted to Eq. 8.2 to extract τ (see Fig. 7.13c) and α

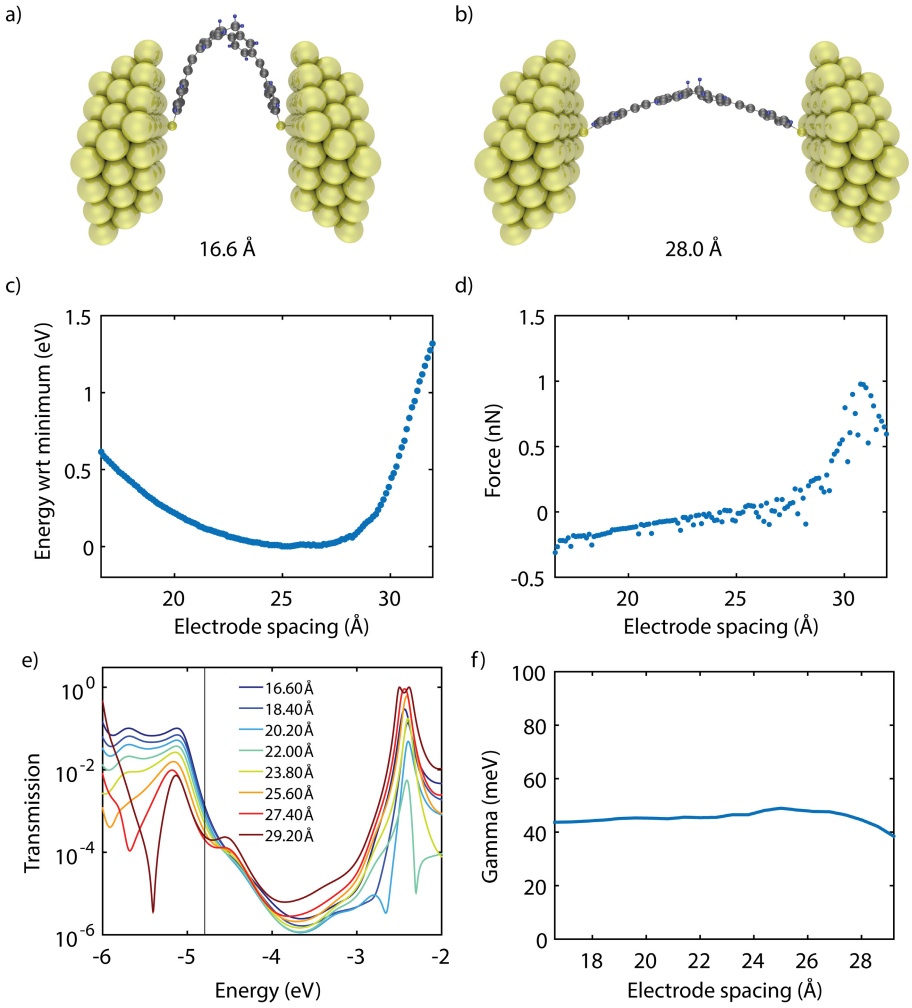

Figure 7.14: **Distance dependence of Γ. a**,**b**, Two junction geometries. (**c**) Energy change during stretching. All values are with respect to the minimum in energy. (**d**) Calculated force during stretching. (**e**) Transmission for various distances (**f**) Estimation of Γ for various distances.

(see Fig. 7.13d). We find that, upon bending of the molecule, τ increases for decreasing S-S distance. On the other hand, α remains almost unaffected upon bending (around 10% change).

The distance dependence of Γ is less straightforward to obtain. As an estimate, we performed DFT + NEGF calculations of the molecule connected to two gold electrodes for various distances. We used a triple-ζ plus polarization (TZP), Slater-type orbital local basis-set and the PBE GGA functional. The molecule was connected to the hollow sites of two electrodes, consisting of 3 layers of 4x4 atoms. The geometry was converged to energy changes of less than 10^{-3} hartree, energy gradients of

less than $1 \cdot 10^{-3}$ hartree/Å maximum and $6.7 \cdot 10^{-4}$ hartree/Å RMS. Starting from a bend geometry with the distance between the two inner gold layers fixed at 16.60 Å we inceased the electrode separation in steps of 0.12 Å while letting the molecule (including the S-atoms) relax.

Two junction geometries are shown in Fig. 7.14a and Fig. 7.14b. Figure 7.14c and d present the energy and force, respectively, during the strechting. The force required to bend the molecule is well below the breaking force of the gold-sulfur bond (around 1 nN), which occurs at 30.5 Å.

Figure 7.14e presents the transmission upon increase of the electrode separation using wide band limit electrodes coupled to the most outer gold layer. To estimate Γ, we extracted the peak width of the HOMO and HOMO-1 by fitting it with a Lorentzian. However, as the peak is not symmetric, we used the right side of the peak only. The estimated Γ is shown in Fig. 7.14f. We find that Γ remains fairly constant. This can be understood from the fact that AH is a flexible molecule. It can easily bend, and therefore the S-Au does not significantly change upon bending.

From the calculations we find that Γ and α, remain fairly constant upon bending of the molecule. τ, on the other hand, is strongly affected. The change in τ may be the origin of the gradual decrease of the junction conductance for increasing electrode separation.

ASYMMETRIC MOLECULES : RECTIFICATION

As mentioned previously, introducing an asymmetry in the molecule can shift the two sites apart, significantly changing the behaviour of the device. For example, if at zero bias the left site is higher in energy than the right site (see Fig. 7.15a), a negative bias voltage will only pull them further apart. They will therefore never be on resonance and the current remains low. At positive bias, on the other hand, they move into resonance, increasing the current until the bias is so large that they are pulled off resonance again, resulting in a peak in the current. This difference in behaviour at positive and negative bias means that such a junction functions works as a rectifier, where, in this case, the left site acts as a donor and the right as an acceptor. To confirm this rectifying concept, we performed DFT + NEGF calculations on an asymmetric AH derivative (see Fig. 7.15b), in which three of the hydrogen atoms on the right side of the dihydro-anthacene core have been replaced with electronegative cyano groups. The HOMO and HOMO-1 (see Fig. 7.15c) are located on the left and right side of the molecule respectively, with a zero-bias energy difference of 445 meV. Figure 7.15d shows the calculated IV characteristic of the asymmetric molecule, clearly displaying diode-like behavior with a rectification ratio of almost 400.

The calculations were performed using the same settings as in section A.2.2. The bias voltage is applied by introducing a uniform electric field along the axis connecting the sulphur atoms. Transmissions are calculated by coupling the p_z-orbitals of the sulphur atoms to wide-band electrodes with a coupling strength of 100 meV. The HOMO is taken to be resonant with the Fermi energy. The maximum current occurs at 0.89 V. This about twice the energy splitting between the HOMO and HOMO-1 as about half of the voltage drop occurs in the molecule.

The device performance (operating voltage and rectification ratio) can be increased even more by tuning the model parameters ϵ_L,ϵ_R, Γ an τ. In general, the operating voltage is directly proportional to the energy difference between the two sites at

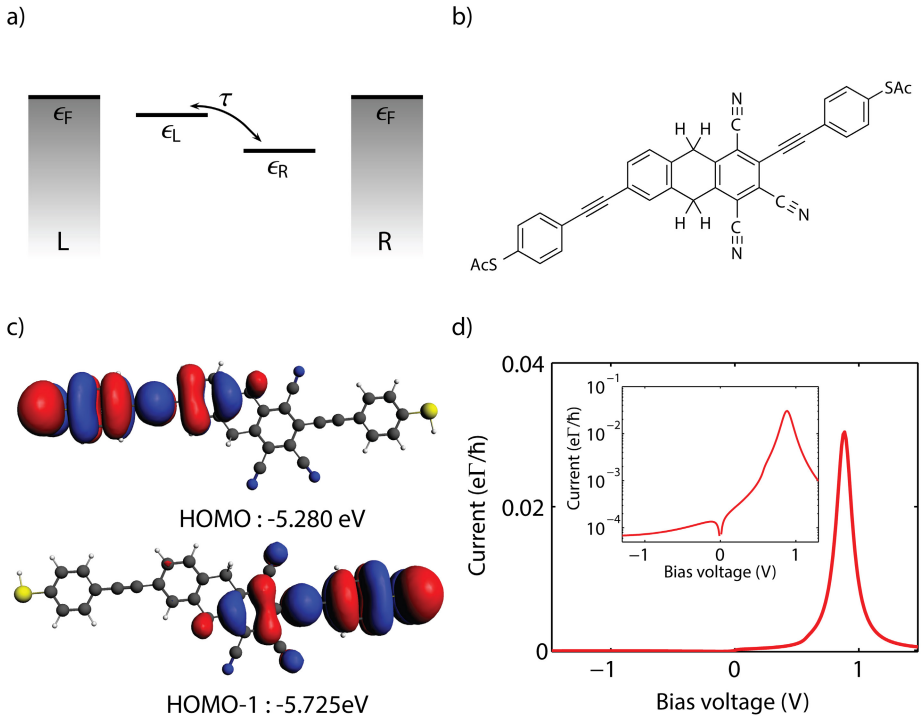

Figure 7.15: **Design for a single-molecule rectifier. a**, Two-site diagram in which the right site has a lower energy than the left one. **b**, Modified AH molecule, in which three of the hydrogen atoms on the right side of the anthracene core have been replaced by cyano groups. **c**, HOMO and HOMO-1 of the molecule in **b**, located on the left and right side of the molecule, respectively. The addition of the cyano groups has introduced an asymmetry in the wave functions and increased the energy difference between the two orbitals to 445 meV. At zero bias, the HOMO acts as a donor and the HOMO-1 as an acceptor, making this junction device a rectifier. **d**, IV characteristic of the molecule in **b** calculated using DFT+NEGF plotted on a linear scale (main) and logarithmic scale (inset).

zero bias, and can be tuned by adding electronegative/electropositive groups to the AH core. The rectification ratio is dependent on Γ and τ. We found that, the smaller Γ, the larger the rectification ratio is. The same holds for τ, the smaller the coupling between the halves of the molecule, the larger the rectification ratio. By keeping this in mind, molecules with much higher rectification ratios can be designed.

A.3. MOLECULAR DYNAMICS

SIMULATION DETAILS

Molecular dynamics (MD) simulations were performed to understand the mechanical behavior of the molecules during the extension and contraction of the junction. These simulations were based on the classical MM3[227] force field as implemented in the Tinker package[228]. The parameters describing the gold atoms, the gold-sulfur bond and the gold-sulfur-carbon bending angle were adapted from the reactive force field ReaxFF[229]. The dihedral force constants involving gold atoms were all set to zero. Additionally, the dihedral force constant of the rotation around a sp_2-

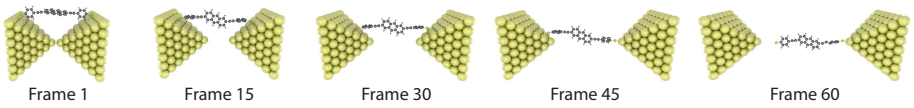

Figure 7.16: **Breaking process on AC using molecular dynamics simulations.** The figure shows a few frames obtained during breaking.

sp_3 carbon bond have been modified such that the bending energy of AH obtained with the classical force field was comparable with the one obtained from DFT calculations.

During the extension simulation, the molecule was initially anchored in a bridge site between two gold atoms. The electrodes were then taken apart in steps of 0.5 Å and the geometry of the molecule was fully relaxed. During this energy minimization, the gold atoms were fixed at their positions. A partially reactive approach was then adopted to simulate the hopping of the molecule between different anchoring sites. At each elongation step the mechanical stress of the molecule was computed as its total potential energy in its current conformation in the junction minus its fully relaxed one. If this stress energy was larger than a given threshold, a conformational search was performed. During this search, different anchoring sites, located in the vicinity of the current one, were considered. The molecule was then sequentially anchored to each potential new site and its geometry was then relaxed. The geometry leading to the lowest potential energy was then kept in the following simulation steps. At the exception of the last anchoring site located on top of the end atom of each electrode, only bridge anchoring sites were considered during the conformational search. The threshold stress energy required to change the anchoring of the molecule was consequently set to the energy barrier between two bridge anchoring sites, for which we used 0.19 eV[230], minus the thermal energy at room temperature. If no suitable anchoring sites were found during the search, and if the stress energy was larger than the binding energy of the molecule to the gold atoms, i.e. 1.0 eV for a top-site[230], the molecule was detached from one electrode.

The simulations of the contraction of the junction were performed in a similar fashion, bringing the electrodes closer to each other at each simulation step. Compared to a full DFT calculation of the mechanical elongation of the junction[231],

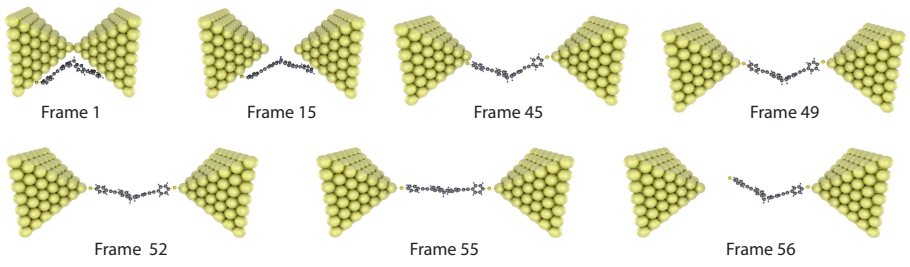

Figure 7.17: **Breaking process on AH using molecular dynamics simulations.** The figure shows a few frames obtained during breaking.

the method outlined above is computationally inexpensive and can therefore be employed to statistically sample the behavior of the molecule in the junction.

RESULTS

We performed molecular dynamics (MD) simulations for both molecules. Figure 7.16 shows five frames of the breaking process of a junction containing AC. The frames show that AC remains planar during the breaking process.

Figure 7.17 presents a breaking trace on AH. In contrast to AC, AH bends and the conformation of the molecule in the junction will adapt itself to variations in the electrode distance. It also shows a gradual evolution from a bent geometry to a more planar configuration for larger separations (frames 45–55).

8

A SINGLE-MOLECULE RESONANT TUNNELING DIODE

A THEORETICAL PROPOSAL

Rectification has been at the foundation of molecular electronics. Most single-molecule diodes realized expimentally so far are based on asymmetries in the coupling with the electrodes or using the donor-acceptor principle. In general, however, their rectification ratios are usually small (<10). Here, we propose a single-molecule diode based on an orbital resonance, while using the highest occupied molecular orbital (HOMO) and HOMO-1 as transport channels. Our proposed diode design is based on an asymmetric two-site model, and analyzed with DFT + NEGF calculations. We find high rectification ratios, even in the case of symmetric coupling to the electrodes. In addition, we show that diode parameters such as the operating voltage and the rectification ratio can be tuned by chemical design.

Parts of this chapter have been published in Journal of Physical Chemistry C, **119**, 5697–5702 (2015) [115].

1. INTRODUCTION

The molecular diode is the seminal device which started the field of single-molecule electronics[1] , with the original design inspired by semi-conducting pn-junctions. As one side of the molecule was electron rich and the other electron poor, one current direction was favored above the other. Since that proposal, other theoretical predictions and models have been proposed based on other mechanisms such as asymmetric tunneling barriers[232, 233] or asymmetric charging[234]. From an experimental point of view, rectification ratios (current ratio between the forward and reverse bias) as high as 100 have been reported in measurements on self-assembled monolayers[235]. On the single-molecule scale, however, this figure of merit has not exceeded 10, whether rectification was based on asymmetries in the coupling to the electrodes[67, 70], quantum interference[68], or the donor-acceptor principle[30, 62, 224, 236].

In this paper, we present a design for single-molecule diodes based on orbital resonances and demonstrate that this mechanism leads to large rectification ratios. Using density functional theory (DFT) and the non-equilibrium Green's function (NEGF) formalism, we investigate how different electron withdrawing and donating substituents alter the current voltage characteristics. Finally, we demonstrate that for an appropriate choice of substituents, unprecedented rectification ratios above 1000 may be achieved.

The diode mechanism we propose is based on intra-molecular coherent resonant transport, in contrast to the Aviram-Ratner rectifier[1], where charge transport is vibrationally assisted. We use a molecule that consists of two conjugated parts that are coupled together through a non-conjugated linker. Due to the non-conjugated linker, the molecule can be seen as two weakly-coupled sites in series. In such a system, resonant transport occurs only when the energy of the two sites is equal. A similar concept has been used recently to generate negative differential conductance (NDC) in a single-molecule junction[34]. The origin of the NDC is explained as follows: at zero bias, the two sites were at equal energy and resonant charge transport occurred. By applying a bias voltage, the energy of the sites were shifted apart, and the resonance condition was lifted, thereby suppr'essing transport.

When an asymmetry is introduced in such a molecular structure, for instance by adding electron withdrawing or donating groups on one side, the energy of the sites becomes different, and the resonance condition between the two halves of the molecule can then only be reached by shifting the energy of the sites with respect to each other. This shift can be achieved for instance by using Stark shifts induced by a bias voltage. However, as the resonant condition can only be reached for a particular bias polarity, the anti-symmetry of the current-voltage characteristics is lifted, and the molecule behaves as a diode.

The diode mechanism is schematically depicted in Fig. 8.1. At zero bias (see Fig. 8.1a), the left site is at energy ϵ_1, while the right one is at ϵ_2. As the zero-bias energy splitting (ϵ_1 - ϵ_2) is non-zero, this leads to a low zero-bias conductance. In the model, $\Gamma_{L,R}$ accounts for the electronic coupling of the left (L) and right (R) site to the corresponding electrode. Upon application of a positive bias, the two sites

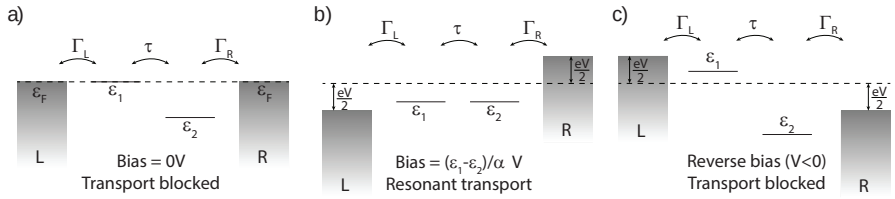

Figure 8.1: **Diode mechanism.** Schematics illustrating charge transport in an asymmetric molecule in the case of (**a**) zero bias, (**b**) forward bias on resonance, (**c**) reverse bias. $\epsilon_{1,2}$ are the on-site energies, τ the inter-site coupling, and α the fraction of the voltage that drops inside the molecule.

are pulled towards each other as a result of a bias-induced Stark Shift, until they reach a resonant condition at a bias voltage of $V_p = (\epsilon_1 - \epsilon_2)/\alpha$, where α describes the fraction of the voltage that drops inside the molecule. It is important to realize that the voltage drop inside the molecule is essential for the rectification mechanism. Upon approaching the resonance condition, the conductance drastically increases (see Fig. 8.1b). For larger bias, the sites are pulled off-resonance again, and the conductance decreases. Therefore, a peak in the current at a bias voltage of V_p is expected. For negative bias, the sites are increasingly pulled away from each other, and the conductance remains low for all voltages (see Fig. 8.1c).

The transport properties of such an asymmetric two-site system can be described using the following Hamiltonian

$$\boldsymbol{H} = \begin{pmatrix} \epsilon_1 + \frac{1}{2}\alpha eV & -\tau \\ -\tau & \epsilon_2 - \frac{1}{2}\alpha eV \end{pmatrix}. \tag{8.1}$$

The eigenstates of this Hamiltonian correspond to the bonding (π) and antibonding (π^*) orbitals where their energy splitting Δ in the presence of a bias voltage is given by

$$\Delta = \sqrt{(\alpha eV)^2 + 2\alpha eV(\epsilon_1 - \epsilon_2) + (\epsilon_1 - \epsilon_2)^2 + (2\tau)^2}. \tag{8.2}$$

We now symmetrically couple the left and right sites to the corresponding leads in the wide-band limit[225, 226]:

$$\boldsymbol{\Gamma}_{\mathrm{L}} = \begin{pmatrix} \Gamma & 0 \\ 0 & 0 \end{pmatrix}, \qquad \boldsymbol{\Gamma}_{\mathrm{R}} = \begin{pmatrix} 0 & 0 \\ 0 & \Gamma \end{pmatrix}. \tag{8.3}$$

The transmission is given by[199, 225, 226]

$$\mathscr{T}(\epsilon) = \mathrm{Tr}\left\{\boldsymbol{\Gamma}_{\mathrm{L}} \boldsymbol{G}^r(\epsilon) \boldsymbol{\Gamma}_{\mathrm{R}} \boldsymbol{G}^a(\epsilon)\right\}, \tag{8.4}$$

where $\boldsymbol{G}^r(\epsilon)$ and $\boldsymbol{G}^a(\epsilon)$ are the retarded and advanced Green's functions, respectively. The former is given by

$$\boldsymbol{G}^r(\epsilon) = \left(\epsilon \mathbf{1} - \boldsymbol{H} + \frac{\mathrm{i}}{2}(\boldsymbol{\Gamma}_{\mathrm{L}} + \boldsymbol{\Gamma}_{\mathrm{R}})\right)^{-1}, \tag{8.5}$$

while $\boldsymbol{G}^a(\epsilon) = \boldsymbol{G}^r(\epsilon)^\dagger$. The current can be calculated via[199, 225, 226]

$$I = \frac{2e}{\hbar}\int \frac{\mathrm{d}\epsilon}{2\pi}\big(f_\mathrm{L}(\epsilon) - f_\mathrm{R}(\epsilon)\big)\mathcal{T}(\epsilon), \tag{8.6}$$

where $f_\mathrm{L}(\epsilon)$ and $f_\mathrm{R}(\epsilon)$ are the Fermi functions of the left and right lead, respectively.

2. DESIGN GUIDELINES

As noted above, charge transport through a molecule consisting of two conjugated parts that are weakly coupled should follow the behavior of the two-site model described above (see discussion Fig. 8.1). The weak coupling between sites can for example be realized either by introducing a twisted biphenyl moiety[61, 63] or a saturated (Csp^3) carbon chain[1]. The former method has the drawback that the degree of conjugation (and thus the conductance) throughout the molecule strongly depends on the torsion angle between the phenyl rings. As a result, the inter-site coupling τ may vary as well, rendering the diode performance very sensitive to the molecular conformation. When using the latter method, one has to keep in mind that the more saturated carbon atoms are connected in series to form the non-conjugated segment, the lower τ becomes. Although this increases the rectification ratio (see section A.2), the decrease in τ is accompanied by a decrease in the maximum elastic current flowing through the molecule down to a negligible value, where only inelastic contributions to the current remain[1]. Another way to create a weak coupling is to use cross-conjugation[55, 93].

Next to the formation of two weakly-coupled halves, the molecule should fulfill additional requirements. We now list some of them. First, transport through the molecule should be dominated by the HOMO and HOMO-1, as their splitting can be tuned more easily compared to for instance the HOMO and LUMO. This can be achieved by using a symmetric backbone in combination with a weak inter-site coupling. This promotes the formation of bonding/anti-bonding orbitals for the HOMO-1 and HOMO, which are closely located in energy and can be used for transport. Second, the molecule should not be too large, to prevent the HOMO-2 and lower lying orbitals from being located so close to the HOMO and HOMO-1 that they also significantly contribute to transport. In that case, the two-site approximation ceases to hold and a parallel transport channel opens up. Third, a proper choice for the anchoring groups has to be made. Next to determining the electronic coupling and the level alignment[71], they also influence how the voltage drops inside the molecule (see section A.3). In addition, the anchoring groups also modify the wave function of the HOMO and HOMO-1 and hence the inter-site coupling τ. Fourth, electron withdrawing/donating groups need to be added to the molecule in an asymmetric way, such that one of the halves is lowered or shifted up in energy. Finally, as we will show in the following, the HOMO should be located as close as possible to the Fermi energy for the highest rectification ratio.

Taking all the above-mentioned considerations into account, we choose molecules which are comparable in chemical structure to the one used by Perrin *et al.* [34], and with comparable values for α and τ. To break the conjugation, we use diphenylethane (see Fig. 8.2a), to which phenylethynyl spacers are connected[237].

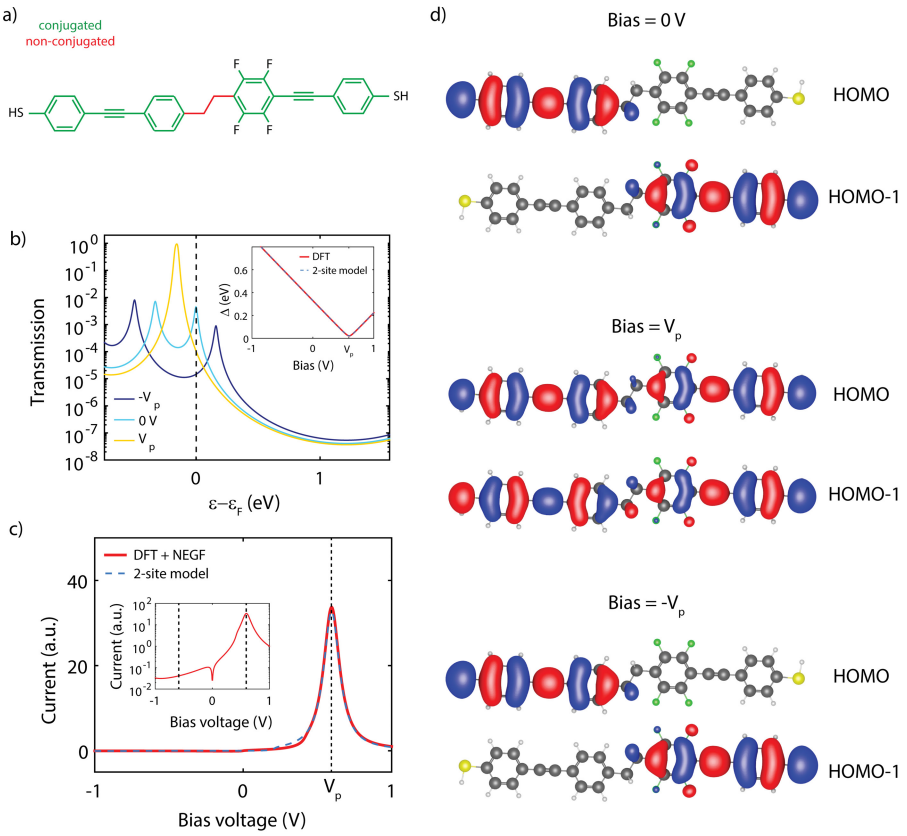

Figure 8.2: **DFT + NEGF calculation on proposed diode molecule.** (**a**) Chemical structure of 1,2-bis(4-(phenylethynyl)phenyl)ethane. In green the conjugated parts of the molecule, in red the non-conjugated ones. (**b**) Transmission for various bias voltages. The dashed line indicates the assumed position of the Fermi energy. The inset shows the energy difference between the HOMO and HOMO-1 (Δ) as a function of bias voltage. The fit parameters are α=0.55, τ=10.9 meV and $\epsilon_1 - \epsilon_2$=329 meV. (**c**) IV characteristic calculated using DFT + NEGF (solid red, Γ=100 meV) and using the two-site model (dashed blue, Γ=29.0 meV.). (**d**) HOMO and HOMO-1 in case of a bias voltage of (upper panel) 0 V, (center panel) V_p and (lower panel) $-V_p$.

Thiols are used as anchoring group, as they favor holes transport[78]. For the symmetric, unsubstituted molecule we find that transport can indead be modeled as two-sites in series, and that a pronounced NDC feature arises, see section A.1. The asymmetry in the molecule is initially introduced by adding four fluorine atoms to the right half of the molecule.

3. RESULTS

To investigate the electronic structure of the molecule, density functional theory (DFT) calculations were performed. Transmissions were calculated from DFT within the non-equilibrium Green's function (NEGF) framework by coupling the p_z-orbitals of the sulfur atoms to wide-band electrodes[34, 238] with a coupling strength of

100 meV. A bias voltage was applied to the molecule by introducing a uniform electric field along the axis connecting the sulfur atoms.

In Fig. 8.2b the transmission through the molecule is plotted. For now, we assume that at zero bias the HOMO is on resonance with the Fermi energy E_F. The HOMO-1 is in this case located 0.33 eV below it. The amplitudes of the transmission peaks corresponding to the HOMO and HOMO-1 resonances are less than $1 \cdot 10^{-2} G_0$. The HOMO-2 (located more than 1 eV away) and the lowest unoccupied molecular orbital (LUMO, 2.3 eV above E_F) are too far from the Fermi energy and do not contribute to transport. The upper panel of Fig. 8.2d shows the HOMO and HOMO-1 at zero bias, each of which is localized on one half of the molecule. Due to their localized character, their transmission remains low, which is reflected in the current-voltage characteristic (IV) plotted in Fig. 8.2c. Upon application of a bias, the HOMO and HOMO-1 shift due to the Stark effect. The inset of Fig. 8.2b displays the energy splitting of the HOMO and HOMO-1, denoted as Δ, accompanied by a fit to equation 8.2, from which the two-site model parameters α, τ and $\epsilon_1 - \epsilon_2$ are obtained. For an increasing positive bias, Δ initially decreases linearly until it reaches a minimum at V_p, which is located at 0.59 V. At V_p, the HOMO and HOMO-1 are delocalized (see the center panel of Fig. 8.2d), and fully extended across the entire molecule. This delocalization causes the amplitude of the resonances to increase to unity. The transmission shows a single resonance, as the HOMO and HOMO-1 are nearly degenerate, with $\Delta << \Gamma_{L,R}$. The current also increases and shows a maximum at V_p. When increasing the bias beyond V_p, Δ increases and the amplitude of the transmission decreases, resulting in a decrease of the current. For negative bias, the orbitals remain localized and Δ increases linearly with bias voltage. As the amplitude of the transmission resonances stays below $1 \cdot 10^{-2} G_0$, the current remains low.

The DFT + NEGF calculation show that this molecule behaves as a diode. Important characteristics of this rectifier are the peak voltage (V_p), and the current ratio between forward and reverse bias. As definition for the rectification ratio (RR), we use the ratio between the current at V_p and -V_p. For the molecule of Fig. 8.1a we obtain RR = 820. Using the values for α, τ and $\epsilon_1 - \epsilon_2$ obtained in the inset of Fig. 8.2b, we can calculate the current-voltage characteristic predicted by the two-site model using expression 8.6, as illustrated by the blue dashed line. The two-site model reproduces the DFT + NEGF calculation well, indicating the two-site model can be used to describe the molecule.

To investigate the role of the side groups on RR and V_p, we calculated the electronic structure and IV-characteristics for nine different functional groups, (CH_3, H, OCH_3, Br, Cl, CF_3, NO_2, CN). We varied the side groups of both halves of the molecule, resulting in 45 different molecules (see Fig. 8.3a). For each molecule we extracted RR and V_p, assuming the HOMO to be on resonance with the Fermi energy at V=0. Figure 8.3b shows a matrix for the 45 different molecule, with the color scale representing V_p. The side groups have been sorted as a function of V_p with on the left side hydrogen atoms (R^1=H), see the highlighted row. On the diagonal, the molecules are symmetric and NDC is observed. As one moves away from the diagonal, the molecule behaves as a rectifier and the absolute value of the peak voltage increases. The matrix is anti-symmetric, as swapping the left and right side groups leads to the same peak at opposite voltage. In Fig. 8.3c, V_p is plotted as a function of the energy

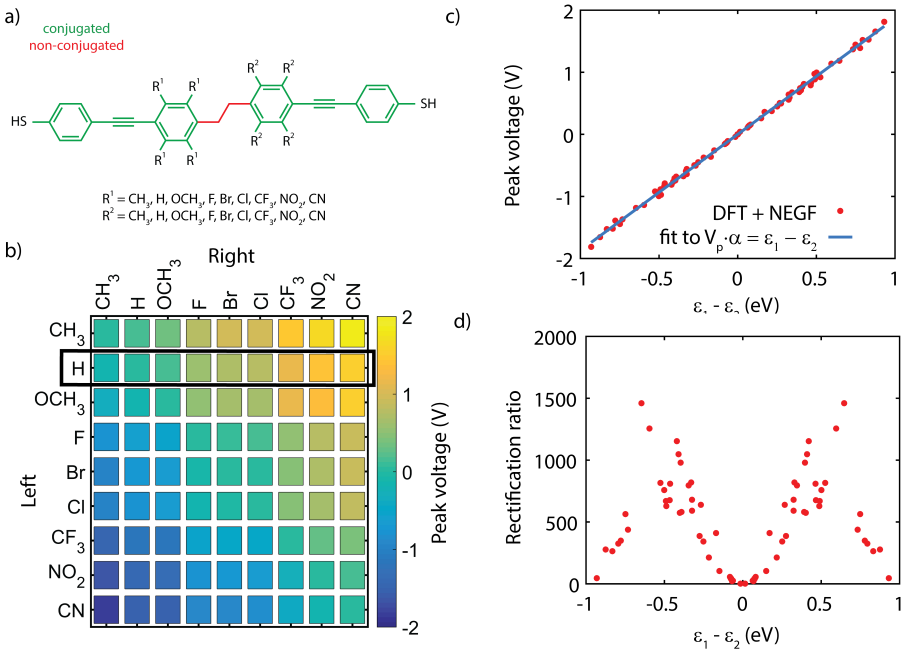

Figure 8.3: **DFT + NEGF calculation upon variation of the functional groups.** (**a**) Chemical structure of all the molecules calculated. In green the conjugated halves of the molecule, in red the non-conjugated segment. (**b**) Peak voltage of all the 45 combinations of molecules. (**c**) Peak voltage as a function of level splitting ϵ_1 - ϵ_2 (red dots). The blue line is a fit to extract the value of α, which is 0.53. (**d**) Rectification ratio as a function of level splitting ϵ_1 - ϵ_2.

splitting. The peak voltage V_p scales linearly with ϵ_1 - ϵ_2. By linearly fitting the data, we obtain a value for α of 0.53. The fact that α is very similar for all the combination of side-groups indicates that α is related to the backbone, and/or the anchoring groups, and not to the side-groups. In addition, the total level splitting obtained when combining two side-groups is close to the sum of the energy splitting of the individual side-groups, *i.e.* one can estimate within 50 meV (see section A.5 for more details) the splitting of a combination of side-groups by adding the level splittings obtained from the highlighted row. The fact that one can simply add the individual level splitting is due to the weak coupling between the two halves of the molecule. In section A.6, we show that in fact the level splitting scales linearly with the Hammett constant.

In Fig. 8.3d, RR is plotted as a function of ϵ_1 - ϵ_2. RR is low for small ϵ_1 - ϵ_2, and increases to a maximum of about 1500 at an energy splitting of around 0.6 eV. For larger splitting, RR decreases again. This trend can be understood as follows. For low energy splitting, the tail of the transmissions of the two sites feel each other, leading to a relatively high reverse bias current, and hence a low RR. Increasing ϵ_1 - ϵ_2 up to 0.6 eV reduces this parasitic current in reverse bias mode, and hence improves RR. For ϵ_1 - ϵ_2 larger than 0.6 eV, however, additional orbitals start to come into play, increasing the reverse current and reducing RR.

In the previous analysis, we took the HOMO to be on resonance with the Fermi energy. From a theoretical point-of view, predicting the exact location of the Fermi energy is very difficult. In Fig. 8.4 we show the diode characteristics for increasing level misalignment between the HOMO and ϵ_F. Figure 8.4a and Fig. 8.4b present the I(V)-characteristics for various level alignments. In Fig. 8.4c and Fig. 8.4d RR and the peak voltage are given. Both remain fairly constant within 150 meV at a value of about 800 and 0.6 V, respectively. For misalignments beyond this bias voltage, RR quickly decays and reaches the value 10 at around 400 meV. The peak voltage, on the other hand, nearly linearly increases up to 0.95 V. For conjugated, thiol-anchored molecular wires, the location of the HOMO is reported to be within 0.5 eV below the Fermi energy[57]. Due to sample-to-sample variation of the level alignment, RR can therefore vary from below 10 to above 100. To realize high rectification ratios in experiments, the use of an electrostatic[21, 43, 56, 81] or chemical gate[69, 136] to control the position of the occupied levels with respect to the Fermi energy may be necessary. Next to variations in the level alignment, different molecular geometries may occur during experiments, leading to variations in τ and Γ, and hence variations in RR.

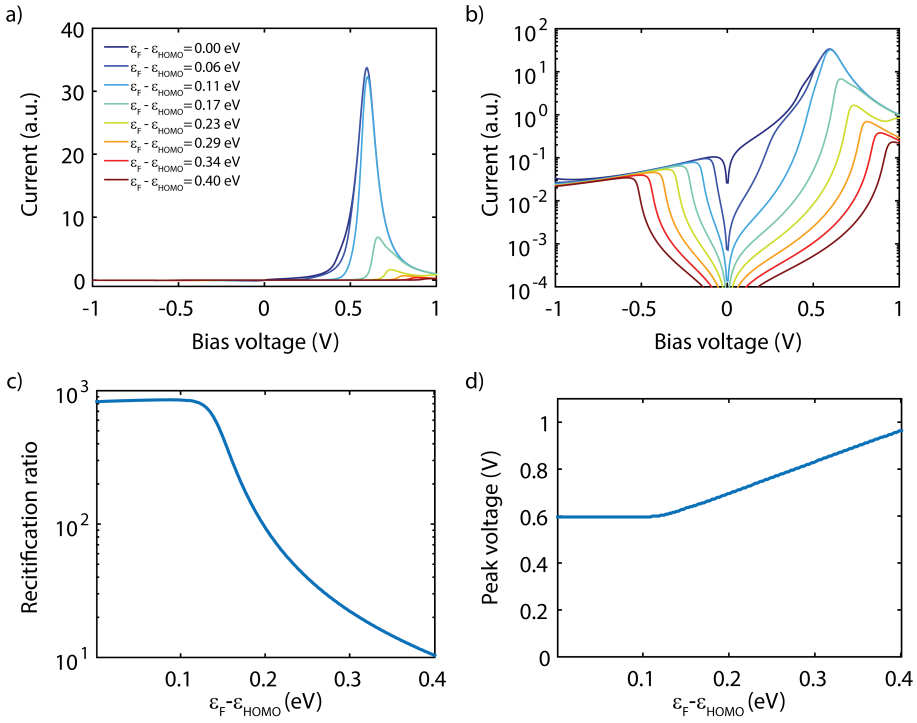

Figure 8.4: **Dependence of diode characteristics on level alignment.** I(V)-characteristics calculated using DFT + NEGF for various level alignment shown on (**a**) linear scale and (**b**) logarithmic scale. (**c**) Rectification ratio and (**d**) peak voltage dependence on the level alignment.

4. DISCUSSION

We would like to emphasize that the fact that the peak voltage can be tuned from milliVolts to Volts is due to the symmetry of the backbone of the unsubstituted molecule. This symmetry is crucial as it yields a HOMO-1 and HOMO that are nearly degenerate and with bonding/anti-bonding character. The splitting between the two orbitals can then easily be changed by introducing electron donating/withdrawing groups and allows for fine tuning of the diode properties.

In the DFT + NEGF calculations, the charge is injected into the p_z-orbtials of the sulphur atoms. Although the π-orbitals constitute the largest contribution to the current through the molecule[238], this approach underestimates the contribution of the σ-orbitals and, hence, slightly overestimates the RR.

In our analysis, we used nine side-groups. In fact, many more could be used, as long as they have electron withdrawing/donating properties. However, one has to make sure that the HOMO and HOMO-1 of the resulting molecule are the ones originating from the two-site structure and yielding rectification. Some substituents, such as OH, COOH, NH_2 and $C(CH_3)_3$, have a HOMO and/or HOMO-1 which is located on the side-groups only and does not contribute to transport. Such substituents are not suited, as one has first to depopulate the localized HOMO and/or the HOMO-1 in order to align the orbitals yielding the rectification with the Fermi energy.

Finally, we note that RR can be improved further by tweaking Γ and τ. As a rule of thumb, the lower Γ and τ, the higher RR becomes (see section II and IV of the Supporting Information), but also the lower the maximum current. RR can be further improved using molecules with the orbitals further apart, thereby reducing the current in reverse bias mode. Another way to suppress the current in reverse bias mode may be to use destructive quantum interference[92]. Other approaches, such as asymmetries in the anchoring groups could also be envisioned.

8

5. CONCLUSION

In conclusion, we discussed the design of a single-molecule resonant tunneling diode of which the operation is based on an intuitive two-site model. The proposed molecule consists of two weakly coupled molecular halves and allows to generate high rectification ratios. Using DFT + NEGF calculations, we explore the different model parameters and relate them to the chemical structure of the molecule. We find that, due to the weak coupling between the two halves of the molecule, the peak voltage and rectification ratio can be tuned by chemically modifying the molecule. Our findings provide design guide-lines for highly efficient single-molecule rectifiers.

A. APPENDIX

A.1. SYMMETRIC MOLECULE

The basis of the diode molecule presented in Fig. 8.2 is the two-site model reported by Perrin *et al.*[34], which was utilized to generate pronounced negative differential conductance (NDC) in a single molecule. Here we introduced an asymmetry in the site energy to obtain rectification. To verify that the molecule designed indeed behaves as two sites in series, we performed additional DFT + NEGF on the symmetric molecule, *i.e.*, with only hydrogen as functional groups. The results are presented in Fig. 8.5. Figure 8.5a shows the chemical structure of the molecule. In Fig. 8.5b we present the localized molecular orbitals, which are obtain by performing a ba-

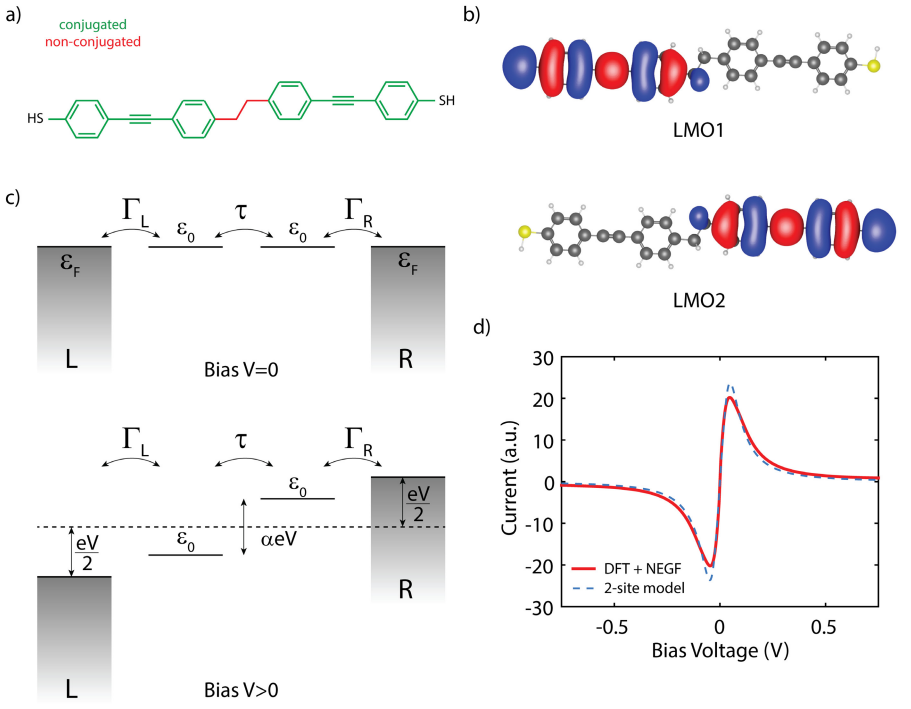

Figure 8.5: **Symmetric molecule.** (**a**) Chemical structure of 1,2-bis(4-(phenylethynyl)phenyl)ethane. In green the conjugated parts of the molecule, in red the non-conjugated ones. In contrast to the molecule shown in Fig. 8.2, this molecule is symmetric. (**b**) The left and right localized molecular orbital obtained by taking the sum and the difference of the HOMO and HOMO-1. (**c**) Since the LMOs are each located on one side of the molecule, the junction can be modelled by two sites, left and right, coupled by $\tau = 16.4$ meV. The sites are coupled to the leads by Γ. In the strong-coupling regime ($\Gamma > \tau$), transport through the molecule is coherent. Due to the symmetry of the molecule, the two sites, at ϵ_L and ϵ_R, are in resonance at zero bias (upper panel), and the conductance is high. Upon application of a bias (lower panel), the sites are pulled off resonance by αeV, where α is the fraction of the voltage drop occurring inside the molecule. Although τ does not change significantly as a function of bias voltage, the off-resonance condition leads to a reduction of the elastic transport through the molecule, lowering the conductance of the junction. (**d**) Calculated IV characteristic using DFT + NEGF in red. The dashed blue line is a fit to the analytical expression for the two-site model. The fit parameters are τ=16.4 meV , α=0.53 and Γ=19.7 meV

sis transformation from the molecular orbitals basis to the left/right site basis. Each LMO is located on one halve of the molecule, as expected for a two-site system. Figure 8.5c illustrates schematically the two-site model. At zero bias, the site are at the same energy ϵ_0. The sites are coupled to each other by τ, and to the left and right lead by Γ_L and Γ_R, respectively. The sites are on resonance and the conductance is high. Upon application of a bias a fraction α of the applied voltage drops inside the molecule, pulling the two sites apart. This level shift lifts the resonance condition and causes the conductance to drop for increasing voltage. Figure 8.5d presents an I(V)-characteristic (red line) calculated using DFT + NEGF on the molecule of Fig. 8.5a. Here, a pronounced NDC is observed. The I(V)-characteristic can be fitted to the analytical expression of the two-site model (see dashed blue line), and reproduces well the DFT + NEGF calculation.

A.2. INCREASING BRIDGE LENGTH

Here, we choose as a weak coupling between the two halves of the molecule 2 saturated carbon atoms, as this yields a value for τ which is similar to the one reported by Perrin *et al.*[34]. In Fig. 8.6 we explore the role of the number of saturated carbon atoms. We varied the number of saturated carbon atoms from 0 to 3, see Fig. 8.6a for the molecular geometries. In Fig. 8.6b the dependence of τ is plotted, which shows a significant decrease of τ upon increases up the number of saturated carbon atom. The rectification ratio, on the other hand, increases drastically, as is visible in Fig. 8.6c. Previous experimental reports[30, 224] have not exceed RR of 10. This can

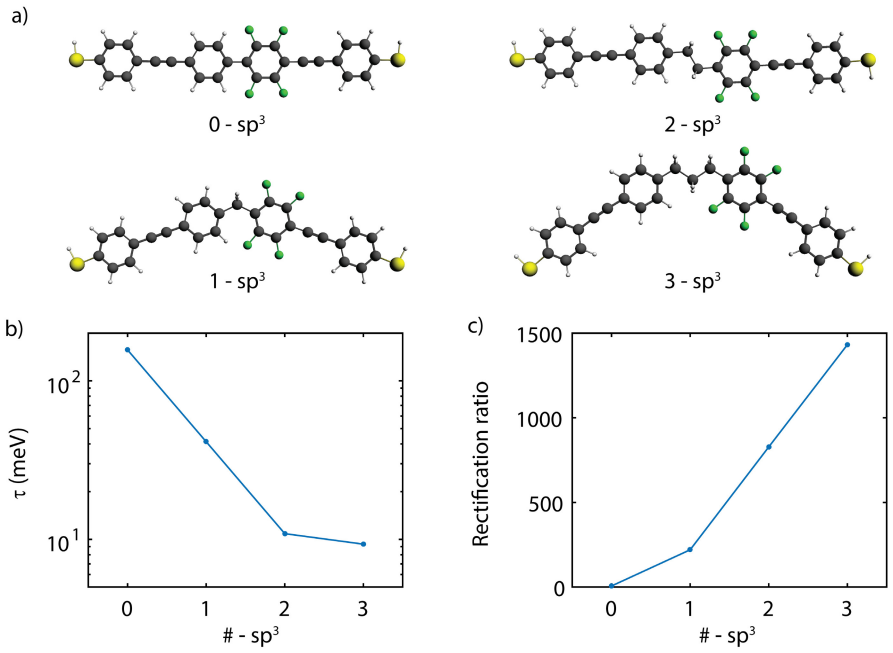

Figure 8.6: **DFT + NEGF calculations for increasing length non-conjugated segment.** (**a**) Molecular geometries. (**b**) Value of τ and (**c**) RR for an increasing number of Csp^3-atoms.

be understood considering the fact that the molecules used in such experiments had no Csp^3 atoms, yielding a high values for τ and hence a low RR.

A.3. A DIFFERENT ANCHORING GROUP

In Fig. 8.3c, we see that the value of α is mostly unaffected by the addition of functional groups to the molecule. To investigate the role of the anchoring groups in the voltage drop, we calculated the peak voltage, rectification ratio and the level splitting for the same combination of functional groups as in Fig. 8.3, but without the thiols anchoring groups. The current is now injected directly into the p_z orbitals of the outer most carbon atoms. Figure 8.7a presents the chemical structure of the molecule. Figure 8.7b shows the peak voltage. In Fig. 8.7c we show the relation between the peak voltage and the level splitting. Here, as in Fig. 8.3, the peak voltage scales linearly with the level splitting. By linearly fitting the data points, we obtain a value for α of 0.42. This is lower than the 0.53 reported previously for the thiol anchored molecule, suggesting the anchoring groups influence the voltage drop inside the molecule. Figure 8.7d shows RR as a function of level splitting. Here a similar trend is found as in Fig. 8.3. RR starts low for low splitting and increases for increasing splitting, and reaches a maximum of about 1500 around 0.5eV. For large splittings, RR

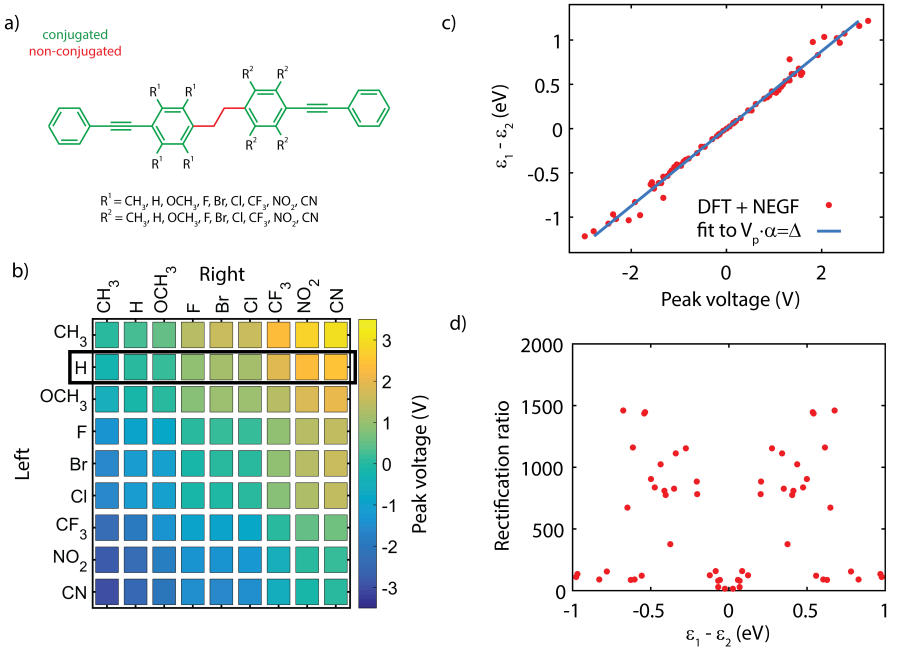

Figure 8.7: **DFT + NEGF calculations for benzene anchoring groups.** (**a**) Chemical structure of all the molecules calculated. In green the conjugated halves of the molecule, in red the non-conjugated segment. In contrast to the molecule shown in Fig. 8.2, this molecule has no thiol anchoring group. (**b**), Peak voltage of all the 100 combinations of molecules. (**c**), Peak voltage as a function of level splitting ϵ_1 - ϵ_2 (red dots). The blue line is a fit to extract the value of α, which is 0.42. (**d**), Rectification ratio as a function of level splitting ϵ_1 - ϵ_2.

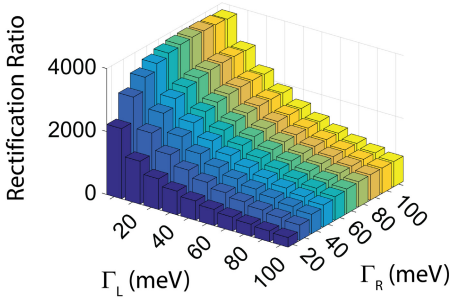

Figure 8.8: **Recification ratio for varying electronic coupling to the left (Γ_L) and right contact (Γ_R).**

decreases again. Hence, RR is mostly determined by the level splitting. Next to that, the peak voltage can be varied by using different anchoring groups.

A.4. Γ VARIATION

Until now, we chose for the DFT + NEGF calculation a fixed value of Γ_L and Γ_R of 100 meV. Here, we investigate the influence of those two couplings on the rectification ratio. Figure 8.8 presents RR for varying values of Γ_L and Γ_R. Upon a symmetric decrease of Γ_L and Γ_R, RR increases from about 800 from 100 meV to about 2200 for 10 meV. When applying a asymmetry in the electronic coupling, RR can enhanced even further in the case of $\Gamma_L < \Gamma_R$ or reduced for $\Gamma_L > \Gamma_R$.

A.5. ERROR ESTIMATING LEVEL SPLITTING $\epsilon_1 - \epsilon_2$

Here, we investigate how accurately the level splitting $\epsilon_1 - \epsilon_2$ of two different side groups can be estimated based on the level splitting of the groups individually. Figure 8.9a shows the molecule with on one side hydrogren atoms, and the other side the functional groups. For those 10 molecules, we obtain the level splittings shown in Fig. 8.9b. We then compare the sum of the individual level splittings with the ones obtained from DFT for all combinations of side groups. Figure 8.9c shows the difference between the two. For most groups the error remains within 20 meV and only a few reach not more than 50 meV.

A.6. HAMMETT CONSTANT

Figure 8.10 presents the Hammett constant (σ_{para}) versus the level splitting ϵ_1 - ϵ_2. The Hammett constant[239] is a chemical constant which describes the reaction rates of aromatic reactants with different subsituents. As all rate are compared to hydrogen, an aromatic moiety with hydrogen atoms has by definition a σ_{para} of zero. The reaction rates, in turn, determine whether substituents are electron-withdrawing, of electron-donating. Electronegative substituents have a positive value of σ_{para}), while electropositive substituents have a negative value. Figure 8.10 shows that the level splitting scales nicely linear with the Hammett constant, supporting the fact that the shift in the energy of the halves of the molecule is indeed caused by the electronegative/electropositive character of the substituents.

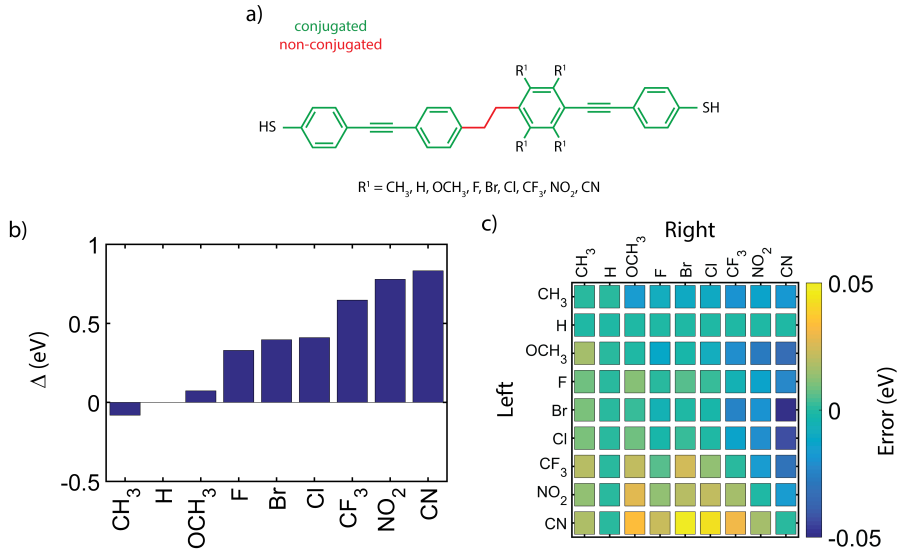

Figure 8.9: **Error estimation for level splitting ϵ_1 - ϵ_2.** (**a**) Chemical structure of the molecules with on the left side hydrogen atoms only. (**b**) Level splitting induced by all the side-groups. (**c**) Energy difference between the sum of the level splittings shown in (b) and the results obtained from DFT.

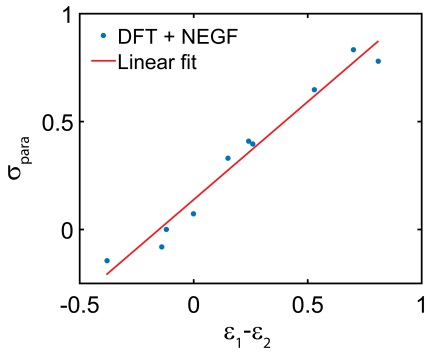

Figure 8.10: **Level splitting ϵ_1 - ϵ_2 as a function of the Hammett constant σ_{para}.** The blue dots are otained from the DFT + NEGF calcuations. The red line presents a linear fit, from which a slope of 0.91 is obtained.

9

A GATE-TUNABLE SINGLE-MOLECULE DIODE WITH HIGH RECTIFICATION RATIOS

In the pursuit of down-sizing electronic components, the ultimate limit is the use of single molecules as functional devices. The first theoretical proposal of such a device is the seminal Aviram-Ratner rectifier that was predicted more than four decades ago. However, the experimental realization of single-molecule rectifiers has proven to be challenging and the devices performances, in particular the rectification ratios, are usually rather poor. In this work, we report on the experimental realization of a new mechanism for rectification in single molecules devices, with unprecedented rectification ratios as high as 600. The mechanism is based on intra-molecular resonant transport and relies on the presence of two conjugated molecular halves that are weakly coupled through a saturated linker. Moreover, in our devices, the presence of a gate electrode allows for tuning of the rectification ratio. The observed gate dependence demonstrates that the proposed rectification mechanism is operative in the molecule.

Parts of this chapter are part of a forthcoming publication.

1. INTRODUCTION

The theoretical design of the first molecular rectifier marked the birth of the field of single-molecule electronics[1]. Since that proposal, many other mechanisms leading to rectification have been explored[12, 232–234]. However, due to experimental limitations, it was not until 2005 that the first single-molecule rectifier was realized[30], albeit with a low rectification ratio (RR) of 10. Since then, many more realizations have been proposed and realized [62, 67, 68, 70, 224, 236], most of them possessing relatively poor rectifying properties (RR≤10). Here, we report on single-molecule devices with a built-in rectification mechanism displaying rectification ratios as high as 600. The molecular junctions are formed employing the mechanically controllable break junction technique[18, 19, 124], using both two-terminal and three-terminal devices. Charge transport through the molecule can be understood from a two-site model, the use of which is supported by quantum chemistry calculations. A unique feature of the measurements presented here is the addition of a gate electrode. Using this gate electrode, the alignment of the electronic levels that are responsible for transport can be altered[115, 130], leading to an enhancement of the rectification ratio.

The molecule used in our study is "DPE-2F", of which the chemical structure is shown in Fig. 9.1a. The molecule consists of two conjugated parts, connected by an saturated ethane bridge that breaks the conjugation. An asymmetry is introduced by two fluorine atoms that are located on one of the phenyl rings, both in the ortho position with respect to the ethane group. The molecule has thiols as anchoring units for coupling to metallic electrodes. Figure 9.1b presents the energy diagram of the molecule, with the energy of the fluorine-containing part lowered by the electron withdrawing character of the fluorine substituents.

2. RESULTS ON TWO-TERMINAL DEVICES

Figure 9.1c shows a current-voltage (IV) characteristic (solid blue line) calculated for DPE-2F using density functional theory (DFT) combined with the non-equilibrium Green's function (NEGF) formalism (see section A.1 for more details). As the energy of the sites is different at zero bias, the current is low. For positive bias, the sites are pulled towards each other and the current increases. At 0.55 V, a pronounced peak is visible. This is the point where the two sites have equal energy and resonant transport occurs. For higher voltages, the sites are pulled off resonance again and the current decreases. For reverse bias, conversely, the Stark shift causes the sites to be increasingly pulled apart. They therefore never align (see lower left panel of Fig. 9.1c) and the current remains low. As current can only go through the molecule for a particular bias polarity, the molecule behaves as a rectifier. The figures of merit for a diode are the operating voltage (OP) and the rectification ratio (RR). As a definition for RR, we use the maximum ratio between the forward and reverse current. For the curve in Fig. 9.1c, this yields a RR of 751 and an operating voltage of 0.55 V.

Figure 9.2a presents an IV characteristic recorded on a sample exposed to DPE-2F. The IV is highly asymmetric, with a peak in the current around -1.15 V. For the same IV, Fig. 9.2b shows the ratio between the forward and reverse current as a function of bias voltage. From this figure, we infer an experimental RR of 519, extracted at an operating voltage of -0.98 V. The forward current is 64.07 nA, while the reverse current

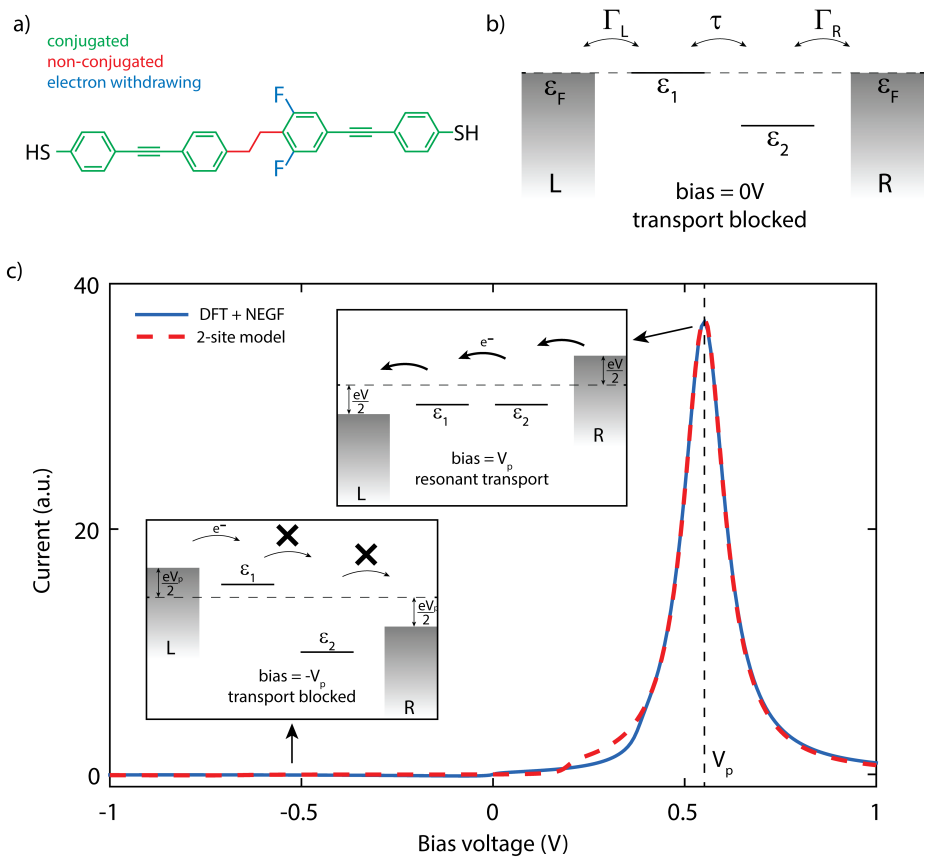

Figure 9.1: **Molecule and diode mechanism.** Chemical structure (**a**) of the DPEdT-2F molecule and its energy diagram (**b**), with the right half being lower in energy than the left one due to the electron withdrawing character of the fluorine substituents. (**c**) Current-voltage characteristic calculated using DFT + NEGF (solid blue, electronic coupling $\Gamma_{L,R}$ = 100 meV) and using the analytical expression for the two-site model (dashed red, electronic coupling $\Gamma_{L,R}$ = 25.8 meV.) The parameters ϵ_L, ϵ_R and τ are obtained from the DFT calculations, and are equal to 0 meV, 299 meV and 11.9 meV, respectively. The good agreement between the two calculated curves indicates that charge transport through the molecule can indeed be described using two sites only, which form a delocalized bonding/anti-bonding HOMO/HOMO-1 (see section A.1 of the appendix). Although in this calculation the peak is at positive bias, in the experiments, the orientation of the molecule cannot be controlled and therefore the peak in the current can be expected both at positive and negative bias voltages.

is only 0.12 nA.

Figure 9.2c shows the evolution of the IV's for a different junction upon a change of 0.9 nm in electrode displacement. Four IV's, recorded while increasing the inter-electrode spacing, are shown. The distance change is with respect to d_0, which is the initial electrode separation after trapping of the molecule. Importantly, the IVs are highly asymmetric with a large onset of the current around +1 V. This rectifying behavior is robust and remains present for displacements close to a nanometer. Figure 9.2d presents the RR and OP during the evolution of this junction. As the voltage range does not reach the peak voltage, the RR is calculated at the voltage where

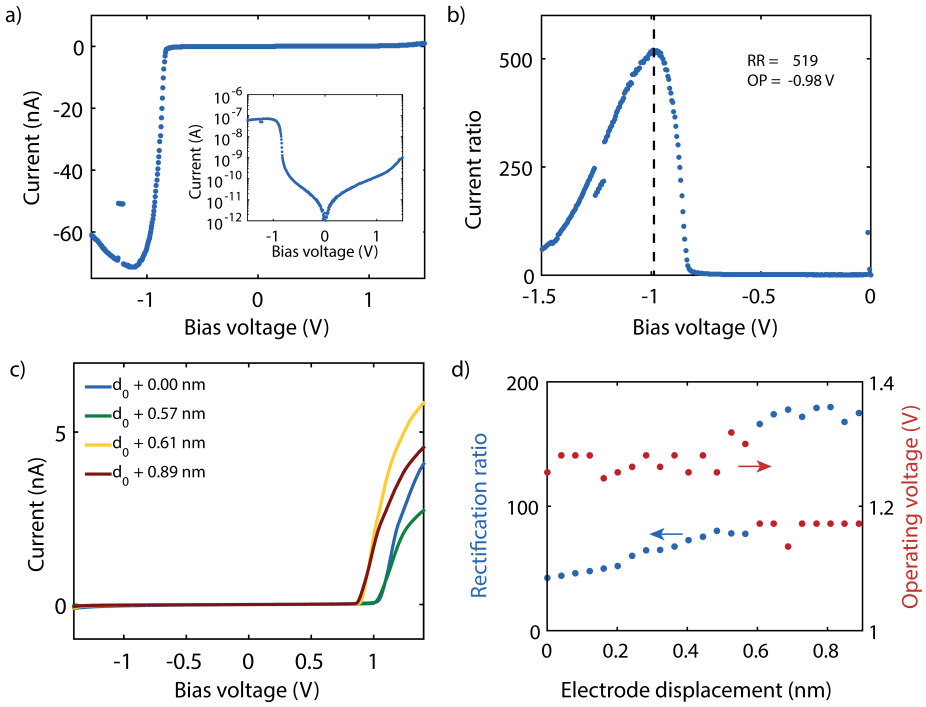

Figure 9.2: **Experimental results obtained on the DPEdT-2F molecule.** (**a**) Current-voltage (IV) characteristic recorded on a junction exposed to DPE-2F on a linear scale. The inset shows the same IV on a logarithmic scale. (**b**) Current ratio (|I(V)/I(-V)|) as a function of bias. The dashed vertical line indicates the operating voltage. (**c**) IVs of a different junction recorded while increasing the electrode separation. (**d**) Rectification ratio (blue) of the junction shown in (c) and operating voltage (red) during the stretching of the junction.

|I(V)/I(-V)| is the largest. This voltage defines OP and it varies between 1.25 V and 1.30 V. The RR starts around 50 and initially rises to 75 at 0.56 nm. At a displacement of 0.60 nm, the OP drops sharply below 1.2 V. The abruptness of the change suggests that this is due to a change in the molecular conformation. The onset of the current also shifts to a voltage closer to zero. Both observations indicate that the molecular level comes closer to the Fermi energy. At the same time, the RR increases to around 175. In the following, we will show experimentally how the level alignment and the RR can be shifted in a controlled fashion by using a gate electrode.

3. RESULTS ON THREE-TERMINAL DEVICES

To gain more insight in the role of the level alignment, we investigate charge transport through DPE-2F using three-terminal MCBJ devices[56, 82, 129, 240]. The presence of the third 'gate' electrode allows to tune the electrostatic potential of the molecule, thereby changing the alignment of the molecular levels responsible for transport with respect to the Fermi energy of the electrodes[241]. To achieve this, the gate electrode needs to be located close to the molecule, but electrically insulated from the source/drain and the molecule[115]. The design of the devices is based on pre-

vious work[129]. Colorized scanning electron micrographs of a device are shown in Fig. 9.3a and Fig. 9.3b. In the graphs, the suspended gate/gate oxide/source-drain sandwich is clearly visible. For more details about the fabrication and the characterization of the devices, we refer to Chapter 3.

The influence of the gate electrode on the charge transport has been investigated by recording IVs at various gate voltages. Figure 9.3c presents three IVs for different gate voltages. The IVs are highly asymmetric, with an appreciable current only flowing for positive bias. To emphasize the difference between the forward and reverse bias, the IVs are plotted on a logarithmic scale. The inset shows the high bias part of the same IVs curves on a linear scale. For increasing gate voltage, the onset of the current moves towards a higher bias voltage, while the maximum current decreases. A map of the current as a function of bias and gate voltage is presented in Fig. 9.3d. The bright areas correspond to areas of high current. The onset of the current shifts towards lower bias for increasingly more negative gate voltage. From this shift, the gate coupling is determined to be about 16 mV/V.

In Fig. 9.4a, the RR of the sample in Fig. 9.3c is shown as a function of gate voltage. The RR is strongly gate tunable: it starts at 280 at a gate voltage of -5 V and gradually decays to 100 while ramping the gate voltage up to 4 V. Figure 9.4b show the gate

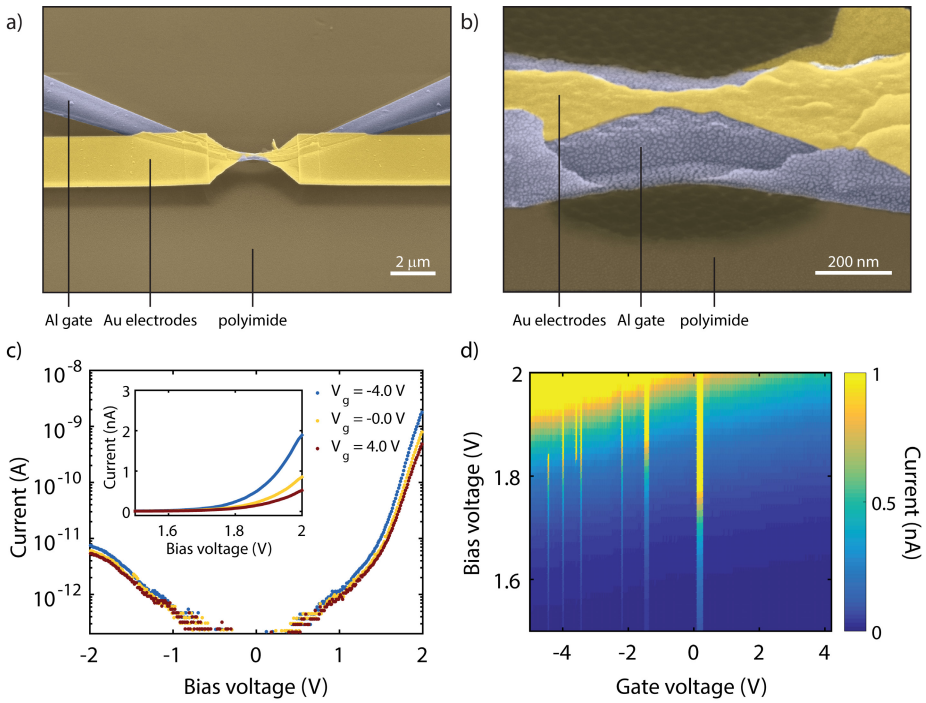

Figure 9.3: **Gate tunability of the diode.** (**a**,**b**) False-color scanning electron micrograph of an unbroken three-terminal MCBJ device taken at two different magnifications. (**c**) IV characteristics recorded at 6 K on a device exposed to DPE-2F. The three IVs are obtained at different gate voltages and plotted on a logarithmic scale in the main figure, and on a linear scale in the inset. (**d**) Color-coded map of the current as a function of bias and gate voltage.

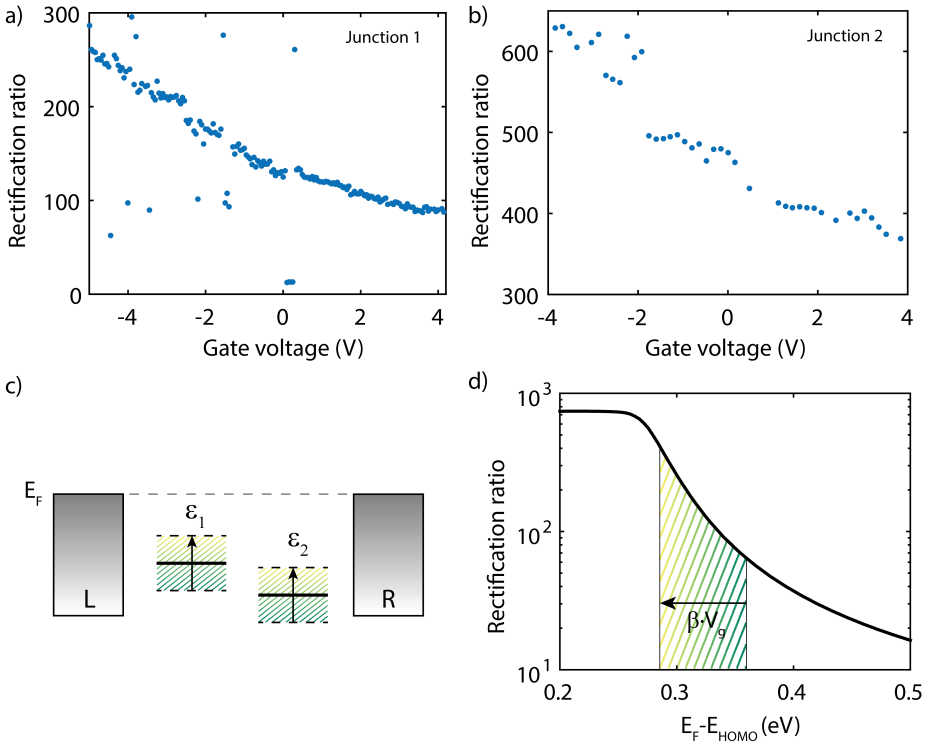

Figure 9.4: **Influence of level alignment for the two-level model.** (**a**) RR versus gate for the junction shown in Fig. 9.3c and Fig. 9.3d. (**b**) RR versus gate voltage for a different junction; for a detailed characterization of this junction we refer to section A.2. (**c**) Schematic of the two-level model, illustrating the level shifts with increasing gate voltage. (**d**) RR calucalted with DFT used to illustrate the effect of applying a positive gate voltage. The hatched area corresponds to the experimentally accessible gate range. We note that the values are for illustrative purposes; we do not claim quantitative correspondence with the experiments.

voltage dependence of the RR for a different junction. Here, the RR can be tuned from 400 at zero gate voltage to above 600 for a negative gate voltage of -4 V.

4. DISCUSSION

The main observations from the three-terminal measurements are that in all eight junctions in whch gate dependence has been studied, the levels move out for positive gate voltage, indicating HOMO-mediated charge transport and that the RR increases when applying a negative gate voltage. The observation of HOMO-mediated transport is consistent with DFT calculations[242]. The change in the RR can be understood considering the change in level alignment induced by the gate, as shown in Figure 9.4c. As previously[242] shown, the RR is the largest when the HOMO is on resonance with the Fermi energy, and decreases for an increasing level misalignment. Conversely, when the sites are not on resonance with the Fermi energy, a highering of the HOMO is predicted to increase the RR significantly. This trend is illustrated in Fig. 9.4d. The RR is plotted as a function of level alignment. Applying a negative volt-

age on the gate moves the HOMO up, towards the Fermi energy, thereby increasing the RR, in agreement with the measurements.

It is important to note that the gate tunability of the RR is opposite to the one expected for a molecule of which transport is dominated by a single HOMO level close to the Fermi energy. In that case, the RR increases when the level is pulled away from the Fermi energy. In section C, we demonstrate that this trend holds across a large range of electronic couplings, even for asymmetries up to a factor 100.

We finally note that we also recorded IVs on junctions exposed to the symmetric DPE, as reference. This molecule has the same molecular backbone as DPE-2F, but without the fluorine substituents. For this molecule, we do not observe the very high RR's observed for DPE-2F. Instead, the molecule exhibits negative differential conductance, symmetrically located in bias, as expected for this molecule (see section 9.7). Upon application of a positive gate voltage, the NDC features shifts towards higher bias voltage. These trends agree with HOMO-mediated transport and the fact that the molecule can be described using two sites[34].

5. CONCLUSION

In conclusion, we measured the DPE-2F molecule using the MCBJ technique. We observed high RRs of more than 500, which can be understood from the internal molecular structure, corroborated by quantum chemistry calculations. The rectifying properties of the molecule persisted upon changes in electrode displacement up to 0.9 nm. We employed electrostatically gateable MCBJ devices to demonstrate that both the RR and OP can be tuned with gate. The gate measurements furthermore show that transport involves HOMO levels and this is observation crucial to understand the increase of the RR with decreasing gate voltage within the framework of the two-site model. Our findings provide a promising approach for designing future devices with even higher RR's by optimizing the internal molecular structure. One could furthermore envision a new class of molecular devices with more than two sites in series preferably with control over the electrostatic energy of the individual sites by the use of local gates. This would allow the realization of functional devices with no inorganic semiconducting counterpart, in which, for instance, a gate terminal is used to transit from negative differential conductance behavior to rectification.

A. APPENDIX

A.1. DFT + NEGF CALCULATIONS DIODE

Density functional theory (DFT) calculations were performed using the Amsterdam Density Functional (ADF) quantum chemistry package with the GGA PBE exchange-correlation functional and the triple-ζ plus polarization (TZP) basis-set[202, 203]. Geometries were converged to energy changes of less than 10^{-3} hartree, energy gradients less than 10^{-3} hartree/Å maximum and $6.7 \cdot 10^{-4}$ hartree/Å RMS. Transmissions were calculated by coupling the p_z-orbitals of the sulphur atoms to wide-band electrodes with a coupling strength of 100 meV. A bias voltage was applied to the molecule by introducing a uniform electric field along the axis connecting the sulphur atoms.

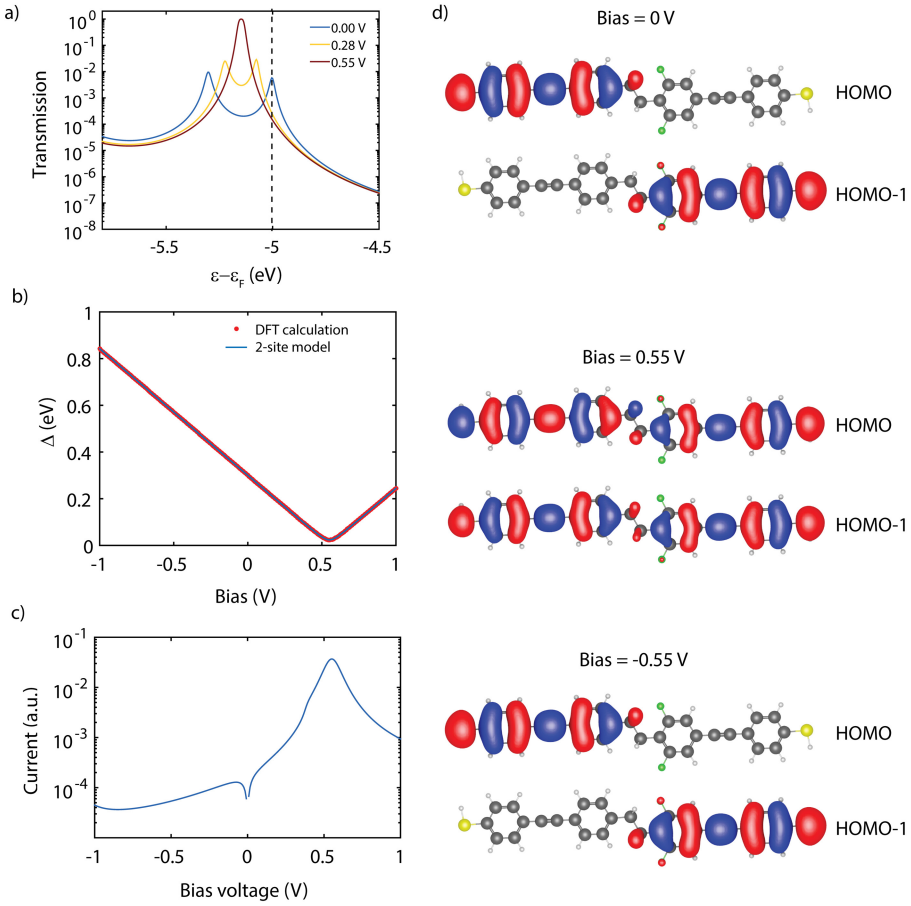

Figure 9.5: **DFT + NEGF calculations on the DPE-2F molecule** (**a**) Transmission for three different bias voltages. (**b**) Energy difference Δ between HOMO and HOMO-1 as calculated from DFT (red). The blue line represents a fit to the two-site model. For more details about the analytical expression, see previous work[242]. (**c**) Current-voltage characteristic calculated using DFT + NEGF plotted on a logarithmic scale. (**d**) Molecular orbitals at zero bias (top), 0.55 V (middle) and -0.55 V (bottom).

The Fermi energy is assumed to be on resonance with the highest occupied molecular orbital (HOMO).

Figure 9.5a shows the transmission of DPE-2F for a bias voltages of 0 V, 0.28 V and 0.55 V. At 0 V two peaks in the transmission are visible, corresponding to the HOMO and HOMO-1. They are split by 300 meV, and have a transmission amplitude of $1{\cdot}10^{-2}$. For increasing bias, the peaks increase in amplitude and move towards each other, until at 0.55 V they meet and the transmission reaches unity. The shift in level splitting is made clearer in Fig. 9.5b, where the energy splitting between the HOMO and HOMO-1 is plotted. At zero bias, it is 300 meV, and it linearly increases for negative bias. This is the reverse bias as the levels are pulled away from each other. For positive bias, the levels move towards each other and reach a minimum splitting of 23.8 meV at 0.55 V. From this value, the inter-site coupling τ can be calculated to be 16.9 meV. Beyond this voltage, the levels shift away from each other again. The blue line represents a fit of the two-site model[242], from which the model parameters τ, α, ϵ_1 and ϵ_2 can be estimated. The fit reproduces the DFT calculations well. The change in amplitude of the transmission peaks can be understood by considering the orbitals shapes (see Fig. 9.5d). For the 0 V and -0.55 V, the HOMO and HOMO-1 are localized on one side of the molecule, leading to poor transport from one sulfur atom to the other. At 0.55 V, on the other hand, the HOMO and HOMO-1 are delocalized, and considering the symmetry of the orbital weight on the sulfur atoms, the transmission goes to unity. The current through the molecule is shown on logarithmic scale in Fig. 9.5c. For zero- and negative bias voltages the current is low. It increases for positive bias voltages and reaches a maximum at 0.55 V, after which it decreases again.

As a result of the asymmetry in the current-voltage characteristic, this molecule is expected to behave as a diode, with an operating voltage and peak voltage of 0.55 V, and a rectification ratio of 751. We note that in the calculations the HOMO is assumed to be on resonance with the Fermi energy. In practice, this may not be true, yielding a lower RR.

A.2. ADDITIONAL MEASUREMENT ON DPE-2F WITH GATE

Figure 9.6 presents an additional measurement recorded with a gate sample exposed to DPE-2F. Figure 9.6a shows an IV characteristic recorded on this junction at zero gate voltage. The IV is highly asymmetric and shows a peak in the current around 1.1 V. The inset zooms in on the current peak and highlights its shift as a result of an applied gate voltage. A positive gate voltage shifts the peak towards a higher bias voltage, while a negative gate voltage does the opposite. The shift of the level with gate is consistent with HOMO-mediated charge transport, as expected for this molecule. In Figure 9.6b, a color-coded map of the differential conductance focusing on bias voltages above 0.5 V is plotted. The black area at the bottom is the low-conductance region in the IV at low bias. The onset in current shows up as the bright yellow area in the dI/dV map. The black area around 1.2 V corresponds to the position of the peak in the current, while the blue area at the highest bias corresponds to the part of the IV where the differential conductance goes negative.

While sweeping the gate from negative to positive bias, the onset of current and the current peak move outwards, as does the negative differential conductance (NDC) region. Figure 9.6c presents the peak voltage for the various gate voltages in

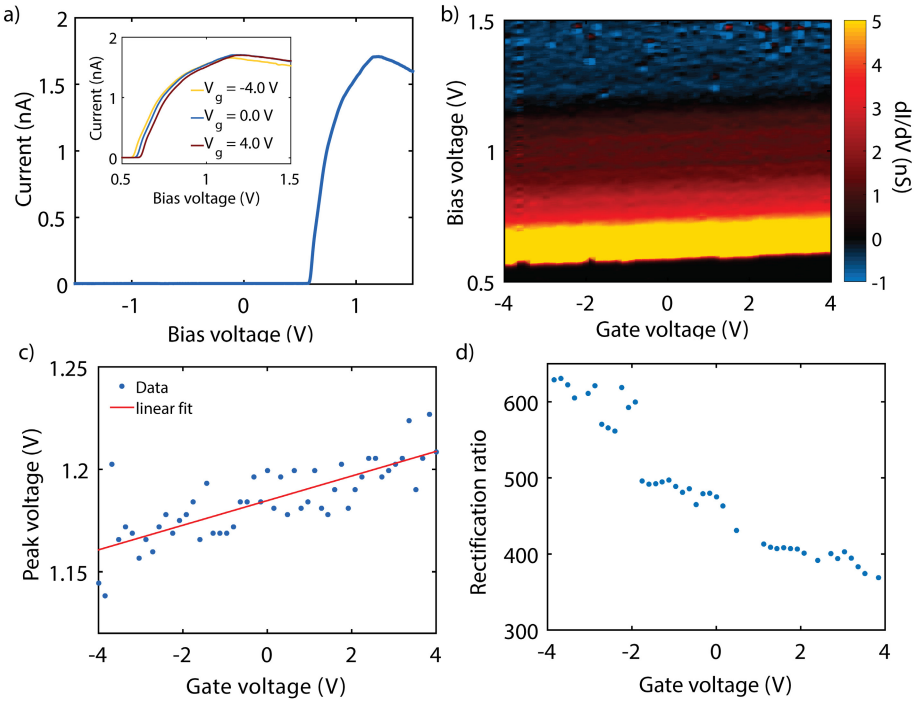

Figure 9.6: **Additional three-terminal measurements on DPE-2F.** (**a**) IV charactersitic recorded on DPE-2F at zero gate voltage. The IV is highly asymmetric, with a peak visible at positive bias. The inset shows IVs around the peak for various gate voltages. (**b**) dI/dV map as a function of bias and gate voltage. (**c**) Peak voltage versus gate voltage plot (blue dots). The red line represents a linear fit with a slope of 6 mV/V. (**d**) Current ratio obtained at the peak voltage shown in (c).

blue dots. To extract the peak shift, a linear fit (red line) is used, yielding a shift of 6 mV/V. The current ratio at the peak, see Fig. 9.6d, is around 600 for a gate voltage of -4 V and decreases steadily to around 300 while sweeping the gate voltage up.

9

B. MEASUREMENT ON DPE WITH GATE

In the main text, measurements on the asymmetric DPE-2F molecule are shown. In the case of the DPE, *i.e.*, the molecule with the same backbone but without the electron withdrawing fluorine groups, the molecule is predicted to behave as a resonant tunneling device, with distinct negative differential conductance in the IV characteristics, similar to previous work[34]. For DFT calculations on DPE, we refer to literature[242].

The chemical structure of DPE is shown in Fig. 9.7a, with the two conjugated halves marked in green and the broken conjugation in the center marked in red. As discussed in the main text, transport though DPE can be described using a model containing two sites in series, each of them corresponding to a conjugated half. For symmetry reason, the energies of the two sites are equal and correspond to ϵ_0. As for the diode, the sites are weakly coupled to each other by τ and to the left and right

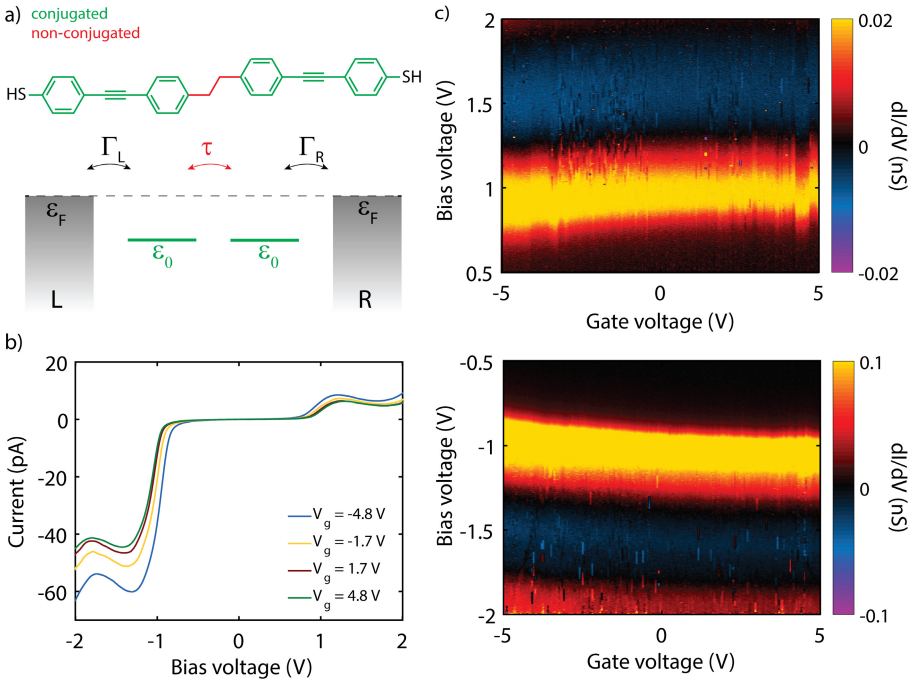

Figure 9.7: **Three-terminal measurements on DPE.** (**a**) Chemical structure of the symmetric DPE molecule, accompanied with a schematic representation of the two-site model. The two halves of the molecule are modelled as two weakly coupled sites in series. For symmetry reasons, the energy of the sites is equal. (**b**) IV charactersitics recorded on DPE for various gate voltages. (**c**) dI/dV map as a function of bias and gate voltage. The plots zoom in around the peak in the current and the NDC at positive (top) and negative (bottom) bias voltage.

lead by Γ_L and Γ_R, respectively.

Figure 9.7b presents IVs recorded on a sample with gate exposed to DPE. Four IVs are shown, obtained at different gate voltages. All IVs have a gap at low bias, and an onset in current around ±1 V. Beyond this onset, the current increases and displays a peak around ±1.2 V. This peak is followed by a decrease in current for increasing voltage, *i.e.*, they show negative differential conductance (NDC). The fact that the features in bias occur at opposite polarities is consistent with the symmetric two-site model, having the two sites at a similar energy. From the presence of a gap in the IV, we can deduce that the levels are not on resonance with the Fermi energy at zero bias[34] ($\epsilon_0 < 0$). The asymmetry in peak high is most likely due to an asymmetry in Γ.

While sweeping the gate voltage from negative to positive voltages, the gap in the IVs becomes larger. Both the peak current and its position shift towards higher bias voltages. This is more clearly visible in Fig. 9.7c, where maps of dI/dV as a function of bias and gate voltage are shown. The top panel zooms in around the peak in the current for positive bias, while the lower panel zooms in at negative bias. In both panels, the black regions at lower bias correspond to the gap, while the bright areas represent the onset of the current. For increasing bias voltage, the differential con-

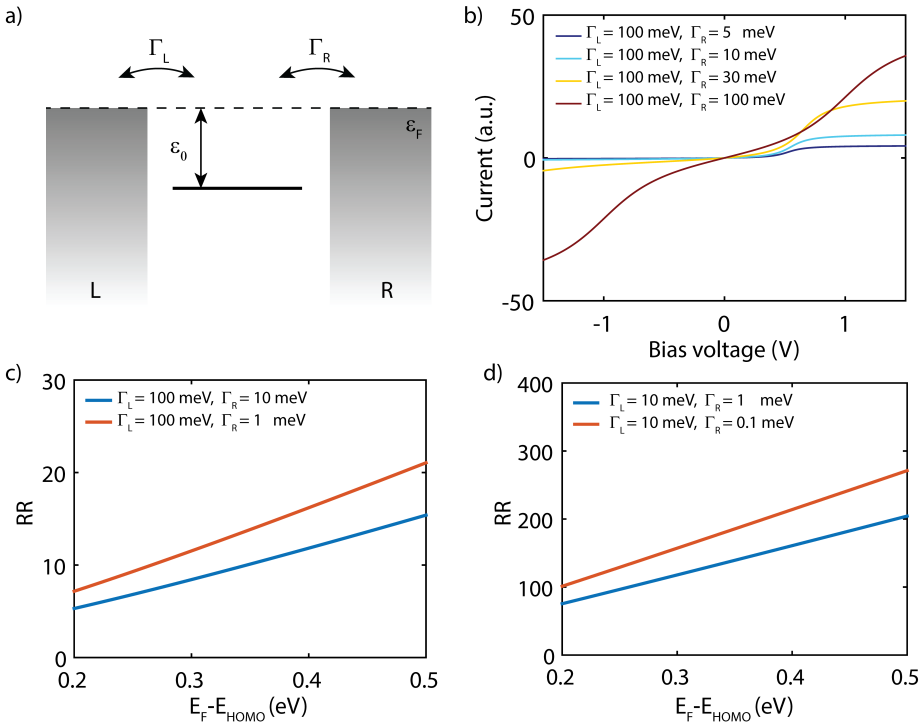

Figure 9.8: **Single-level model calculations.** (**a**) Diagram of a single level located at ϵ_0 away from the Fermi energy, coupled to the two electrodes with $\Gamma_{L,R}$. (**b**) Current-voltage characteristics for four different asymmetries between Γ_L and Γ_R, calculated using the analytical expression[57]. (**c**,**d**) Rectification ratios as a function of level alignment for two asymmetries between Γ_L and Γ_R.

ductance decreases, until it reaches a black area, corresponding to the peak in the current. Beyond this point, the NDC sets in, visible as a blue area. We note that the shift of the level with gate is consistent with HOMO-mediated charge transport, as expected for this molecule.

Next to the shift of the features (gap, peak, NDC) with gate, the current at the peak is also modulated by the gate. The closer the level is to the Fermi energy, the higher the peak current. Again, this is consistent with calculations performed previously on the same class of molecules[34].

C. SINGLE-LEVEL MODEL

We have also investigated rectification based on an alternative model containing a single-level with asymmetric coupling to the electrodes. In this model, see Fig. 9.8a, transport is described using a single level which is positioned at an energy of ϵ_0 below the Fermi energy. This level is then coupled with Γ_L and Γ_R to the left and right electrode, respectively. Transport through such a system can be calculated analytically[57].

Figure 9.8b shows IV characteristics calculated using the single-level model, with

Γ_L set to 100 meV, while varying Γ_R between 5 meV and 100 meV. ϵ_0 was set to -0.5 eV, assuming HOMO-mediated transport, as the three-terminal measurements indicate. Figure 9.8c presents the extracted RR for an asymmetry of 10 and 100 between Γ_L and Γ_R for level alignments varying between -0.5 eV and -0.2 eV. At -0.5 eV, RR is around 21 for an asymmetry of 100 and around 15 for an asymmetry of 10. For both asymmetries, the RR decreases monotonously when the level is moved towards the Fermi energy, as indicated in Fig. 9.8c. Figure 9.8d presents the same plot as Fig. 9.8c, but with Γ_L = 10 meV.

Importantly, across a wide range of electronic couplings, the single-level model predicts an increase of RR when shifting the level away from the Fermi energy. This is in contrast with the experiments and the two-level model, in which RR is the highest when on resonance with the Fermi energy[242] and decreases when the level is moved away from it.

D. JUNCTION STATISTICS

We measured a total of 4172 junctions. The histogram of the measured RR is presented in Fig. 9.9. To compose this histogram, all junctions (also those without molecular features) were considered and no data selection was performed. For 317 of those junctions (about 8%) the RR is larger than 2 and for 40 junctions RR>10. The distinctive feature of this molecule is the observation of RR larger than 100, which has been found in 10 junctions.

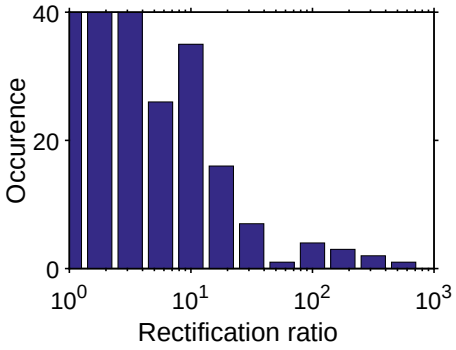

Figure 9.9: **Junction statistics.** Histogram illustrating the occurrence of the RRs.

REFERENCES

[1] A. Aviram and M. A. Ratner, *Molecular rectifiers,* Chem. Phys. Lett. **29**, 277 (1974).

[2] F. Schwierz, *Graphene transistors,* Nature Nanotechnology **5**, 487 (2010).

[3] F. L. Carter, *The molecular device computer: Point of departure for large scale cellular automata,* Physica D: Nonlinear Phenomena **10**, 175 (1984).

[4] T. S. Arrhenius, M. Blanchard-Desce, M. Dvolaitzky, J.-M. Lehn, and J. Malthete, *Molecular devices: Caroviologens as an approach to molecular wires – synthesis and incorporation into vesicle membranes,* Proc. Natl. Acad. Sci. U. S. A. **83**, 5355 (1986).

[5] K. L. Kompa and R. D. Levine, *A molecular logic gate,* Proc. Natl. Acad. Sci. U. S. A. **98**, 410 (2001).

[6] B. H. Robinson and N. C. Seeman, *The design of a biochip: a self-assembling molecular-scale memory device,* Protein Eng. **1**, 295 (1987).

[7] J. J. Hopfield, J. N. Onuchic, and D. N. Beratan, *A molecular shift register based on electron transfer,* Science **241**, 817 (1988).

[8] H. Taube, *The electron transfer between metal complexes: a retrospective,* Science **226**, 1028 (1984).

[9] C. P. Collier, E. W. Wong, M. Belohradsky, F. M. Raymo, J. F. Stoddart, P. J. Kuekes, R. S. Williams, and J. R. Heath, *Electronically configurable molecular-based logic gates,* Science **285**, 391 (1999).

[10] C. P. Collier, G. Mattersteig, E. W. Wong, Y. Luo, K. Beverly, J. Sampaio, F. M. Raymo, J. F. Stoddart, and J. R. Heath, *A [2]catenane-based solid state electronically reconfigurable switch,* Science **289**, 1172 (2000).

[11] J. Andréasson, U. Pischel, S. D. Straight, T. A. Moore, A. L. Moore, and D. Gust, *All-photonic multifunctional molecular logic device,* J. Am. Chem. Soc. **133**, 1641 (2011).

[12] R. M. Metzger, *Unimolecular electrical rectifiers,* Chem. Rev. **103**, 3803 (2003).

[13] M. A. Reed, J. Chen, A. M. Rawlett, D. W. Price, and J. M. Tour, *Molecular random access memory cell,* Appl. Phys. Lett. **78**, 3735 (2001).

[14] J. H. Burroughes, D. D. C. Bradley, A. R. Brown, R. N. Marks, K. Mackay, R. H. Friend, P. L. Burns, and A. B. Holmes, *Light-emitting diodes based on conjugated polymers,* Nature **347**, 539 (1990).

[15] G. Yu, J. Gao, J. C. Hummelen, F. Wudl, and A. J. Heeger, *Polymer photovoltaic cells: enhanced efficiencies via a network of internal donor-acceptor heterojunctions,* Science **270**, 1789 (1995).

[16] C. J. Brabec, N. S. Sariciftci, and J. C. Hummelen, *Plastic solar cells,* Adv. Funct. Mater. **11**, 15 (2001).

[17] C. Joachim, J. K. Gimzewski, R. R. Schlittler, and C. Chavy, *Electronic transparence of a single C_{60} molecule.* Phys Rev Lett. **74**, 2102 (1995).

[18] M. A. Reed, C. Zhou, C. J. Muller, T. P. Buring, and J. M. Tour, *Conductance of a molecular junction,* Science **278**, 252 (1997).

[19] J. M. Krans, J. M. van Ruitenbeek, V. V. Fisun, I. Y. Yanson, and L. J. de Jongh, *The signature of conductance quantization in metallic point contacts,* Nature **375**, 767 (1995).

[20] J. M. van Ruitenbeek, A. Alvarez, I. Piñeyro, C. Grahmann, P. Joyez, M. H. Devoret, D. Esteve, and C. Urbina, *Adjustable nanofabricated atomic size contacts,* Rev. Sci. Instrum. **67**, 108 (1996).

[21] H. Park, J. Park, A. K. L. Lim, E. H. Anderson, A. P. Alivisatos, and P. L. McEuen, *Nanomechanical oscillations in a single-C_{60} transistor,* Nature **407**, 57 (2000).

[22] D. Gerster, J. Reichert, H. Bi, J. V. Barth, S. M. Kaniber, A. W. Holleitner, I. Visoly-Fisher, S. Sergani, and I. Carmeli, *Photocurrent of a single photosynthetic protein,* Nat. Nanotechnol. **7**, 673 (2012).

[23] S. Y. Quek, M. Kamenetska, M. L. Steigerwald, H. J. Choi, S. G. Louie, M. S. Hybertsen, J. B. Neaton, and L. Venkataraman, *Mechanically controlled binary conductance switching of a single-molecule junction,* Nat. Nanotechnol. **4**, 230 (2009).

[24] Z. Li, M. Smeu, S. Afsari, Y. Xing, M. A. Ratner, and E. Borguet, *Single-molecule sensing of environmental pH an STM break junction and NEGF-DFT approach,* Angew. Chem. Int. Ed. **53**, 1098 (2013).

[25] Y. Tian, P. Navarro, and M. Orrit, *Single molecule as a local acoustic detector for mechanical oscillators,* Phys. Rev. Lett. **113**, 135505 (2014).

[26] B. Warner, F. El Hallak, H. Prüser, J. Sharp, M. Persson, A. J. Fisher, and C. F. Hirjibehedin, *Tunable magnetoresistance in an asymmetrically coupled single-molecule junction,* Nat. Nanotechnol. **10**, 259 (2015).

[27] C. Joachim and J. K. Gimzewski, *An electromechanical amplifier using a single molecule,* Chemical Physics Letters **265**, 353 (1997).

[28] D. Dulić, S. J. van der Molen, T. Kudernac, H. T. Jonkman, J. J. D. de Jong, T. N. Bowden, J. van Esch, B. L. Feringa, and B. J. van Wees, *One-way optoelectronic switching of photochromic molecules on gold,* Phys. Rev. Lett. **91**, 207402 (2003).

[29] Y. Kim, T. J. Hellmuth, D. Sysoiev, F. Pauly, T. Pietsch, J. Wolf, A. Erbe, T. Huhn, U. Groth, U. E. Steiner, and E. Scheer, *Charge transport characteristics of diarylethene photoswitching single-molecule junctions,* Nano Lett. **12**, 3736 (2012).

[30] M. Elbing, R. Ochs, M. Koentopp, M. Fischer, C. von Hanisch, F. Weigend, F. Evers, H. B. Weber, and M. Mayor, *A single-molecule diode,* Proc. Natl. Acad. Sci. U.S.A. **102**, 8815 (2005).

[31] M. Baghernejad, X. Zhao, K. B. Ørns, M. Füeg, P. Moreno-García, A. V. Rudnev, V. Kaliginedi, S. Vesztergom, C. Huang, W. Hong, P. Broekmann, T. Wandlowski, K. S. Thygesen, and M. R. Bryce, *Electrochemical control of single-molecule conductance by fermi-level tuning and conjugation switching,* J. Am. Chem. Soc. **136**, 17922 (2014).

[32] J. S. Meisner, M. Kamenetska, M. Krikorian, M. L. Steigerwald, L. Venkataraman, and C. Nuckolls, *A single-molecule potentiometer,* Nano Lett. **11**, 1575 (2011).

[33] X. H. Qiu, G. V. Nazin, and W. Ho, *Vibrationally resolved fluorescence excited with submolecular precision,* Science **299**, 542 (2003).

[34] M. L. Perrin, R. Frisenda, M. Koole, J. S. Seldenthuis, J. A. Celis Gil, H. Valkenier, J. C. Hummelen, N. Renaud, F. C. Grozema, J. M. Thijssen, D. Dulić, and H. S. J. van der Zant, *Large negative differential conductance in single-molecule break junctions,* Nat. Nanotechnol. **9**, 830 (2014).

[35] R. Vincent, S. Klyatskaya, M. Ruben, W. Wernsdorfer, and F. Balestro, *Electronic read-out of a single nuclear spin using a molecular spin transistor,* Nature **488**, 357 (2012).

[36] S. Thiele, F. Balestro, R. Ballou, S. Klyatskaya, M. Ruben, and W. Wernsdorfer, *Electrically driven nuclear spin resonance in single-molecule magnets,* Science **344**, 6188 (2014).

[37] H. Nejoh, *Incremental charging of a molecule at room-temperature using the scanning tunneling microscope,* Nature **353**, 640 (1991).

[38] E. Di Fabrizio, L. Grella, M. Gentili, M. Baciocchi, Mastrogiacomo, and P. Morales, *Fabrication of 5 nm resolution electrodes for molecular devices by means of electron beam lithography,* Jpn. J. Appl. Phys **36**, L70 (1997).

[39] A. F. Morpurgo, C. M. Marcus, and D. B. Robinson, *Controlled fabrication of metallic electrodes with atomic separation,* Appl. Phys. Lett. **74**, 2084 (1999).

[40] H. Park, A. K. L. Lim, A. P. Alivisatos, J. Park, and P. L. McEuen, *Fabrication of metallic electrodes with nanometer separation by electromigration,* Appl. Phys. Lett. **75**, 301 (1999).

[41] T. Nagase, T. T. Kubota, and S. Mashiko, *Fabrication of nano-gap electrodes for measuring electrical properties of organic molecules using a focused ion beam,* Thin Solid Films **438**, 374 (2003).

[42] Q. Qing, P. G. Chen, F. andLi, W. H. Tang, Z. Y. Wu, and Z. Liu, *Finely tuning metallic nanogap size with electrodeposition by utilizing high-frequency impedance in feedback,* Angew. Chem. Int. Ed. **44**, 7771 (2005).

[43] S. Kubatkin, A. Danilov, M. Hjort, J. Cornil, J. L. Bredas, N. Stuhr-Hansen, P. Hedegard, and T. Bjornholm, *Single-electron transistor of a single organic molecule with access to several redox states,* Nature **425**, 698 (2003).

[44] D. J. Wold and C. D. Frisbie, *Formation of metal-molecule-metal tunnel junctions: Microcontacts to alkanethiol monolayers with a conducting AFM tip,* J. Am. Chem. Soc. **122**, 2970 (2000).

[45] L. D. Qin, S. Park, L. Huang, and C. A. Mirkin, *On-wire lithography,* Science **309**, 113 (2005).

[46] J. G. Kushmerick, D. B. Holt, J. C. Yang, J. Naciri, M. H. Moore, and R. Shashidhar, *Metal-molecule contacts and charge transport across monomolecular layers: Measurement and theory,* Phys. Rev. Lett. **89**, 086802 (2002).

[47] A. M. Rawlett, T. J. Hopson, I. Amlani, R. Zhang, J. Tresek, L. A. Nagahara, R. K. Tsui, and H. Goronkin, *A molecular electronics toolbox,* Nanotechnology **14**, 377 (2003).

[48] E. A. Weiss, R. C. Chiechi, G. K. Kaufman, J. K. Kriebel, Z. Li, M. Duati, M.-A. Rampi, and G. M. Whitesides, *The influence of defects on the electrical characteristics of mercury-drop junctions: A study of self-assembled monolayers (SAMs) of N-alkanethiolates on rough and smooth silver,* J. Am. Chem. Soc. **129**, 4336 (2007).

[49] R. C. Chiechi, E. A. Weiss, M. D. Dickey, and G. M. Whitesides, *Eutectic gallium–indium (EGaIn): A moldable liquid metal for electrical characterization of self-assembled monolayers,* Angew. Chem. Int. Ed. **47**, 142 (2008).

[50] W. Wang, T. Lee, and M. A. Reed, *Mechanism of electron conduction in self-assembled alkanethiol monolayer devices,* Phys. Rev. B **68**, 035416 (2003).

[51] H. B. Akkerman, P. W. M. Blom, D. M. de Leeuw, and B. de Boer, *Towards molecular electronics with large-area molecular junctions,* Nature **441**, 69 (2006).

[52] M. T. González, S. Wu, R. Huber, S. J. van der Molen, C. Schönenberger, and M. Calame, *Electrical conductance of molecular junctions by a robust statistical analysis,* Nano Letter **6**, 2238 (2006).

[53] C. A. Martin, D. Ding, J. K. Sorensen, T. Bjornholm, J. M. van Ruitenbeek, and H. S. J. van der Zant, *Fullerene-based anchoring groups for molecular electronics,* J. Am. Chem. Soc. **130**, 13198 (2008).

[54] S. Wu, M. Gonzalez, R. Huber, S. Grunder, M. Mayor, S. C., and M. Calame, *Molecular junctions based on aromatic coupling,* Nat. Nanotechnol. **3**, 569 (2008).

[55] W. Hong, H. Valkenier, G. Meszaros, D. Z. Manrique, A. Mishchenko, A. Putz, P. M. Garcia, C. J. Lambert, J. C. Hummelen, and T. Wandlowski, *An MCBJ case study: The influence of π-conjugation on the single-molecule conductance at a solid/liquid interface,* Beilstein J. Nanotechnol. **2**, 699 (2011).

[56] M. L. Perrin, C. O. Verzijl, C. A. Martin, A. J. Shaikh, R. Eelkema, J. H. van Esch, J. M. van Ruitenbeek, J. M. Thijssen, H. S. J. van der Zant, and D. Dulić, *Large tunable image-charge effects in single-molecule junctions,* Nat. Nanotechnol. **8**, 282 (2013).

[57] R. Frisenda, M. L. Perrin, H. Valkenier, J. C. Hummelen, and H. S. J. van der Zant, *Statistical analysis of single-molecule breaking traces,* Physics Status Solidi B **250**, 2431 (2013).

[58] M. Frei, S. V. Aradhya, M. Koentopp, M. S. Hybertsen, and L. Venkataraman, *Mechanics and chemistry: Single molecule bond rupture forces correlate with molecular backbone structure,* Nano Lett. **11**, 1518 (2011).

[59] C. Nef, P. Frederix, J. Brunner, C. Schönenberger, and M. Calame, *Force-conductance correlation in individual molecular junctions,* Nanotechnology **23**, 365201 (2012).

[60] M. Frei, S. V. Aradhya, M. S. Hybertsen, and L. Venkataraman, *Linker dependent bond rupture force measurements in single-molecule junctions,* J. Am. Chem. Soc. **134**, 4003 (2012).

[61] L. Venkataraman, J. E. Klare, C. Nuckolls, M. S. Hybertsen, and M. L. Steigerwald, *Dependence of single-molecule junction conductance on molecular conformation,* Nature **442**, 904 (2006).

[62] I. Diez-Perez, J. Hihath, Y. Lee, L. Yu, L. Adamska, M. A. Kozhushner, I. I. Oleynik, and N. Tao, *Rectification and stability of a single-molecular diode with controlled orientation,* Nature Chemistry **1**, 635 (2009).

[63] A. Mishchenko, D. Vonlanthen, V. Meded, B. Marius, C. Li, I. V. Pobelov, A. Bagrets, J. K. Viljas, F. Pauly, F. Evers, M. Mayor, and T. Wandlowski, *Influence of conformation on conductance of biphenyl-dithiol single-molecule contacts,* Nano Lett. **10**, 156 (2010).

[64] I. Diez-Perez, J. Hihath, T. Hines, Z.-S. Wang, G. Zhou, K. Müllen, and N. J. Tao, *Controlling single-molecule conductance through lateral coupling of π-orbitals,* Nat. Nanotechnol. **6**, 226 (2011).

[65] C. Bruot, J. Hihath, and N. Tao, *Mechanically controlled molecular orbital alignment in single-molecule junctions,* Nat. Nanotechnol. **7**, 35 (2012).

[66] J. Widawsky, P. Darancet, J. Neaton, and L. Venkataraman, *Simultaneous determination of conductance and thermopower of single molecule junctions,* Nano Letters **12**, 354 (2012).

[67] A. Batra, P. Darancet, Q. Chen, J. S. Meisner, J. R. Widawsky, J. B. Neaton, C. Nuckolls, and L. Venkataraman, *Tuning rectification in single-molecular diodes,* Nano Lett. **13**, 6233 (2013).

[68] A. Batra, J. S. Meisner, P. Darancet, Q. Chen, C. Steigerwald, M.L. Nuckolls, and L. Venkataraman, *Molecular diodes enabled by quantum interference,* Faraday Discussions **174**, 79 (2014).

[69] M. Baghernejad, D. Z. Manrique, C. Li, T. Pope, U. Zhumaev, I. Pobelov, P. Moreno-García, V. Kaliginedi, C. Huang, W. Hong, C. Lambert, and T. Wandlowski, *Highly-effective gating of single-molecule junctions: an electrochemical approach,* Chem. Commun. **50**, 15975 (2014).

[70] T. Kim, Z. F. Liu, C. Lee, J. Neaton, and L. Venkataraman, *Charge transport and rectification in molecular junctions formed with carbon-based electrodes,* Proc. Natl. Acad. Sci. U. S. A. **111**, 10928 (2014).

[71] V. Kaliginedi, A. V. Rudnev, M. Moreno-García, P. Baghernejad, C. Huang, W. Hong, and T. Wandlowski, *Promising anchoring groups for single-molecule conductance measurements,* Phys. Chem. Chem. Phys. **16**, 23529 (2014).

[72] E. Leary, A. La Rosa, M. T. Gonz'alez, G. Rubio-Bollinger, N. Agraït, and N. Martín, *Incorporating single molecules into electrical circuits. the role of the chemical anchoring group,* Chem. Soc. Rev. **44**, 920 (2014).

[73] M. L. Perrin, F. Prins, C. A. Martin, A. J. Shaikh, R. Eelkema, J. H. van Esch, T. Briza, R. Kaplanek, V. Kral, J. M. van Ruitenbeek, H. S. J. van der Zant, and D. Dulić, *Influence of the chemical structure on the stability and conductance of porphyrin single-molecule junctions,* Angew. Chem. Int. Ed. **50**, 11223 (2011).

[74] M. L. Perrin, C. A. Martin, F. Prins, A. Shaikh, R. Eelkema, J. H. van Esch, J. M. van Ruitenbeek, H. S. J. van der Zant, and D. Dulić, *Charge transport in a zinc-porphyrin single-molecule junction,* Beilstein J. Nanotechnol. **2**, 714 (2011).

[75] R. H. M. Smit, Y. Noat, C. Untiedt, N. D. Lang, M. C. van Hemert, and J. M. van Ruitenbeek, *Measurement of the conductance of a hydrogen molecule,* Nature **419**, 906 (2002).

[76] Y. Kim, H. Song, F. Strigl, H.-F. Pernau, T. Lee, and E. Scheer, *Conductance and vibrational states of single-molecule junctions controlled by mechanical stretching and material variation,* Phys. Rev. Lett. **106**, 196804 (2011).

[77] C.-l. Chiang, C. Xu, Z. Han, and W. Ho, *Real-space imaging of molecular structure and chemical bonding by single-molecule inelastic tunneling probe,* Science **344**, 885 (2014).

[78] S. V. Aradhya and L. Venkataraman, *Single-molecule junctions beyond electronic transport,* Nat. Nanotechnol. **8**, 399 (2013).

[79] S. V. Aradhya, J. S. Meisner, M. Krikorian, S. Ahn, R. Parameswaran, M. L. Steigerwald, C. Nuckolls, and L. Venkataraman, *Dissecting contact mechanics from quantum interference in single-molecule junctions of stilbene derivatives,* Nano Lett. **12**, 1643 (2012).

[80] W. Lee, K. Kim, W. Jeong, L. A. Zotti, F. Pauly, J. C. Cuevas, and P. Reddy, *Heat dissipation in atomic-scale junctions,* Nature **498**, 209 (2013).

[81] J. Park, A. N. Pasupathy, J. I. Goldsmith, C. Chang, Y. Yaish, J. R. Petta, M. Rinkoski, J. P. Sethna, H. D. Abruna, P. L. McEuen, and D. C. Ralph, *Coulomb blockade and the Kondo effect in single-atom transistors,* Nature **417**, 722 (2002).

[82] A. R. Champagne, A. N. Pasupathy, and D. C. Ralph, *Mechanically adjustable and electrically gated single-molecule transistors,* Nano Lett. **5**, 305 (2005).

[83] J. J. Parks, A. R. Champagne, T. A. Costi, W. W. Shum, A. N. Pasupathy, E. Neuscamman, S. Flores-Torres, P. S. Cornaglia, A. A. Aligia, C. A. Balseiro, G. K.-L. Chan, H. D. Abruña, and D. C. Ralph, *Mechanical control of spin states in spin-1 molecules and the underscreened kondo effect,* Science **328**, 1370 (2010).

[84] H. M. Lee, S. M. Jin, H. M. Kim, and Y. D. Suh, *Single-molecule surface-enhanced raman spectroscopy: a perspective on the current status,* Phys. Chem. Chem. Phys. **15**, 5276 (2013).

[85] S. W. Wu, N. Ogawa, and W. Ho, *Atomic-scale coupling of photons to single-molecule junctions,* Science **312**, 1362 (2006).

[86] H. B. Heersche, Z. de Groot, J. A. Folk, H. S. J. van der Zant, C. Romeike, M. R. Wegewijs, L. Zobbi, D. Barreca, E. Tondello, and A. Cornia, *Electron transport through single Mn_{12} molecular magnets,* Phys. Rev. Lett. **96**, 206801 (2006).

[87] E. Burzurí, A. S. Zyazin, A. Cornia, and H. S. J. van der Zant, *Direct observation of magnetic anisotropy in an individual fe_4 single-molecule magnet,* Phys. Rev. Lett. **109**, 147203 (2012).

[88] C. B. Winkelmann, N. Roch, W. Wernsdorfer, V. Bouchiat, and F. Balestro, *Superconductivity in a single-C_{60} transistor,* Nat. Phys. **5**, 876 (2009).

[89] K. J. Franke, G. Schulze, and J. I. Pascual, *Competition of superconducting phenomena and kondo screening at the nanoscale,* Science **332**, 940 (2010).

[90] B. W. Heinrich, L. Braun, J. I. Pascual, and K. J. Franke, *Protection of excited spin states by a superconducting energy gap,* Nat. Phys. **9**, 765 (2013).

[91] H. Vazquez, R. Skouta, S. T. Schneebeli, M. Kamenetska, R. Breslow, L. Venkataraman, and M. S. Hybertsen, *Probing the conductance superposition law in single-molecule circuits with parallel paths,* Nat. Nanotechnol. **7**, 663 (2012).

[92] C. M. Guedon, H. Valkenier, T. Markussen, K. S. Thygesen, J. C. Hummelen, and S. J. van der Molen, *Observation of quantum interference in molecular charge transport,* Nat. Nanotechnol. **7**, 304 (2012).

[93] C. R. Arroyo, S. Tarkuc, R. Frisenda, J. S. Seldenthuis, C. H. M. Woerde, R. Eelkema, F. C. Grozema, and H. S. J. van der Zant, *Signatures of quantum interference effects on charge transport through a single benzene ring,* Angew. Chem. Int. Ed. **52**, 3152 (2013).

[94] V. Rabache, J. Chaste, P. Petit, M. L. Della Rocca, P. Martin, J.-C. Lacroix, R. L. McCreery, and P. Lafarge, *Direct observation of large quantum interference effect in anthraquinone solid-state junctions,* J. Am. Chem. Soc. **135**, 10218 (2013).

[95] H. J. Lee and W. Ho, *Single-bond formation and characterization with a scanning tunneling microscope,* Science **286**, 1719 (1999).

[96] L. Vitali, G. Levita, R. Ohmann, A. Comisso, A. De Vita, and K. Kern, *Portrait of the potential barrier at metal-organic nanocontacts,* Nat. Mater. **9**, 320 (2010).

[97] P. Liljeroth, J. Repp, and G. Meyer, *Current-induced hydrogen tautomerization and conductance switching of naphthalocyanine molecules,* Science **317**, 1203 (2007).

[98] G. V. Nazin, X. H. Qiu, and W. Ho, *Visualization and spectroscopy of a metal-molecule-metal bridge,* Science **302**, 77 (2003).

[99] Y. Sugimoto, P. Pou, M. Abe, P. Jelinek, R. Pérez, S. Morita, and O. Custance, *Chemical identification of individual surface atoms by atomic force microscopy,* Nature **446**, 64 (2007).

[100] L. Gross, F. Mohn, N. Moll, P. Liljeroth, and G. Meyer, *The chemical structure of a molecule resolved by atomic force microscopy,* Science **325**, 1110 (2009).
[101] L. Gross, F. Mohn, N. Moll, B. Schuler, A. Criado, E. Guitián, D. Peña, A. Gourdon, and G. Meyer, *Bond-order discrimination by atomic force microscopy,* Science **337**, 1326 (2012).
[102] K. S. Thygesen and A. Rubio, *Renormalization of molecular quasiparticle levels at metal-molecule interfaces: Trends across binding regimes,* Phys. Rev. Lett. **102**, 046802 (2009).
[103] K. Burke, *Perspective on density functional theory,* J. Chem. Phys. **136**, 150901 (2012).
[104] C. Toher, A. Filippetti, S. Sanvito, and K. Burke, *Self-interaction errors in density-functional calculations of electronic transport,* Phys. Rev. Lett. **95**, 146402 (2005).
[105] K. Kaasbjerg and K. Flensberg, *Strong polarization-induced reduction of addition energies in single-molecule nanojunctions,* Nano Lett. **8**, 3809 (2008).
[106] S. Y. Quek, L. Venkataraman, H. J. Choi, S. G. Louie, M. S. Hybertsen, and J. B. Neaton, *Amine–gold linked single-molecule circuits: Experiment and theory,* Nano Lett. **11**, 3477 (2007).
[107] S. Y. Quek, H. J. Choi, S. G. Louie, and J. B. . Neaton, *Thermopower of amine–gold–linked aromatic molecular junctions from first principles,* ACS Nano **5**, 551 (2011).
[108] J.-D. Chai and M. Head-Gordon, *Systematic optimization of long-range corrected hybrid density functionals,* J. Chem. Phys. **128**, 084106 (2008).
[109] S. Grimme, *Accurate description of van der waals complexes by density functional theory including empirical corrections.* J. Comput. Chem. **25**, 463 (2004).
[110] C. Lee, W. Yang, and R. G. Parr, *Development of the colle-salvetti correlation-energy formula into a functional of the electron density,* Phys. Rev. B **37**, 785 (1998).
[111] X. Blase, C. Attaccalite, and V. Olevano, *First-principles GW calculations for fullerenes, porphyrins, phtalocyanine, and other molecules of interest for organic photovoltaic applications,* Phys. Rev. B **83**, 115103 (2011).
[112] I. Tamblyn, P. Darancet, S. Y. Quek, S. A. Bonev, and J. B. Neaton, *Electronic energy level alignment at metal–molecule interfaces with a GW approach,* Phys. Rev. B **84**, 201402 (2011).
[113] P. Darancet, J. R. Widawsky, H. J. Choi, L. Venkataraman, and J. B. Neaton, *Quantitative current–voltage characteristics in molecular junctions from first principles,* Nano Lett. **12**, 6250 (2012).
[114] M. Dell'Angela, A. Kladnik, G. Cossaro, A. Verdini, M. Kamenetska, I. Tamblyn, S. Y. Quek, J. B. Neaton, D. Cvetko, A. Morgante, and L. Venkataraman, *Relating energy level alignment and amine–linked single molecule junction conductance,* Nano Lett. **10**, 2470 (2010).
[115] M. L. Perrin, E. Burzurí, and H. S. J. van der Zant, *Single-molecule transistors,* Chem. Soc. Rev. **44**, 902 (2015).
[116] S. Datta, *Quantum Transport: Atom to Transistor* (Cambridge University Press, 2005).
[117] J. C. Cuevas and E. Scheer, *Molecular Electronics: An Introduction to Theory and Experiment* (World Scientific, 2010).
[118] M. Paulsson, F. Zahid, and S. Datta, *Handbook of Nanoscience, Engineering, and Technology, Third Edition*, edited by W. A. Goddard III, D. Brenner, S. E. Lyshevski, and G. J. Lafrate (CRC Press, 2012).
[119] H. Haug and A.-P. Jauho, *Quantum Kinetics in Transport and Optics of Semiconductors : Second, Substantially Revised Edition* (Springer Berlin Heidelberg, 2009).
[120] G. D. Scott and D. Natelson, *Kondo resonances in molecular devices,* ACS Nano **4**, 3560 (2010).
[121] J. Moreland and J. W. Ekin, *Electron-tunneling experiments using NB-SN break junctions,* J. Appl. Phys. **58**, 3888 (1985).
[122] C. Zhou, C. J. Muller, M. R. Deshpande, J. W. Sleight, and M. A. Reed, *Microfabrication of a mechanically controllable break junction in silicon,* Appl. Phys. Lett. **67**, 1160 (1995).
[123] A. I. Yanson, G. Rubio Bollinger, H. E. van den Brom, N. Agraït, and J. M. van Ruitenbeek, *Formation and manipulation of a metallic wire of single gold atoms,* Nature **395**, 783 (1998).
[124] E. Scheer, N. Agraït, J. C. Cuevas, A. Levy Yeyati, B. Ludoph, A. Martín-Rodero, G. Rubio Bollinger, J. M. van Ruitenbeek, and C. Urbina, *The signature of chemical valence in the electrical conduction through a single–atom contact,* Nature **394**, 154 (1998).
[125] N. Agrait, A. L. Yeyati, and J. M. van Ruitenbeek, *Quantum properties of atomic-sized conductors,* Phys. Rep. **377**, 81 (2003).
[126] C. Schirm, M. Matt, F. Pauly, J. C. Cuevas, P. Nielaba, and E. Scheer, *A current-driven single-atom memory,* Nat. Nanotechnol. **8**, 645 (2013).
[127] C. A. Martin, R. H. M. Smit, R. van Egmond, H. S. J. van der Zant, and J. M. van Ruitenbeek, *A versatile low-temperature setup for the electrical characterization of single-molecule junctions,* Rev. Sci. Instrum. **82**, 053907 (2011).
[128] M. T. Gruter, L .and Gonzalez, R. Huber, M. Calame, and C. Schönenberger, *Electrical conductance of atomic contacts in liquid environments,* Small **1**, 1067 (2005).

[129] C. A. Martin, J. M. van Ruitenbeek, and H. S. J. van der Zant, *Sandwich-type gated mechanical break junctions,* Nanotechnology **21**, 265201 (2010).

[130] K. Moth-Poulsen and T. Bjornholm, *Molecular electronics with single molecules in solid-state devices,* Nat. Nanotechnol. **4**, 551 (2009).

[131] E. A. Osorio, K. O'Neill, N. Stuhr-Hansen, O. F. Nielsen, T. Bjornholm, and H. S. J. van der Zant, *Addition energies and vibrational fine structure measured in electromigrated single-molecule junctions based on an oligophenylenevinylene derivative,* Adv. Mat. **19(2)**, 281 (2007).

[132] E. Burzurí, Y. Yamamoto, M. Warnock, X. Zhong, K. Park, A. Cornia, and H. S. J. van der Zant, *Franck-condon blockade in a single-molecule transistor,* Nano Letters **14**, 3191 (2014).

[133] W. J. Liang, M. P. Shores, M. Bockrath, J. R. Long, and H. Park, *Kondo resonance in a single-molecule transistor,* Nature **417**, 725 (2002).

[134] A. S. Zyazin, J. W. G. van den Berg, E. A. Osorio, H. S. J. van der Zant, N. P. Konstantinidis, M. Leijnse, M. R. Wegewijs, F. May, W. Hofstetter, C. Danieli, and A. Cornia, *Electric-field controlled magnetic anisotropy in a single molecule,* Nano Lett. **10**, 3307 (2010).

[135] N. J. Tao, *Probing potential-tuned resonant tunneling through redox molecules with scanning tunneling microscopy,* Phys. Rev. Lett. **76**, 4066 (1996).

[136] B. Capozzi, Q. Chen, P. Darancet, M. Kotiuga, M. Buzzeo, J. B. Neaton, C. Nuckolls, and L. Venkataraman, *Tunable charge transport in single-molecule junctions via electrolytic gating,* Nano Lett. **14**, 1400 (2014).

[137] J. Zhang, A. M. Kuznetsov, I. G. Medvedev, Q. Chi, T. Albrecht, P. S. Jensen, and J. Ulstrup, *Single-molecule electron transfer in electrochemical environments,* Chem. Rev. **108**, 2737 (2008).

[138] H. Valkenier, E. H. Huisman, P. A. van Hal, D. M. de Leeuw, R. C. Chiechi, and J. C. Hummelen, *Formation of high-quality self-assembled monolayers of conjugated dithiols on gold: Base matters,* J. Am. Chem. Soc. **133**, 4930 (2011).

[139] M. T. González, E. Leary, R. García, P. Verma, M. A. Herranz, G. Rubio-Bollinger, N. Martín, and N. Agra"it, *Break-junction experiments on acetyl-protected conjugated dithiols under different environmental conditions,* J. Phys. Chem. C **115**, 17973 (2011).

[140] K. Hansen, S. K. Nielsen, M. Brandbyge, E. Laegsgaard, I. Stensgaard, and F. Besenbacher, *Current-voltage curves of gold quantum point contacts revisited,* Appl. Phys. Lett. **77**, 708 (2000).

[141] H. Ohnishi, Y. Kondo, and K. Takayanagi, *Quantized conductance through individual rows of suspended gold atoms,* Nature **395**, 780 (1998).

[142] M. Tsutsui, M. Taniguchi, and T. Kawai, *Fabrication of 0.5 nm electrode gaps using self-reaking technique,* Appl. Phys. Lett. **93**, 163115 (2008).

[143] J. G. Simmons, *Generalized formula for electric tunnel effect between similar electrodes separated by a thin insulting film,* J. Appl. Phys. **34**, 1793 (1963).

[144] C. A. Martin, D. Ding, H. S. J. van der Zant, and J. M. van Ruitenbeek, *Lithographic mechanical break junctions for single-molecule measurements in vacuum: Possibilities and limitations,* New J. Phys. **10**, 065008 (2008).

[145] I. A. Solov'yov, A. V. Yakubovich, P. V. Nikolaev, I. Volkovets, and A. V. Solov'yov, *Meso bio nano explorer – a universal program for multiscale computer simulations of complex molecular structure and dynamics.* Journal of Computational Chemistry **33**, 2412 (2012).

[146] S. A. G. Vrouwe, E. van der Giessen, S. J. van der Molen, D. Dulić, M. L. Trouwborst, and B. J. van Wees, *Mechanics of lithographically defined break junctions,* Phys. Rev. B **71**, 035313 (2005).

[147] C. Untiedt, A. I. Yanson, R. Grande, G. Rubio-Bollinger, N. Agrait, S. Vieira, and J. M. van Ruitenbeek, *Calibration of the length of a chain of single gold atoms,* Phys. Rev. B **66**, 085418 (2002).

[148] M. Tsutsui, K. Shoji, M. Taniguchi, and T. Kawai, *Formation and self-breaking mechanism of stable atom-sized junctions,* Nano Lett. **8**, 345 (2008).

[149] M. Jurow, A. E. Schuckman, J. D. Batteas, and C. M. Drain, *Porphyrins as molecular electronic components of functional devices,* Coord. Chem. Rev. **254**, 2297 (2010).

[150] S. Mohnani and D. Bonifazi, *Supramolecular architectures of porphyrins on surfaces: The structural evolution from 1D to 2D to 3D to devices,* Coord. Chem. Rev. **254**, 2342 (2010).

[151] V. Iancu, A. Deshpande, and S.-W. Hla, *Manipulating kondo temperature via single molecule switching,* Nano Lett. **6**, 820 (2006).

[152] G. Sedghi, K. Sawada, L. J. Esdaile, L. J. Hoffmann, H. L. Anderson, D. Bethell, W. Haiss, S. J. Higgins, and R. J. Nichols, *Single molecule conductance of porphyrin wires with ultralow attenuation,* J. Am. Chem. Soc. **130**, 8582 (2008).

[153] G. V. Qiu, X. H.and Nazin and W. Ho, *Mechanisms of reversible conformational transitions in a single molecule,* Phys. Rev. Lett. **93**, 196806 (2004).

[154] J. Brede, M. Linares, S. Kuck, J. Schwöbel, A. Scarfato, S.-H. Chang, R. Hoffmann, G.and Wiesen-

danger, R. Lensen, P. Kouwer, J. Hoogboom, A. Rowan, M. Bröring, M. Funk, S. Stafström, F. Zerbetto, and R. Lazzaroni, *Dynamics of molecular self-ordering in tetraphenyl porphyrin monolayers on metallic substrates,* Nanotechnology **20**, 275602 (2009).

[155] L. Scudiero, D. E. Barlow, U. Mazur, and K. W. Hipps, *Scanning tunneling microscopy, orbital-mediated tunneling spectroscopy, and ultraviolet photoelectron spectroscopy of metal(II) tetraphenylporphyrins deposited from vapor,* J. Am. Chem. Soc. **123**, 4073 (2001).

[156] Z.-L. Cai, M. J. Crossley, J. R. Reimers, R. Kobayashi, and R. D. Amos, *Density functional theory for charge transfer: The nature of the N-bands of porphyrins and chlorophylls revealed through CAM-B3LYP, CASPT2, and SAC-CI calculations,* J. Phys. Chem. B **110**, 15624 (2006).

[157] N. J. Tao, *Electron transport in molecular junctions,* Nat. Nanotechnol. **1**, 173 (2006).

[158] M. Kamenetska, M. Koentopp, A. C. Whalley, Y. S. Park, M. L. Steigerwald, C. Nuckolls, M. S. Hybertsen, and L. Venkataraman, *Formation and evolution of single-molecule junctions,* Phys. Rev. Lett. **102**, 126803 (2009).

[159] D. Dulić, F. Pump, S. Campidelli, P. Lavie, G. Cuniberti, and A. Filoramo, *Controlled stability of molecular junctions,* Angew. Chem. Int. Ed. **48(44)**, 8273 (2009).

[160] E. A. Osorio, M. Ruben, J. S. Seldenthuis, J.-M. Lehn, and H. S. J. van der Zant, *Conductance switching and vibrational fine structure of a* $[2x2]$ $CoII_4$ *gridlike single molecule measured in a three-terminal device,* Small **6**, 174 (2010).

[161] S. T. Schneebeli, M. Kamenetska, Z. Cheng, R. Skouta, L. Friesner, R. A. Venkataraman, and B. R., *Single-molecule conductance through multiple π–π stacked benzene rings determined with direct electrode-to-benzene ring connections,* J. Am. Chem. Soc. **133**, 2136 (2011).

[162] S. Martin, I. Grace, M. R. Bryce, C. Wang, R. Jitchati, A. S. Batsanov, C. J. Higgins, S. J. Lambert, and R. J. Nichols, *Identifying diversity in nanoscale electrical break junctions,* J. Am. Chem. Soc. **132**, 9157 (2010).

[163] W. Haiss, C. Wang, I. Grace, A. S. Batsanov, D. J. Schiffrin, S. J. Higgins, M. R. Bryce, C. J. Lambert, and R. J. Nichols, *Precision control of single-molecule electrical junctions,* Nat. Mater. **5**, 995 (2006).

[164] M. Ruben, A. Landa, E. Lortscher, H. Riel, M. Mayor, H. Gorls, H. B. Weber, A. Arnold, and F. Evers, *Charge transport through a cardan-joint molecule,* Small **4(12)**, 2229 (2008).

[165] B. Q. Xu and N. J. Tao, *Measurement of single-molecule resistance by repeated formation of molecular junctions,* Science **301**, 1221 (2003).

[166] X. Xiao, B. Xu, and N. Tao, *Conductance titration of single-peptide molecules,* J. Am. Chem. Soc. **126**, 5370 (2004).

[167] R. Liu, S.-H. Ke, H. U. Baranger, and W. Yang, *Negative differential resistance and hysteresis through an organometallic molecule from molecular-level crossing,* J. Am. Chem. Soc. **128**, 6274 (2006).

[168] F. Chen, X. Li, J. Hihath, Z. Huang, and N. J. Tao, *Effect of anchoring groups on single-molecule conductance: Comparative study of thiol-, amine-, and carboxylic-acid-terminated molecules,* J. Am. Chem. Soc. **128**, 15874 (2006).

[169] Y. S. Park, A. C. Whalley, M. Kamenetska, M. L. Steigerwald, M. S. Hybertsen, C. Nuckolls, and L. Venkataraman, *Contact chemistry and single-molecule conductance: A comparison of phosphines, methyl sulfides, and amines,* J. Am. Chem. Soc. **129**, 15768 (2007).

[170] X. Li, J. He, Jin Hihath, B. Xu, S. M. Lindsay, and N. Tao, *Conductance of single alkanedithiols: Conduction mechanism and effect of molecule-electrode contacts,* J. Am. Chem. Soc. **128**, 2135 (2006).

[171] G. Rubio, N. Agraït, and S. Vieira, *Atomic-sized metallic contacts: Mechanical properties and electronic transport,* Phys. Rev. Lett. **76**, 2302 (1996).

[172] L. Venkataraman, J. E. Klare, I. W. Tam, C. Nuckolls, M. S. Hybertsen, and M. L. Steigerwald, *Single-molecule circuits with well-defined molecular conductance,* Nano Lett. **6**, 458 (2006).

[173] J. Reichert, R. Ochs, D. Beckmann, H. B. Weber, M. Mayor, and H. von Lohneysen, *Driving current through single organic molecules,* Phys. Rev. Lett. **88**, 176804 (2002).

[174] J. González, M.T.and Brunner, R. Huber, S. Wu, C. Schönenberger, and M. Calame, *Conductance values of alkanedithiol molecular junctions,* New J. Phys. **10**, 065018 (2008).

[175] H. Ishii, K. Sugiyama, E. Ito, and K. Seki, *Energy level alignment and interfacial electronic structures at organic/metal and organic/organic interfaces,* Adv. Mat. **11(8)**, 605 (1999).

[176] N. Koch, *Energy levels at interfaces between metals and conjugated organic molecules,* J. Phys.: Condens. Matter **20(18)**, 184008 (2008).

[177] S. Braun, W. R. Salaneck, and M. Fahlman, *Energy-level alignment at organic/metal and organic/organic interfaces,* Adv. Mat. **21**, 1450 (2009).

[178] J. Hwang, A. Wan, and A. Kahn, *Energetics of metal-organic interfaces: New experiments and assessment of the field,* Mater. Sci. Eng. R **64**, 1 (2009).

[179] I. Lange, J. Blakesley, J. Frisch, A. Vollmer, N. Koch, and D. Neher, *Band bending in conjugated*

polymer layers, Phys. Rev. Lett. **106**, 216402 (2011).

[180] B. Broker, O. T. Hofmann, G. M. Rangger, P. Frank, R. P. Blum, R. Rieger, L. Venema, A. Vollmer, K. Muellen, J. P. Rabe, A. Winkler, P. Rudolf, E. Zojer, and N. Koch, *Density-dependent reorientation and rehybridization of chemisorbed conjugated molecules for controlling interface electronic structure,* Phys. Rev. Lett. **104**, 246805 (2010).

[181] J. Otsuki, *Stm studies on porphyrins,* Coord. Chem. Rev. **254**, 2311 (2010).

[182] H. Ishii, H. Oji, E. Ito, N. Hayashi, D. Yoshimura, and K. Seki, *Energy level alignment and band bending at model interfaces of organic electroluminescent devices,* J. Lumin. **61**, 87 (2000).

[183] G. Heimel, L. Romaner, E. Zojer, and J.-L. Bredas, *The interface energetics of self-assembled monolayers on metals,* Acc. Chem. Res. **41**, 721 (2008).

[184] L. Romaner, G. Heimel, M. Gruber, J.-L. Bredas, and E. Zojer, *Stretching and breaking of a molecular junction,* Small **2**, 1468 (2006).

[185] F. Amy, C. Chan, and A. Kahn, *Polarization at the gold/pentacene interface,* Org. Electron. **6**, 85 (2005).

[186] J. D. Barr, C. A. Stafford, and J. P. Bergfield, *Effective field theory of interacting π-electrons,* Phys. Rev. B **86**, 115403 (2012).

[187] C. Toher, R. Temirov, A. Greuling, F. Pump, M. Kaczmarski, G. Cuniberti, M. Rohlfing, and F. S. Tautz, *Electrical transport through a mechanically gated molecular wire,* Phys. Rev. B **83**, 155402 (2011).

[188] C. Kergueris, J. P. Bourgoin, S. Palacin, D. Esteve, C. Urbina, M. Magoga, and C. Joachim, *Electron transport through a metal-molecule-metal junction,* Phys. Rev. B **59**, 12505 (1999).

[189] C. J. O. Verzijl and J. M. Thijssen, *DFT-based molecular transport implementation in ADF/BAND,* J. Chem. Phys. C **116**, 24393 (2012).

[190] Y. Xue and M. A. Ratner, *Microscopic theory of single-electron tunneling through molecular-assembled metallic nanoparticles,* Phys. Rev. B **68**, 115406 (2003).

[191] J. Nara, W. T. Geng, H. Kino, N. Kobayashi, and T. Ohno, *Theoretical investigation on electron transport through an organic molecule: Effect of the contact structure,* J. Chem. Phys. **121**, 6485 (2004).

[192] R. B. Pontes, A. R. Rocha, S. Sanvito, A. Fazzio, and A. J. R. da Silva, Ab Initio *calculations of structural evolution and conductance of benzene-1,4-dithiol on gold leads,* ACS Nano **5**, 795 (2011).

[193] J. M. Garcia-Lastra, C. Rostgaard, A. Rubio, and K. S. Thygesen, *Polarization-induced renormalization of molecular levels at metallic and semiconducting surfaces,* Phys. Rev. B **80**, 245427 (2009).

[194] P. Myohanen, R. Tuovinen, T. Korhonen, G. Stefanucci, and R. van Leeuwen, *Image charge dynamics in time-dependent quantum transport,* Phys. Rev. B **85**, 075105 (2012).

[195] N. V. Smith, C. T. Chen, and M. Weinert, *Distance of the image plane from metal surfaces,* Phys. Rev. B **40(11)**, 7565 (1989).

[196] K. Kaasbjerg and K. Flensberg, *Image charge effects in single-molecule junctions: Breaking of symmetries and negative-differential resistance in a benzene single-electron transistor,* Phys. Rev. B **84**, 115457 (2011).

[197] J. B. Neaton, M. S. Hybertsen, and S. G. Louie, *Renormalization of molecular electronic levels at metal-molecule interfaces,* Phys. Rev. Lett. **97**, 216405 (2006).

[198] D. J. Mowbray, G. Jones, and K. S. Thygesen, *Influence of functional groups on charge transport in molecular junctions,* J. Chem. Phys. **128**, 111103 (2008).

[199] Y. Meir and N. S. Wingreen, *Landauer formula for the current through an interacting electron region,* Phys. Rev. Lett. **68**, 2512 (1992).

[200] S. Datta, *Nanoscale device modeling: the Green's function method,* Superlatt. Microstruct. **28**, 253 (2000).

[201] G. te Velde and E. J. Baerends, *Precise density-functional method for periodic structures,* Phys. Rev. B **44**, 7888 (1991).

[202] C. Fonseca Guerra, J. G. Snijders, G. te Velde, and E. J. Baerends, *Towards an order-N DFT method,* Theor. Chem. Acc. **99**, 391 (1998).

[203] G. te Velde, F. M. Bickelhaupt, S. J. A. van Gisbergen, C. Fonseca Guerra, E. J. Baerends, J. G. Snijders, and T. Ziegler, *Chemistry with ADF,* J. Comput. Chem. **22**, 931 (2001).

[204] Y. Xue and M. A. Ratner, *Microscopic study of electrical transport through individual molecules with metallic contacts. I. Band lineup, voltage drop, and high-field transport,* Phys. Rev. B **68**, 115406 (2003).

[205] D. Q. Andrews, R. Cohen, R. P. Van Duyne, and M. A. Ratner, *Single molecule electron transport junctions: Charging and geometric effects on conductance,* J. Chem. Phys. **125**, 174718 (2006).

[206] H. Kondo, H. Kino, J. Nara, T. Ozaki, and T. Ohno, *Contact-structure dependence of transport properties of a single organic molecule between Au electrodes,* Phys. Rev. B **73**, 235323 (2006).

[207] R. M. Martin, *Electronic structure : basic theory and practical methods* (Cambridge University Press,

2004).

[208] Q. Wu and T. Van Voorhis, *Direct optimization method to study constrained systems within density-functional theory,* Phys. Rev. A **72**, 024502 (2005).

[209] M. S. Hybertsen and S. G. Louie, *Electron correlation in semiconductors and insulators: Band gaps and quasiparticle energies,* Phys. Rev. B **34**, 5390 (1986).

[210] F. Aryasetiawan and O. Gunnarsson, *The GW method,* Rep. Prog. Phys. **61**, 237 (1998).

[211] Y. Xue, S. Datta, S. Hong, R. G. Reifenberger, J. I. Henderson, and C. P. Kubiak, *Negative differential resistance in the scanning-tunneling spectroscopy of organic molecules,* Phys. Rev. B **59**, R7852 (1999).

[212] N. P. Guisinger, M. E. Greene, R. Basu, A. S. Baluch, and M. C. Hersam, *Room temperature negative differential resistance through individual organic molecules on silicon surfaces,* Nano Lett. **4**, 55 (2004).

[213] X. Tu, G. Mikaelian, and W. Ho, *Controlling single-molecule negative differential resistance in a double-barrier tunnel junction,* Phys. Rev. Lett. **100**, 126807 (2008).

[214] J. Gaudioso, L. J. Lauhon, and W. Ho, *Vibrationally mediated negative differential resistance in a single molecule,* Phys. Rev. Lett. **85**, 1918 (2000).

[215] I. Kratochvilova, M. Kocirik, A. Zambova, J. Mbindyo, T. E. Mallouk, and T. S. Mayer, *Room temperature negative differential resistance in molecular nanowires,* J. Mater. Chem. **12**, 2927 (2002).

[216] E. D. Mentovich, I. Kalifa, A. Tsukernik, A. Caster, N. Rosenberg-Shraga, H. Marom, M. Gozin, and S. Richter, *Multipeak negative differential resistance molecular device,* Small **4**, 55 (2008).

[217] J. He and S. Lindsay, *On the mechanism of negative differential resistance in ferrocenylundecanethiol self-assembled monolayers,* J. Am. Chem. Soc. **127**, 11932 (2005).

[218] J. Chen, M. A. Reed, A. M. Rawlett, and J. M. Tour, *Large on-off ratios and negative differential resistance in a molecular electronic device,* Science **286**, 1550 (1999).

[219] J. Chen, L. Xu, J. Lin, Y. Geng, L. Wang, and D. Ma, *Negative differential resistance effect in organic devices based on an anthracene derivative,* Appl. Phys. Lett. **89**, 083514 (2006).

[220] D. Fracasso, H. Valkenier, J. C. Hummelen, G. C. Solomon, and R. C. Chiechi, *Evidence for quantum interference in SAMs of arylethynylene thiolates in tunneling junctions with eutectic Ga-In (EGaIn) top-contacts,* J. Am. Chem. Soc. **133**, 9556 (2011).

[221] V. Kaliginedi, P. Moreno-Garcia, H. Valkenier, W. Hong, V. M. Garcia-Suarez, P. Buiter, J. L. H. Otten, J. C. Hummelen, C. J. Lambert, and T. Wandlowski, *Correlations between molecular structure and single-junction conductance: A case study with oligo(phenylene-ethynylene)-type wires,* J. Am. Chem. Soc. **134**, 5262 (2012).

[222] H. Valkenier, C. M. Guedon, T. Markussen, K. S. Thygesen, S. J. van der Molen, and J. C. Hummelen, *Cross-conjugation and quantum interference: a general correlation?* Phys. Chem. Chem. Phys. **16**, 653 (2013).

[223] J. Cornil, Y. Karzazi, and J. L. Bredas, *Negative differential resistance in phenylene ethynylene oligomers,* J. Am. Chem. Soc. **124**, 3516 (2002).

[224] E. Lörtscher, B. Gotsmann, Y. Lee, L. Yu, C. Rettner, and H. Riel, *Transport properties of a single-molecule diode,* ACS Nano **6**, 4931 (2012).

[225] A.-P. Jauho, N. S. Wingreen, and Y. Meir, *Time-dependent transport in interacting and noninteracting resonant-tunneling systems,* Phys. Rev. B **50**, 5528 (1994).

[226] H. Haug and A.-P. Jauho, *Quantum Kinetics in Transport and Optics of Semiconductors* (Springer, Berlin, Heidelberg, 1997).

[227] N. L. Allinger, Y. H. Yuh, and J. H. Lii, *Molecular mechanics. the MM3 force field for hydrocarbons.* Journal of the American Chemical Society **111**, 8551 (1989).

[228] J. Ponder, *Tinker: Software tools for molecular design 6.3,* Washington University School of Medicine: Saint Louis, MO (2014).

[229] T. T. Järvi, A. C. T. van Duin, K. Nordlund, and W. A. Goddard, *Development of interatomic ReaxFF potentials for Au-S-C-H systems,* The Journal of Physical Chemistry A **115**, 10315 (2011).

[230] J. Gottschalck and B. Hammer, *A density functional theory study of the adsorption of sulfur, mercapto, and methylthiolate on* Au(111), The Journal of Chemical Physics **116**, 784 (2002).

[231] M. Paulsson, C. Krag, T. Frederiksen, and M. Brandbyge, *Conductance of alkanedithiol single-molecule junctions: A molecular dynamics study,* Nano Letters **9**, 117 (2009).

[232] P. E. Kornilovitch, A. M. Bratkovsky, and R. Stanley Williams, *Current rectification by molecules with asymmetric tunneling barriers,* Phys. Rev. B **66**, 165436 (2002).

[233] J. Taylor, M. Brandbyge, and K. Stokbro, *Theory of rectification in Tour wires: The role of electrode coupling,* Phys. Rev. Lett. **89**, 138301 (2002).

[234] M. Paulsson, F. Zahid, and S. Datta, *Handbook of Nanoscience, Engineering, and Technology*, edited by W. A. Goddard III, D. Brenner, S. E. Lyshevski, and G. J. Iafrate (CRC Press, 2003).

[235] C. A. Nijhuis, W. F. Reus, and G. M. Whitesides, *Molecular rectification in metal-SAM-metal oxide-metal junctions,* J. Am. Chem. Soc. **131**, 17814 (2009).

[236] J. Hihath, C. Bruot, H. Nakamura, Y. Asai, I. Diez-Perez, Y. Lee, L. Yu, and N. Tao, *Inelastic transport and low-bias rectification in a single-molecule diode,* ACS Nano **5**, 8331 (2011).

[237] K. Stokbro, J. Taylor, and M. Brandbyge, *Do Aviram–Ratner diodes rectify?* J. Am. Chem. Soc. **125**, 3674 (2003).

[238] C. J. O. Verzijl, J. S. Seldenthuis, and J. M. Thijssen, *Applicability of the wide-band limit in DFT-based molecular transport calculations,* J. Chem. Phys. **138**, 094102 (2013).

[239] L. P. Hammett, *Some relations between reaction rates and equilibrium constants.* Chem. Rev. **17**, 125 (1935).

[240] S. Ballmann and H. B. Weber, *An electrostatic gate for mechanically controlled single-molecule junctions,* New J. Phys. **14**, 123028 (2012).

[241] H. Song, K. Youngsang, J. Y. Hee, J. Heejun, and L. Reed, M. A.and Takhee, *Observation of molecular orbital gating,* Nature **462**, 1039 (2009).

[242] M. L. Perrin, E. Galan, R. Eelkema, F. C. Grozema, J. M. Thijssen, and H. S. J. van der Zant, *A single-molecule resonant tunneling diode,* J. Phys. Chem. C **119**, 5697 (2015).

SUMMARY

1. SINGLE-MOLECULE ELECTRONICS

A single molecule constitutes the smallest object of a chemical substance that still retains its composition and properties. In the pursuit of down-sizing electronic components, they therefore constitute the ultimate limit for functional devices. Besides being the smallest entity, single molecules can be tailored to exhibit a variety of physical and chemical properties. Supported by the endless capabilities of synthetic chemistry, molecules can be designed to suit a particular function, ranging from electronic circuit elements (resistors, diodes, transistors, tunnelling diodes, switches, etc...) to sensors (gas, light, pressure, environment, pH, sound, electric field, magnetic field, etc...) and transducers (solar cells, light emitters, thermoelectrics, etc...).

Despite the tremendous opportunities molecules offer, the research field of molecular electronics is still in its infancy, and many challenges remain to be solved. One of them is how to make reliable electric contact to single molecules. Contacting molecules has attracted much attention, both from the electrode side and in terms of molecular design. In particular, questions such as 'how to limit the spread in junction formation' and 'how to form a strong connection between the molecule and the electrodes' do not have a straight forward answer. Another challenge is the reduction of the large discrepancies between experiments and theory. Finally, many processes occurring at the nanoscale, and in particular at the molecule/electrode interface, are not understood yet. For a deeper understanding, one needs to go beyond the standard conductance measurements. Although such measurements allowed for great advances in the field, they do not suffice for solving many of the complex physical process occurring at the nanoscale. For this purpose, additional probes are required, such as the use of magnetic field, thermopower, light/matter interaction, mechanical degrees of freedom and (electrostatic or chemical) gates.

2. THE MECHANICALLY CONTROLLABLE BREAK JUNCTION TECHNIQUE

This dissertation describes the results of a PhD research project directed towards the understanding of the physics governing charge transport through molecules. For this purpose, single molecule were trapped between gold electrodes using the mechanically controllable break junctions (MCBJ) technique in order to electrically address them. In this technique, a lithographically defined gold constriction is broken by bending the substrate in a three-point bending mechanism. Upon rupture of the gold contact, two atomically sharp electrodes are formed, of which the separation can be tuned by adjusting the bending of the substrate. Here lies the strength of the MCBJ. The freshly formed electrodes possess an exceptionally high stability and their spacing can be tuned with picometer precision. When breaking the gold wire in the

presence of a molecule, it can bridge the electrodes, thereby forming a molecular junction. Typical measurements involve low-temperature current-voltage characteristics from which spectroscopic features are extracted. These features correspond to molecular levels which are responsible for charge transport through the molecule. We extensively exploited the mechanical degrees of freedom to investigate the influence the molecular conformation and molecule/electrode interface on charge transport. In addition, three-terminal samples incorporating a gate electrode were developed and employed. The presence of this third electrode allows for changing the electrostatic potential of the molecule, independent from that of the electrodes, thereby modifying the alignment of the transport levels with respect to the Fermi energy of the electrodes. Gated MCBJ samples therefore offer the unique ability for controlling the electrode spacing and at the same time the level alignment. More details about the MCBJ technique and the employed measurement schemes were presented in Chapter 3.

3. RESULTS

In this Thesis, three topics have been covered. In the first part (Chapter 4 and Chapter 5), the junction formation of porphyrin derivatives has been studied. In Chapter 4, room-temperature conductance histograms were employed to investigate the junction formation of porphyrin derivatives. We have demonstrated that porphyrin molecules can form stable bridging molecular junctions even without thiol anchoring groups. Moreover, we found that porphyrins can form a variety of different junction configurations. Adding thiol end groups and pyridine axial groups to the porphyrin backbone, respectively, increases the stability of the junctions and leads to an increased spread in conductance. This is a result of the formation of different junction configurations. In Chapter 5, we combined low-bias statistical measurements with spectroscopy measurements of the molecular levels using current-voltage characteristics. This unique combination allowed us to probe different junction configurations and monitor changes in the molecular level alignment upon fusing or breaking of a molecular junction. Both methods showed that multiple stable single–molecule junction configurations can be obtained by stretching or fusing the junction. In addition, we demonstrated that different ZnTPPdT-Pyr junction configurations can lead to different spectroscopic features for similar low-bias conductance values. Thus, current-voltage spectroscopy measurements can provide additional information compared to statistical low-bias conductance histograms, enabling a more in-depth characterization of charge transport through a single molecule.

Building on the knowledge gained from the current-voltage characteristics recorded in the previous chapters, in the second part of this Thesis (Chapter 6), we investigated the processes occurring at the molecule/electrode interface. To do so, we have studied the alignment of the molecular orbital levels as a function of electrode separation in porphyrin single-molecule junctions using electrostatically-gated MCBJ devices. Using this method we demonstrated experimentally a combined effect of mechanical and electrostatic gating of the molecular levels. We found that both occupied and unoccupied levels move significantly towards the Fermi level

upon reduction of the electrode spacing. We attributed this to a gap renormalization as a result of electrons interacting with image charges in the metal leads. Our findings are corroborated by DFT-based calculations. The experiments showed surprisingly large level shifts, suggesting that image-charge effects may be responsible for the large spread in conductance values that is often observed in single-molecule junctions. Image-charge effects should therefore be considered in quantitative comparisons between computations and experiment in single-molecule junctions.

As the molecule/electrode interface heavily influences charge transport, in the last part of this Thesis, we focused on molecules through which transport is dictated by their intrinsic properties. For this purpose, we have chosen a class of molecules which consists of two similar conjugated parts that are coupled together through a non-conjugated bridge. Charge transport through such molecules can be described using an intuitive model involving two weakly-coupled sites in series. In such a system, current passes through when the resonance condition between the sites is met, *i.e.*, when the energy of the two sites of the molecule is equal. Each of the sites is connected to the electrodes, and upon application of a bias voltage across the molecular junction, part of the voltage drops inside the molecule. This is due to the weak intersite coupling and results in a Stark shift of the energy of the two sites.

In the case of a symmetric molecule, we showed in Chapter 7 that pronounced negative differential conductance is observed. This could be understood as follows: at low bias, for symmetry reasons, the sites have the same energy and the conductance is high. Upon application of a bias voltage, the sites are pulled apart, lifting the resonance condition and reducing the current. The NDC effect could be accurately described by the two-site model. The model is confirmed by DFT + NEGF calculations.

As a follow-up, in Chapter 8 we theoretically studied an asymmetric version of the two-site model. By introducing electron-donating or electron-withdrawing groups to one side of the molecule, the energy of the sites can be changed. This asymmetry is reflected in the current-voltage characteristics, and the molecule behaves as a rectifier. Using DFT + NEGF calculations, we explored the different model parameters and related them to the chemical structure of the molecule. We found that, due to the weak coupling between the two halves of the molecule, the diode properties could be tuned by chemically modifying the molecule. Based on the quantum chemistry calculations, we presented a design for single-molecule diodes based on orbital resonances. The design guidelines yield highly efficient single-molecule rectifiers with rectification ratios up to 1500.

In Chapter 9, we performed experiments on one of the asymmetrically substituted molecules proposed theoretically in Chapter 8. We observed unprecedentedly high rectification ratios of more than 500. In addition, the rectifying properties of the molecule persisted upon large changes in electrode displacement. Finally, we employed electrostatically gateable MCBJ devices to shift the levels responsible for transport. The junction is the first realisation of a gate-tunable single-molecule rectifier. We demonstrated that both the rectification ratio and operating voltage can be tuned with gate. The gate measurements also supported the use of the proposed two-site model to describe transport. In contrast, a model involving just a single level would show a trend in rectification ratio versus gate voltage opposite to the experi-

mental one.

4. OUTLOOK

To reduce the influence of the interface on the device performances, devices should be designed to exploit the intrinsic features of a molecule. In Chapter 7, Chapter 8 and Chapter 9, the first steps towards this goal have been made. From a more general point of view, our results introduce a new and widely applicable route towards more complex molecular components which may contain multiple weakly coupled sites. Moreover, one could envision molecular devices with the use of local gates rather than a single gate. This would allow control over the individual sites, enabling the realisation of novel functional devices with no semiconducting counterpart. As an example, one could consider a multi-level molecule in which the gate terminal is used to transit from negative differential conductance to rectification.

Another important aspect in controlling molecular charge transport is that finite bias effects, such as Stark shifts, play an important role. The problem in studying such effects is that increasing the bias voltage also increases the bias window, and that the measured current is a convolution of both contributions. To disentangle the two contributions, one could combine DC and AC measurements. A DC voltage is then applied to induce shifts of the transmission function. On top of that, a small AC voltage is added to probe the low-bias conductance, without having the drawback of an increased bias window. Combining this method with an electrostatic gate would allow to change the level alignment, thereby creating a direct reconstruction of the bias-shifted transmission function.

Another promising intra-molecular quantum effect is destructive quantum interference (QI). QI occurs when different transport channels have the same amplitude, but an opposite phase. The channels then destructively interfere, resulting in a anti-resonance in the transmission function. This dip, on its turn, results in a very low current. This effect may be very beneficiary in switch applications, or to reduce the reverse current contributions in diode molecules, thereby enhancing their rectification ratios. Although much research has been done in this direction, both theoretically as well as experimentally, no measurement has been reported so far in which the anti-resonance in the transmission has been directly observed. First of all, to be on resonance with the dip and directly measure it, the use of a gate electrode to obtain the correct level alignment may be necessary. Second, close to the dip, although the current should be very low, the slope of the transmission should increase significantly. Thermopower measurement allow for a direct probe of the slope of the transmission, rather than the transmission itself. Combined with a gate electrode, such measurements may yield unambiguous proof for destructive quantum interference.

Combining a gate electrode with thermopower capability may also yield novel applications involving the Seebeck and the Peltier effect. The Seebeck coefficient, and therefore the temperature gradient in a material, depends on the slope of the transmission at the Fermi energy. Using the gate, one could shift a resonance (or anti-resonance) through the Fermi energy. While doing so, the slope of the transmission changes sign, as does the Seebeck coefficient. The ability of reversing the sign of the Seebeck coefficient is a property which no material to date has been showing.

Moreover, close to a (anti-)resonance, the slope in transmission is the largest, yielding very high Seebeck coefficients, and therefore improved thermoelectricity generation. Both effects may find potential applications in novel energy harvesting approaches. The Peltier effect is the opposite of the Seebeck effect and can be used to pump heat, i.e., it converts electricity into temperature gradients. This effect is used in Peltier elements for cooling applications. As for the Seebeck effect, using a gate to sweep the (anti)resonance through the Fermi energy would allow for much larger temperature gradients than nowadays possible and for a gradient reversal.

To conclude, understanding the physical and chemical processes occurring at the nanoscale remains a major challenge but with active research in the field, functional devices may arise with improved performances or even novel functionality in the domain of sensing, solar-energy harvesting, thermoelectricity and catalysis.

SAMENVATTING

1. ELEKTRONICA GEMAAKT VAN EEN ENKEL MOLECUUL

Een enkel molecuul vormt het kleinste onderdeel van een chemische stof dat zijn samenstelling en eigenschappen behoudt. Bij het realiseren van als maar kleinere elektronische componenten vormen zij dus de uiterste limiet. Naast het feit dat ze zo klein zijn, kunnen enkele moleculen ook ontworpen worden met een verscheidenheid aan fysische en chemische eigenschappen. Door de bijna eindeloze mogelijkheden van de synthetische chemie kunnen moleculen dusdanig worden ontworpen dat ze een bepaalde functie vervullen, variërend van elektronische componenten (weerstanden, diodes, transistors, tunneling diodes, schakelaars, enz...) tot sensoren (gas, licht, druk, milieu, pH, geluid, elektrisch veld, magnetisch veld, enz...) en energieomzetters (zonnecellen, lichtbronnen, thermo-elektriciteit, enz...).

Ondanks de enorme kansen die moleculen kunnen bieden, staat het onderzoeksgebied van de moleculaire elektronica nog in de kinderschoenen en bestaan er nog vele horden die overkomen moeten worden. Eén daarvan is het elektrisch contact maken met een enkel molecuul op een betrouwbare manier. Er is veel onderzoek gedaan naar wat de beste manier is om contact te maken met moleculen, zowel van de kant van de elektrodes, als ook op het gebied van het molecuul zelf. Vragen zoals 'hoe kan de variatie in junctieformatie worden beperkt' en 'hoe kan een robuuste binding tussen het molecuul en de elektroden worden gevormd' staan daarbij centraal. Een ander probleem dat zich voordoet, is dat er grote verschillen zijn tussen experimenten en de theoretisch beschrijvingen ervan. Ten slotte, vele processen op de nanoschaal worden nog niet begrepen, en een belangrijk aspect daarvan is de interactie tussen het molecuul en de elektrodes. Voor een beter begrip van die processen moet men verder gaan dan de standaard metingen waarbij alleen de geleiding wordt gemeten. Hoewel dergelijke metingen geleidt hebben tot een grote vooruitgang van het vakgebied, zijn deze dikwijls niet voldoende om de complexe fysische fenomenen die op de nanoschaal plaatsvinden te ontrafelen. Om dit te bereiken zijn extra hulpmiddelen nodig, zoals het gebruik van magnetische velden, thermo-elektrische effecten, interactie tussen licht en materie, mechanische vrijheidsgraden en (elektrostatische of chemische) gates.

2. DE MECHANISCH REGELBARE BREEKJUNCTIE METHODE

Dit proefschrift beschrijft de resultaten van een promotieonderzoek gericht op het begrijpen van de fysica van ladingstransport door enkele moleculen. Om dit te realiseren werden enkele moleculen gevangen tussen goud elektroden. Deze elektroden worden door middel van mechanisch regelbare breekjuncties (MCBJ) gevormd, en met dezelfde methode worden de moleculen ook elektrisch uitgelezen. In dergelijke experimenten wordt een gouddraadje met een dikte van enkele tientallen nanome-

ters gebroken door het substraat waar deze op rust te buigen. Bij het breken van het gouddraadje worden twee atomair scherpe elektroden gevormd waarvan de onderlinge afstand aangepast kan worden door de buiging van het substraat in te stellen. Eén van de voordelen van deze methode is dat de gevormde elektroden beschikken over een uitzonderlijk hoge stabiliteit en dat hun onderlinge afstand met picometer precisie kan worden afgestemd.

Wanneer het gouddraadje wordt gebroken in de aanwezigheid van een molecuul, kan deze de elektroden overbruggen, waardoor een moleculaire junctie ontstaat. Tijdens experimenten worden de spectroscopische eigenschappen van dergelijke juncties uitgelezen, gebruikmakend van stroom-spanning karakteristieken. Hiermee kan men informatie verkrijgen over de moleculaire niveaus die verantwoordelijk zijn voor ladingstransport door het molecuul. In dit werk hebben we uitvoerig gebruik gemaakt van de mechanische vrijheidsgraden die deze techniek biedt en hebben de invloed van de moleculaire conformatie onderzocht. Daarnaast hebben we ook natuurkundige fenomenen bekeken die zich afspelen op het raakvlak van het molecuul en de elektroden. Ten slotte hebben we ook gewerkt aan de ontwikkeling van juncties met een gate elektrode. De aanwezigheid van deze derde elektrode maakt het mogelijk de elektrostatische potentiaal van het molecuul aan te passen ten opzichte van die van de elektroden. Deze juncties bieden daarom de unieke mogelijkheid om mechanische vrijheidsgraden te combineren met de elektrostatische controle over de moleculaire energieniveaus. De MCBJ techniek en de gebruikte meetmethodes worden uitvoerig behandeld in Hoofdstuk 3.

3. RESULTATEN

In dit proefschrift zijn drie thema's aan bod gekomen. In het eerste deel (zie Hoofdstuk 4 en 5) zijn juncties van verschillende porfyrine moleculen bestudeerd. In Hoofdstuk 4, hebben we gebruik gemaakt van kamertemperatuur metingen van de geleiding om de vorming van porfyrine juncties te onderzoeken. We hebben aangetoond dat porfyrine moleculen stabiele moleculaire juncties kunnen vormen, zelfs zonder thiol groepen die normaal gebruikt worden als verankeringspunt van het molecuul met de elektrodes. Bovendien hebben we laten zien we dat porfyrinen een grote verscheidenheid aan junctieconfiguraties kunnen aannemen. Het toevoegen thiol eindgroepen en pyridine groepen verhoogt de stabiliteit van de juncties en leidt tot een toename in de spreiding van de geleiding. Dit is een gevolg van de toename van het aantal mogelijke junctieconfiguraties.

In Hoofdstuk 5 hebben we metingen van de geleiding bij lage spanningen gecombineerd met spectroscopische metingen van de moleculaire niveaus door middel van stroom-spanning metingen. Met deze unieke combinatie hebben we verschillende junctie geometrieën onderzocht en het effect van de onderlinge electrode afstand op de structuur van de moleculaire niveaus bestudeert. Beide methoden laten zien dat er een verscheidenheid aan stabiele junctieconfiguraties bestaat. Daarnaast laten we zien dat verschillende juncties kunnen leiden tot verschillende spectroscopische eigenschappen, terwijl de geleiding bij lage spanningen vergelijkbaar is. Spectroscopische metingen verschaffen dus aanvullende informatie ten opzichte van statistische lage-spanning metingen.

Voortbouwend op de kennis die is opgedaan met behulp van de stroom-spanning metingen in het voorgaande hoofdstuk, onderzoeken we in het tweede deel van dit proefschrift (Hoofdstuk 6) de processen die zich afspelen op het raakvlak van het molecuul met de elektrodes. Om dat voor elkaar te krijgen volgen we de uitlijning van de moleculaire niveaus als functie van de onderlinge elektrodeafstand. Dit doen we opnieuw met behulp van porfyrine moleculen en met MCBJ juncties die nu uitgerust zijn met een gate electrode. Met deze methode combineren we mechanische en elektrostatische controle over de moleculaire niveaus. Onze metingen laten zien dat zowel de bezette als de onbezette energieniveaus aanzienlijk verplaatsen in de richting van het Ferminiveau van de goud electrode wanneer de onderlinge electrode afstand verkleind wordt. Deze renormalisatie van de transportniveaus kennen wij toe aan de interactie van de ladingen op het molecuul met de beeldladingen die in de elektrodes gevormd worden. Onze bevindingen worden bevestigd door DFT-gebaseerde berekeningen. De experimenten tonen verrassend grote niveauverschuivingen aan, wat suggereert dat beeldladingen verantwoordelijk kunnen zijn voor de grote spreiding in geleiding die vaak wordt waargenomen in ladingstransport door enkele moleculen. Deze effecten dienen daarom in rekening gebracht te worden in kwantitatieve vergelijkingen tussen berekeningen en experimenten.

Aangezien de interactie tussen het molecuul en de elektrodes het ladingstransport sterk beïnvloedt, gaan we ons in het laatste deel van dit proefschrift richten op moleculen waarbij transport bepaald wordt door intrinsieke moleculaire eigenschappen. Hiervoor kiezen we een klasse van moleculen die bestaat uit twee soortgelijke geconjugeerde delen die aan elkaar zijn gekoppeld door middel van een niet-geconjugeerd segment. Ladingstransport in dergelijke moleculen kan worden beschreven met behulp van een intuïtief model waarbij twee zwak gekoppelde niveaus in serie zijn geplaatst. Door een dergelijk systeem kan stroom alleen maar lopen wanneer er resonantie plaats vindt tussen de twee helften van het molecuul, in andere woorden, wanneer de energie van beide niveaus gelijk is. Elk niveau staat in verbinding met de elektroden en bij het aanleggen van een spanning over de moleculaire junctie valt een deel van de spanning in het molecuul. Dit is het gevolg van de zwakke koppeling tussen de twee helften en leidt tot een Stark verschuiving van de energie van de twee niveaus.

In het geval van een symmetrisch molecuul laten we in Hoofdstuk 7 zien dat er negatieve differentiële geleiding (NDG) optreedt. Dit kan als volgt uitgelegd worden. Bij een lage spanning zijn de energieën van de twee niveaus gelijk vanwege symmetrie redenen, en is de geleiding hoog. Bij het verhogen van de spanning worden de energieën van de twee niveaus uit elkaar getrokken, waarbij de resonantie tussen de twee helften wordt verbroken. Dit leidt tot een afname van de stroom. Het is belangrijk te vermelden dat het NDG effect zijn oorsprong vindt in een interne resonantie die voortkomt uit de moleculaire structuur. Het NDG effect kan nauwkeurig beschreven worden aan de hand van een twee-niveau model, dat door kwantum chemische berekeningen bevestigd wordt.

Als uitbreiding hierop hebben we in Hoofdstuk 8 een theoretische studie verricht naar een asymmetrische versie van het twee-niveau model. Door het toevoegen van elektrondonerende en/of donerende groepen kan de energie van de niveaus aange-

past worden. Een asymmetrie in het molecuul leidt dan tot een asymmetrie in de stroom-spanning karakteristieken en het molecuul gedraagt zich als een diode. Dit komt doordat resonantie nu alleen bij een bepaalde polariteit van de spanning kan optreden. Gebruikmakend van DFT + NEGF berekeningen onderzoeken we het effect van de chemische structuur op de verschillende parameters van het model. Eén van onze bevindingen is dat de eigenschappen van de diode eenvoudig afgestemd kunnen worden door verschillende zijgroepen te substitueren. Dit is een direct gevolg van de zwakke koppeling tussen de twee helften van het molecuul. Aan de hand van kwantumchemische berekeningen presenteren we richtlijnen om efficiënte diodes te ontwerpen, met een verhouding tussen de stroom in de doorlaatrichting en de sperrrichting tot wel 1500.

In Hoofdstuk 9 hebben wij experimenteel één van de asymmetrische moleculen gemeten die in Hoofdstuk 8 aan bod zijn gekomen. We hebben hoge stroomverhoudingen van meer dan 500 waargenomen. Bovendien bleven de diodeeigenschappen gehandhaafd tijdens grote verplaatsingen van de onderlinge electrodeafstand. Ten slotte hebben we MCBJ juncties gebruikt met een elektrostatisch gate waarmee de energieniveaus die verantwoordelijk zijn voor het ladingstransport door het molecuul verschoven kunnen worden. Hiermee fabriceren wij de eerste diode die uit slechts een enkel molecuul bestaat waarvan de eigenschappen regelbaar zijn door middel van een gate. De gate-metingen bevestigen ook dat het twee-niveau model de correcte beschrijving is voor ladingstransport, in tegenstelling tot een model met slechts één niveau voor de diodeeigenschappen, dat een trend tegengestelde aan die van de metingen voorspelt.

4. VOORUITZICHTEN

Om de invloed van de omgeving, en met name de interactie met de elektrodes te minimaliseren, zouden elektronische circuits moeten worden ontworpen die gebaseerd zijn op intrinsieke moleculaire eigenschappen. In Hoofdstuk 7, 8 en 9 hebben we een eerste stap gezet in deze richting. Vanuit een breder oogpunt gezien beschrijven onze resultaten een nieuwe en breed inzetbare manier om complexere moleculaire componenten te ontwerpen, gebruikmakend van meerdere aan elkaar gekoppelde niveaus. Een verdere uitbreiding zou bijvoorbeeld kunnen zijn om lokale gates te gebruiken, die de energie van afzonderlijke niveaus kunnen regelen. Hiermee zouden elektronische componenten kunnen worden gemaakt waarin bijvoorbeeld de gate ervoor zorgt dat een NDG component in een gelijkrichter kan worden omgezet. Met huidige halfgeleiders is het niet mogelijk om een dergelijke functionaliteit in één te realiseren.

Een ander belangrijk aspect is dat spanningsval in het molecuul en de Stark verschuiving waar we gebruik van hebben gemaakt in het voorgaande, een belangrijk rol spelen in ladingstransport. Echter, wanneer men dit soort effecten wil bestuderen zorgt de toename van de spanning niet alleen voor een verschuiving van de transmissiefunctie, maar ook voor een toename van het *bias window*. Door DC en AC metingen te combinerenom zouden deze twee contributies uit elkaar gehaald kunnen worden. De aangelegde DC zorgt dan voor de veranderingen in de transmissiefunctie, terwijl de AC metingen gebruikt kunnen worden om de geleiding bij een lage spanning te bepalen, zonder het probleem van een te grote bias window te hebben.

Een andere veelbelovend intrinsiek moleculair effect is destructieve kwantuminterferentie (QI). QI treedt op wanneer verschillende transportkanalen dezelfde amplitude hebben, maar een tegenovergestelde fase. Deze kanalen interfereren dan destructief met elkaar, wat leidt tot een anti-resonantie in de transmissiefunctie. Deze antiresonantie gaat gepaard met extreem lage stromen, wat gebruikt zou kunnen worden voor efficiënte schakelaars, of om de lekstroom van een diode te verkleinen. Ondanks het feit dat er veel onderzoek wordt gedaan naar QI, zowel theoretisch als experimenteel, is er nog geen direct waarneming geweest van deze anti-resonantie. Eén van de redenen hiervoor is dat een gateelectrode noodzakelijk is om de Fermienergie precies uitgelijnd te krijgen met de anti-resonantie. Echter, ondanks het feit dat de transmissie laag is, zou de afgeleide ervan juist erg groot moeten zijn. De afgeleide van de transmissie kan direct worden uitgelezen door middel van thermoelektrische metingen. Het gebruik van een gateelectrode in combinatie met thermoelektrische metingen zou dus een uitkomst kunnen bieden om QI direct aan te tonen.

Los van de interesse in QI vanuit een fundamenteel oogpunt, zouden QI moleculen kunnen leiden tot nieuwe toepassingen waar gebruik wordt gemaakt van het Seebeck effect en het Peltier effect. De Seebeck coëfficiënt, en daarmee de spanning die in een materiaal wordt opgewerkt onder invloed van een temperatuurgradiënt hangt af van de afgeleide van de transmissie bij de Fermienergie. Door middel van een gate zou men een (anti)resonantie door het Fermi niveau heen kunnen schuiven en daarmee het teken van de Seebeck coëfficiënt kunnen omdraaien. Voor zover bekend bestaan er geen materialen waarin het teken van het Seebeck coëfficiënt omgedraaid kan worden. Daarnaast zou een QI molecuul over een uitzonderlijk hoge Seebeck coëfficiënt moeten beschikken rond de (anti)resonantie, wat zou kunnen leiden tot een verhoogde productie van thermo-elektriciteit. Het Peltier effect is het tegenovergestelde van het Seebeck effect, waarbij elektriciteit wordt omgezet in een temperatuurgradiënt. Dit effect wordt gebruikt in Peltier koel elementen. Net als voor het Seebeck effect geldt dat wanneer een gateelectrode gebruikt wordt om de (anti)resonantie door de Fermi energie heen te verschuiven, dit zou leiden tot veel hogere temperatuur gradiënten dan momenteel mogelijk is, en voor een ommekeer van die gradiënt.

Samenvattend, het begrijpen van de fysische en chemische processen op de nanoschaal is en blijft een grote uitdaging, maar door veel onderzoek zou het kunnen leiden tot elektrische componenten met nieuwe en/of verbeterde prestaties op het gebied van sensoren, zonne-collectoren, thermo-elektrische devices en katalysatoren.

ACKNOWLEDGMENTS

I have truly enjoyed my time as a PhD student and the research I have been doing. I was lucky to have an excellent supervisor and for sure the nice atmosphere in the group also contributed. Herre, I don't want to thank you just for the outstanding guidance, or for all the aspects of research you tough me. What I am also very grateful for the freedom you gave me in terms of research. I can still remember the start of my PhD when you said I was not bound to any project, just that my research should be about molecules. That allowed me to explore a lot of different aspects of single molecules, from 'being lost' in DFT, to trying desperately to improve the gate samples, or even the thermopower project I started but never had time to continue. Also, I very much enjoyed all the talks outside the lab, at the BBQs and the conferences. Jos T., I am happy you accepted to be in the committee, especially after all the discussions we had about theory, and your help with DFT calculations. In addition, your feedback when writing papers has been invaluable, and for that I am grateful. And then the most colorful person I have ever met, Diana. Thanks for all your help with everything and all the discussions we had. The lab has been very dull and quiet without you. I am happy you could be present at my defense and wish you and Elena all the best in Chile! Jan van Esch and Jan van Ruitenbeek, thank you for being part of my committee and for the collaboration on the porphyrins. Jan van Ruitenbeek, I am also very grateful that the new MCBJ setup stayed in Delft so we could use it. Otherwise I would not have been able to measure half of what I did! Maarten Wegewijs, I am happy you accepted being part of my committee and I enjoyed the chats we had during conferences. Michel Calame, I still remember the time I was in Basel growing nanotubes and breaking carbon fiber composites. It was a beautiful experience and I would like to thank you for the good times inside and outside the lab, and for the many discussions during conferences every since I started my PhD. I am happy you could be part of my committee. Finally, I would like to thank Peter for being substitute in the committee.

I would like to thank Maria, Irma and Dorine for helping me with the administrative stuff, Peter Bloom for helping me with all my problems on the cluster, and Raymond for answering my questions about the electronics, and in particular for making the switch module. Also, Ron, Masha, Tino, you helped me a lot with the setups, pumps, maintenance, etc... Every time I had a question or (more often) a problem, you were there to help me, thank you for that. I also want to express my gratitude to all the staff of the Kavli Nanolab, Frank, Emile, Marc, Marco (2x), Arnold, Anja, Roel, Charles, Hozanna, Eugene, and Ewan, for your advices and the smooth operation of the cleanroom. Finally, I would like to thank Bram, Remco en Jelle for providing me with liquid helium.

Coming to the daily days in the lab, I owe a big part of my practical knowledge to Christian. Thanks for training me on the MCBJ setup and in the cleanroom. I have to say that the MCBJ setup was remarkably well designed, and with little maintenance, it was able to operate 24/7 throughout my entire PhD! In addition, your contribution

to the porphyrin papers is highly appreciated. I would also like to thank Roel and Jeppe for help in the lab when I started as a master student. In the last few years, not a day passed without a discussion with Riccardo. Thanks for all the ideas we discussed, the many conferences we attended together (some even with your xbox) and for being my paranymph. The train trips have definitely become less interesting when you moved to Delft. That brings me to the new generation of PhDs on the break junctions, Nandini, Ignacio and Davide, good luck with continuing the MCBJ legacy! On the experimental side I should also thank Max Kondo, for all the work he did as a master student, for the many many discussions we had and conferences we attended. Good luck with GW! There is also the evil 'magnetic' part of the molecule lab. Thanks Rocco, for the discussions on fabrication and python. Alexandra, your expertise in fabrication has helped me a lot, and thanks for all the chats we had. Rocco and Joshua, thanks for the interesting new project on superconducting electrodes, and thank you Enrique for the collaboration when writing the review paper. From the theory side, I owe a big big thanks to Jos S., the ADF bible of the group, who introduced me to the world of DFT and ADF. I also enjoyed our many discussions, whether it was about railguns, exploding whales or milking cows. My other favorite theorist/banker is Chris, the theorist at the dark side of the corridor. Thank you for the wonderful collaboration and the many chats we had. And, Jose, I am happy you took over the BAND calculations and thanks for helping me with ADF and the calculations on the dihydro molecule. Fatemeh, thanks for all the chats, the ping pong sessions, and the climbing. From the chemistry side, I was lucky to get a lot of help from Elena, Rienk and Ferdinand. Thank you for the fruitful collaboration on the diode. I really enjoyed working together with you, and Nico, I am grateful for the MD calculations. Also from Groningen I received invaluable help. Thank you Hennie en Kees for the molecules, the nice collaboration and the many useful discussions. And of course thanks to the master and bachelor students that helped me during my projects, Max, Adi, Stijn en Ton.

There are also a lot of people in the group I did not had the pleasure to work with, but who contributed greatly the atmosphere. Samir, Ferry, Menno, Edgar, Hidde, Harold, MED lost a part of its soul when you left! Ronald and Ben, thanks for the many chats and for joining me for climbing. Ronald, I am happy you continued climbing, so keep up the good work! Thanks Dejan for teaching me how to pretend to be rich and impress Russian ladies, Julien for the wooden dick that still hangs in the lab, Warner, Vibor and Joshua for being my office mates, and Anna and Sander for the research practicum. I am also a big fan of skiing. Giordano, Dejan, Floris, Max, Rocco, Alessandro and Christian, thanks for the good times at the 'winter retreat' in Courchevel. Andres, Enrique, Carlos, Aday, the food definitely improved when you came to the group. But Michele, you definitely set a new standard! Andrea and Nicola, I hope your ideas with the break juncties will work out, and Andrea, thanks for all the chats we had. Gary, thanks for the most elaborated explanation of the double dot ever. And of course thanks to the rest of the group: Santiago, Shun, Venkatesh, Big Ben, Mingyun, Anastasia, Robin, Mafalda, Dirk, Emre, Ranko, Vera, Martijn, Samer, Simmon and Richard. Thanks you all for making MED a really nice place to work. Many thanks also to Jan van Oostaay, Hedde, Jelmer, Jetty, Bob, Vincent, Orkide, Lena, Julia, Gesa, Marije, Simone, Maddy and Jan van Ruitenbeek for the enjoyable platform meetings and the great organisation of the spring schools!

I am also very grateful to all my friends and family. Vincent and Jerome, thanks for all the good times during our physics study and the many 'voute avonden', where the discussion level usually dropped very soon and remained low for the rest of the evening. I would also like to thank the ASAC for all the climbing weekends in Belgium, Germany and France and other activities. I met to many great ASAC people to name everyone here, but I would like to thank in particular some of the ones who helped me to become instructor. Thank you Bas, Jeroen, Jesper and Elout! I would also like to mention some of the people I climbed with. Sytse, Julius, Sylvan, Boris and Menno, thanks for the nice climbs. Especially Sytse for quite a few trips to the alps, although we ended up several times in the zero star hotel of the Aiguille du Midi! Mark and Guus, I enjoyed doing the BOTS with you. Koen, we did some unbelievably tiring races together. 32 hours ... but we surely did a great job! Life is good! Marco and Linda, thanks for all the trainings, climbing sessions and valuable lessons. I especially enjoyed the trainings at your place. Marco, thanks also for being the DJ at the party! Ignace, thanks for being a great friend for all those years, and I am happy to have you as my paranymph. And then my sweet Asja, thank you for your love, for always being there for me and for taking good care of me. You're my angel with a heart of gold. Peter, Thea, Mischa, thank you for everything and I am in particular very grateful for your hospitality, when I spend more time at your place than I did at home! Wesh les cousins, heureux que vous soyez venu de France pour la soutenance. Merci pour tous les bons moments et bien sûr les visites inoubliables à Amsterdam et au quartier! Et un grand merci à tout le reste de la famille (qui ne cesse de s'agrandir). Et bien sûr Vincent, Kim, papa et maman pour le soutien quotidien toutes ces années, et pour tous les bons moments. Sans vous je n'aurais jamais pu arriver où j'en suis aujourd'hui.

About the author

Mickael Lucien Perrin

13-08-1987 Born in Thonon-les-Bains, France.

Education

1999-2005 High School
Barlaeus Gymnasium, Amsterdam, the Netherlands

2005–2008 Bachelor Applied Physics
Delft University of Technology, Delft, the Netherlands
Thesis: Anisotropic Dry Etching of Silicon at -40°C Using High Density $SF_6/O_2/SiF_4$ Plasma's
Supervisors: Ing. Marc R. Zuiddam & Dr. Emile W.J.M. van der Drift

2008–2010 Master Applied Physics (*cum laude*)
Delft University of Technology, Delft, the Netherlands
Thesis: Electronic Transport Through Single Porphyrin Molecules : Two- and Three-Terminal Characterization
Supervisors: Dr. Diana Dulić & Prof. dr. ir. Herre S.J. van der Zant

2009 Internship
Univsersity of Basel, Basel, Switzerland
Title: Advanced Carbon Fibers for Next Generation Toughened Composites: Gecko Like Interfaces
Supervisors: Dr. Michel Calame, Dr. Matthias Gäber & Prof. dr. Christian Schönenberger

2011–2015 PhD
Delft University of Technology, Delft, the Netherlands
Title: Charge Transport Through Single-Molecule Junctions : Experiments and Theory
Promotor: Prof. dr. ir. H.S.J. van der Zant

List of Publications

1. **Mickael L. Perrin**, Ferry Prins, Christian A. Martin, Ahson J. Shaikh, Rienk Eelkema, Jan H. van Esch, Tomas Briza, Robert Kaplanek, Vladimir Kral, Jan M. van Ruitenbeek, Herre S.J. van der Zant, Diana Dulić, *Influence of the Chemical Structure on the Stability and Conductance of Porphyrin Single-Molecule Junctions*, Angewandte Chemie International Edition **50**, 11223–11226 (2011).

2. **Mickael L. Perrin**, Christian A. Martin, Ferry Prins, Ahson J. Shaikh, Rienk Eelkema, Jan H. van Esch, Jan M. van Ruitenbeek, Herre S.J. van der Zant, Diana Dulić, *Charge transport in a zinc–porphyrin single-molecule junction*, Beilstein Journal of Nanotechnology **2**, 714–719 (2011).

3. Venkatesh Seshan, Carlos R. Arroyo, Andres Castellanos-Gomez, Ferry Prins, **Mickael. L. Perrin**, S. D. Janssens, Ken Haenen, Milos Nesládek, Ernst J. R. Sudhölter, Louis C. P. M. de Smet, Herre S. J. van der Zant, and Diana Dulić,*Current-induced nanogap formation and graphitization in boron-doped diamond films*, Applied Physics Letters **101**, 193106–(2012)

4. **Mickael L. Perrin**, Christopher J. O. Verzijl, Christian A. Martin, Ahson J. Shaikh, Rienk Eelkema, Jan H. van Esch, Jan M. van Ruitenbeek, Joseph M. Thijssen, Herre S. J. van der Zant and Diana Dulić, *Large tunable image-charge effects in single-molecule junctions*, Nature Nanotechnology **8**, 282–287 (2013).

5. Riccardo Frisenda, **Mickael L. Perrin**, Hennie Valkenier, Jan C. Hummelen and Herre S. J. van der Zant, *Statistical analysis of single-molecule breaking traces*, physica status solidi (b) **250**, 2431–2436 (2013).

6. **Mickael L. Perrin**, Riccardo Frisenda, Max Koole, Johannes S. Seldenthuis, Jose A. Celis Gil, Hennie Valkenier, Jan C. Hummelen, Nicolas Renaud, Ferdinand C. Grozema, Joseph M. Thijssen, Diana Dulić and Herre S. J. van der Zant, *Large negative differential conductance in single-molecule break junctions*, Nature Nanotechnology **9**, 830–834 (2014).

7. **Mickael L. Perrin**, Enrique Burzurí, H. S. J. van der Zant, *Single-molecule transistors*, Rev. Chem. Soc. **44**, 902–919 (2015).

8. **Mickael L. Perrin**, Elena Galán, Rienk Eelkema, Ferdinant C. Grozema, Joseph M. Thijssen, Herre S.J. van der Zant, *A single-molecule resonant tunneling diode*, J. Phys. Chem. C, **119**, 5697–5702 (2015).

9. Riccardo Frisenda, Simge Tarkuc, Elena Galán, **Mickael L. Perrin**, Rienk Eelkema, Ferdinand C. Grozema, and Herre S. J. van der Zant, *Electrical properties and mechanical stability of anchoring groups for single-molecule electronics*, Accepted in Beilstein Journal of Nanotechnology.

10. Christopher J.O. Verzijl, Jose A. Celis Gil, **Mickael L. Perrin**, Diana Dulić, Herre S.J. van der Zant, and Joseph M. Thijssen, *Image Effects in Transport at Metal-Molecule Interfaces*, Submitted.

11. **Mickael L. Perrin**, Elena Galán, Rienk Eelkema, Ferdinant C. Grozema, Joseph M. Thijssen, Herre S. J. van der Zant, *A gate-tunable single-molecule diode with high rectification ratios*, Submitted.

12. **Mickael L. Perrin**, Riccardo Frisenda, and Herre S. J. van der Zant, *Inelastic electron tunneling spectroscopy in OPE3 single-molecule junctions*, Submitted.

13. Elena Galán, **Mickael L. Perrin**, Ferdinand Grozema, Herre S. J. van der Zant, Rienk Eelkema, *Synthesis of Unsymmetrically Substituted 1,2-bis(4-bromophenyl)ethane Wires: Key Intermediates for Single-Molecule Diodes*, Submitted.

Patents

1. Michel Calame, Matthias Gräber, **Mickael L. Perrin**, Christian Schönenberger, *Process to grow carbon nanotubes onto fibers*, Patent WO 2012019819 A1.

Journal Covers

1. Back cover :Physica status solidi (b), volume **250** Issue 11, 2013.

2. Front cover : Chemical Society Reviews special Issue *Molecular Wires*, **2015**.

(a) (b)

Covers. (**a**) Back cover PSS(b). (**b**) Front cover Chemical Society Reviews.